

Birthe Rubehn

# **Polymer-Based Microimplants for the Neurosciences**

Dissertation zur Erlangung des Doktorgrades  
der Technischen Fakultät der Albert-Ludwigs-Universität  
Freiburg im Breisgau

Oktober 2010





**Dekan**

Prof. Dr. Bernd Becker

**Gutachter**

Prof. Dr. Thomas Stieglitz (Freiburg)

Prof. Dr. Ulrich G. Hofmann (Lübeck)

**Tag der Abgabe:** 13.10.2010

**Tag der Prüfung:** 15.12.2010

Dipl.-Ing. Birthe Rubehn

Lehrstuhl für Biomedizinische Mikrotechnik

Institut für Mikrosystemtechnik (IMTEK)

Technische Fakultät

Albert-Ludwigs-Universität Freiburg im Breisgau





# Abstract

This thesis describes the development and fabrication of flexible MEMS-processed implants and their application in neuroscientific research. The standard fabrication process of polyimide-platinum-polyimide thin-films on wafer-level was used and further developed to manufacture microelectrodes that meet the demands emerging from certain fields of contemporary neuroscientific research.

In the neuroengineering community, polyimide has been proposed as a suitable material for flexible and chronic microimplants. As it was also used as a substrate material in this work, an *in vitro* study on the long-term mechanical properties of three commercially available polyimides was conducted with micro-processed specimens stored in phosphate buffered saline at different temperatures over the course of 20 months.

A highly flexible 252-channel epicortical electrode array was developed for high-channel chronic recording from large areas of the primate cortex in the field of cognitive neuroscience. Apart from interfaces for the brain surface, penetrating approaches have been investigated. A shaft microelectrode with multimodal capabilities was fabricated in order to contact the brain with fluids, light and electrode recording sites. This microdevice can be chronically implanted to conduct optogenetic experiments in rodents. The polymer-based microelectrodes presented here can be implemented in different applications, opening new possibilities for basic neuroscientific research.



# Kurzbeschreibung

Diese Arbeit beschreibt die Entwicklung und Realisierung mikrotechnisch hergestellter Implantate und ihre Anwendung in der neurowissenschaftlichen Forschung. Der Standardherstellungsprozess für Polyimid-Platin-Polyimid-Dünnschichten auf Waferoberfläche wurde benutzt und für die Anforderungen spezieller Fragestellungen der Neurowissenschaften weiterentwickelt.

Im Bereich der Neurotechnik wird Polyimid schon lange als ein mögliches Material für chronische Nervenimplantate vorgeschlagen. Da es auch in der vorliegenden Arbeit als Substratmaterial verwendet wurde, wurde eine Langzeitstudie mit drei kommerziell erhältlichen Polyimiden durchgeführt. Über einen Zeitraum von 20 Monaten wurden mikrotechnisch hergestellte Probekörper in phosphatgepufferter Kochsalzlösung bei verschiedenen Temperaturen gelagert und ihre mechanischen Eigenschaften monatlich untersucht.

Für das Gebiet der kognitiven Neurowissenschaften wurde ein flexibles, epikortikales Elektrodenarray mit 252 Elektrodenflächen für die hochkanalige Ableitung großer Kortexareale des Primaten entwickelt. Neben Nervenschnittstellen für die Gehirnoberfläche wurden auch penetrierende Ansätze verfolgt. Eine schaftförmige Mikroelektrode wurde hergestellt, die es ermöglicht tief liegende Gehirnareale der Maus elektrisch, optisch und mit Flüssigkeiten zu kontaktieren. Diese chronisch implantierbare Schaftelektrode vereinigt alle Modalitäten in einem Implantat, die für die Durchführung optogenetischer Versuche benötigt werden. Diese polymerbasierten Mikroelektroden können für verschiedenste Anwendungen eingesetzt werden und eröffnen neue Möglichkeiten für die neurowissenschaftlichen Grundlagenforschung.



# Table of Contents

<b>1</b>	<b>Introduction</b>	<b>1</b>
<b>2</b>	<b>Neuroscience</b>	<b>4</b>
2.1	A Brief History of Neuroscience.....	4
2.2	Neuroscience Today.....	10
2.2.1	The Binding Problem .....	11
2.2.2	The Microcircuitry of Fear Conditioning .....	13
<b>3</b>	<b>The Nervous System</b>	<b>16</b>
3.1	The Neuron.....	16
3.2	The Brain.....	19
3.2.1	The Cerebral Cortex .....	20
3.2.2	The Meninges.....	21
<b>4</b>	<b>Interfacing the Brain</b>	<b>22</b>
4.1	Standard Electrical Brain Signals .....	23
4.2	Concepts of Neurotechnical Interfaces to the Brain.....	26
4.2.1	The Electrode-Electrolyte Interface.....	26
4.2.2	Precision Engineered Electrodes.....	31
4.2.3	MEMS-based Electrodes .....	40
4.2.4	Flexible Polymer-Based MEMS Electrodes .....	44
4.2.5	Possibilities and Limitations of MEMS Electrodes .....	50
4.3	Assessment of Interface Concepts .....	52
4.4	Clinical Applications Today.....	55
4.5	Fluidic Contact to Neural Tissue.....	58
4.5.1	Fundamentals of Microfluidic Channels .....	59
4.5.2	Integration of Channels into Polymer-Based Implants .....	60
4.6	Optical Stimulation of Neural Tissue.....	61
4.6.1	Optical Waveguide Fundamentals .....	62
4.6.2	Polymer-Based Optical Waveguides .....	66
<b>5</b>	<b>Materials</b>	<b>68</b>
5.1	Polyimide.....	68
5.1.1	Polyimide Fundamentals.....	69
5.1.2	PI2611 .....	70
5.1.3	U-Varnish-S .....	71
5.1.4	Durimide 7510 .....	71
5.2	SU-8 .....	71

<b>6</b>	<b>Aim and Own Approach</b>	<b>73</b>
6.1	Aim of this Thesis .....	73
6.2	Own Approach.....	73
<b>7</b>	<b>Polyimide Material Testing</b>	<b>76</b>
7.1	Test Paradigms and Methods.....	76
7.1.1	Tensile Tests .....	76
7.1.2	Gravimetric Analysis.....	78
7.1.3	Optical Analysis.....	78
7.1.4	Measurement of Foil Defects.....	79
7.2	Results .....	80
7.3	Discussion .....	90
<b>8</b>	<b>ECoG-Electrode Array</b>	<b>97</b>
8.1	Material and Methods.....	99
8.1.1	Implant Layout.....	99
8.1.2	MEMS Processing.....	100
8.1.3	Assembly and Packaging .....	101
8.1.4	Electrode Characterization .....	102
8.1.5	Implantation .....	103
8.1.6	Recordings .....	103
8.2	Results .....	104
8.2.1	In Vitro .....	104
8.2.2	In Vivo .....	107
8.3	Discussion.....	109
<b>9</b>	<b>Transdural Shaft Electrodes</b>	<b>112</b>
9.1	Implant Design .....	112
9.1.1	Insertion Tool and Implantation Concept.....	112
9.1.2	Polyimide Shaft Electrode .....	114
9.2	Manufacturing and Assembly .....	114
9.2.1	MEMS Processing of the Polyimide Shaft .....	114
9.2.2	MEMS Processing of the U-profile.....	114
9.2.3	Assembly and Packaging .....	115
9.2.4	Artificial Brain Model.....	115
9.2.5	Implantation and Recording.....	116
9.3	Results .....	116
9.3.1	In Vitro .....	116
9.3.2	In Vivo .....	117
9.4	Discussion.....	119
<b>10</b>	<b>Multimodal Electrodes</b>	<b>121</b>
10.1	Implant Concept .....	121

10.2	MEMS Processing .....	122
10.3	Hybrid Assembly .....	123
10.4	In Vitro Results .....	124
10.4.1	Characterization of the Fluidic Channel .....	126
10.4.2	Characterization of the Optical Waveguide .....	126
10.5	In Vivo Results .....	128
10.5.1	Experimental Procedure .....	128
10.5.2	First Results .....	128
10.6	Discussion .....	128
10.6.1	In Vitro .....	128
10.6.2	In Vivo .....	130
<b>11</b>	<b>Discussion</b>	<b>131</b>
<b>12</b>	<b>Summary</b>	<b>137</b>
<b>13</b>	<b>Outlook</b>	<b>139</b>
	<b>Literature</b>	<b>141</b>
	<b>Own Publications</b>	<b>170</b>
	<b>Curriculum Vitae</b>	<b>174</b>
	<b>Acknowledgements</b>	<b>175</b>

## List of Figures

Fig. 2.1.	Drawing made by Ramón y Cajal depicting the different layers of the human visual cortex .....	5
Fig. 2.2.	Electrical signals of the brain and the heart recorded with a string galvanometer by Berger .....	6
Fig. 2.3.	Brodmann's classification of the human cortex based on its cytoarchitecture..	8
Fig. 2.4.	The sensory and motor homunculus as published by Penfield .....	9
Fig. 3.1.	The first published intracellular recording of an action potential .....	17
Fig. 4.1.	Physical representation of the three different types of charge transfer across a metal-electrolyte interface .....	27
Fig. 4.2.	Basic equivalent circuit of an electrode-electrolyte interface .....	28
Fig. 4.3.	Signal distortion of a rectangular current pulse passed in saline solution and recorded with different electrode materials .....	30
Fig. 4.4.	SEM micrograph of Hubel's microelectrodes .....	32
Fig. 4.5.	SEM micrograph of a stereotrode .....	33
Fig. 4.6.	Tetrode manufactured by Thomas Recording GmbH .....	33
Fig. 4.7.	Drawing of the electrode wire array manufactured by Krüger .....	34

## List of Figures

---

Fig. 4.8.	Sketch of the implantation site of the floating electrode introduced by Salcman .....	35
Fig. 4.9.	Sketch of the manufacturing process of Barna's shaft electrode.....	37
Fig. 4.10.	Sketch of the manufacturing process and an assembled shaft electrode with a linear array as published by Jellema.....	40
Fig. 4.11.	Sketch of the first micromachined electrode array made for neural recording by Wise.....	41
Fig. 4.12.	Processing steps and a photograph of a micromachined Michigan Probe ....	41
Fig. 4.13.	Photograph of an assembled Michigan Array .....	42
Fig. 4.14.	SEM micrograph of the Utah Array .....	42
Fig. 4.15.	Photograph of an assembled NeuroProbes Array.....	43
Fig. 4.16.	PI-based cuff electrodes, Hybrid cuff electrode combining PI with silicone, Schematic and photograph of a PI-based sieve electrode.....	45
Fig. 4.17.	Intracortical two by three shaft array made of PI.....	46
Fig. 4.18.	Design concept of a foldable PI ribbon cable with an integrated electrode array .....	47
Fig. 4.19.	Flexible PI-based electrode array: Schematic of the array placement in the rat and a photograph of the assembled array.....	48
Fig. 4.20.	Flexible PI-based microelectrodes with integrated fluidic channels.....	49
Fig. 4.21.	Foreign body reaction of mammalian tissue to a synthetic biomaterial over time.....	53
Fig. 4.22.	Incidence of a ray of light on a core-to-cladding interface .....	65
Fig. 4.23.	SU-8 waveguide integrated on a Michigan.....	67
Fig. 5.1.	Chemical structure of the imide group .....	69
Fig. 5.2.	The imidization process of a PMDA-ODA type PI (Kapton).....	70
Fig. 5.3.	Chemical structure of the BPDA-PPD type PI.....	70
Fig. 5.4.	Chemical structure of the epoxy oligomer EPON contained in SU-8 .....	72
Fig. 7.1.	Measurement set-up for defect detection.....	79
Fig. 7.2.	Exemplary stress-strain curve with specific values .....	81
Fig. 7.3.	Stress-strain curves of different samples of PI2611 .....	81
Fig. 7.4.	Overview of the tensile test results .....	83
Fig. 7.5.	The development of the mass of a PI film (Upilex25S, UBE) stored in PBS at 85 °C .....	86
Fig. 7.6.	The development of the mass of PI films (Upilex25S, UBE) stored in PBS at 37 °C, 60 °C, and 85 °C and in deionized water at 85 °C.....	86
Fig. 7.7.	Scanning electron microscope picture of a crease in an Upilex25S foil.....	87
Fig. 7.8.	Fourier transform infrared spectroscopy (FTIR) measurement of Upilex25S foils.....	88
Fig. 7.9.	X-Ray Diffractometry (XRD) of Upilex25S.....	88
Fig. 7.10.	XPS measurement of the Upilex25S foils .....	89



Fig. 7.11.	Gas bubble caused by a defect in the PI layer .....	90
Fig. 7.12.	SEM photograph of the edge of a tensile test specimen structured with an oxygen plasma.....	91
Fig. 8.1.	Three-dimensional plastic model of the macaque brain made by using MRI data .....	98
Fig. 8.2.	Schematic diagram of the flexible foil and its position .....	99
Fig. 8.3.	Layout of the ECoG-array with 252 electrodes on 11 fingers .....	100
Fig. 8.4.	Process steps of the electrode array foil .....	101
Fig. 8.5.	Soldering procedure of the omnetics connectors into the PI foil .....	102
Fig. 8.6.	The complete soldering jig, a cross-sectional view of a slot with the foil and a connector in place while soldering.....	102
Fig. 8.7.	Fully assembled electrode array; the diameter of the coin is 16 mm. ....	104
Fig. 8.8.	Impedance spectra of all 252 electrodes of the array .....	105
Fig. 8.9.	The electrical impedance spectrum of two neighbouring connector paths....	106
Fig. 8.10.	The input impedance of Plexon's headstage HST/32V-G20.....	106
Fig. 8.11.	Example of 3 s of local field potential (LFP) activity observed in 12 of the 252 channels of the ECoG-electrode array .....	107
Fig. 8.12.	Comparison between average and single trials of stimulus locked LFPs after implantation surgery .....	108
Fig. 8.13.	Signal stability over time: The development of the beta, alpha, and delta-theta band power over implantation time.....	109
Fig. 9.1.	Insertion tool comprising one tapered tungsten rod to penetrate the dura mater and cortical tissue .....	113
Fig. 9.2.	Schematic of the transdural shaft concept .....	113
Fig. 9.3.	Schematic cross-section of the U-profile processing .....	114
Fig. 9.4.	Direct connection of a PI shaft electrode and a SMD connector.....	115
Fig. 9.5.	Scanning electron micrograph of an assembled transdural shaft electrode..	116
Fig. 9.6.	Electrical impedance spectroscopy of 8 electrode sites from one transdural shaft .....	117
Fig. 9.7.	Insertion of a transdural shaft into the brain phantom.....	117
Fig. 9.8.	Event related potentials in the LFP signal .....	118
Fig. 9.9.	Event related MUA signals of one trial recorded with two electrode .....	118
Fig. 9.10.	The thresholded waveforms of MUA signals recorded in 240 trials .....	119
Fig. 10.1.	Schematic diagram of the polymer-based shaft electrode assembly with electrode sites, an optical waveguide, and a microchannel.....	122
Fig. 10.2.	MEMS process steps of a PI shaft with integrated SU-8 waveguide .....	123
Fig. 10.3.	Fully assembled multimodal shaft electrode with electrical connector, optical adapter and fluidic adapter .....	124
Fig. 10.4.	Photograph of the tip of the multimodal shaft electrode from below. ....	125
Fig. 10.5.	Electrical impedance spectroscopy of 9 electrode sites from one multimodal shaft.....	125

Fig. 10.6. The flow rate as a function of fluid pressure.....126

Fig. 10.7. The waveguide's output power as a function of waveguide length.....127

## List of Tables

Tab. 4.1 Classification of recording techniques of brain signals.....23

Tab. 4.2 Classification of standard electrical brain signals.....24

Tab. 4.3: Overview of the commercially available, handcrafted multiple  
microelectrodes and their reported use in science.....38

Tab. 5.1 Overview of the material properties of the three tested PIs.....69

Tab. 7.1 Number of measured defects.....90

Tab. 8.1. Dimensions and number of electrodes of different ECoG arrays  
used in research and clinical practice .....97

## List of Symbols

Symbol	Unit	Description
$A$	%	water absorption
$C_H$	F	Helmholtz double layer capacity
$c$	m/s	light velocity in vacuum
$cl$	dB	coupling loss
$E$	GPa	Young's modulus
$H$	m	channel height
$K$	J/K	Boltzmann constant ( $1.3806504 \cdot 10^{-23}$ K/J)
$L$	m	tube length (Hagen-Poiseuille)
$m_{dry}$	g	foil mass after drying for 24 h at 85 °C
$m_{im}$	g	foil mass after immersion
$n_1$		refractive index of the waveguide core
$n_2$		refractive index of the waveguide cladding
$n_{medium}$		refractive index of a certain medium
$P_{out}$	W	output power
$P_{in}$	W	input power
$p$		probability value
$Q$	μL/min	volumetric flow rate
$Q_{inj}$	μC/cm <sup>2</sup>	charge injection capacity
$Q_{10}$		reaction rate coefficient
$R$	Ω	Ohmic electrode resistance

$r$	m	radius of the circular cross-section of a tube
$R_{ac}$	$\Omega$	access resistance
$R_F$	$\Omega$	Faraday resistance
$S$	m	liquid-solid-gas interface line
$T_{at}$	K	ambient temperature
$T_{el}$	K	elevated test temperature
$time_{at}$	months	time duration of the usage at the ambient temperature $T_{at}$
$time_{el}$	months	time duration of the test at the elevated temperature $T_{el}$
$v_{medium}$	m/s	speed of light in a certain medium
$w$	m	channel width
$U_N$	V	Johnson noise
$z$	m	distance along a waveguide
$\alpha$	$\text{cm}^{-1}$	loss factor
$\alpha_{dB}$	dB/cm	loss factor in dB
$\gamma$	N/m	surface tension coefficient
$\Delta f$	Hz	bandwidth
$\Delta P$	Pa	pressure drop
$\varepsilon_{max}$	%	strain at break
$\eta$	Pa·s	dynamic viscosity
$\Theta$	°	deflection angle in XRD measurement
$\theta$	°	wetting angle
$\theta_C$	°	critical angle of incident
$\sigma_{max}$	MPa	tensile strength
$\sigma_{10}$	MPa	stress at 10 % strain

## Abbreviations

BCB	benzocyclobutene
BCI	brain computer interface
BOLD	blood-oxygen-level dependence
BPDA-PPD	biphenyldianhydride / 1,4-phenylenediamine (polyimide type)
CIC	charge injection capacity
CNS	central nervous system
ECoG	electrocorticogram
EDP	ethylene-diamine pyrocatechol

## Abbreviations

---

EEG	electroencephalography
EPSP	excitatory postsynaptic potential
FDA	Food and Drug Administration (United States of America)
fMRI	functional magnetic resonance imaging
FTIR	Fourier transformed infrared spectroscopy
GABA	gamma-aminobutyric acid
HMDS	hexamethyldisilazane
IPSP	inhibitory postsynaptic potential
LFP	local field potential
LIFE	longitudinal intra-fascicular electrode
LTP	long-term potentiation
MEG	magnetoencephalographic
MEMS	microelectromechanical systems
MUA	multi unit activity
NGF	nerve growth factor
NMP	n-methyl-2-pyrrolidone
PBS	phosphate buffered saline
PCB	printed circuit board
PDMS	polydimethylsiloxane
PEG	polyethylene glycol
PET	positron emission tomography
PI	polyimide
PMDA-ODA	pyromellitic dianhydride / 4,4'-oxydiphenylamine (polyimide type)
PMMA	poly(methyl methacrylate)
PNS	peripheral nervous system
POF	plastic optical fibre
PTFE	polytetrafluoroethylene
RIE	reactive-ion etching
SEM	scanning electron microscope
SfN	Society for Neuroscience
SMD	surface mounted device
SUA	single unit activity
SUAP	single unit action potential
TIME	transverse intrafascicular multichannel electrode system
XPS	X-ray photoelectron spectroscopy
XRD	X-ray diffractometry

# 1 Introduction

For centuries, humans have been exploring the brain and trying to unravel the mechanisms that underlie phenomena such as movement, perception, behaviour, language, feelings and consciousness, as well as their respective pathologies.

As a look into the history of neuroscience reveals, technical achievements were always adopted quickly or even invented by neuroscientists who were in the need of advanced technical systems and methods to cope with the complexity of the brain.

Today, highly specialized fields of research coexist in neuroscience, medicine or engineering and often scientists have a limited awareness of some of the questions, problems and achievements beyond their respective fields. However, the combination of different disciplines has synergistic effects and can yield results which would not have been possible for one group alone. For this reason, combined disciplines such as neural engineering emerged in the last years to provide therapy and basic research with highly sophisticated neural devices. Motivated by these developments, this thesis deals with the application of common microelectromechanical systems (MEMS) fabrication methods and materials for neuroscientific research, especially the introduction of novel polyimide-based implants into basic brain research.

The implants described in this work were developed for two cutting-edge fields of neuroscience which reached the limit of the contemporary available electrode manufacturing technology: high-channel chronic recording from large areas of the primate cortex in the field of cognitive neuroscience, and the interfacing of the brain with fluids, light and electrode sites via a chronically implanted microdevice in rodents in the field of optogenetics.

It is obvious that MEMS-based implants with a large number of electrode sites and small dimensions can provide an electrical interface to the nervous system with a large number of channels and a high spatial resolution. Due to their microscopic dimensions, such devices can be implanted with less tissue damage compared to macroscopic implants comprising the same amount of channels. For this reason, a number of microimplants were developed and found their way into neuroscientific research. For example, the implants used as standard MEMS-tools in neuroscience are mainly single silicon-based needles or needle arrays that can be inserted into cortical brain tissue.

While these devices are frequently used by neuroscientists all over the world, there are still applications for MEMS implants that require other approaches than the use of silicon-based devices. One such application is the recording of local field potentials (LFPs) from the brain's surface. This does not require insertion of a device into cortical tissue but can be achieved by the placement of an electrode array on the cortex. To obtain relevant data from large-scale LFP recording, many channels, i.e. many electrode sites, are needed to cover the cortical surface.

The spatial resolution of interest is in the range from 50  $\mu\text{m}$  to 5 mm which results in implant dimensions that are in between those of MEMS-based microelectrodes and hand-made precision mechanics electrode arrays used in clinical practice. Thus, the dimensions of this implant would be larger than with a pure microscale device but have to use MEMS fabrication techniques to accommodate the multitude of channels. However, a rigid silicon implant at mesoscale would not be suitable. If this implant is supposed to cover large cortical regions with a large number of electrode sites, the implant cannot be rigid but has to adapt to the curved surface topology of the brain. This also holds true for electrodes that are implanted deeply into brain with the connectors attached to the skull. These electrodes have to float with the brain matter in order not to apply forces on the neural tissue which eventually results in an increased foreign body response.

Due to their flexibility, polymers are the material of choice and besides PDMS, polyimide (PI) was found to be a promising candidate for such applications. This is due to its good chemical and mechanical durability, electrical insulation properties and its processability with standard cleanroom equipment. Therefore, PI was already used in a number of neuroprosthetic application studies and was also chosen as the main substrate material in this work.

As PI plays a major role in the development of flexible, chronically implantable neural implants, there is the need to evaluate its long-term stability in the body environment. In this work, a step towards a better understanding of its long-term behaviour as an implant material was made by long-term testing the mechanical properties of PI stored in a saline solution at 37 °C resembling body environment as well as at elevated temperatures to further stress the material and provoke accelerated aging.

In this thesis, the reader will be guided through a brief history of neuroscience and will be given a short introduction into the two fields of contemporary neuroscience mentioned above (chapter 1) to gain an insight into the requirements and technical limitations of neuroscientific research. Chapter 3 introduces some basic brain anatomy which is needed to understand the following discussion of different implant designs, implantation techniques as well as the discussion of possibilities and limitations of today's microelectrodes (chapter 4). This chapter is closed with a short introduction to fluidic systems and optical stimulation used in neuroscience. The following chapters present the work which was conducted in this thesis. They provide information about the mechanical long-term testing of different commercially available PIs (chapter 7), describe the development and application of different polymer-based microimplants used for chronic, high-channel epicortical recording of local field potentials (chapter 8), intracortical recording of multi unit activity and local field potentials (chapter 9), and describe a microimplant with fluidic, optical and electrical capabilities which was developed to contact deeply laying brain structures of mice in order to apply fluids and light to the target tissue and to record neural activity from it with one single microdevice (chapter 10).

While this thesis deals with the development of implants for basic neuroscientific research, the novel data obtained with these implants could help to enhance our knowledge of the

central nervous system and in turn give rise to new therapy strategies. By the same token, new approaches in the use of biomaterials and electrode fabrication, developed for neuroscientific applications can make their way into the manufacturing of neuroprostheses that help to overcome certain neurological disorders.

## 2 Neuroscience

Neuroscience is the umbrella term for all fields of scientific research dedicated to study the nervous system. It ranges from studies on molecular and cellular processes to the exploration of higher and complex brain functions like perception, attention, decision making and behaviour (Squire 2008).

The term “neuroscience” itself is young. 40 years ago, neuroscience was not considered as a separate discipline. This changed in 1969 when the Society for Neuroscience (SfN) was founded. The society’s mission is i.a. to bring together scientists of different backgrounds such as biology, psychology, medicine, physics, mathematics, and chemistry to progress the understanding of the brain and the nervous system. Since then, the neuroscience community has been growing. In 1971 when the SfN held its first annual meeting, it was visited by about 1400 attendees. In 2005 on the 35<sup>th</sup> meeting, nearly 35000 visitors were counted (SfN 2010).

### 2.1 A Brief History of Neuroscience

However, the study of the brain is much older and dates back to prehistoric times. A number of articles were published in recent years that were dedicated to the examination of prehistoric skulls showing trepanation which is the opening of a skull by drilling or scraping a hole in it. Evidence of trepanation was found in the indigenous civilizations of North, Meso-, and South America (Andrushko 2008; Stone 1990), in Africa and Asia as well as in medieval Europe (Weber 2001). While the trepanation in ancient Africa, in pre-Columbian Mesoamerica, and in Celtic culture likely served a ritualistic and mystical purpose, in ancient Egypt, Greece, and in the Roman Empire it was used for therapeutic reasons like draining underlying hematoma caused by blunt weapons. The Greek physicians Hippocrates and Galen using a scientific approach of examining head injuries, setting out the knowledge in writing, and separating the medical aspects from religion and rituals (Missios 2007). Most of the examined prehistoric skulls showed bone healing which gave evidence that a lot of the prehistoric patients survived this surgical procedure. The survival rate could be calculated to about 80 % (Andrushko 2008; Carod-Artal 2004) to 90 % (Stone 1990).

Although some knowledge about the brain and brain surgery was collected and developed in the ancient Greek and Roman Empires and additional information about the anatomy of the nervous system was gathered since the Renaissance, it was not until the nineteenth century, that the scientific foundation was laid on which today’s neuroscience is based upon. By using the microscope technology that was further developed in the eighteenth century, biological tissue could be studied and described by scientists. In 1839 Theodor Schwann published his book (Schwann 1839) in which he proposed the cell theory stating that all living tissues consist of microscopic units called cells. Camillo Golgi and Santiago Ramón y Cajal could show that this is also true for neural tissue. Golgi developed a tech-



nique to visualize neurons by staining them with silver salts. Due to this technique it was shown that brain tissue is not a homogenous matter but consists of cells (Fig. 2.1). Ramón y Cajal used Golgi's staining technique to stain single cells and could show that the tissue was not a continuous web but a network of discrete cells (Sotelo 2003).

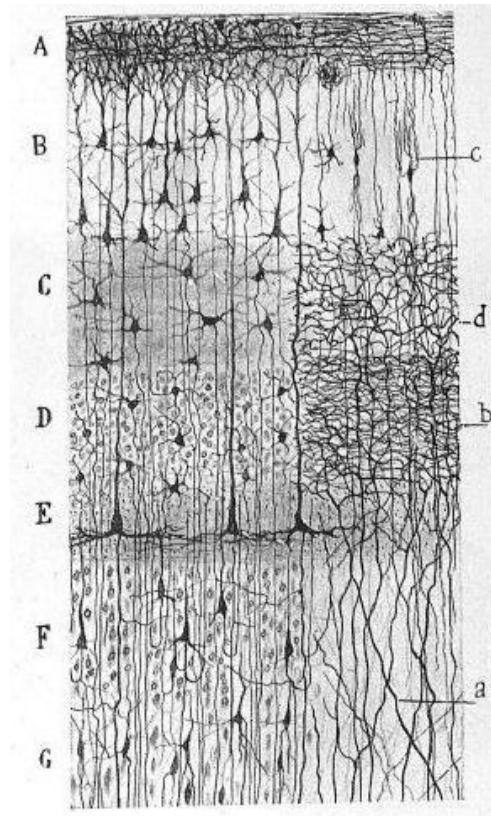
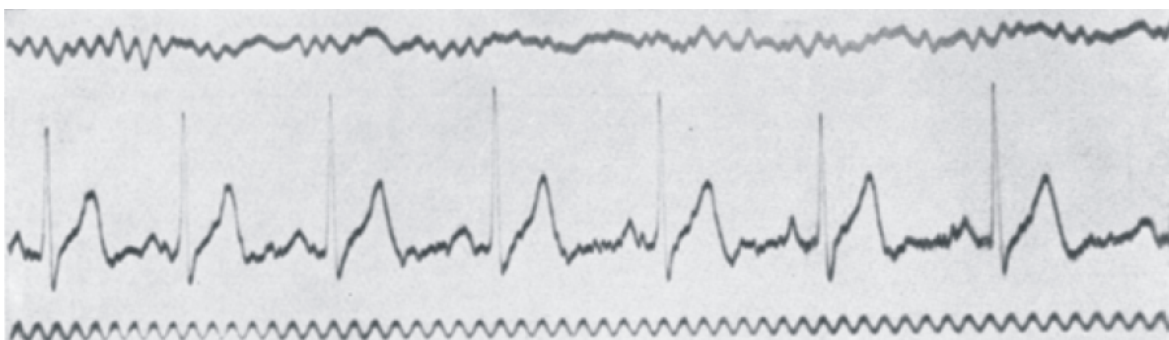


Fig. 2.1. Drawing made by Ramón y Cajal depicting the different layers of the human visual cortex (Ramón y Cajal 1923).

Although Golgi and Ramón y Cajal shared the Nobel Prize of 1906, they remained life-long opponents on the question whether the cells they made visible are fused to a network like the arteries and veins in the circulatory system or are single functional signalling units being somehow connected to a network. While Golgi was of the opinion that nerve tissue consists of fused cells, called the *reticular theory*, Ramón y Cajal argued for the *communication by contact, not continuity* theory which was known as the *neuron doctrine* derived from the more general theory of cells stated by Schwann. This discussion went on for some decades and was finally brought to an end in the 1950s with the use of the newly developed electron microscope. The electron microscope using an electrode beam instead of light has a dramatically larger resolution than the conventional light microscope giving a new insight into cell structure (Palay 1955). Thus, for the first time, the synaptic gap, which was identified as the contact point of communication between two neurons, could be shown with the help of the electron microscope (DeRobertis 1954) proving the neuron doctrine right. Vesicles and their role in transmitting electrical signals across the synaptic junction were revealed (DeRobertis 1957).

Not only the knowledge of nerve cells and their structure progressed in the nineteenth century but also the understanding of how neurons transmit and process information. At the end of the eighteenth century, Luigi Galvani discovered that electricity effects muscle contraction in dissected animals. It was not him but his contemporary Alessandro Volta drawing the right conclusion of these experiments that the voltage was due to the contact of two different metals both connected to a frog's leg stimulating the muscle. The contracting muscle was only the indicator but not the source of electricity. Following this first notion that electricity effects living things, the three physiologists Johannes Müller (Müller 1834), Emil du Bois-Reymond, and Hermann von Helmholtz established a new field of research by working on the electrical phenomena concerning the body, called electrophysiology. They found that neurons communicate by generating and transmitting distinct electrical excitations, termed action potentials (Du Bois-Reymond 1848), and that these action potentials travel at a finite velocity which was measured by Helmholtz (Helmholtz 1850a; Helmholtz 1850b) promoting a new understanding of nerves acting like wires transmitting electrical signals.

A major drawback for neuroscience research in these times was the lack of appropriate instrumentation. Like insufficient magnification in microscopy led to the discussion about the neuron doctrine, the absence of electrical measurement devices and amplifiers made it difficult for researchers to measure neural activity in the brain or in peripheral nerves to reveal the working principles of the nervous system.



*Fig. 2.2. Electrical signals of the brain and the heart recorded with a string galvanometer by Berger. The upper graph shows brain signals recorded with lead foil attached to the forehead and the back of the head. The graph in the middle depicts the signal of the heart recorded with lead foils at both arms. The lower graph is the time scale with a cycle duration of 0.1 s (Berger 1929).*

In 1875, however, the physician Richard Caton presented his experimental results on the annual meeting of the British Medical Association in Edinburgh. He reported on the measurement of electrical current on the surface of the cerebral cortex of dogs and monkeys by using a galvanometer (Caton 1875). The physician Adolf Beck could record changes in electrical activity in the occipital and temporal lobe of the cerebral cortex of rabbits and dogs when exposed to visual and auditory stimuli, respectively (Finger 1994). In 1929, Hans Berger reported on the first measurements in humans (Fig. 2.2) by recording the electrical signals of the brain non-invasively on the skull's surface (Berger 1929). He used

lead foil as electrodes that were fixated on the head by elastic bandage. The skin resistance was overcome by a 20 % saline solution. He used a string galvanometer as engineered by Willem Einthoven at the beginning of the 20<sup>th</sup> century to measure and to write the data. He found that the measured electrical activity of the brain changed with respect to the mental state of the subject like relaxation or concentration on a mental task. By measuring two wave forms with about 10 Hz (relaxation) and 20-30 Hz (concentration) respectively, Berger was the first to measure the electrical oscillations of the human brain. In his 1929 publication he suggested the term *Elektrenkephalogramm* for the measured rhythmic activity according to the word *Elektrokardiogramm* describing the measured electric activity of the heart muscle. As Berger hoped at that time, recording the electroencephalogram (EEG) became a standard method in clinical diagnostics, in critical care units, and in brain research (Swartz 1998). Even with this rudimentary measurement instrumentation, Berger could identify the oscillatory nature of brain signals. As we will see, oscillations are discussed to play a major role in neural signal processing and are an area of interest in neuroscientific research today (see the following chapter 2.2.1).

As the measurement instrumentation and brain surgery techniques were improved over the course of the 20th century, more and more details about the functional architecture of the CNS were revealed. In the middle of the 19th century, scientists debated about whether certain brain regions were responsible for different functions or whether the responsibility for all functions was equally distributed over all parts of the brain. Important steps towards our contemporary understanding of the brain having different areas which are responsible for certain tasks while being connected and working together to accomplish complex mental tasks were done in 1836 and in 1861, when the French neurologists Marc Dax and Paul Broca published their observations on language impaired patients respectively. They showed that patients having problems with the use of language had brain damages in the left hemisphere and that different functions of the brain like speaking and understanding of language have distinct positions in the cerebrum (Broca 1865; Cubelli 1994). Due to these findings scientists inferred that different cortex segments are responsible for different brain functions and the search for the cortical locations of other behavioural functions began. In 1870 Gustav Fritsch and Eduard Hitzig electrically stimulated the cortex of dogs and found sites where the stimulation led to limb movements (Fritsch 1870). After localizing the cortex area responsible for the movement of a forepaw, they resected a small part of this area with the size of only a few millimetres. After recovering from the surgery the dogs showed disordered paw movements. With this experiment Fritsch and Hitzig could disprove the opinion of Jean Pierre Flourens who, in 1824, stated that each part of the cerebral hemispheres was involved in all higher mental functions, called the *aggregated-field* theory.

Flourens who experimented with resecting brain parts in rabbits and pigeons could show that the brain stem, the cerebellum, and the cerebral hemispheres fulfil different tasks but believed that higher cognitive functions were performed by all parts of the cerebrum equally (Flourens 2007). Fritsch and Hitzig compared their own with Flourens' results and

concluded that Flourens resected too large amounts of cortical matter to be able to observe distinct changes in the animals' behaviour (Fritsch 1870).

In 1876 Carl Wernicke published his observations on patients with aphasia. In contrast to Broca's patients who could not speak but understand language, Wernicke's patients could speak but not understand and had lesions in a different part of the brain than Broca described. Combining his findings with the work of Broca, Fritsch, and Hitzig, Wernicke developed a new theory of language processing. He stated that a complex brain function is distributed over several functional sites in the cerebral cortex and that each region is responsible for a certain component of this brain function. A single behaviour emerges from the interconnection of a number of different functional sites. Wernicke's work gave the first evidence for the theory of *distributed processing* which formed the understanding of brain function as it is today (Wernicke 1874).

While Broca and Wernicke inferred the function of certain brain sites by observing patients with cognitive dysfunctions, Korbinian Brodmann divided the human cerebral cortex in different functional areas by comparing the cytoarchitecture of the tissue. Brodmann conducted histology by staining the nerve tissue and examining it with help of a microscope. He found 52 distinct regions in the cortex that varied in cell morphology and arrangement (Brodmann 1909). These areas determined solely by cytoarchitecture were found to be in agreement with the functional areas. Brodmann's classification and nomenclature is with further refinement still used today.

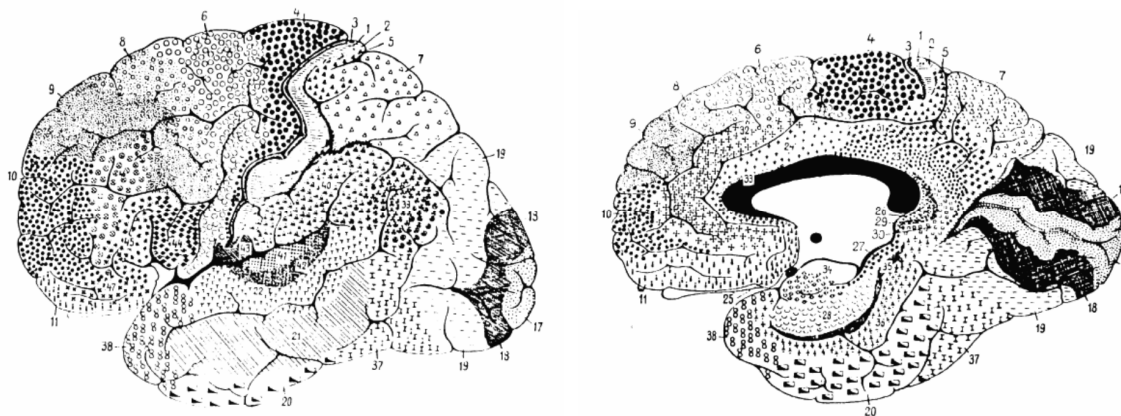
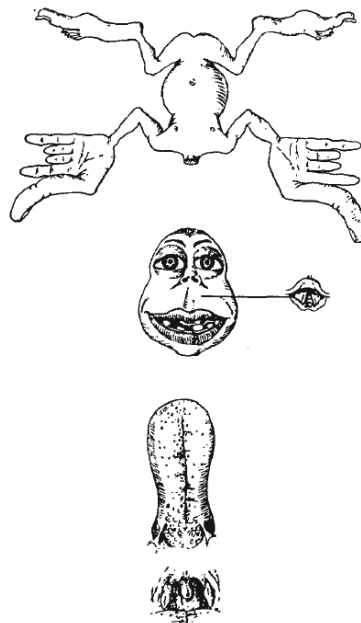


Fig. 2.3. Brodmann's classification of the human cortex based on its cytoarchitecture (Brodmann 1909)

Despite these findings, the *aggregate-field* theory was still the dominant interpretation of brain function in the first half of the 20<sup>th</sup> century with influential advocates such as the psychologist Karl Lashley (Lashley 1931). But more and more evidence for the localization of function was found. In 1937 and 1938, Wade Marshall and Philip Bard reported on the cortical representation of somatosensory stimuli in cats and monkeys (Bard 1938; Marshall 1937). By stimulating the skin with a brush while recording from the surface of the cerebral cortex with electrodes, the representation of the body surface on the cortex could

be mapped. Edgar Adrian found cortical representations of the body in cats, rabbits, dogs, and monkeys (Adrian 1941).

Due to his work as a neurosurgeon, Wilder Penfield was able to create a map of the cortical representation of the body in humans. Penfield helped his patients by destroying the brain area that was responsible for the epileptic seizures or by removing tumours from brain tissue. During the surgery he electrically stimulated the brain in the awake patient to localize the seizure focus or the tumour as closely as possible to circumvent side effects that were due to the deletion of healthy brain tissue. Because the patients were only under local anaesthesia, they could report on sensations when stimulated during the surgery. In an article published in 1937, Penfield summarized the data collected from 126 patients in cortical maps describing the motor and sensory representation of the different body parts on the cortex (Penfield 1937). Based on this data, Penfield drew a little man whose body parts were sized according to the dimension of the cortex area representing this body part in the brain. The resulting drawing, called the *cortical homunculus*, showed a bizarrely distorted human with unproportionally huge thumbs, lips, and tongue. Body parts with a high motor and sensory resolution occupy a larger cortical area due to the larger number of nerve cells they comprise receiving and sending information from and to the brain respectively.



*Fig. 2.4. The sensory and motor homunculus as published by Penfield (Penfield 1937). The size of the single body parts in this drawing corresponds to the size of the cortical areas representing the respective body parts.*

Until recently, most of the knowledge of brain functions came from animal studies, from patients with brain lesions, or from patients undergoing brain surgery. With the development of positron emission tomography (PET) in 1975 (Phelps 1975) and functional magnetic resonance imaging (fMRI) in 1990 (Ogawa 1990) a completely new field of brain

studies arose. For the first time in the history of neuroscience it became possible to observe the working brain in healthy humans. While basic working principles of nerve cells and the brain can be examined in animal studies, higher brain functions like the use of language can only be studied in humans. Using the new imaging techniques scientists were no longer dependent on rare pathological cases such as lesions in the Wernicke area but could non-invasively study the information processing in the normal human brain. PET shows the blood flow and metabolism of the brain with the help of a radioactive tracer. Radioactive isotopes are bound to sugar molecules which are transported to and metabolized by active brain tissue. By fMRI, active areas can be detected due to different magnetic properties of oxygenated and deoxygenated blood. The blood-oxygen-level dependence (BOLD) contrast differentiates between active and inactive brain regions due to the changes in oxygenated blood flow. With the BOLD contrast, MRI does not only image brain structure but, as PET, also its function and thus termed fMRI.

In imaging studies, subjects are told to conduct a certain cognitive task while being scanned with PET or fMRI. Thus, areas that are active during this task can be found. From these studies we learned that complex cognitive tasks are highly localized in such a way that different aspects of a task are represented in different parts of the brain. For example, by using PET, Steven Petersen, Michael Posner and coworkers (Petersen 1988; Posner 1988) could show that language is processed by different pathways when words were heard or read by the subject. When subjects were hearing a word, Wernicke's area became active but it was inactive when the words were seen on a screen. The information of the visual input seems to have a direct pathway to functionally higher regions of the cortex.

The last 150 years of neuroscience laid the foundation of how we understand the brain today. A lot of knowledge of the anatomy and the function of the nervous system were gathered. This would not have been possible without the advancements in medicine and technology. Surgical methods were improved and the importance of aseptic technique was introduced. Due to the parallel evolvement of technology more and more tools such as microscopes, electrical stimulators and amplifiers, PET, and fMRI could be used to explore the brain. While important steps towards the understanding of the brain have been made, much remains unclear providing many challenges to today's scientists. Some of the questions which are currently discussed among researchers are described in the following chapter.

## 2.2 Neuroscience Today

This chapter addresses some of the current topics neuroscientists of today are interested in. Due to the large multiplicity and the high specialization of the field, this chapter is not meant to give an overview but rather focus on two specific examples of contemporary neuroscience research which are related to the work presented in this thesis.

### 2.2.1 The Binding Problem

One of the major goals in neuroscience research is to determine the mechanisms that are responsible for neuronal interaction between several neuronal populations. As we already saw in chapter 2.1, the brain processes different portions of a complex mental task in certain neuronal groups which are distributed over different regions of the cortex. While spatially segregated, these neuronal groups have to communicate with each other somehow to create coherent perception or to accomplish coordinated action.

The question of how the brain composes a unified perception from a multitude of sensations is called the *binding problem*. This question has been discussed since the middle of the 20<sup>th</sup> century, first, with respect to visual perception. How are two features of an object which activate different neurons in the visual cortex combined to generate one perception? In 1974 Peter Milner and in 1981 Christoph von der Malsburg addressed this question theoretically (Malsburg 1981; Malsburg 1986; Malsburg 1999; Milner 1974). How does the neural network combine these two features of an object to differentiate it from another one? If we see a red circle and a blue square, the information of the feature sensing neurons has to be combined in the right way i.e. the attributes *red* and *circle* and the attributes *blue* and *square*. Moreover, how is an object with all its features represented in parts of the brain? Taking all objects and features into account, the number of possible combinations would be too large as each combination could be represented by its own cell. They stated that the relation between neurons could be temporally controlled. By discharging in synchrony two neurons or two groups of neurons are bound together to combine e.g. the attributes *red* and *circle* of a visually perceived object.

In the 1980s, it was Wolf Singer's group at the Max Planck Institute for Brain Research in Frankfurt who were the first to obtain experimental data from anesthetized cats supporting the *binding-by-synchrony* hypothesis (Gray 1989; Roskies 1999). They found that spatially separated groups of neurons were synchronized by an oscillating activity at 40 Hz when a certain visual stimulus was given. In each group, the firing of the neurons was synchronized at 40 Hz as well as the oscillation of one group related to the other. They assumed that synchronization could be the mechanism to establish a relation between features recognized by different feature-selective cells distributed over the visual field (Gray 1987; Gray 1989). Following this groundbreaking discovery (a historical retrospect on this topic is given by György Buzsáki in (Buzsáki 2006)), different research groups started to address this phenomenon (Eckhorn 1988; Engel 2001; Engel 1997; Gray 1999; Kreiter 1992; Niebur 1993; Salinas 2000; Singer 1995; Singer 1999). While the first experiments were conducted with anaesthetized cats, Kreiter and Singer could for the first time show that synchronization can be also found in awake, behaving monkeys. In the vicinity of a single electrode, neurons were found that responded in synchrony to their preferred stimulus (Kreiter 1992). Bressler et al. recorded with up to 15 electrodes from the cortical surface of behaving monkeys. The electrodes were distributed over one hemisphere and thus signals origination from different cortical areas could be compared. During a visual discrimination task the widely distributed sites lying in sensory, motor or higher-order cortical areas were synchronized (Bressler 1993).

Synchronization of neural activity seems not only to bind the neural representation of different visual features of an object but also to play a role in attention which is the ability to selectively concentrate on one certain aspect of the environment while ignoring others. Roelfsema et al. found that during the attentive processing of a task (a motor response to a visual stimulus), the involved cortical areas in cats showed synchronized activity which stopped after completing the task (Roelfsema 1997). A difference in synchrony can be seen in the response of neurons to attended and unattended visual stimuli. Fries et al. could show that an attended stimulus induced stronger local synchronization in the monkey visual cortex than an unattended (Fries 2001a).

All these findings led to a renaissance of interest in oscillation and timing of neural signals. The first recorded brain signals were of oscillatory nature (Berger 1929) which can be used to identify different mental states such as sleep, arousal and coma. However, with the introduction of the single cell recording technique (see chapter 4.1), the correlation between the intensity of a sensory stimulation and the firing rate of a neuron was found (Adrian 1926). This strengthened the notion that information in the neural system is coded by the frequency at which a neuron is activated, a phenomenon termed *rate coding*. In the following years, most of the knowledge of the function of the brain was obtained by measuring and analysing the firing patterns of single neurons recorded one after each other. Due to the small signal amplitude and the neuronal variability, the commonly applied method of single cell recording uses averaging over successive trials in order to increase the signal-to-noise ratio.

With this process, the amplitude, firing rate and position of the neuron can be revealed but the information about the temporal structure of the neural activity which is not precisely locked to the stimulus is lost. Thus, in most single cell recordings, time was not used as a dimension for coding. Moreover, while the single cell recording studies were able to demonstrate that the variation in firing rate of a neuron can be related to a given stimulus, no information could be gained about how this stimulus affects the response of different neurons at the same time and how it affects the interaction between these neurons. However, in the last decades the interest in the temporal relations between distributed neurons, activated by the same stimulus returned and by studying oscillations and synchrony, this precise temporal relationship was proposed as a coding dimension (Singer 1993).

As a result, an interest in measuring not only single cell but cell assemblies emerged. In contrast to single cell recording which measures the signal of one neuron, the signal of a cell assembly, called local field potential (LFP), is a summation signal generated by numerous cells. If the cells in the assembly are activated in synchrony, their signals superpose and oscillate at a certain frequency. Thus, the temporary relations between cells in an assembly is directly shown in the LFP signal (Gray 1992).

In 2005, Pascal Fries expanded the *binding-by-synchrony* theory by hypothesizing that synchrony, or coherence, is a general mechanism for neuronal communication. He stated that synchronous oscillations applied not only to the binding of features of a perceived object but that it subserved the communication between groups of neurons. A neuronal



group with an oscillating activity generates temporal windows in which it is excitable. If two neuronal groups have a coherent activity their temporal windows for excitability overlap and effective communication between these groups becomes possible. He termed this theory the *communication-through-coherence* hypothesis (Fries 2005). This theory gives an explanation for how effective connectivity between different neuronal groups can be switched without changing the structural connectivity of the neural circuits (Fries 2009). For instance, cognitive control can change the attention from one object in the visual field to another in a few hundred milliseconds. As this timescale is too short to alter anatomical connections, the brain has to have another strategy for different neuronal groups to connect and communicate.

In the following years, a number of articles were published by different groups with data supporting the *communication-through-coherence* hypothesis (Gielen 2010; Lewis 2009; Roopun 2010; Srinivasan 1999; Womelsdorf 2010; Womelsdorf 2007b). Cohen et al. recorded from two neuronal groups in humans during a decision making task. They found information coded in the oscillatory synchrony between these two groups which could not be obtained from the recorded data of a single electrode (Cohen 2009). Womelsdorf et al. recorded from cat and monkey cortical areas of awake animals obtaining a certain rhythmic activity in each recorded group of neurons. They found that the mutual influence between these neuronal groups depended on the phase relation between the group's inherent oscillations (Womelsdorf 2007a).

To reveal the strategies of large-scale communication (Varela 2001) between distinct neural ensembles, multielectrode neurophysiological recordings from different regions distributed all over the brain are required. While a large number of electrode sites is needed to obtain a sufficient resolution, the whole implant has to match the brain anatomy of the particular animal. These requirements can be realized with a MEMS-processing approach (chapters 8 and 9).

### 2.2.2 The Microcircuitry of Fear Conditioning

While the previous chapter described the research dedicated to the role of attention and synchrony in visual perceptions, this chapter deals with the revealing of processes and brain circuits involved in learning, memory and emotion. Learning is the process of acquiring new information in order to adapt behaviour. Memory is the brain's ability to store and retrieve this information. Exploring learning and memory in the neural circuitry of emotions such as fear can help to understand the processes of posttraumatic stress disorder. This can lead to a therapy with which the symptoms of such disorders can be controlled.

It is thought that information is stored by altering the connectivity between neurons. This synaptic strength is not static but can vary. Hence, the process is called *synaptic plasticity* (Hebb 1949). Long-term potentiation (LTP) is a type of synaptic plasticity and is considered to be one of the basic mechanisms of learning and memory. However, a direct link between LTP and learning and memory has not yet been demonstrated (Sah 2008). If two neurons are active at the same time, the link between these two cells is strengthened i.e.

the efficiency of the synaptic transmission is abruptly and sustainably increased (Bliss 1993). Synapses strengthened by LTP were first found in the hippocampus (see chapter 3.2.1) (Bliss 1973) which was extensively studied in the last decades. While LTP in the hippocampus is used as an important model for activity-dependent synaptic plasticity, it has also been observed in other regions of the mammalian brain, e.g. parietal cortex (Banerjee 2009).

Memory and learning are involved in and can be studied with classic (Pavlovian) fear conditioning. By presenting an unconditioned stimulus (an inherently aversive stimulus, e.g. an electrical foot shock) together with a conditioned stimulus (an inherently neutral stimulus, e.g. a flash of light), the animal learns to associate the conditioned with the unconditioned. Thus it starts to react with the expression of fear even though only the former neutral stimulus is presented.

In the 1950s, the amygdala which is an evolutionary older structure in the middle of the brain (chapter 3.2.1) was identified to play a major role in the experience, processing, and expression of emotional behaviour such as fear and aggression (LeDoux 2000). Thus fear conditioning is well suited to study the neural circuits of the amygdala which are involved in emotional learning and memory modulation. Acquisition and extinction of fear memory can be studied in mice by observing the activity of the amygdala and comparing it to the animal's behaviour.

Over the last two decades associative learning has been studied by investigating projection neurons, which send information over relatively long distances, and their excitatory neurotransmitter glutamate. Recent work indicates that interneurons involved in modifying local inhibitory circuits may play a major role in achieving a better understanding of amygdala circuit function (Ehrlich 2009). The fact that modulation of synaptic plasticity by inhibitory neurons occurs in the neural circuits of the amygdala offers the possibility to relate changes in synaptic transmission efficiency to behaviour. That is, the role of inhibitory gating of LTP can be studied by manipulating the microcircuits of the amygdala which results in a change of the animal's emotional state that is clearly displayed in its behaviour.

The expression of fear in a fear conditioned animal can be suppressed. If the conditioned stimulus is repeatedly presented without the unconditioned stimulus, the fear response decreases progressively. However, this phenomenon, called extinction, is neither robust nor permanent. Fear responses to the conditioned stimulus can be renewed by presenting the stimulus in another environment but can also spontaneously recover after extinction training (Myers 2006). The extinction training does not delete the originally conditioned fear response but is learned additionally. Thus, fear and extinction memory coexist while their retrieval is context dependent (Ehrlich 2009). An example of how the functioning of neural circuits can be revealed using the combination of electrical recording in the amygdala and observing the animal's behaviour was published by Herry and Ciocchi. They could identify two different neuronal populations in the basal amygdala which are involved in the learning and extinction of a conditioned stimulus (Herry 2008). Changes in the bal-

ance of activity between these two distinct neuronal populations trigger the transition between states of high and low fear.

While fear memory in adult animals is permanent and cannot be erased by extinction training, this is possible in rats during early postnatal development (Kim 2007a; Kim 2007b). Gogolla et al. found that fear memory in adult rats is protected from erasure by perineuronal nets which are absent in the first few weeks of postnatal development (Gogolla 2009). Perineuronal nets are a neuron supporting extracellular matrix containing chondroitin sulfate proteoglycans, a type of glycoprotein which is involved in the development and plasticity of neural circuitry (Celio 1998; Galtrey 2007).

To understand the acquisition, encoding and extinction of fear memory and their underlying cellular processes, scientist use a multidisciplinary approach encompassing in vitro and in vivo electrical recordings, imaging, behavioural techniques as well as pharmacologic and genetic manipulation of certain cell types. That is why this field of research can benefit from MEMS-based implants which can provide the scientist with electrical, fluidic and optical connections to neural tissue (chapters 4.5, 4.6, and 10)

# 3 The Nervous System

This chapter gives a brief overview of the nervous system of vertebrates with the emphasis on the central nervous system by starting with the single nerve cell and its functions and proceeding with the most complex and to this day still not fully understood organ, the brain.

The nervous system of vertebrates can be divided into two sections the central nervous system (CNS) and the peripheral nervous system (PNS). The CNS consists of the brain and the spinal cord both enveloped by the meninges and also protected by bone structures of the skull and the vertebrae, respectively. The PNS comprises all nerves outside the CNS connecting the latter with the target organs. Within the nervous system, information can travel in two directions. Efferent nerve cells direct signals from the brain through the spinal cord and the peripheral system towards the effectors e.g. skeletal muscles. Afferent nerve cells collect sensory input e.g. temperature or pain from the receptor cells of the body and direct it towards the brain.

## 3.1 The Neuron

The smallest functional entity of the nervous system is the neuron, or nerve cell, which is able to conduct and to process information in form of electrical excitation and chemical substances. While neurons can have very different shapes, four main parts can always be distinguished: the soma, the dendrites, the axon, and the axon terminals (Martin 2003). The soma, or cell body, contains the nucleus and cellular organelles which are responsible for the cell's vitality by maintaining the cell metabolism. The dendrites are extensions of the soma that receive electrical excitation from other neurons. The axon, or nerve fibre, is a unique projection of the soma which can be up to about 1 m in length in peripheral neurons (Purves 2001). It carries the electrical excitation from the soma to the axon terminal where it transmits the electrical excitation to adjacent neurons.

### *The Action Potential*

A neuron maintains a potential difference across its cell membrane called the *membrane potential*. That is, a voltage can be measured between an electrode inside the cell and a second electrode outside the cell. In a non-excited state neurons maintain a *resting potential* of about -70 mV with respect to the outside. The concentration of potassium ions in the cell is higher than outside the cell, and vice versa for sodium ions. The membrane potential can rise and fall due to synaptic input or external stimulation. When rising to the threshold value of about -55 mV, the voltage-sensitive sodium channels in the membrane open and the membrane potential rises due to the sodium ion influx. The increase of the membrane potential, called depolarization, reaches a peak at about +40 mV and is followed by a decrease, the repolarization. This is due to the likewise voltage-sensitive but slower opening potassium channels resulting in an efflux of potassium ions out of the cell which coincides with the time-dependent closing of the sodium channels. The potassium

channels close when the membrane reaches its resting potential. As it takes a few milliseconds for the potassium channels to close, the potassium influx decreases the membrane potential even below the resting potential which is called hyperpolarization (Kandel 2000).

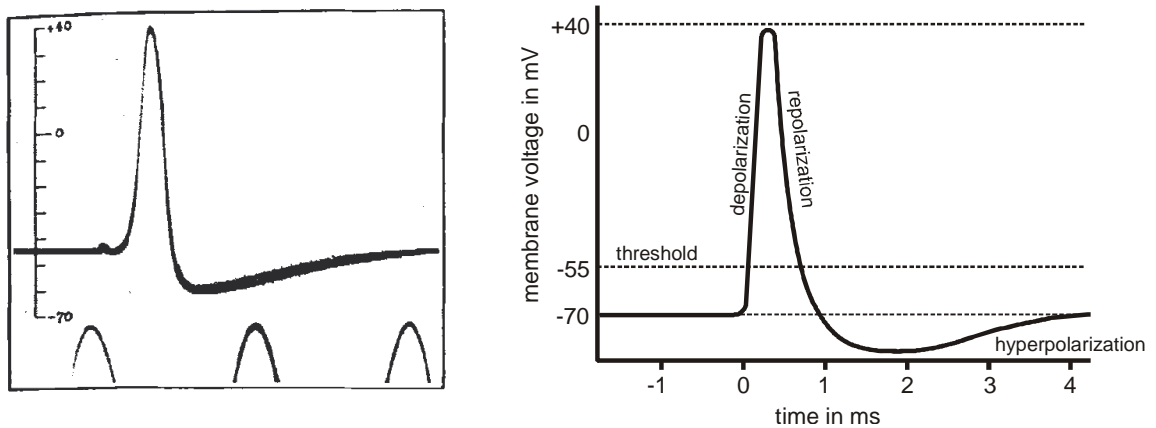


Fig. 3.1. The first published intracellular recording of an action potential (Hodgkin 1939) (left)\* The vertical scale shows the inside cell potential with respect to the outside in millivolt. The cycle period of the time marker is 2 ms. The schematic of an action potential depicts the characteristic parts (right). \* Reprinted by permission from Macmillan Publishers Ltd: *Nature* (Action Potentials Recorded from Inside a Nerve Fibre. 144: 710-711), copyright (1939).

It is due to the phenomenon of the action potential that electrical signals can be sent over long distances e.g. in an axon reaching from the spinal cord to the foot. Action potentials exhibit an *all or nothing* working principle, i.e. a membrane potential above threshold causes an action potential while a membrane potential below threshold does not generate an action potential. Thus, all neural information is binary coded and thereby less corrupted by noise or signal attenuation.

A tube with some micrometres in diameter, filled with saline solution is not a very good conductor. If the axon was such a passive conductor, the signal would be attenuated after approximately 2 mm (Purves 2001). Due to an above threshold change in membrane potential an action potential is caused and a current flows passively along the axon and depolarizes the adjacent region which in turn generates an action potential. Thus, the signal is renewed constantly along the axon and therewith kept above threshold reaching conduction velocities from about 0.5 to 10 ms<sup>-1</sup>. A strategy that further improves the conduction via action potentials is *saltatory propagation*. Oligodendrocytes (in the CNS) and Schwann cells (in the PNS) wrap the axon in myelin. Comprising multiple layers of glial membranes, the myelin acts as an insulator for the axonal membrane preventing the current from leaking out. This increases the distance for a current to flow passively along the axon. Every few millimetres, the myelin sheath is discontinued and exposes the uninsulated axonal membrane. At these so-called *nodes of Ranvier*, ion exchange takes place via the membrane's ion channels and renews the action potential. As the electrical excitation is only present at the nodes of Ranvier, the time-consuming generation of action potentials is brought to a minimum. The combination of long sections of passive current flow

with only few and short sections of ion exchange over the membrane leads to conduction velocities up to  $150 \text{ ms}^{-1}$ .

#### *The Synapse*

The axon terminal is part of the contact structure of two neurons called the synapse which is responsible for the transfer of information from one neuron to the next. The synapse's main parts are the presynaptic terminal, which is the axon terminal of the first neuron, the synaptic cleft, and the postsynaptic terminal which is located at a dendrite or at the soma of the second neuron. The presynaptic terminal contains synaptic vesicles which are membrane-bounded spherical organelles filled with one or more certain types of chemical substances, called neurotransmitters. When an action potential travels along the axon and reaches the presynaptic terminal, the vesicles merge with the presynaptic membrane and release the neurotransmitters into the synaptic cleft. By diffusing through the cleft which has a width of about 20 nm, the neurotransmitters reach the postsynaptic terminal. Here they bind to receptor molecules in the postsynaptic membrane which causes an opening of ion channels located in the postsynaptic membrane changing the postsynaptic potential. Depending on the type of neurotransmitter and receptor, an excitatory (EPSP) or inhibitory (IPSP) postsynaptic potential is caused in the postsynaptic terminal. An EPSP increases the likelihood of the generation of a postsynaptic action potential while an IPSP decreases this likelihood. In most cases, one EPSP is well below the threshold to trigger an action potential in the postsynaptic neuron. However, a neuron has dendritic connections to thousands of other neurons. Postsynaptic potentials (both EPSP and IPSP) are summed up in the postsynaptic neuron and the result of this summation will trigger or inhibit an action potential. Postsynaptic potentials are summed up not only in space, i.e. coming from different synapses, but also in time. That is, if postsynaptic potentials arrive at a certain point in a short-enough time window, they sum up.

#### *Glial Cells*

Neuroglial cells, often just called glial cells, are non-neuronal cell in the CNS and can be categorized in different types such as astrocytes, oligodendrocytes and microglia. In primates, they account for about 50 % of the mass of the brain (Laming 1998) and fulfil different functions in the neural tissue. Glial cells are a mechanical support structure for the neurons and guide axonal sprouting. They electrically insulate neurons from each other. Oligodendrocytes enhance the neuron's conductance properties by insulating the axons with a myelin sheath. Glial cells supply nutrients and oxygen for the neurons and play a major role in immune defence. Microglia are the macrophages of the CNS and remove infectious agents, plaque and dead neurons. Thus, glial cells are present at any traumatic injury of neural tissue. In the last decades more information about the neural-glial interaction was gained, changing the role of glial cells from passive maintenance structures to active components of the neural tissue modulating synaptic transmission (Laming 1998). .

## 3.2 The Brain

The most important and complex part of the nervous system is the brain. It can be divided into four sections: the cerebrum, the diencephalon, the cerebellum, and the brainstem.

The cerebrum, also called telencephalon or cerebral hemispheres, is the largest part of the human brain. It consists of the cerebral cortex, the underlying white matter, and three further structures which lie deep within the cerebral hemispheres: the hippocampus, the amygdala, and the basal ganglia. The hippocampus plays an important role in long-term memory and spatial orientation. The amygdala is mainly involved in emotional learning and behaviour such as the development of fear and the evaluation of threatening situations. The basal ganglia participate in the modulation of movements and cognitive functions. The terms grey and white matter derive from the fact that the cerebral cortex which consists of cell bodies appears grey while the underlying tissue of myelinated axons appears white. The cerebrum is engaged in perceptual, motor, and cognitive functions and contains the youngest structure in the phylogenesis of the brain: the cerebral cortex.

The diencephalon is located below the cerebrum and above the brainstem and contains the thalamus and the hypothalamus as two main parts. The thalamus is involved in the transfer and modulation of sensory information that travels from the sensory receptors to the cerebrum. The hypothalamus controls certain body processes by regulating the hormone secretions of the hypophysis. These body processes are, amongst others, growth, thyroid gland function, blood pressure, energy metabolism, and reproductive functions. Together, the cerebrum and the diencephalon are referred to as the forebrain.

The cerebellum, Latin for “little brain”, is located below the cerebrum and in the back of the brainstem. Although it is much smaller in volume it contains a greater number of neurons than the cerebrum. In contrast to the cerebrum, its circuitry is comparatively well understood because it contains only a few types of neurons (Kandel 2000). The cerebellum is mainly concerned with advanced motor control functions like coordination of head and eye movement or posture but also takes part in cognitive functions like language processing or attention.

The brainstem sits below the diencephalon. It comprises three parts: the midbrain, the pons, and the medulla. The brainstem connects the other parts of the brain with the spinal cord as well as the cerebrum with the cerebellum. It links components of the motor system located in the cerebrum and the cerebellum. The brainstem is involved in respiration, taste, and sleep. Furthermore, it receives sensory input and gives motor output to the 12 cranial nerves that innervate the head, neck, and face and contact the parasympathetic system.

While the function of single neurons and synapses is mostly understood, the precise nature of the cooperation between neurons in groups and between groups of neurons across the brain still remains unanswered. This is due to the enormous complexity of the brain. The human brain contains about  $10^{11}$  neurons with each neuron having on average 1000 synaptic connections to other neurons (Purves 2001). Half of the brain's mass is occupied by glial cells supporting and modulating neural transmission (Laming 1998).

### 3.2.1 The Cerebral Cortex

Because of its key role in human behaviour and cognition, the cerebral cortex is described in detail in this chapter. While life-sustaining functions are controlled by the diencephalon, the brainstem, and the spinal cord, the cerebral cortex is responsible for i.a. precise motor planning as well as for the more abstract functions not directly related to sensory input and motor output like cognition, memory, language and consciousness.

The cerebral cortex is the thin outer layer of the cerebrum. The thickness of this layer varies from 2 mm to 4 mm depending on the cortical area in question but is nearly the same in all mammals. Thus, species do not differ in the structure of the cortex, but in its amount. The area occupied by the cerebral cortex is larger in higher primates, particularly in humans. The human cortex comprises  $10^9$  to  $10^{10}$  neurons with an average number of synapses per neuron around 24000 to 80000 (Braitenberg 1998). It is strongly convoluted so that large areas cannot be seen from outside the brain but only in sections. The grooves of this folded shape are called gyri and the elevations sulci. The cerebral cortex comprises different types of cortices which are mainly distinguished by the number of cell layers. It can be classified in three areas, the neocortex, the archicortex and the paleocortex. The archi- and paleocortex are deeper lying, phylogenetically older structures containing three to four cell layers. The hippocampus is part of the archicortex and the parahippocampal gyrus is part of the paleocortex. The neocortex is the youngest and most developed structure of the brain. It is only found in mammals and has dramatically expanded during human evolution. Most of the cerebral cortex is neocortex. It covers the entire cerebrum and comprises six cell layers. It is folded in humans, less in monkeys, and not at all in rats. Due to its size and importance, neuroscientists frequently use the term cortex when talking and writing about the neocortex. If left unqualified, the term cortex refers to cerebral neocortex.

The neocortex can be divided into four lobes. They are named after their overlying cranial bones: frontal, parietal, temporal, and occipital. The main sulci which have a relatively consistent position in human brains act as landmarks to distinguish the lobes. The central sulcus separates the frontal and the parietal lobe which both lie above the lateral sulcus while the temporal lobe lies beneath it. The occipital lobe lies in the rearmost part of the brain. Due to the absence of characteristic sulci, it cannot be so clearly spotted by looking on the brain's surface. While the division into the four lobes is rather coarse distinguishing the single parts mainly by their position, the widely used classification by Brodmann is based on the cytoarchitecture of the tissue. By staining the tissue one can observe that certain regions of the cerebral cortex have different composition of cell types, density and connectivity. Using these anatomical criteria, Brodmann divided the cerebral cortex into 52 regions (Fig. 2.3). These regions do not only have a different appearance but also perform different functions. Why look and function of the tissue coincide can be explained by looking on the lamellar structure of the cerebral cortex. The cells of the neocortex are arranged in six characteristic layers numbered from the outermost layer (layer I) which is adjacent to the pia mater to the innermost layer (layer VI) that is directly above the white matter. By comparing, for instance, Brodmann's area 4 with area 17, one observes that



area 4 (primary motor cortex) has nearly no layer IV, while area 17 (primary visual cortex) has a distinctive layer IV which can even be split up into sublayers. Layer IV contains granule cells that are connected to the thalamus. The thalamus directs sensory input coming from receptor cells to layer IV of the cerebral cortex. The visual cortex receives a large input of visual information, thus, it has a pronounced layer IV. The primary motor cortex, in contrast, directs mainly motor output directly to the spinal cord and therefore needs no large input layer.

### **3.2.2 The Meninges**

As all invasive stimulation or recording techniques are associated with placing electrodes on the brain's surface or inserting them into brain tissue, the meninges play an important role in neurosurgery as well as in the developing of neural implants. The meninges are a durable membrane surrounding and protecting the CNS. If one wants to contact the brain directly, this membrane has to be opened or penetrated.

The meninges consist of three layers. The outermost membrane is the strong and fibrous dura mater which is attached to the skull. The middle layer is the arachnoid membrane which is attached to the dura mater. The very thin pia mater is the innermost membrane and is adhered to the brain following the convolutions of the brain's surface. Between the arachnoid membrane and the pia mater the subarachnoid space is located which is filled with cerebrospinal fluid and hosts blood vessels whose branches penetrate the nervous tissue of the hemispheres. The insertion of electrodes can cause bleedings both at the surface of the cortex or within the brain matter if deep lying blood vessels are damaged.

# 4 Interfacing the Brain

Obtaining information from the brain either in neuroscience or in medical diagnosis requires a certain interface to the brain. While information about the brain can also be inferred by talking to the patient or observing his behaviour, the focus of this chapter is on the technical interfaces to the brain, through which we can observe its activity more directly. The most prominent criterion to classify brain interfacing methods is the invasiveness of the measurement procedure. One differentiates between non-invasive and invasive approaches. Non-invasive recording methods like EEG and MEG as well as the imaging methods fMRI and PET are widely-used in diagnosis and in human brain research. While these methods do not require surgery with all its risks, they have certain limitations. EEG and MEG have poor spatial resolution and can only detect synchronously active cortical areas in the centimetre range, but have a good temporal resolution (Cooper 1965; DiLorenzo 2008; Ferree 2001; Niedermeyer 2005). In contrast, PET and fMRI have a low temporal resolution of seconds to minutes, while exhibiting a good spatial resolution (Cheng 2001; DiSalle 2006; Niedermeyer 2005; Pfeuffer 2002). Furthermore, interfacing methods such as MEG, fMRI, and PET require that the subject is positioned in large stationary sensor equipment. Thus, such recordings can only be made in an artificial lab environment where the subject is not allowed to move or to behave naturally.

Invasive recording methods require the opening of the skull to contact the brain directly. With invasive methods better signal qualities such as spatial resolution or signal-to-noise ratio can be obtained. This is due to the absence of the skull which attenuates and spatially averages the signal (Cooper 1965). Moreover, the skull acts as a low-pass filter, thus, signals recorded directly at the brain's surface comprise more high frequencies which tend to be produced by smaller cortical assemblies and has therefore a better spatial resolution than EEG (DiLorenzo 2008).

One can distinguish between different levels of invasiveness (Tab. 4.1). If an electrode is placed onto the dura mater one refers to it as an epidural recording. Although the skull has to be opened, the meninges remain intact and thus reduce the risk of infections and damage to the nervous tissue. The next more invasive scenario is the subdural recording. Here, the dura mater or even the pia mater is opened and the electrode is placed directly onto layer I of the cortical tissue. The most invasive method is the intracortical recording which requires electrodes penetrating the cortex to measure inside the nervous tissue. By inserting an electrode into the cortex, some cortical tissue will be damaged. Neurons and glial cells will either be displaced or injured by a metal wire or electrode shaft entering the tissue.

To record signals with such invasive methods, electrodes are used called *electrocorticogram (ECoG) electrodes*. ECoG electrodes comprise a lot of different electrode types and different signals can be recorded. In neural engineering the term ECoG electrode is often used to describe electrodes on the surface of the cortex either epidurally or subdurally.

However, as the cortex is a tissue layer with a certain thickness, shaft electrodes penetrating the cortex are ECoG electrodes, too. To differentiate between these two types of ECoG electrodes, the terms *epicortical* and *intracortical* electrode can be used. As electrical signals from the cortex are used in *brain computer interfaces (BCI)* to help paralyzed patients to communicate by electrodes recording their brain signals, the recording methods are also classified in BCI classes I to III (Tab. 4.1) (Stieglitz 2009).

*Tab. 4.1 Classification of recording techniques of brain signals*

Interface	Recording Technique	Signals	Placement	Spatial Resolution	Temporal Resolution
fMRI	voltage induced into the sensor coil by relaxation of precessing magnetic moments of hydrogen protons, difference in water content is and hemodynamics are visible	mass activity	non-invasive, the subject's head is placed in MRI scanner system	3-10 mm (DiSalle 2006) (standard 1.5 T tomograph) 0.5 mm (Cheng 2001; Pfeuffer 2002) (7 T and 4 T tomograph respectively)	change in hemodynamics occurs 1-5 s after neural activity (DiSalle 2006) after seconds to minutes (Niedermeyer 2005)
PET	metabolic activity	mass activity	non-invasive, the subject's head is placed in PET scanner system	millimetres (Niedermeyer 2005)	seconds to minutes (Niedermeyer 2005)
MEG	magnetic field amplitude deriving from ionic currents in activated neurons	mass activity from large neural populations	non-invasive, the subject's head is placed in MEG scanner system	centimetres (Niedermeyer 2005)	milliseconds (Niedermeyer 2005)
EEG (BCI class I)	voltage recorded with an electrode	mass activity from large neural populations	non-invasive, electrodes are placed on the scalp surface, 2-3 cm away from the cortex surface	centimetres (Ferree 2001; Niedermeyer 2005) 3-5 cm (DiLorenzo 2008) 6 cm <sup>2</sup> (Cooper 1965)	milliseconds (Niedermeyer 2005)
epicortical ECoG (BCI class II)	voltage recorded with an electrode	mass activity, LFP	invasive, electrodes are placed on the surface of the cortex (epi- or subdurally)	0.5-3 mm (Logothetis 2003) 1 cm (Asano 2005) 0.5-1 cm (DiLorenzo 2008)	5 ms (Asano 2005)
intracortical ECoG (BCI class III)	voltage recorded with an electrode	SUA, MUA, LFP	invasive, electrodes are inserted into the cortex	100 $\mu$ m (Schwartz 2006) 0.2-1 mm (DiLorenzo 2008)	10-50 Hz (Schwartz 2006)

## 4.1 Standard Electrical Brain Signals

In this chapter, I will concentrate on the different electrical brain signals which can be obtained by electrode recording. All these signals have amplitudes in the microvolt range and represent extracellular potentials that are generated by neurons in the cortex. I.e. the

electrode does not penetrate the cell membrane of the neuron to record intracellularly but is located in the extracellular space in the vicinity of one or more neurons to pick up the extracellular potentials generated by neural activity.

The classification of recorded signals is a matter of the volume size of the brain tissue they are recorded from and a matter of the signal frequency. The volume, or voxel, from which signals can be recorded depends on the size, placement, and impedance of the electrode and the amplitude of the neural signal. The frequency depends on the filtering of the monitored signal. The filtering includes anatomical conditions (recording from the skin leads to the attenuation of certain frequencies due to the skin, skull, cerebrospinal fluid, and dura mater lying in between recording electrode and brain tissue), electrode specifications like electrode material or surface morphology, and the hardware and software of the recording system such as the amplifier and the evaluation software.

*Tab. 4.2 Classification of standard electrical brain signals*

Signal	Frequency and Standard Filters	Amplitude	Source
SUA	>500 Hz (Siegel 2010) high-pass filtered >300 Hz (Waldert 2009)	0.05-5 mV (Humphrey 1990) 0.05-0.3 mV (Humphrey 1990) 0.1-0.5 mV (Cogan 2008)	1 neuron large (pyramidal) cells neuronal output via soma and axon (Logothetis 2001)
MUA	>500 Hz (Siegel 2010) high-pass filtered >300 Hz (Waldert 2009)	0.05-5 mV (Humphrey 1990)	>1000 neurons (Logothetis 2003) a sphere with 50-350 $\mu\text{m}$ radius around the electrode tip (Logothetis 2003) neuronal output via soma and axon (Logothetis 2001)
LFP	<300 Hz (Pesaran 2009) <250 Hz (Siegel 2010) low-pass filtered <250 Hz (Pesaran 2002)	0.05-5 mV (Humphrey 1990)	several hundreds of neurons (Siegel 2010) 0.5-3 mm around the electrode tip (Logothetis 2003) neuronal input via dendrites (Logothetis 2001; Scherberger 2005)
Mass Activity (ECoG)	<500 Hz (in epileptic seizures (Staba 2002) low-pass filtered <100 Hz (Mehring 2004)	0.05-1 mV (ECoG) (Humphrey 1990)	> 100.000 neurons large dendrites of pyramidal neurons, arranged in parallel to each other and orientated perpendicular to the cortical surface (Siegel 2010)
Mass Activity (EEG)	<100 Hz (Niedermeyer 2005) low-pass filtered <100-300 Hz (Niedermeyer 2005) <50-100 Hz (Nunez 2006)	0.02-0.05 mV (Nunez 2006)	square millimetres to centimetres synchronized cortical tissue (Lopes da Silva 1991; Schwartz 2006) large dendrites of pyramidal neurons, arranged in parallel to each other and orientated perpendicular to the cortical surface (Siegel 2010)

Thus, depending on the electrode design and the recording system including amplifiers and filters, different brain signals can be recorded. We can differentiate between five main recordable signals representing certain spatial resolutions. (1) Mass activity is measured

either by electrodes sitting outside the head on the skin (EEG) or (2) by electrodes sitting on the brain surface (epicortical ECoG). EEG signals are recorded within a spatial domain of 3 cm (Schwartz 2006) whereas epicortical ECoG electrode grids used in human epilepsy diagnosis have spatial resolution of about 5 mm. (3) Microelectrodes used in an epicortical ECoG recording are able to measure local field potentials (LFP) in a spatial domain of 0.1 mm (Tsytsarev 2006). LFPs can be recorded from the brain's surface as well as from electrodes penetrating the brain tissue measuring intracortically. (4) Multi unit activity (MUA) as well as (5) single unit activity (SUA) are measured intracortically with a microelectrode inserted into the tissue.

### *Single-Unit Activity (SUA)*

The term single-unit refers to a single neuron. A single-unit activity is the signal of a discharging neuron which is intracortically measured by a microelectrode. The electrode picks up all signals generated in the vicinity (100  $\mu\text{m}$ ) of the tip. The largest signals originate from the large pyramidal cells of layer V which have a cell body size of about 10-30  $\mu\text{m}$  (Braitenberg 1998). After high-pass filtering the signal at >300 Hz, neurons can be distinguished from others by their signal shape. By spike detection and sorting, each spike signal is assigned to its corresponding neuron (Waldert 2009). SUA is a digital signal. It tells whether a neuron is firing or not. Thus, the information is not contained in the signal amplitude but in the firing rate. As the microelectrode measures only in a small volume close to a neuron, the largest signal it records is the change in the extracellular potential field of the nearest cell (Humphrey 1990). This signal is larger in amplitude and shorter in signal duration (1-2 ms (van Rotterdam 1982)) than the signals described below. The firing rate of a single, well isolated neuron has been the main parameter used in systems neuroscience for decades. As the extracellular fluid has low-pass filter properties, SUA is a strong signal only locally, and is attenuated rapidly over the distance some micrometres away from the electrode tip (Logothetis 2003).

### *Multi-Unit Activity (MUA)*

Like SUA, MUA is recorded by an intracortical electrode. Using an electrode with a lower impedance (40-120 k $\Omega$  (Logothetis 2003)) and placing it further away from the large, spike generating cells, the signal is not dominated by the activity of one principal neuron. Within a sphere around the electrode tip having a radius of 50-350  $\mu\text{m}$ , signals are recorded that consists of spikes coming from multiple neurons (Waldert 2009) as well as from dendrite activity. By high-pass filtering this compound signal, a weighted sum of action potentials from all neurons in the recorded volume is obtained. The weighing of the different action potentials is given by the distance between each neuron and the electrode site (Logothetis 2003).

### *Local Field Potential (LFP)*

If the same compound signal, described in the paragraph above, is low-pass filtered, one obtains a LFP. Compared to SUA and MUA, the LFP is an analogue signal. It is the summation signal of dendritic potentials that are presenting the input signals of the cells. Thus

the LFP is an averaged measure of pre- and postsynaptic activity within a volume of neuronal tissue (Katzner 2009; Mitzdorf 1985) whereas SUA and MUA show single action potentials of large pyramidal cells (Scherberger 2005). Postsynaptic potentials have a signal duration of 10-250 ms (van Rotterdam 1982), and by overlapping lead to synchronic activity that can be measured. To eliminate the high-frequency components of single spikes, the signal is low-pass filtered <300 Hz. LFPs appear to convey relevant information that is not present in neuronal spike activity (Scherberger 2005; Wilke 2006; Womelsdorf 2006; Womelsdorf 2007a) such as attention (Fries 2001a) or predicting the time of a planned movement (Mehring 2003; Pesaran 2002). In addition, LFP fluctuations are also closely correlated with hemodynamic changes measured by fMRI (Logothetis 2001; Logothetis 2003) and underlie the generation of EEG and MEG measurements (van Rotterdam 1982). LFPs can either be measured with an intracortical or with an epicortical electrode.

### *Mass Activity*

According to its name, the mass activity is a summation signal reflecting the activity of a large neuronal population. As the LFP, mass activity exhibits average properties and does not represent single neuron activity or interconnections. If signals are recorded non-invasively on the scalp, they are very small due to the attenuation taking place between the cortex surface and the scalp. Thus only the synchronised activity of a large group of neurons is possible to record. An area of several square millimetres or even centimetres of synchronised cortical tissue is needed to generate a measurable voltage in the mV range on the scalp (Lopes da Silva 1991; Schwartz 2006). Mass activity can also be recorded by epicortical electrodes. Compared to intracortical microelectrodes, they have a relatively large electrode area and low impedance. The position on the cortical surface instead of inserting them into the cortex results in a placement further away from the large cortical neurons. Thus, the recorded signals consist more of dendrite activity than single neuron action potentials.

## **4.2 Concepts of Neurotechnical Interfaces to the Brain**

In this chapter, I will give an overview of the electrode types used in neuroscience and show the engineering approaches to develop micromachined electrodes that fit the requirements of the ongoing neuroscientific research. To provide a better understanding of microelectrodes, their working principles and properties, the following subchapter will deal with the interface between the biological tissue and the technical device, the electrode.

### **4.2.1 The Electrode-Electrolyte Interface**

Extra- and intracellular fluids are electrically conductive liquids, called electrolytes. In such liquids, charge is transferred by the movement of free ions. In contrast, the metal electrode sites and conductor paths of an implanted device are electrically conductive due to free electron movement. The electrode-electrolyte interface is the surface of the electrode site where the metal is in direct contact with the body fluid. The transmission from ion to

electron conduction and vice versa takes place at this interface. Recording from or stimulating neurons requires a charge transfer across this interface. One can differentiate between three types of charge transfer: capacitive redistribution, reversible Faradaic and irreversible Faradaic processes (Merrill 2005).

### *Capacitive Redistribution*

A very simple model of the phase boundary between metal and fluid is the Helmholtz double layer (Helmholtz 1853). It describes two layers of opposed charged particles that face each other at the metal-electrolyte interface (Fig. 4.1). In a, for example, negatively charged metal electrode, electrons will build a surface charge on the solid while positively charged free ions of the solution will arrange a second layer facing the first one. A single layer of water molecules, acting as electrical dipoles, adheres to the metal surface. In the solution, the free ions are likewise surrounded by water molecules. Thus, the two charged layers are separated by a dielectric layer of oriented water molecules and can be described as a simple parallel plate capacitor. The capacitance of the double layer has a relatively large value of about 10-20  $\mu\text{F}/\text{cm}^2$  which is due to the only one water molecule thick dielectric layer (Robblee 1990).

With capacitive redistribution, charge is transferred by charging and discharging the double layer without particles actually crossing the interface. The ions in the solution are just shifted toward the electrode site or away from it, every time a change in electrode potential occurs (Fig. 4.1a). With capacitive redistribution, only small amounts of charge can be transferred across the interface which is mostly the effect during recording (Stieglitz 2004).

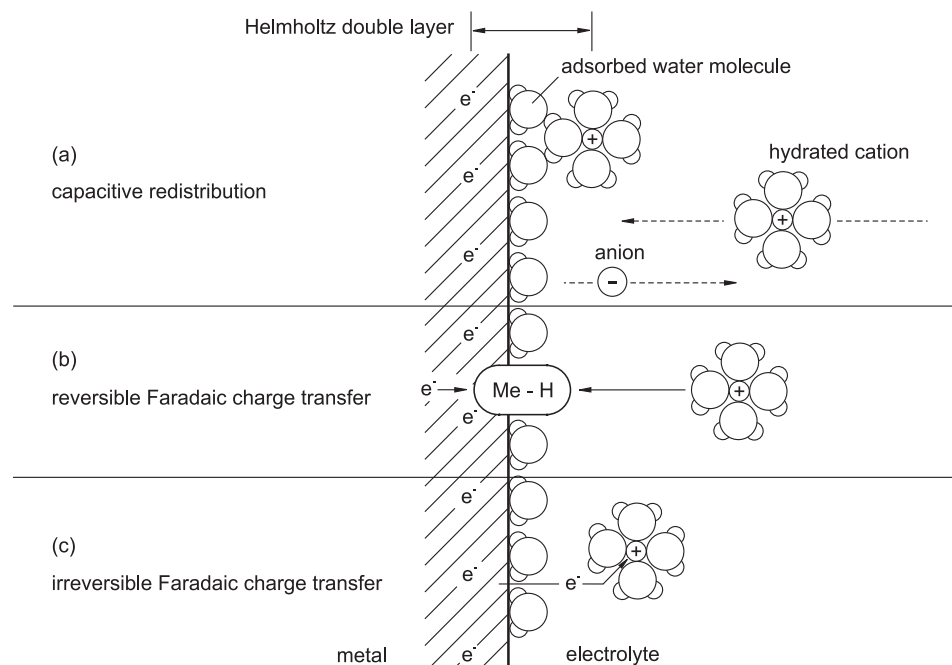
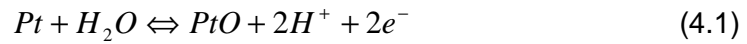


*Fig. 4.1. Physical representation of the three different types of charge transfer across a metal-electrolyte interface: (a) redistribution of charge, (b) reversible charge transfer (here, hydrogen atom plating) and (c) irreversible charge transfer (here, reduction of a cation in solution)*

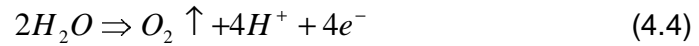
### *Reversible Faradaic Charge Transfer*

Faradaic charge transfer always involves electron transport across the interface. This is due to chemical reactions at the surface of the electrode site. Particles at the surface are oxidized or reduced by either emitting an electron to the positively charged electrode or by receiving an electron from the negatively charged electrode. If the reaction products stay immobilized at the electrode surface, this reaction can be reversed by applying a second phase with an inverted electrode potential causing the reverse reaction. With this stimulation paradigm, called charge balancing, the initial state of the interface is restored (Brummer 1977). Immobilized reaction products are e.g. the oxide formation of platinum (Eq. 4.1) and the hydrogen complex formation, the hydrogen atom plating (Eq. 4.2, Fig. 4.1b), at a platinum surface (Cogan 2008).



### *Irreversible Faradaic Charge Transfer*

Faradaic charge transfer is called irreversible, if the reaction products diffuse into solution (Eq. 4.3, Fig. 4.1c) or evolve as gas (Eq. 4.4) and thus are not available anymore for a reverse reaction. While the two first charge transfer principles are used in recording and stimulation, the latter has to be prevented. Irreversible Faradaic reactions result in electrode corrosion by dissolution of the metal and in changes of the electrolyte such as gas formation due to electrolysis of the water and pH shifts of the biological environment.



### *Equivalent Circuit Model*

The electrode-electrolyte interface can be modelled with standard electrical circuit components. A simple model is depicted in Fig. 4.2. A capacitor  $C_H$  represents the Helmholtz double layer, in parallel to an ohmic resistance  $R_F$  which enables the actual charge transfer across the phase boundary, and the access resistance  $R_{ac}$  representing the ohmic resistance of the electrolyte. While this is a very elementary model, it was adequate to describe the electrodes manufactured in this thesis. More sophisticated models of the interface are discussed in i.a. (Cantrell 2008; Franks 2005; Geddes 1997; Kovacs 1994; Weiland 2000).

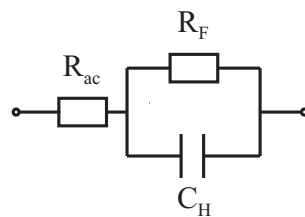


Fig. 4.2. Basic equivalent circuit of an electrode-electrolyte interface



### *Evaluation of Electrodes*

There is the need to evaluate different types of electrodes and electrode materials with respect to their application in neural recording and stimulation. The electrodes of interest for neuroprosthetic applications are polarizable electrode. I.e. these electrodes change the voltage across their interface if charge is transferred. Non-polarizable electrodes, such as the standard hydrogen electrode or the silver/silver chloride electrode, do not change their potential transferring charge and thus are used as reference electrodes in recording and electrochemical measurements. However, non-polarizable electrodes are not implantable due to their configuration and materials. Thus, developing implantable devices, the main focus is on polarizable electrodes using materials that will be mentioned in the following paragraphs.

In recording, one important parameter is the signal-to-noise ratio with the noise being dependent on the real part of the interface's impedance (Koch 2002; Liu 2008). The thermal noise can be calculated as

$$U_N = \sqrt{4kTR\Delta f}, \quad (4.5)$$

where  $U_N$  is the Johnson noise in Volt,  $k$  the Boltzmann constant,  $T$  the absolute temperature,  $R$  the interface's resistance and  $\Delta f$  the bandwidth (Stieglitz 2004). Thus, the interface impedance should be low to have a large signal-to-noise ratio which can be a problem with microelectrodes which show high impedance due to their small surface area.

The Johnson noise should not be confused with the biological noise present in SUA recording which comprises mainly diffuse neural background activity such as signals from cells surrounding the neuron of interest (Ferster 1996).

Another property of recording electrodes is the transfer behaviour of the interface. In contrast to non-polarizable electrodes, polarizable electrodes act as a high-pass filter and thus, do not transmit low frequency and DC components of a biological signal. Different filter characteristics can be observed with different materials. Platinum e.g. transfers the low-frequency components better than gold or stainless steel (Fig. 4.3). However, this behaviour is only present, if the input impedance of the amplifier is small (e.g. 750 k $\Omega$  for the signals measured in Fig. 4.3). In this case, the electrode-electrolyte impedance is in the same range as the amplifier input impedance. Thus, the voltage of the biosignal is divided between the interface impedance and the amplifier input impedance and only a fraction of the voltage is amplified by the recording system. However, this is rather a historical problem as today's biosignal amplifiers comprise input impedances in the gigaohm range while large electrode-electrolyte impedances are about 1 M $\Omega$ . With such a electrode-to-amplifier impedance ratio, even lower frequency signals which are only partly transmitted due to the electrode-electrolyte high-pass filter characteristics are amplified (Geddes 1989).

For stimulation, the most important characteristic of an electrode site is the amount of charge which can be transferred across the electrode-electrolyte interface without damag-

ing the electrode or the tissue, i.e. without causing irreversible Faradaic reactions. Electrodes can be compared by measuring their reversible charge injection capacity  $Q_{inj}$ , or charge injection density, which is a measure of how much charge can be stored in the double layer and the reversible Faradaic reactions during the time period of a stimulation pulse. The unit of  $Q_{inj}$  is  $\mu\text{C}/\text{cm}^2$ . However, the charge injection capacity alone is not sufficient to estimate whether an electrical stimulation is safe. The electrochemical processes at the interface also depend on the phase duration of a stimulation pulse, the charge per phase, and the pulse rate (Weiland 2003). Thus, these parameters have to be taken into account evaluating the electrode-electrolyte interface.

If microelectrodes are used for stimulation, high charge densities occur due to the small electrode surface which can lead to electrode corrosion and tissue damage (McCreery 1990). In recording, high-impedance microelectrodes exhibit large noise values and a non-linear transfer behaviour (Cogan 2008).

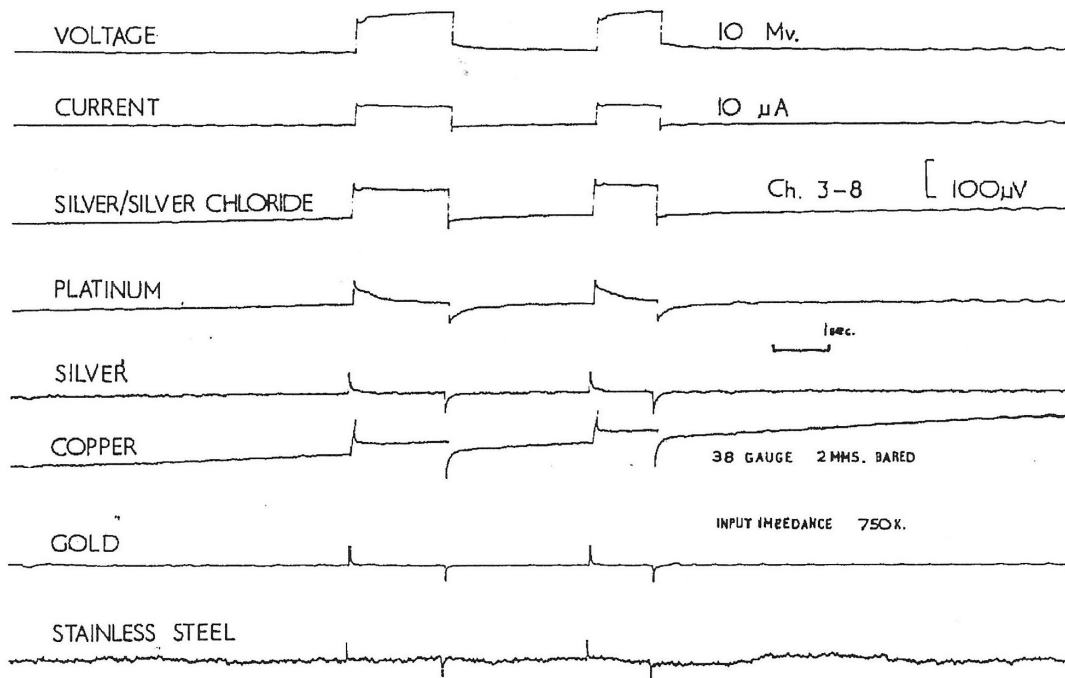


Fig. 4.3. Signal distortion of a rectangular current pulse passed in saline solution and recorded with different electrode materials. For all metals, the electrode area was  $0.1 \text{ mm}^2$  and the input impedance of the amplifier was  $750 \text{ k}\Omega$ . The time bar is 1 s (Cooper 1963).

### Electrode Materials

For recording as well as for stimulation, electrode materials should form a small and long-term stable impedance at the phase boundary to assure a reliable contact to the neural tissue. Moreover, they have to be biocompatible and resistant to corrosion.

Implantable electrode materials used for stimulation are platinum, platinum-iridium alloy, iridium oxide, titanium nitride, tantalum and poly(ethylenedioxythiophene) PEDOT. For recording it is tungsten, platinum, platinum-iridium alloys, iridium oxide, stainless steel, titanium nitride, palladium, rhodium, gold and PEDOT (Cogan 2008; Merrill 2005; Robblee

1990). Among these, platinum and platinum-iridium are the most commonly used. Depending on the pulse characteristics, safe charge injection limits were found to be 100-400  $\mu\text{C}/\text{cm}^2$  for platinum (Weiland 2003) and 2-4  $\text{mC}/\text{cm}^2$  for iridium oxide (Beebe 1988).

For stimulation, the charge which can be injected into the tissue over an electrode-electrolyte interface is the important value and materials have to be chosen according to this criterium. In recording, this parameter does not play an important role because the neural signals are small and the input impedance of the amplifier is high so that only very small amounts of charge are crossing the interface. That is why e.g. gold is also often used as an electrode material in recording applications. Nevertheless, gold has some drawbacks in comparison to platinum. Gold has a larger electrochemical impedance (45  $\text{k}\Omega$ ) than platinum (15  $\text{k}\Omega$ , both for an electrode with 35  $\mu\text{m}$  in diameter at 1 kHz, with 0.9 % NaCl as electrolyte and a measurement amplitude of 10 mV, after an electrochemical cleaning with 3 V at 1kHz for 10 s (Rubehn 2010b)) and thus exhibits a higher thermal noise (Eq. 4.5) which decreases the signal-to-noise ratio of the neural signal. From the technical point of view, the main drawbacks of gold as a microimplant material are its low adhesion to PI and the fact that solder pads made of a 300 nm thick gold thin-film are destroyed during soldering even with low-temperature melting solder pastes.

#### 4.2.2 Precision Engineered Electrodes

##### *The Metal Rod Microelectrode*

When electrical signals are measured directly in the brain of anesthetized or awake animals the standard and most common measurement tool in electrophysiological neuroscience is a metal rod, or wire (Gallese 1996; Janssen 2008; Maffei 1965). In 1942, Harry Grundfest and Berry Campbell used insulated steel rods with a grinded tip to record proprioceptive signals from the dorsal spinocerebellar tract of cats (Grundfest 1942). The electrode tips were shaped by grinding and had a size of 5-10  $\mu\text{m}$ . Grundfest refined his manufacturing by electropolishing the tips by immersing them in an acid and applying a DC voltage of 6 V to the electrode obtaining tip sizes of less than 0.2  $\mu\text{m}$  (Grundfest 1950). Numerous different types of the rod electrode were manufactured and described in literature. However, all were based on the same principle introduced by Grundfest. A metal rod with a diameter of about 25  $\mu\text{m}$  to 250  $\mu\text{m}$  is completely coated with a lacquer or glass insulation. Only the electrolytically tapered tip (Fig. 4.4) is not insulated and acts as the electrode site which contacts the neural tissue electrically.

Nobel Laureate David Hubel manufactured lacquer-insulated, electro-polished tungsten rods (Fig. 4.4). In 1957, he named these devices *microelectrodes* (Hubel 1957), a term still used today. Further variants were stainless steel rods with lacquer insulation (Green 1958), platinum-iridium alloy with glass insulation (Wolbarsht 1960), and glass-insulated silver electrodes coated with platinum-black by Gray and Svaetichin (Gray 1951).

Depending on the size and impedance of the electrode site, mostly SUA or MUA are recorded albeit LFP recordings can also be obtained (Scherberger 2005). The advantages of the classic microelectrode are the thin shaft and the sharp tip in the micrometer range

as well as its potential to penetrate the tough dura mater of cats and monkeys. The main drawback is that it has only one electrode site to record from. Thus, only one neuron or a few neurons (in SUA recordings) can be monitored at the same time. Microelectrodes are mostly used in acute recordings i.e. they are withdrawn after the experimental session and have to be inserted again in the following session. This makes it impossible to record from a larger number of electrode sites simultaneously due to the time it takes to insert all microelectrodes and to find an adequate neuron while the time of an experimental session is limited.

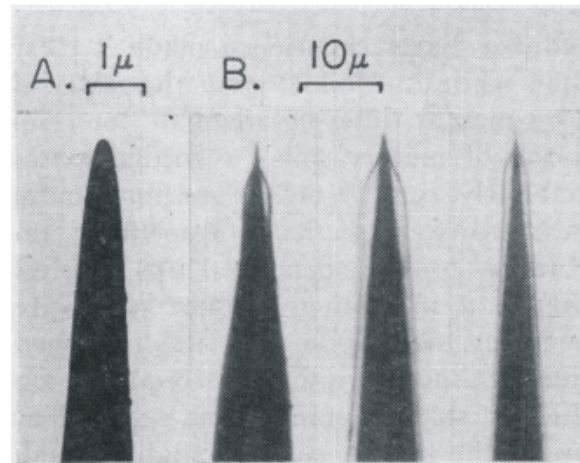


*Fig. 4.4. SEM micrograph of Hubel's microelectrodes: an uncoated sharpened tungsten rod (A) and optical micrographs of coated electrodes (B) (Hubel 1957); From Hubel DH. Tungsten Microelectrode for Recording from Single Units. Science. 1957. 125(3247): 549-550; Reprinted with permission from AAAS*

### *The Tetrode*

If more than one neuron is recorded with an electrode site, the signals of the different cells vary in shape and amplitude. However, if these parameters are not constant it is not possible to distinguish between different neurons recorded with the same microelectrode. This is e.g. the case in the hippocampus where neurons are densely packed and action potential amplitudes vary strongly. This problem was addressed by Bruce McNaughton and co-workers in 1983 by manufacturing an electrode wire with two electrode sites which they called the *stereotrode* (McNaughton 1983). To achieve this they used two Teflon-insulated wires made of a platinum-iridium alloy with a diameter of 25  $\mu\text{m}$ , twisted them and cut them at the end to obtain two electrode sites lying side by side separated by a layer of insulating Teflon with a thickness of 6  $\mu\text{m}$ . The impedance was reduced to about 500  $\text{k}\Omega$  by electroplating platinum on the electrode sites. If the activity of one neuron is recorded with two electrodes the spike signal will be larger on the electrode that is closer to the neuron. The ratio of the signal recorded at the first electrode to the signal recorded at the second electrode will be constant irrespective of the changes in signal amplitude generated by the neuron.

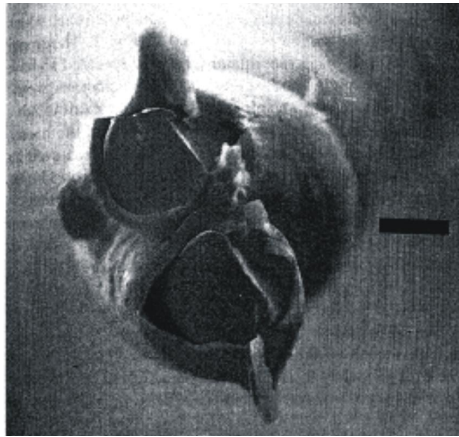


Fig. 4.5. SEM micrograph of a stereotrode (McNaughton 1983)\*; two Teflon coated wires are twisted and cut open at the tip by scissors. The calibration bar is 20  $\mu\text{m}$  long. \* Reprinted from *Journal of Neuroscience Methods*. 1983; 8: 391-397, McNaughton BL, O'Keefe J, and Barnes CA, *The Stereotrode: A New Technique for Simultaneous Isolation of Several Single Units in the Central Nervous System from Multiple Unit Records*, Copyright (1983), with permission from Elsevier

As McNaughton et al. pointed out in their publication of 1983, the position of the neuron in a three-dimensional space cannot be uniquely localized with two electrodes. They proposed a tetrode, an electrode with an array of four electrode sites closely spaced so that the electrode sites record from overlapping populations of neurons. In 1993, Matthew Wilson and Bruce McNaughton reported on neural signal discriminated using a tetrode (Wilson 1993). They used the same manufacturing approach as for the stereotrode: four strands of nickel-chromium alloy were twisted to form a wire of 40  $\mu\text{m}$  in diameter. A second group published their results using a tetrode based on the stereotrode principle in 1993 as well. John O'Keefe and Michael Recce used four Teflon-coated platinum-iridium strands with a diameter of 25  $\mu\text{m}$  each that were twisted to record single units from the rat hippocampus (O'Keefe 1993). Charles Gray and co-workers compared recordings from single electrodes, stereotrodes, and tetrodes in cat visual cortex and could show that with a tetrode multiple SUA could be easily separated whereas the single electrode and the stereotrode failed (Gray 1995). A second tetrode design was developed by Thomas RECORDING GmbH (Marburg, Germany) which comprises four metal electrode sites in one tapered glass rod with a shaft diameter of about 100  $\mu\text{m}$ .

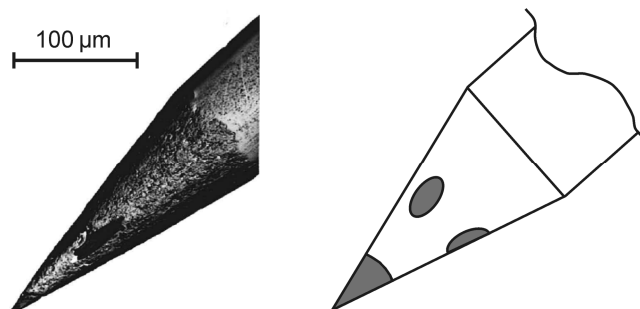
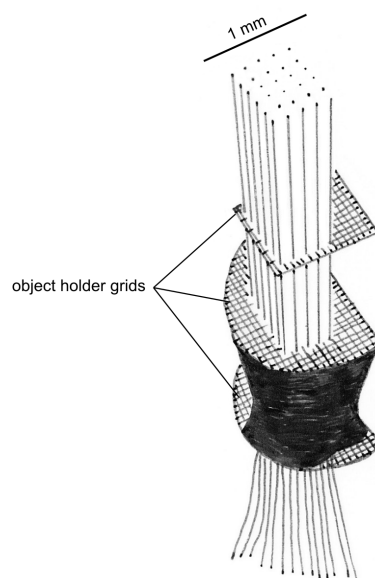


Fig. 4.6. Tetrode manufactured by Thomas RECORDING GmbH (Thomas 2010). SEM micrograph (left)\*, schematic drawing of the glass tip with electrode sites (right) \* (courtesy of Thomas RECORDING GmbH)

### *Electrode Arrays*

Besides listening to some single neurons by inserting one or a few individual wires into the brain neuroscientists are interested in recording from large ensembles of neurons. In 1956 Verzeano was probably the first to record from two rigidly assembled electrodes (Verzeano 1956). However, one of the first approaches to manufacture an electrode array with fine electrode spacing and a larger number of electrode sites was made by Jürgen Krüger. In 1981, he published his work on an array of 5 by 6 quartz-glass-coated platinum-iridium wires with a 160  $\mu\text{m}$  spacing (Krüger 1981). The wires had a diameter of 5  $\mu\text{m}$  without and 30  $\mu\text{m}$  with insulation. The electrode tips were sharpened by grinding. To obtain such a fine spacing in the micrometer range Krüger inserted the wires into the grid of an electron microscope object holder and glued them together with pitch.



*Fig. 4.7. Drawing of the electrode wire array manufactured by Krüger; wires are arranged in three SEM object holder grids to obtain a constant spacing. By gluing the wires to two of the grids, the array is fixated (modified after (Krüger 1981)).*

A lot of scientists (Musallam 2004; Scherberger 2003) are using electrode arrays of the type introduced by Krüger: conventional metal rods with insulation are arranged in a jig and subsequently glued together to form an array. Today such electrode arrays are commercially available from different manufacturers (Tab. 4.3).

### *Microelectrodes for Chronic Recording*

As mentioned above the standard microelectrode is removed after the recording session. To be able to record chronically from freely moving and behaving ground squirrels Felix Strumwasser established a new implantation method in the late 1950s (Strumwasser 1958). He inserted up to six insulated stainless steel wires with a diameter of 80  $\mu\text{m}$  into the brain. At the tip, the insulation was exposed to form the electrode at the cross-section of the wire. For each wire a hole with about 340  $\mu\text{m}$  in diameter was drilled into the skull. After inserting the wires through these holes dental cement was applied around the base of the wires and the latter were soldered to flexible leads. John O'Keefe used Strum-

wasser's technique in 1969 to record with nickel-chromium wires from freely moving cats (O'Keefe 1969).

When recording chronically from brain structures of small animals metal rod electrodes and electrode arrays can be fixated on the skull. This does not work for larger animals like cats or primates due to the relative movement between the brain and the skull. If a stiff electrode is attached to and moves with the skull it will affect or even destroy the soft brain tissue (Biran 2007). Scientists were solving this problem by developing *floating* electrodes. The concept of such an electrode is to mechanically decouple the electrode part inserted into the brain matter from the connector part which is fixated on the skull. The problem of a relative movement between the skull and the cortex was addressed by Burns and Robson who published a rather complicated implant assembly in 1960 (Burns 1960). A chlorided silver wire inside a micropipette used as the electrode was spring suspended to follow the movement of the cortex due to breathing and heart beat. While they could record SUA without a change in amplitude normally caused by a relative movement between the recording site and the brain tissue, this assembly could not be used for chronic recordings and electrodes were removed after a maximum recording time of 6 hours. Gualtierotti and Bailey presented an equally advanced electrode setup to achieve neutral buoyancy of the electrode and could record up to 2-5 days in the vestibular nerve of bullfrogs (Gualtierotti 1968).

In 1973, Salcman and Bak presented a much simpler and easier to use electrode assembly capable for chronic implantation (Salcman 1973). A Teflon-coated platinum-iridium wire with a diameter of 25  $\mu\text{m}$  was electrolytically tapered and inserted into a glass micropipette. The shaft of the glass pipette was broken and removed in order to obtain a 2 mm long glass cone at the tip of the metal wire. The electrode tip was inserted through the intact pia mater until the glass cone was completely embedded in the cortex Fig. 4.8. The

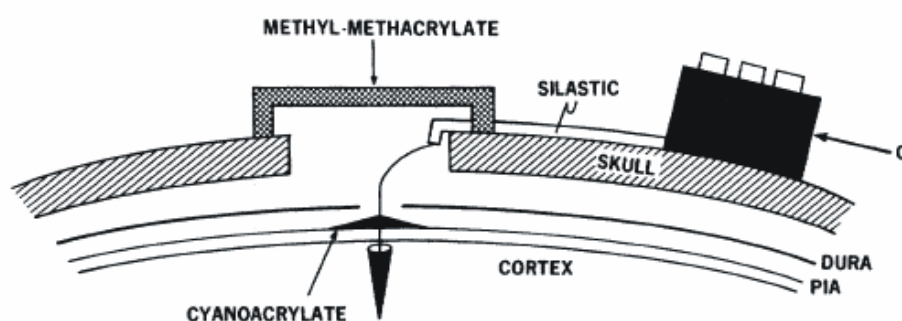


Fig. 4.8. Sketch of the implantation site of the floating electrode introduced by Salcman in 1973 (Salcman 1973)\*; the glass tip can move with the cortex while it is connected to the connector on the skull by a flexible platinum-iridium wire.

\* © 1973 IEEE. Reprinted, with permission, from Salcman M and Bak MJ. Design, Fabrication, and in Vivo Behavior of Chronic Recording Intracortical Microelectrodes. IEEE Transactions on Biomedical Engineering. 1973

wire was glued to the pia by isobutyl cyanoacrylate, led through the trepanation hole, and connected to the skull-mounted connector. The trepanation hole was covered with a

methyl-methacrylate chamber which had feed-throughs for the electrode wire. Due to the thin and flexible platinum-iridium wire, the glass tip and the connector can move independently without applying force to the electrode part and to the brain. Salcman and Bak reported on an even more simplified assembly of a floating electrode and could record from completely unrestrained cats (Salcman 1976). A 2 mm long pure iridium wire acted as the electrode and was welded to a pure gold wire used as the cable to connect the electrode to the connector on the skull. Both wires had a diameter of 25  $\mu\text{m}$  and were insulated with Parylene-C. Due to the difference in elasticity of the two metals, the iridium wire is stiff enough to penetrate the pia mater whereas the gold wire is so flexible that it could follow the brain movements. Schmidt et al. used the same electrodes to record long-term signals of single neurons from the motor cortex of monkeys. They could measure SUA up to 223 days (Schmidt 1976). A similar approach was made by Loeb et al. who recorded SUA from dorsal root ganglia of a freely moving cat by chronically inserting insulated platinum-iridium wires 50  $\mu\text{m}$  through a small laminotomy in the spine (Loeb 1977).

Not only single electrodes were implanted by using the floating electrode approach but also electrode arrays. To stimulate the visual cortex in humans, Bak et al. assembled a floating microelectrode array using iridium rods welded to flexible 25  $\mu\text{m}$  diameter gold wires (Bak 1990). At the region of the weld joints, two or three electrodes were assembled to one array by applying epoxy. The whole array was insulated with Parylene-C. Bradley et al. assembled 8 iridium rods that were welded to platinum wires and insulated with Parylene-C into an array with an electrode spacing of 500  $\mu\text{m}$  using a mould for the casting epoxy. The 8 platinum leads were coiled around a silicone rubber tubing with a diameter of 0.5 mm and coated with silicone to obtain a flexible cable (Bradley 2005). Several of these arrays were inserted into the visual cortex of a monkey and used for stimulation.

Musallam et al. developed a floating multi-electrode array together with the company MicroProbes for Life Science (Gaithersburg, MD, USA) (Musallam 2007). A 250  $\mu\text{m}$  thick alumina ceramic plate was laser-structured to house 18 electrochemically tapered platinum-iridium rods with a diameter of 80  $\mu\text{m}$  and a length between 0.5 mm and 10 mm. The rods were inserted into the alumina platform and contacted with gold wires with a diameter of 25  $\mu\text{m}$  forming a flexible cable. Today, arrays with up to 36 rods can be purchased from MicroProbes for Life Science.

Over the years a lot of different designs of hand-made electrode were developed to address different problems in neurophysiology. Reitböck and Kralik could even present arrays in which each electrode wire could be moved separately to adjust the position of the electrode tip inside the cortex (Kralik 2001; Reitböck 1983).

### *Shaft Microelectrodes with Linear Electrode Arrangement*

At the same time Krüger developed the 30-channel microelectrode array, first approaches were reported on the manufacturing of shaft electrodes with multiple recording sites. Instead of having an array of separate rods with an electrode site on each tip, the shaft electrode is one rod with several electrode sites aligned on the side.



James Barna et al. described the manufacturing of a shaft electrode with 16 electrode sites in 1981 (Barna 1981). In order to record with closely spaced electrodes from deep and superficial cerebral sites at the same time, they assembled 16 insulated stainless steel wires with a diameter of  $25\ \mu\text{m}$  within a stainless steel tube with an outer diameter of  $300\ \mu\text{m}$ . At the tip the tube was ground so that only half of it remained as an open form. The wires exit the closed tubing and were bent and aligned at the remaining half of the tube to form a linear array. After gluing the wires to the tubing by epoxy the wires were cut to one length so that they end at the outer diameter of the tube.

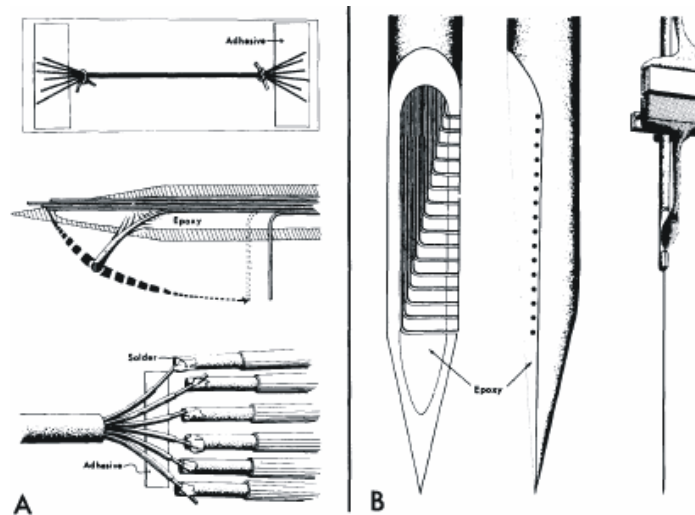


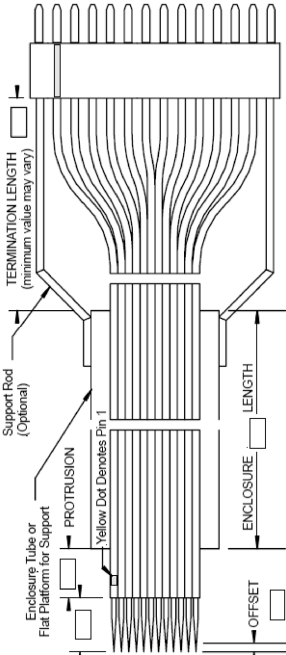
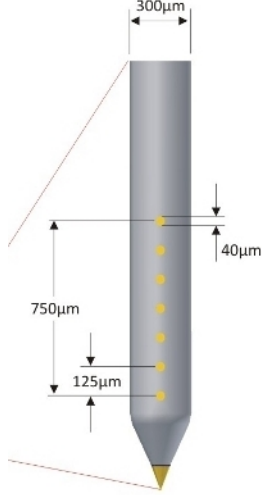
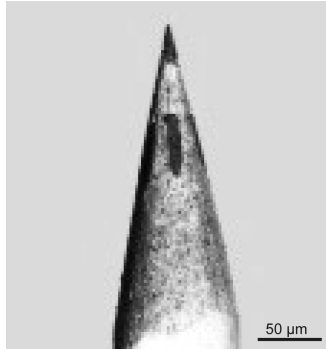
Fig. 4.9. Sketch of the manufacturing process of Barna's shaft electrode (Barna 1981)\* (A) and the assembled linear electrode array (B) \* Reprinted from *Electroencephalography and Clinical Neurophysiology*. 1981; 52(5): 494-496, Barna JS, Arezzo JC, and Vaughan J, A New Multielectrode Array for the Simultaneous Recording of Field Potentials and Unit Activity, Copyright (1981), with permission from Elsevier

Another type of shaft electrode was introduced by Jellema and Weijnen in 1991 (Jellema 1991). They used a Teflon half tube with an inner diameter of  $300\ \mu\text{m}$  as a casting mould form. The Teflon half tube was pierced with a fine metal needle attached to a micro-manipulator to obtain 12 equidistant holes  $150\ \mu\text{m}$  apart. An insulated nickel-chromium wire with a metal diameter of  $25\ \mu\text{m}$  was inserted in each hole. The wires were bent and aligned in parallel as a bundle within the Teflon tube. Subsequently, the tube was filled with epoxy resin to embed the wires. After curing the epoxy shaft was removed from the tube (Fig. 4.10). Due to the use of the Teflon form, the electrode site spacing can be better controlled than in Barna's approach.

## 4 Interfacing the Brain

**Tab. 4.3: Overview of the commercially available, handcrafted multiple microelectrodes and their reported use in science**

<p><b>Microelectrode Arrays</b></p> <p>MicroProbes for Life Science (Gaithersburg, MD, USA) (courtesy of Micro-Probes for Life Science)</p>		<p>max. 128 tungsten, platinum-iridium or iridium wires, 75 <math>\mu\text{m}</math> diameter, insulated with Parylene-C, array arrangement (Scherberger 2003)</p>
<p><b>Linear Microelectrode Array</b></p> <p>MicroProbes for Life Science (Gaithersburg, MD, USA) (courtesy of Micro-Probes for Life Science)</p>		<p>max. 24 platinum-iridium wires, 12.5-50 <math>\mu\text{m}</math> diameter, insulated with PI, wires are inserted in PI shaft, shaft diameter 200-560 <math>\mu\text{m}</math>, linear array arrangement (Naylor 2005; Starr 2005)</p>
<p><b>Floating Microelectrode Array</b></p> <p>MicroProbes for Life Science (Gaithersburg, MD, USA) (courtesy of Micro-Probes for Life Science)</p>		<p>max. 36 platinum-iridium or iridium wires, 50-80 <math>\mu\text{m}</math> diameter, 400 <math>\mu\text{m}</math> electrode spacing, wire length between 0.5 mm and 10 mm (Musallam 2007)</p>
<p><b>Mircowire Array</b></p> <p>MicroProbes for Life Science (Gaithersburg, MD, USA) (courtesy of Micro-Probes for Life Science)</p>		<p>different numbers (e.g. 4 x 8) of stainless steel or platinum/iridium wires, 25 <math>\mu\text{m}</math> or 50 <math>\mu\text{m}</math> diameter, 250 <math>\mu\text{m}</math> or 500 <math>\mu\text{m}</math> electrode spacing, length up to 30 mm (Wheeler 2005)</p>
<p><b>Bundle</b></p> <p>NB Labs (Denison, TX, USA)</p>		<p>8, 16 or 32 stainless steel wires, 50 <math>\mu\text{m}</math> diameter, insulated with Teflon, bundle or array arrangement (Isaacs 2000)</p>

<p><i>Matrix Microelectrode</i></p> <p>FHC Inc. (Bowdoin, ME, USA) (courtesy of FHC Inc.)</p>		<p>custom number of electrode sites, tungsten, stainless steel or platinum-iridium, glass or epoxy insulation, array arrangement (Starr 2005)</p>
<p><i>Multitrode</i></p> <p>Thomas RECORDING GmbH (Marburg, Germany) (courtesy of Thomas RECORDING GmbH)</p>		<p>8 electrodes, gold contacts, wires inserted in stainless steel shaft, wires are lacquer-insulated, linear array arrangement with one electrode at the tip (Jensen 2009)</p>
<p><i>Tetrode / Heptrode</i></p> <p>Thomas RECORDING GmbH (Marburg, Germany) (courtesy of Thomas RECORDING GmbH)</p>		<p>4 or 7 electrodes, platinum-tungsten electrode sites, quartz-glass insulation, electrode site size 5 µm by 10 µm, shaft diameter 100 µm, pencil like tip shape with one centred electrode at the tip and concentric arrangement of the other electrode sites (Kaneko 1996)</p>

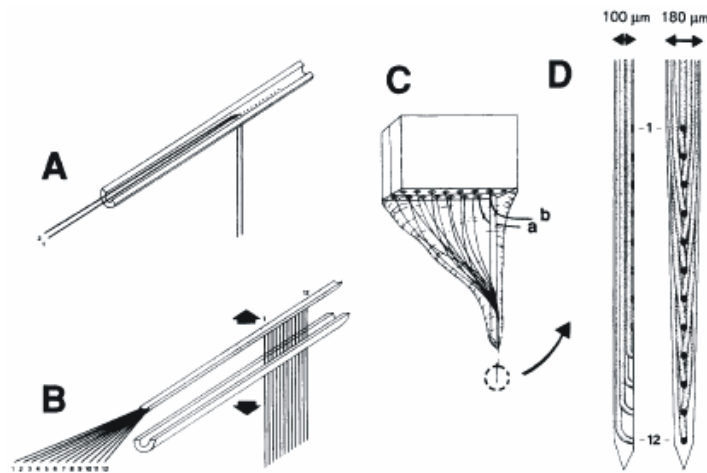


Fig. 4.10. Sketch of the manufacturing process (A, B, C) and an assembled shaft electrode with a linear array as published by Jellema in 1991 (Jellema 1991) Reprinted from *Journal of Neuroscience Methods*. 1991; 40(2-3): 203-209, Jellema T and Weijnen JAWM, *A Slim Needle-Shaped Multiwire Microelectrode for Intracerebral Recording*, Copyright (1981), with permission from Elsevier

For the assembly of most of the precision engineered shaft electrodes with multiple electrode sites, no special equipment is necessary and a lot of neuroscientific research labs manufacture electrodes in their own facilities. However, today a variety of wire arrays and shafts with linear electrode site arrangement can be purchased from different manufacturers (Tab. 4.3).

### 4.2.3 MEMS-based Electrodes

With the development of the production technology for microelectronics and microelectromechanical systems (MEMS) in the middle of the 20<sup>th</sup> century new opportunities came up for the manufacturing of microelectrode implants used for multiple extracellular recordings. With microelectronic manufacturing tools it became possible to reach very small feature sizes of a few micrometers and to place a large number of electrode sites on a small area.

#### *The Michigan Array*

The first report on a microelectrode realized with the integrated circuit production technique was published by Wise, Angell, and Starr in 1969 (Wise 1969; Wise 1970). On a thermally oxidized silicon substrate three gold conductor paths were formed and covered with silicon oxide. At the tip of the substrate the gold conductor tracks and the silicon oxide insulation protruded over the rim of the silicon substrate. The insulation at the gold tips was selectively removed to form the electrodes sites. The electrode tip diameters could be manufactured as small as 2 μm with an interelectrode spacing down to 10 μm.

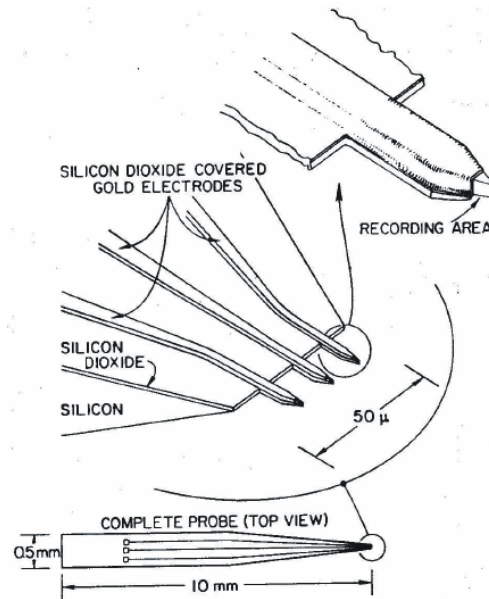


Fig. 4.11. Sketch of the first micromachined electrode array made for neural recording by Wise in 1969 (Wise 1969); © 1969 IEEE. Wise KD, Angell JB, and Starr A. *An Integrated Circuit Approach to Extracellular Microelectrodes*. *Digest of the 8th ICMBE*. 1969

Further development of this microelectrode array led to an implant type which is known as the *Michigan Array* today. A simplified process flow of the electrode shaft fabrication is shown in Fig. 4.12. By selective diffusion of boron into a silicon wafer the shape of the later shaft substrate is defined. Subsequently dielectric materials are deposited on the substrate, followed by a metal layer which is structured to define the conductor paths.

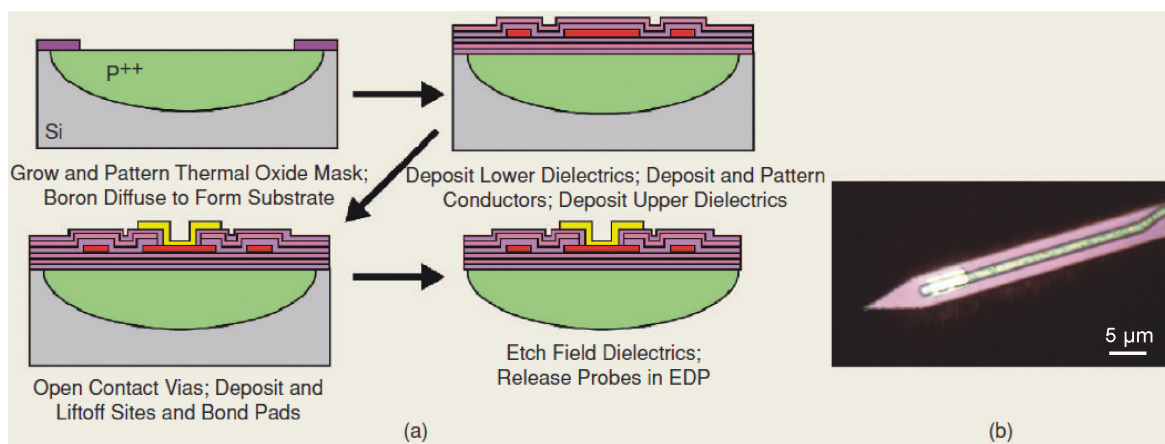


Fig. 4.12. Processing steps (a) and a photograph (b) of a micromachined Michigan Probe (Wise 2005); © 2005 IEEE. Wise KD. *Silicon Microsystems for Neuroscience and Neural Prostheses*. *IEEE Engineering in Medicine and Biology Magazine*. 2005; 24(5): 22-29

The metal is covered by a second layer of dielectrics to completely insulate the metal conductors. The electrode sites and bond contact pads are opened by etching the dielectric material above them. A special electrode material can now be deposited on the electrode sites. As a last step the non-doped silicon is etched to obtain the final form of the shafts.



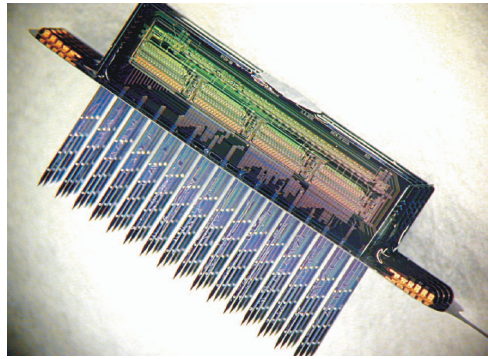


Fig. 4.13. Photograph of an assembled Michigan Array (Wise 2005); © 2005 IEEE. Wise KD. *Silicon Microsystems for Neuroscience and Neural Prostheses*. *IEEE Engineering in Medicine and Biology Magazine*. 2005; 24(5): 22-29

Multiple shafts can be combined to a comb structure which can be processed as one device on wafer level. Such combs can be assembled to form a three-dimensional array with up to 1024 electrode sites and integrated electronics for signal processing (Fig. 4.13) (Bai 2000; Wise 2004). Today, *Michigan Probes* are fabricated and distributed by the company NeuroNexus Technologies (Ann Arbor, MI, USA). Different designs can be purchased up to 64 electrode sites on a comb structure with 8 shafts.

### *The Utah Array*

A completely different approach to a MEMS-based silicon microelectrode array was presented by Campbell in 1991 (Campbell 1991). He did not etch the electrode shafts in the wafer plane as done with the *Michigan Array* but formed the shafts perpendicular to the wafer surface (Fig. 4.14). An array of 10 by 10 shafts was defined by the thermomigration of 100 aluminium pads through an n-type silicon wafer. These aluminium-doped parts were conductive but insulated from each other by the remaining n-type regions.

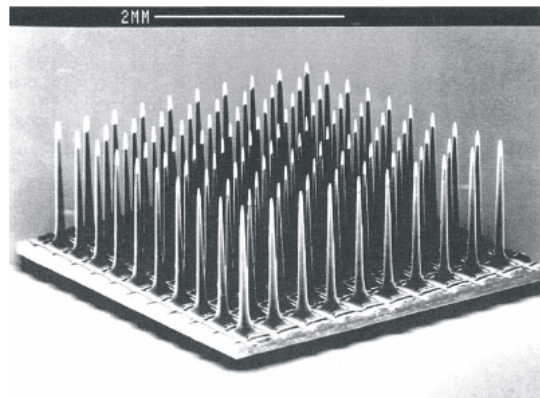


Fig. 4.14. SEM micrograph of the Utah Array (Badi 2003); © 2003 The American Laryngological, Rhinological and Otological Society, Inc.; *Development of a Novel Eighth-Nerve Intraneural Auditory Neuroprosthesis*. *The Laryngoscope*. 2003; 113(5): 833-842; This material is reproduced with permission of John Wiley & Sons, Inc.

To form the rectangular shafts, 11 by 11 deep cuts with a pitch of 400  $\mu\text{m}$  and centred at the n-type regions were made in each array with a dicing saw. Instead of cutting through

the whole wafer, a 150  $\mu\text{m}$  thick silicon block remained uncut as a substrate housing the shafts. The rods with a square cross-section are wet-etched to obtain a needle shape and to polish the rough edges from sawing. As a subsequent step, the needle tips are pushed through a metal foil and coated by sputtered platinum while the basis of the array is masked by the metal foil. Each needle is then electrically contacted by bonding PI coated gold wires to the aluminium pad on the back site of the array. The passivation of the whole array is done by coating the bonding sites and the basis of the needles with diluted PI. While the array itself is small, the 100 gold wires for electrical connection form a relatively rigid cable and cannot be implanted as floating device. However, scientists at the University of Utah aim to develop a fully implantable wireless system (Harrison 2007). The *Utah Array* was commercialized as BrainGait™ by Cyberkinetics Neurotechnology Systems Inc. (MA, USA) and is the only systems that proved its performance as a recording electrode in a spinal cord injured human for 18 months used in a BCI setup to control a computer cursor (Hochberg 2006). In this trial, the wires were still routed to a percutaneous connector that was connected via cable to a preamplifier unit and to a computer controlled signal acquisition system.

#### *The NeuroProbes Array*

The most recent approach to a silicon-based three-dimensional array was made in the NeuroProbes project, a research project funded by the European Commission. Analogue to the fabrication of the *Michigan Probe*, the NeuroProbes shafts are MEMS-processed in the wafer plane.

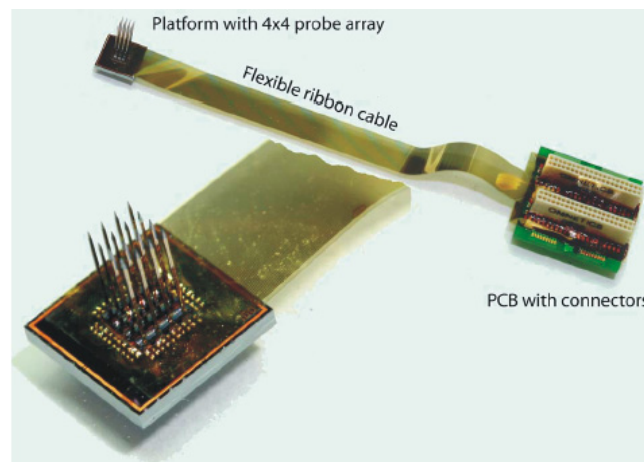


*Fig. 4.15. Photograph of an assembled NeuroProbes Array (Neves 2007) © 2007 IEEE. Neves HP and Ruther P. The NeuroProbes Project. Proceedings of the 29th Annual International Conference of the IEEE/EMBS, Aug.22-26, Lyon, France. 2007. 6442-6444*

Thin-film metal structures define 9 electrode sites and conductor paths on the silicon shaft with a length of 2 mm, 4 mm or 8 mm. Comb-like structures that consist of 4 shafts are fabricated as one device in the wafer plane and can subsequently be assembled to a three-dimensional array by inserting them into the cavities of a silicon platform (Aarts 2008). In addition to the standard shafts with electrical recording sites, shafts with biosensors or fluidic channels can be inserted into the standardized platform (Ruther 2008). Sin-

gle shafts, combs, and whole arrays are bonded to flexible PI-based ribbon cables which connect the electrode sites to a recording system via a commercially available standard connector (Kisban 2008).

A detailed review on further silicon-based arrays can be found in Karen Cheung's article on implantable microscale neural interfaces (Cheung 2007).

### 4.2.4 Flexible Polymer-Based MEMS Electrodes

The standard metal rods as well as the silicon-based microelectrodes are stiff and rigid. This is an advantage during implantation because they can penetrate the brain matter, the pia mater and some of them even the dura mater without buckling or breaking. However, this poses a problem when the electrodes are chronically implanted. Brain matter has a jelly-like consistency and can be affected or damaged by a rigid device (Edell 1992). Due to the difference in mechanical properties of the brain tissue and the electrode material, a permanent micromotion between the electrode and the brain will result in chronic inflammation and strong tissue reaction (Polikov 2005; Seymour 2007). Another disadvantage of stiff electrodes is the fact that they cannot adapt to the form of the organ they should be implanted in. That is for example the curvature of the cerebral cortex when measuring cortical activity with an ECoG electrode or stimulating the auditory nerve by inserting an electrode into the cochlea. These electrode types were the first scientist tried to manufacture on a completely flexible substrate.

An early attempt to develop a flexible electrode array was made in the late 1960s. Hanna and Johnson used printed circuit board (PCB) production techniques to assemble stainless steel electrode tips on a Mylar foil with conductor paths etched in copper (Hanna 1968). This was rather a precision engineered approach with coarse feature sizes and it was followed by the first flexible electrode arrays using MEMS fabrication tools in the early 1970s. In order to manufacture a stimulation electrode that could be inserted into the cochlea, an electrode was needed which was not only floating by means of a flexible cable attached to the stiff electrode but had to be flexible itself. Only with a flexible electrode substrate it would be possible to follow the curvature of the spiralled shape of the cochlea. In 1973, Sonn and Feist presented such an electrode which was made of a polymer substrate such as PTFE, Parylene-C or Mylar carrying thin-film electrodes and conductor paths made of sputtered platinum (Sonn 1974). The metal parts were insulated by dip-coating the electrode in silicone rubber and were opened by cutting the silicone with a scalpel.

#### *Polyimide-Based Electrodes*

Searching for an electrode substrate material which is flexible, electrically insulating, chemically inert, biocompatible, and processible with standard MEMS equipment, researchers found PI to be a promising candidate. The first development of a PI-based electrode to be used as a neural prosthesis was reported by Shamma-Donogue et al. in 1982 (Shamma-Donoghue 1982). They sandwiched a sputtered platinum-on-tantalum layer between two layers of spin-coated PI (Pyralin PI2555; DuPont, today: HD Microsystems



LLC, Parlin; NJ, USA) on a silicon wafer. To expose the electrode sites, the upper layer of PI was structured with positive photoresist developer before curing the PI at 300 °C. The perimeters of the implant were defined by cutting them with a dicing saw and peeling the flexible polymer off the silicon wafer.

### *Polyimide Electrodes for the PNS*

Following this first approach, a multitude of devices for different applications was fabricated using PI as a flexible substrate. A lot of implants were developed for the PNS such as the cuff electrode which is a tube-like three-dimensional implant. This electrode can be wrapped around a peripheral nerve either as a pure PI-based design (Rodriguez 2000) or as a hybrid design using a combination of PI and silicone rubber (Schuettler 2000). Another PNS application is the sieve electrode which can be implanted into a nerve after a traumatic lesion to regenerate the nerve by stimulating the neural outgrowths electrically.

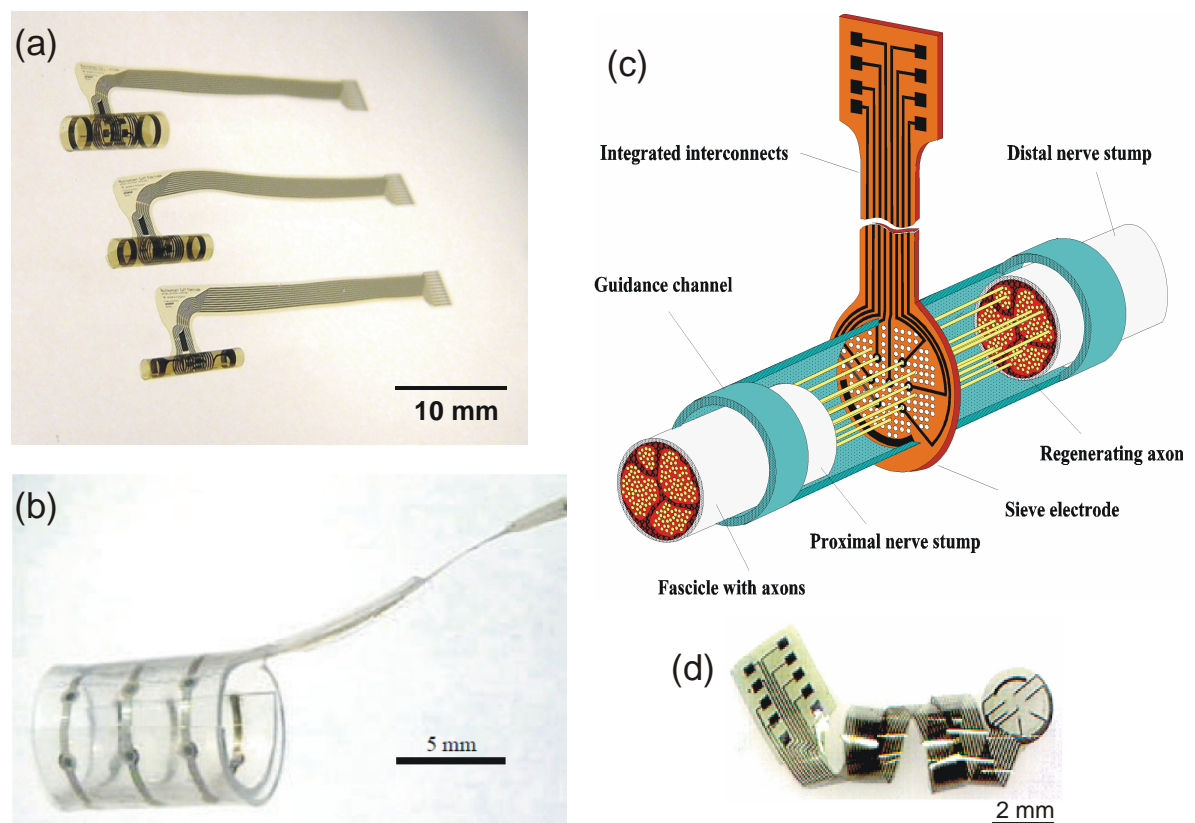


*Fig. 4.16. (a) PI-based cuff electrodes (courtesy of Martin Schuettler). (b) Hybrid cuff electrode combining PI with silicone (Schuettler 2000). (c) Schematic and (d) photograph of a PI-based sieve electrode (Stieglitz 1997b) Reprinted from Sensors and Actuators A: Physical. 1997; 60(1-3): 240-243, Stieglitz T, Beutel H, and Meyer J-U. A Flexible, Light-Weighted Multichannel Sieve Electrode with Integrated Cables for interfacing Regenerating Peripheral Nerves, Copyright (1997), with permission from Elsevier*

In 1997, Stieglitz et al. presented a sieve electrode which consisted of a planar PI foil with electrode sites and perforations (Stieglitz 1997b). If inserted between the two parts of the injured nerve, the axons can grow through the perforation and intimately connect to the electrode sites (Navarro 1998). Further designs of sieve electrodes were presented in the

following years. A combination of a PI sieve electrode with a containment for embryonic spinal cord cells was developed to bridge a nerve lesion (Stieglitz 2002). A three-dimensional guiding structure with embedded electrode sites which can also be used as a peripheral nerve regeneration implant was presented by Lacour et al. (Lacour 2008). After fabricating a PI-metal-PI electrode structure, grooves were formed on that structure by spin-coating and structuring a 20  $\mu\text{m}$  thick PI layer. Subsequently, the device was peeled off the wafer, rolled and inserted into a silicone tube to obtain parallel microchannels that can serve as an axon guiding structure.

Another electrode design which was transferred into a MEMS-based PI implant is the thin-film longitudinal intrafascicular electrode (LIFE), a long stripe of PI with several electrode sites which is inserted longitudinally into a nerve to sit between the fascicles (Yoshida 2000). A related approach to the LIFE is the transverse intrafascicular multichannel electrode (TIME) concept currently dealt with in an ongoing European Commission project (EU 2009). Compared to the LIFE, the TIME is inserted transversally into the nerve to reach fascicles in the whole nerve cross-section (Boretius 2009).

### *Polyimide Electrodes for the CNS*

The use of flexible PI electrodes in the PNS is well documented. In the last decade, more and more applications for flexible MEMS electrodes implanted into the CNS were published and with them the work on the first flexible CNS implants of the 1960/70s is continued today.

In the late 1990s, for the development of vision prostheses PI-based electrode arrays were processed as a flexible connection to the retina (Stieglitz 1997a). Rousche et al. presented PI shaft electrodes arranged in an array of one by three or two by three shafts that could be inserted into the cerebral cortex. To circumvent the buckling of the PI shafts, small slits were cut into the pia mater through which the shafts were inserted. At the tip of each shaft a via was etched through the PI and filled with a hydrogel which can be seeded with bioactive species e.g. a nerve grow factor (NGF) to improve the contact between the nerve tissue and the electrode (Rousche 2001).

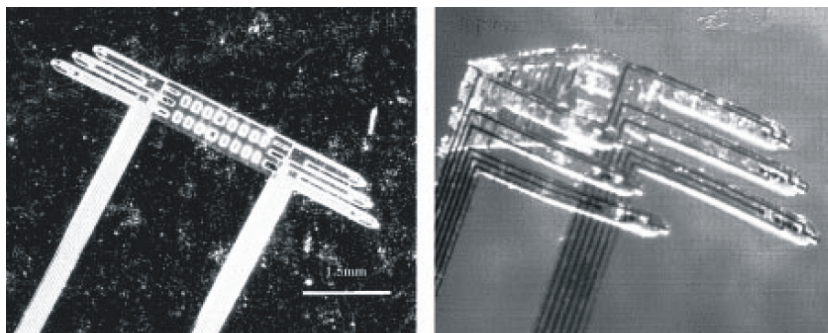


*Fig. 4.17. Intracortical two by three shaft array made of PI (Rousche 2001) ©2001 IEEE. Rousche PJ, Pellinen DS, Pivin Jr DP, Williams JC, Vetter RJ, and Kipke DR. Flexible Polyimide-Based Intracortical Electrode Arrays with Bioactive Capability. IEEE Transactions on Biomedical Engineering. 2001; 48(3): 361-371*

Lee et al. addressed the buckling problem by manufacturing PI-metal-PI shaft electrodes having a 5  $\mu\text{m}$  thick silicon backbone. To maintain the flexibility of the electrode the stiff shaft tip with silicon backbone was followed by a shaft segment without silicon. This segment contains only PI as the substrate material and hence is flexible (Lee 2004b).

The optimal shaft electrode to be implanted into the cerebral cortex would be stiff while inserting and flexible after inserting when sitting in the brain matter. This problem was solved by different approaches. Kipke et al. attached a thin silicon needle to a flexible PI shaft. Because of the small dimensions of the stiff silicon needle the tissue damage is minimal. After insertion, the polyethylene glycol (PEG) used as glue was dissolved by the brain fluid and the silicon insertion tool can be withdrawn (Kipke 2002). Another approach was presented by Singh et al. in 2004. They dip coated a flexible shaft with normal table sugar. Due to the coating the shaft was stiff enough to penetrate the brain tissue. After insertion, the sugar was dissolved by the brain fluid and the shaft became flexible again (Singh 2004).

#### *Polyimide-Based Epicortical ECoG Electrodes*

While the flexibility is needed for long-term recording with shaft implants, it is essential for electrode arrays measuring cortical surface potentials even in acute recordings. If an electrode array is used to record from a large cortical surface area, it has to follow the curved topography of the cortex to obtain a good contact to the tissue. For this reason, a lot of publications can be found dealing with the use of PI-based epicortical electrocorticogram (ECoG) electrode arrays. Takahashi et al. fabricated a 69-channel electrode array on a

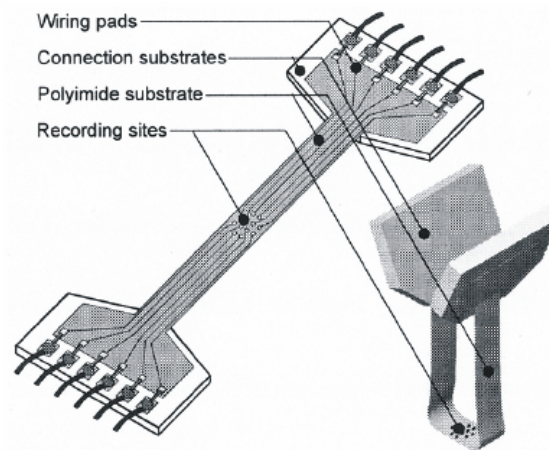


*Fig. 4.18. Design concept of a foldable PI ribbon cable with an integrated electrode array (Takahashi 2003) © 2003 IEEE. Takahashi H, Ejiri T, Nakao M, Nakamura N, Kaga K, and Herve T. Microelectrode Array on Folding Polyimide Ribbon for Epidural Mapping of Functional Evoked Potentials. IEEE Transactions on Biomedical Engineering. 2003; 50(4): 510-516*

2 mm by 2 mm area by structuring gold electrode sites and conductor paths on a 25  $\mu\text{m}$ -thick Kapton foil. The metal pattern was insulated by a layer of photosensitive PI. The perimeters of the electrode were defined by cutting. A laser was used to cut through-holes into the contact pads of the PI foil. The holes were then filled with conductive epoxy to

connect the foil to two underlying PCBs (Takahashi 2003). By bending the foil (Fig. 4.18), a good electro-mechanical contact is established between the array and the surface of the dura. An electrode similar to that presented by Takahashi was manufactured by Hollenberg et al. in 2005. Like Takahashi, they used a Kapton foil as substrate and deposited a 300 nm thick layer of gold, structured it, and insulated it with a layer of the photosensitive polymer SU-8. An array of 8 by 8 electrode sites with a diameter of 150  $\mu\text{m}$  and an electrode spacing of 750  $\mu\text{m}$  was obtained (Hollenberg 2006). Contacts were made to a PCB that housed the connectors which fit into the recording system. The same manufacturing process was used by Yeager et al. in 2008 who used this electrode array to record from the somatosensory and auditory cortex of a rat (Yeager 2008).

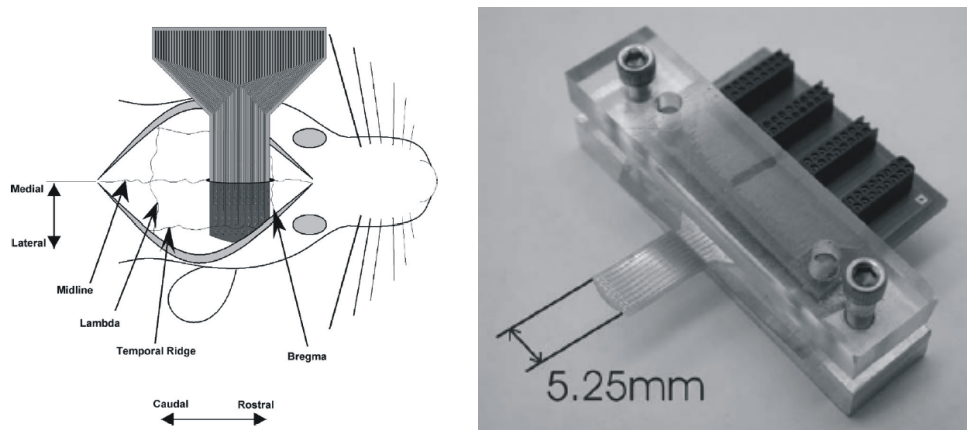


*Fig. 4.19. Flexible PI-based electrode array: Schematic of the array placement (left) in the rat and a photograph of the assembled array (right) (Hollenberg 2006) Reprinted from Journal of Neuroscience Methods. 2006; 153: 147-153, Hollenberg BA, Richards CD, Richards R, Bahr DF, and Rector DM. A MEMS Fabricated Flexible Electrode Array for Recording Surface Field Potentials*

Molina-Luna et al. used a PI-metal-PI foil with spin-coated PI layers, gold conductor paths, and 72 titanium nitride electrode sites to epidurally stimulate the motor cortex of a rat. The electrode sites are distributed over an area of 6 mm by 4.5 mm with a pitch of 750  $\mu\text{m}$  and 640  $\mu\text{m}$  respectively (Molina-Luna 2007).

### *Variations on the Polyimide-Metal-Polyimide Process*

In 2001, Stieglitz presented a double-sided electrode array. A stack of alternating layers of spin-coated PI (three layers) and sputtered platinum (two layers) was processed on a wafer. After opening the front side electrode sites in an oxygen plasma in the reactive ion etch (RIE), the complete PI foil was peeled off the wafer and flipped over to open the back side electrode sites by plasma etching (Stieglitz 2001).

In 2004, Metz et al. reported on PI-based electrodes with integrated microfluidic channels (Metz 2004a). They processed a foil of spin-coated photosensitive PI, platinum, and a second layer of PI on a wafer with a sacrificial aluminium layer. The electrode sites were opened and grooves defined in the second PI layer by an UV light exposure and development step. A third layer of PI was prepared on a second wafer. A polymer foil was attached to this wafer by a thin layer of vacuum grease. The PI was spin-coated onto this



foil followed by a soft-bake step on a hotplate. The second wafer was flipped over and laminated to the first wafer. After removing the wafer and the extra polymer foil, the third PI layer was photostructured and cured in an oven under nitrogen atmosphere. The finished devices were released from the wafer by anodic metal dissolution of the sacrificial aluminium layer.

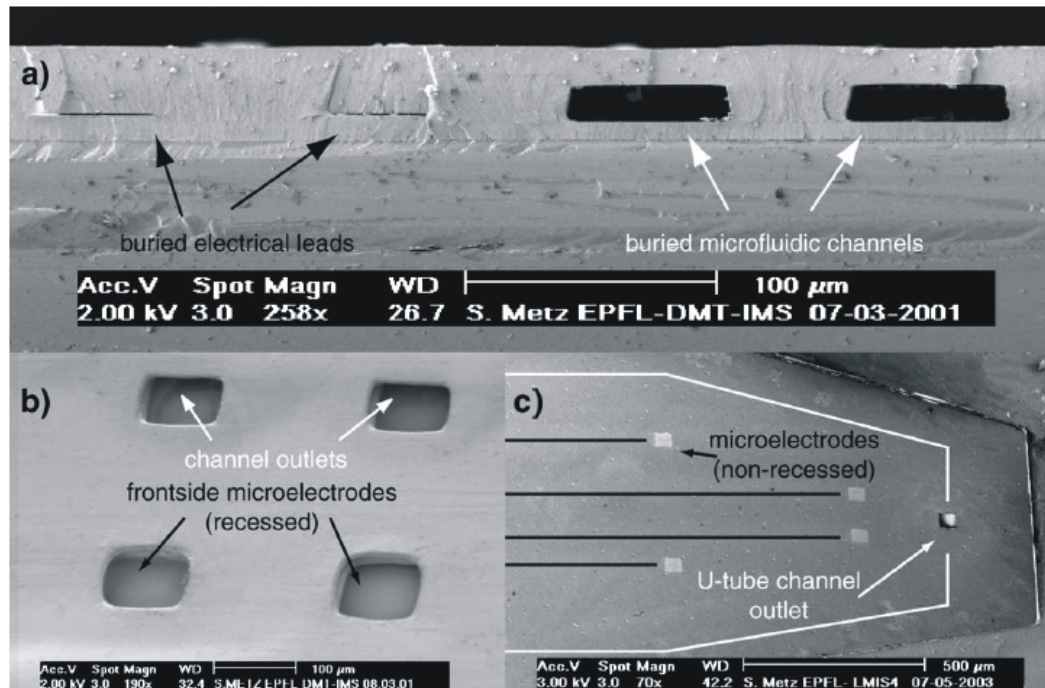


**Fig. 4.20.** Flexible PI-based microelectrodes with integrated fluidic channels (a) Cross-sectional view of the electrical conductor paths and the microfluidic channel (b) Top view of the electrode tip with microelectrodes and channel outlets (c) Electrode tip with four non-recessed microelectrodes and one channel outlet (Metz 2004a) Reprinted from *Bio-sensors and Bioelectronics*. 2004a; 19(10): 1309-1318, Metz S, Bertsch A, and Renaud P. *Flexible Polyimide Probes with Microelectrodes and Embedded Microfluidic Channels for Simultaneous Drug Delivery and Multi-Channel Monitoring of Bioelectric Activity*

#### Other Polymer Electrodes

Besides PI, a number of other polymers were introduced as microelectrode substrate materials. Lee and colleagues used benzocyclobutene (BCB) as a substrate and insulating material (Lee 2004b). They also presented channels made of BCB on a shaft electrode with a stiff silicon backbone (Lee 2004a).

Due to its FDA approval as an implant material, Parylene-C is used in flexible microelectrodes. Rodger et al. reported on an epiretinal electrode array with 1024 electrode site whereof 60 were electrically connected by an integrated Parylene-based cable with two layers of platinum as conductor paths (Rodger 2008). Takeuchi et al. fabricated Parylene-based flexible microelectrodes with integrated fluidic channels (Takeuchi 2005). To circumvent the problem of the flexible electrode during insertion, they filled the channel with PEG to stiffen the electrode. Suzuki et al. presented an analogous approach to Rousche's three-dimensional recording array based on PI (Rousche 2001) by using parylene as a flexible substrate and aluminium as electrode material (Suzuki 2003).

One of the most promising polymer implant materials is polydimethylsiloxane (PDMS), or silicone. It has been used for decades in humans and thus is very well known and accepted as an implant material. By only using materials that are approved for human applications, scientists hope to fabricate microimplants that can be transferred into human applications soon. Schüttler and Suaning presented such an approach in 2005 (Schuettler 2005). They used the two traditional implant materials silicone and platinum to manufacture microelectrode arrays to be used as high-channel neuroprostheses. A platinum foil was sandwiched between two layers of spin-coated silicone. All layers were structured by a laser to define the electrode sites, conductor paths, electrode openings, and perimeters. While this laser-cutting technology could not produce as fine feature sizes as photolithography in standard MEMS processing, the feature sizes were still much smaller and more reproducible than obtained by precision engineering.

In 2006, Kitzmiller et al. fabricated an ECoG-electrode array using silicone and platinum (Kitzmiller 2006). They structured a 200 nm thick layer of electron beam evaporated platinum on a silicon wafer to form a 4 by 4 electrode array. The electrode sites were contacted by aluminium bond wires. Electrodes sites and wires were subsequently embedded in PDMS and peeled off the wafer. While the author claimed the arrays should be used in human studies, he used aluminium which is not biocompatible and not adequate as electrode material.

### **4.2.5 Possibilities and Limitations of MEMS Electrodes**

The main advantage of micromachined electrodes is the small feature size which can be processed down to some micrometers. Thus, a number of electrodes sites can fit on a very small device which keeps the damage to the nervous tissue to a minimum and can be chronically implanted. A larger number of electrodes can be implanted without increasing the volume of displaced tissue. Thus, multi-channel recording from a small area of the tissue with a high spatial resolution becomes possible. Due to the MEMS processing, the implants have a reproducible design and known dimensions such as the area of the electrode sites or the spacing between sites. This is an advantage over the wire bundle or wire array electrodes which cannot be assembled that accurately. In addition, such electrodes can change their electrode arrangement and spacing when the wires are bent during insertion. In terms of production, MEMS electrodes can be batch processed so that a multitude of devices can be manufactured at the same time which decreases time-consuming manual production steps.

#### *Assembly and Packaging*

However, micromachined electrodes come with some drawbacks, too. A major issue of microelectrodes which is often not discussed in the publications of new manufacturing alternatives is the assembly and packaging of the complete device. With precision engineering, it is possible to reduce the dimensions of an electrode array. But implementing a large number of electrodes, that are individually connected to wires forming a bulky cable, leads to a large and rigid device which cannot be chronically implanted (Tsytarev 2006).

With MEMS-processing it is easy to arrange a large number of microelectrodes inside a small area. But even most of the MEMS arrays described in literature do not have a larger number of electrodes than precision engineered arrays because they are as well limited by the assembly. Even if the electrode array is processed on wafer level, cables and connectors are still necessary to connect the electrodes to a measurement setup. Often small microarrays with less than 100 electrode sites are joined to printed circuit boards or to a bunch of cables making the microdevice bulky and rigid (Hollenberg 2006; Kitzmiller 2006; Molina-Luna 2007; Takahashi 2003). While this is not a problem in an acute animal study it is crucial for the success of a chronically implanted device for animal studies as well as for human applications. Assembly and packaging is always an issue in chronic implantations because the connection of the MEMS part to cables or connectors can cause failure. This is an even severer problem as the number of electrodes increases. There is a limited knowledge of how an assembled microimplant behaves in the body environment over years. Besides testing the materials for long-term stability, the combination of different materials and the connection techniques have to be investigated whether they can withstand the body environment (Schuettler 2003).

#### *Hermeticity of Microimplant Housings and Multichannel Feed-Throughs*

To circumvent the problem of connecting a MEMS electrode to a macroscopic recording and/or stimulation unit outside the body researchers try to design fully implantable devices. The recording and/or stimulation unit is developed as an integrated circuit (IC) (Ghovanloo 2007) which is hermetically sealed. The connection between the chip inside the packaging and the electrode array in the body fluid outside the hermetic packaging is realized by feed-throughs which are connector paths crossing the hermetic sealing without destroying it. Energy and information transfer to equipment outside the body is done by telemetry. Although first prototypes of that concept were already presented in the last years at the University of Michigan (Wise 2004), a lot of problems are still unsolved. It has to be proven that the hermetic packaging of microimplants is reliable and long-term stable. Materials and material combinations that are not used in standard implant technology have to be long-term tested. Designs with a large number of feed-throughs and packaging fabricated on wafer level have to be investigated.

#### *Thin-Film Metallization*

A further difference between standard implants such as a cochlea implant and a MEMS-based electrode is the use of thin-films in microelectrodes. The electrode sites of MEMS electrodes consist of a metal layer which is only some hundreds of nanometres to some micrometres thick. Thus, this electrode sites are very susceptible to electrochemical corrosion. If too much charge is transferred over the metal-electrolyte interface during electrical stimulation, the metal site dissolves. While the electrode sites of standard implants contain more metal and can stand the loss of some metal atoms, this can be fatal for a thin-film metal layer. If histology is conducted after an experiment, the position of the electrode in the tissue has to be identified. This can be done by passing a current through the electrode site which is large enough to cause a lesion. Jellema and Weijnen used a cur-

rent of 5  $\mu\text{A}$  over a time period of 25 s to mark a spherical lesion with a diameter of 150  $\mu\text{m}$ . However, these parameters led to the dissolution of metal which was tolerable for wire electrodes in this case but would be fatal for a MEMS electrode (Jellema 1991).

### *Handling of Advanced Microimplants*

Another practical issue of MEMS-based microelectrodes is the handling of the devices especially during surgery. In contrast to tungsten rod electrodes which are robust and very tough, MEMS electrodes can exhibit very different properties depending on their design and the used materials. For example, silicon-based shaft electrodes are very stiff but brittle and fracture easily if force is applied in an adverse direction. Devices that consist of thin polymer foils are very flexible but can be ruptured. Due to the small dimensions, surface tension and electrostatic forces play a major role in the handling of MEMS electrodes. A device can be attached to a surface with a drop of water and it is often a problem to detach a thin piece of PI foil from a pair of tweezers. As there are as many MEMS electrode designs as MEMS engineers working in neural engineering, each electrode setup behaves differently and neuroscientists have to train the handling before using these devices.

In contrast to standard tungsten rods, most MEMS-based electrodes are fragile and/or brittle and thus, cannot be used to penetrate the meninges. This has to be taken into account while planning a surgery. The meninges have either to be opened prior to implantation or special insertion tools or strategies have to be developed for the respective microimplant. In addition, microelectrode assemblies often comprise a number of different materials which has to be taken into account while planning the sterilization procedure for a certain implant.

## **4.3 Assessment of Interface Concepts**

In long-term applications, the main problem of active implants and especially of active microimplants is the degradation of the electrical interface between the electrode site and the target neuron(s) due to tissue response (Polikov 2005; Ward 2009). Even if the implant materials are not damaged by corrosion or deterioration, the device can be rendered useless, if a degradation of the electrode-electrolyte interface takes place such as the encapsulation of the electrode site by fibrous cells. This increases the electrical impedance of the interface, decreases the signal-to-noise value when recording, and increases the needed values of the stimulation parameters. Thus, the implant materials, implantation techniques, electrode design, and electrode coating have to be improved to prevent tissue damage and reaction which leads to the encapsulation of the electrodes with fibrous tissue (Marin 2010; Rousche 2004).

When inserting an implant into the brain, neural tissue cells as well as blood vessels can be damaged (Zhong 2008). While it is possible to circumvent the damage of larger blood vessels which would cause a bleeding into the tissue, some cells and small blood vessels will be affected. Even with no cell directly damaged, tissue will be displaced due to the



volume which is occupied by the electrode shaft. This can lead to a change in the environment of cells in the vicinity of the implant such as changes in the extracellular pH value (Johnson 2007). Their biological and chemical balance is disturbed due to the displacement and can cause cell death in the worst case.

After insertion, a foreign body reaction takes place (Fig. 4.21). This includes unspecific protein adsorption at the implant surface and the adhesion of different cells such as monocytes, leukocytes, and platelets which are also present in normal wound healing. This may lead to inflammatory processes. As the implant is too large to be phagocytosed, a chronic inflammation follows and the macrophages fuse together to giant cells which can persist over the complete implantation time of the device. The last step of the foreign body reaction is the encapsulation of the implant into a layer of collagenous fibrous tissue with a thickness of 50-200  $\mu\text{m}$  (Ratner 2004).

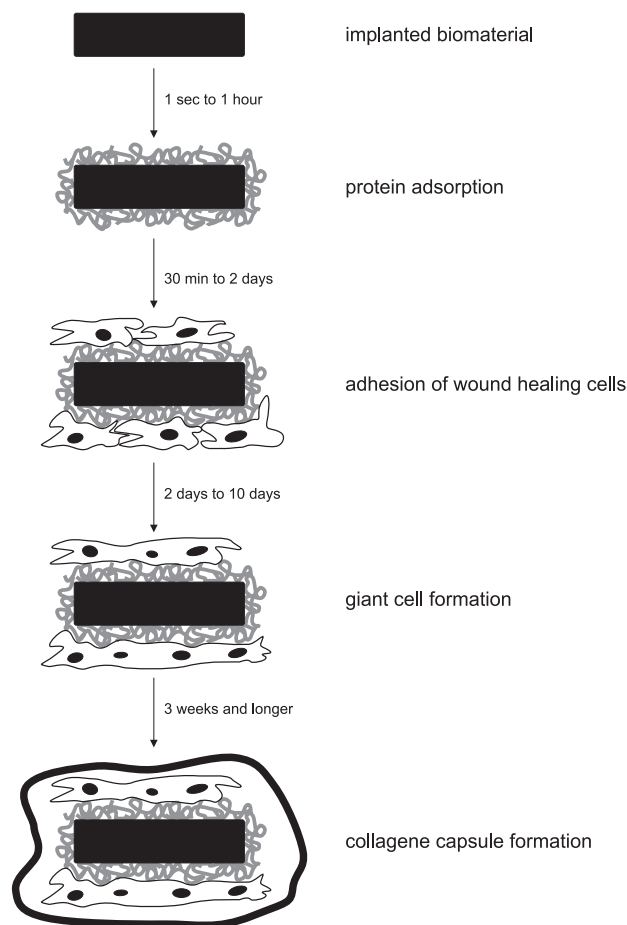


*Fig. 4.21. Foreign body reaction of mammalian tissue to a synthetic biomaterial over time (modified after (Ratner 2004))*

By understanding the tissue response which is triggered by inserting a technical device into body tissue, it becomes clear why this response is a crucial factor in the success of active microelectrodes used in long-term applications. Williams et al. could show a predictable relationship between tissue reaction and impedance measurements conducted with implanted wire electrode arrays. Extensive tissue reactions resulted in increasing

electrode impedances (Williams 2007). This poses a problem for the small microelectrodes such as the *Michigan Probe*. This electrode type has very small electrode sites with high impedance from the beginning. If the electrode is encapsulated by fibrous tissue after implanting, the impedance will rise and attenuate the signal. In contrast, wire electrodes or the *Utah Array* have comparably large electrode sites that can be even too large to discriminate SUA. If these electrodes are encapsulated due to foreign body reaction, their impedance increases to a value which is suited for SUA recording (Schwartz 2004). Thus, the challenge in neural engineering is to provide microelectrodes that are long-term stable, do not suffer from foreign body reaction of their host tissue, and are able to record the wanted neural signal.

Johnson and Otto used a rejuvenation protocol on *Michigan Probes* by applying a voltage of 1.5 V DC and 4 s duration between an electrode site and a stainless steel screw as a counter electrode (electrode site positive) (Johnson 2005; Otto 2006). These voltage pulses were followed by a decrease in noise and impedance. Another approach to circumvent the tissue reaction is the coating of the implants with bioactive material. Certain molecules immobilized on a device surface attract neuron and support neurite outgrowth while preventing astrocytes and meningeal cells (Leach 2010).

A promising result was reported by Krüger et al. who implanted a 64-channel wire electrode array into the premotor cortex of a macaque monkey and could record SUA as well as MUA from about a third of the electrode sites over the course of 7.5 years (Krüger 2010). The electrode array which was handcrafted and comprised rather large electrode sites (Ni-Cr-Al wires with a diameter of 12.5  $\mu\text{m}$ , deinsulated at a length of 1 mm) was inserted into the cortex via the white matter. The results showed that long-term recording with intracortical electrodes over a clinically relevant time period can be possible without tissue response inhibiting the measurements. However, electrodes sites were lost over time. While after a year, two thirds of the electrodes were still working, only one third was recording signals after 7 years.

Besides the effect of the material's chemical composition on the biological tissue, the overall structure and surface texture play a role in the biocompatibility of the implant as well. Regarding intracortical shaft electrodes, the size of the shaft was found to affect the density of encapsulating cells around the shaft (Seymour 2007). Stiff devices such as metal rods or silicon shafts tend to irritate the delicate neural tissue more than soft and flexible materials (Edell 1992). For this reason, polymer-based implants are promising candidates for neuroprosthetic devices. As already mentioned earlier in this chapter, micromotions caused by a stiff implant rigidly attached to the skull induce a chronic irritation of the tissue in the vicinity of the implant. Thus, flexible materials have to be used as connecting cables to obtain a floating device (Kim 2004).

While intracortical electrodes will always have to deal with the insertion problem and its impact on the tissue, epicortical electrodes could be an alternative for long-term recording. Lying on the surface of the cortex, they do not damage blood vessels or displace neural tissue. Epicortical electrode cannot have such a high resolution and the ability to measure

SUA as intracortical electrodes. However, one should carefully evaluate which type of signal and resolution is necessary for a certain application. It can be worth taking a lower spatial resolution into account for the sake of long-term stable signals. In the last years, data from intracortical SUA and LFP measurements were compared with epicortical LFP measurements with respect to use them as BCI control signals. Mehring et al. could show that an LFP of a single channel carried about the same amount of information about a hand movement as a SUA spike train (both signals were recorded intracortical) (Mehring 2003). However, comparing intra- and epicortical LFP signals from the motor cortex of monkeys and humans, the intracortical recordings carried twice as much information about movement direction than the epicortical recording (Mehring 2004). Still, researchers estimated that epicortical signals could be applied as BCI control signals (Pesaran 2002; Pistohl 2007; Rickert 2005). It has to be evaluated whether epicortical recordings are really long-term stable and whether tissue will grow between the cortex and the epicortical electrode array and will alter the signal quality. However, as I will show in chapter 8.2, the noise of signals recorded with an epicortical electrode array remained constant over the course of 4.5 months which indicates that the tissue reaction did not interfere with the signal quality.

## 4.4 Clinical Applications Today

The work presented in this thesis deals with electrodes for animal studies in fundamental brain research. However, I would like to give a short overview of the neural implants contacting the CNS or PNS which are commercially available and used in clinical practice today to show concepts that already made the transition from fundamental research to human applications.

### *Artificial Cardiac Pacemaker*

Although not implanted in nervous tissue, the cardiac pacemaker has to be mentioned as the first and most often implanted electrically active device whose concept was then adapted to further active implants such as the deep brain stimulator or the cochlear implant. The cardiac pacemaker can be fully implanted and is functioning reliably over decades in the human body. The first fully implantable device was implanted into a patient in 1958. Today, the basic concept of the cardiac pacemaker is a hermetic titanium housing accommodating a battery and the recording and stimulation electronics which are connected to electrode cables via feed-throughs. The electrodes sit at the tip of the cables and consist of a platinum-iridium alloy. While the electrodes are inserted into the heart, the housing is implanted in the shoulder region below the collarbone and can easily be exchanged when a new battery is needed. Being the most implanted active device, cardiac pacemakers are manufactured by numerous companies such as Medtronic Inc. (Minneapolis, MN, USA), Biotronik SE & Co. KG (Berlin, Germany), CCC medical devices (Montevideo, Uruguay), Sorin SPA (Milano, Italy), Boston Scientific Corporation (Natick, MA, USA), Medico SPA (Rubano, Italy), St. Jude's Medical (St. Paul, MN, USA), and Vitatron BV (Arnhem, The Netherlands).

### *Spinal Cord Stimulator*

By 2004, the most often implanted neuroprostheses is the spinal cord stimulator with >130000 implanted devices (Rijkhoff 2004). By delivering electrical pulses to the spinal cord via electrodes implanted into the epidural space, pain signals are suppressed. The stimulator is used relieving chronic pain originating from the lower back or the legs. Analogue to the cardiac pacemaker, the spinal cord stimulator comprises a hermetic metal housing implanted into the abdominal or gluteal region which is connected to the electrodes via feed-throughs and cables. Spinal cord stimulators are manufactured by Medtronic Inc., Boston Scientific Corporation, and St. Jude's Medical.

### *Cochlear Implant*

The electrode of a cochlear implant is inserted into the coil shaped cochlea to stimulate the auditory nerve of a deaf patient. First experiments of implanting electrodes into the inner ear were conducted in the late 1950s (Djourno 1957). In 1984, a single channel cochlear implant developed by William House and Jack Urban was the first neural prosthesis to be approved by the FDA (Seitz 2002). Today's implants consist of a hermetic housing for the electronics, a linear electrode array with up to 24 electrode sites and a coil to obtain inductively coupled energy and data from the external device comprising the external coil, speech processor electronics, a microphone and a battery. The success of the development of a device contacting the nervous system via the cochlea is due to the tonotopic organization of the cochlea. The nerve cells are positioned corresponding to the frequency they response to sorted from high to low frequencies. Thus, it is easy to determine where to stimulate the cochlea to evoke an auditory impression with a certain frequency. Today, there are more than 100000 implanted devices (Stieglitz 2009). The manufacturers of cochlear implants today are Advanced Bionics (CA, USA), Cochlear (Sydney, Australia), Med-El (Innsbruck, Austria), AllHear (Envoy Medical, St. Paul, MN, USA), and Neurelec SA (Vallauris, France).

### *Deep Brain Stimulation*

Stimulating deeply lying structures of the brain with electric impulses is an alternative to surgical ablation or medication. It helps in cases of medication resistance and has the advantage of being reversible and adjustable due to only stimulating not ablating neural tissue. The design of a deep brain stimulator, or brain pacemaker, is based on the cardiac pacemaker approach. Electronics and battery are placed in a titanium housing implanted in the chest region below the collarbone. The cable is threaded below the skin to the head. The electrode comprises a linear array of four electrode sites embedded in silicone. The electrode is inserted into the brain through a small hole in the skull and placed in the respective brain area using stereotaxis. By 2004, more than 20000 devices were implanted (Rijkhoff 2004). The manufacturers of deep brain stimulators are Medtronic Inc. and St. Jude's Medical. Today, the deep brain stimulator has a FDA approval and the CE mark for the European marked for the treatment of essential tremor, Parkinson's disease, and dystonia (CE 2009; FDA 2003; Wichmann 2006). However, it is also used to treat other neurologic disorders like epilepsy (Kerrigan 2004; Schulze-Bonhage 2009), chronic pain

(Kringelbach 2007), and even psychiatric disorders (Pereira 2007) obsessive compulsive disorder, Tourette's syndrome, and depression (Wichmann 2006).

#### *Vagus Nerve Stimulator*

The vagus nerve is the tenth cranial nerve. Coming from the brainstem it does not enter the spinal cord but runs through the neck and directly innervates the viscera. It comprises afferent and efferent neurons. Thus, by stimulating the vagus nerve, structures in the brain are reached and affected. Still, little is known about the mechanism of brain modulation by stimulating the vagus nerve. However today, the vagus nerve stimulation has a FDA approval and the CE mark for epilepsy and depression (CE 2004; FDA 2005; George 2000). According to the manufacturer Cyberonics Inc. (Houston, TX, USA), 45000 patients were implanted by 2007. The device is also based on the cardiac pacemaker concept: the pulse generator electronics placed in a hermetic titanium housing is implanted under skin of the chest. A wire connects it to two electrodes with a helical form to be tethered to the left vagus nerve.

#### *Sacral Nerve Stimulator for Urinary Urge Incontinence*

The involuntary loss of urine can be caused by the involuntary contraction of the detrusor muscle. A stimulator with a design similar to the pacemaker concept is manufactured by Medtronic. While the housing is subcutaneously implanted in the upper buttock or lower abdomen, a cable with four electrodes at the tip is placed in the foramen of the third sacral vertebra. While the neural processes during bladder stimulation are still unclear, it is believed that the bladder overactivity is inhibited by inhibitory reflexes triggered by the electrical stimulation (Rijkhoff 2004). According to Medtronic, 60000 sacral nerve stimulators were implanted by 2009.

#### *Sacral Anterior Root Stimulator for Bladder Emptying*

The sacral anterior root stimulator, or bladder stimulator, is used by patients with paraplegia to empty their bladder at will. The implant helps to achieve continence and to empty the bladder with only a small residual volume which is important to avoid the infection of the urine. First implantations were conducted in the 1970s. The implant developed and implanted by Giles Brindley comprises three parts: the electrodes, the cable and the implanted radio receiving block. The electrodes are made of silicone and are shaped to trap the sacral roots as if they were clamped between the pages of a book (Brindley 1972). The cables consist of an insulated platinum-iridium alloy covered with silicone rubber. The circuitry unit consists of passive electrical components and is not hermetically sealed but cast with silicone rubber (Brindley 1982). The Brindley system is being manufactured and distributed by Finetech Medical Ltd. (Welwyn Garden City, Hertfordshire, UK) and was implanted in 2400 patients by 2004 (Rijkhoff 2004).

#### *Drop Foot Stimulator*

Patients who suffer from hemiplegia after a stroke often have no control over their foot on the paralyzed half of their body. This leads to walking problems because patients cannot

lift this foot and thus, easily stumble during walking. The drop foot stimulator electrodes are implanted on the peroneal nerve below the knee. A footswitch in the shoe senses the lifting of the heel and transmits the status to an external unit worn at the belt. The external unit triggers the stimulation of the peroneal nerve by sending stimulation pulses over an inductive interface to the implant. The stimulation results in lifting the foot. When the heel contacts the ground again the stimulation stop and the patient can put his weight on this foot during the walking cycle (Kenney 2002). The drop foot stimulator is also a product of Finetech Medical Ltd. Another implant has been commercialized by Neurodan AS and got the CE mark in 2006 (Aalborg, Denmark, now run by Otto Bock, Duderstadt, Germany) (Burridge 2007; CE 2006).

### *Phrenic Nerve Stimulator*

Patients with high spinal cord injuries, central sleep apnea or a paralyzed diaphragm are dependent on mechanical ventilation because of their impaired or complete loss of respiratory function. An alternative to mechanical ventilation is the use of a phrenic nerve stimulator. This device comprises of an electrode implanted around the phrenic nerve in the chest or neck. The stimulation pulses are transmitted from an external unit to the implant via inductive coupling. Two companies manufacture these neuroprostheses: Avery Biomedical Devices (Commack, NY, USA) and Atrotech (Tampere, Finland). By 2004, more than 1600 devices were implanted (Rijkhoff 2004).

## **4.5 Fluidic Contact to Neural Tissue**

Besides electrical recording and stimulation of neurons, scientists are interested in establishing a fluidic connection to the nervous tissue. As neuronal communication is not only an electrical but also a chemical phenomenon involving the release, transport and uptake of neurotransmitter molecules, technical interaction with the nervous system can also happen on the basis of chemical agents via fluid transport. The concept of controlling fluids in vivo can be useful for neuroscientific research as well as for the field of medical applications. While microelectrodes can precisely stimulate and record even from single neurons in vivo, microchannels could be used to apply drugs to the cells of interest or to take samples of extracellular fluid with the same precision.

As neurotransmitters play a crucial role in the working brain as well as in neuronal diseases, it is of great interest to monitor neurotransmitters and the cells releasing them in the vicinity of electrical recording and stimulation sites (Kennedy 2002; Ungerstedt 2009; Wilson 2005). Another important issue is the monitoring of metabolic events such as changes in the extracellular glucose level, pH or  $pO_2$  value (Silver 1994; Urban 2009).

All these applications need direct contact to the extracellular fluid. Microfluidic components can serve as transport medium for fluids between the tissue and extracorporeal devices or intracorporeal implants. With the implementation of microfluidic channels into neural implants, it becomes possible to draw samples of extracellular fluid, conduct mi-

croodialysis, apply drugs to enhance or to suppress neuronal activity as well as to inject agents which can genetically modify target neurons (Stieglitz 2010).

In the following subchapters I will give a short introduction into the special characteristics of microfluidic channels and compile the different approaches to microfluidic, polymer-based channels found in the literature.

#### 4.5.1 Fundamentals of Microfluidic Channels

A microsystems engineer's bread and butter is the downscaling of devices from the macroworld (in the range from kilometres to centimetres) to the microworld (dimensions below 1 mm). That is, e.g. transferring a water pipe into a microfluidic channel or turning a test glass into a reaction chamber with an edge length of 100  $\mu\text{m}$  and a volume of <1 nl (Andersson 2000). While the laws of physics do not change, the importance of certain terms describing the force acting on the channel's fluid does change. In a tube with a cross-sectional diameter of 1 m, the fluid running through it is mainly affected by earth's gravity while the surface tension of the fluid is negligible. This situation is inverted if the tube shrinks to a cross-section with a diameter of 100  $\mu\text{m}$ . In such channel the fluid can flow "uphill" showing that surface tension and not gravity is the driving force for the fluid's motion.

##### *The Scaling Phenomenon*

The flow pattern is dependent on the dimension of the setup due to the scaling phenomenon. Objects interact with their surrounding either via their surface or with the whole volume, or mass, which scale in a different way than their linear dimension (Thornell 1998). Thus, changing the linear dimension  $D$  of a droplet's diameter, results in a change of surface and volume proportional to  $D^2$  and  $D^3$  respectively. In a microchannel, the dominating value is the capillary force which is a combination of surface tension and liquid-solid adhesion. It is a line force appearing at the liquid-solid-gas interface

$$F_{cap} = S\gamma\cos(\theta), \quad (4.6)$$

where  $S$  is the length of the interface line,  $\gamma$  the surface tension coefficient in N/m, and  $\theta$  the wetting angle. One can recalculate the capillary force at the phase interface to an equivalent pressure

$$P_{cap} = \frac{F_{cap}}{A} \quad (4.7)$$

which is often used in engineering (van der Wijngaart 2002), where  $A$  is the cross-sectional area of the channel.

If we turn the microchannel into a macroscopic channel, the capillary force will scale with  $L$  while the force of gravity

$$F_{grav} = mg, \quad (4.8)$$

where  $m$  is the mass and  $g$  the gravitational acceleration, will scale with  $L^3$  as  $m$  is proportional to  $L^3$ . By increasing  $L$ , the capillary force increases linearly whereas the force of gravity increases with the power of 3. Thus, gravity is becoming the dominating value affecting the fluid's motion in a macroscopic channel.

### *The Hagen-Poiseuille Equation*

Laminar flow of an incompressible fluid through a tube with a circular cross-section can be described by the Hagen-Poiseuille equation

$$Q = \Delta P \frac{\pi r^4}{8\eta L}, \quad (4.9)$$

where  $\Delta P$  is the pressure drop over the tube length  $L$ ,  $\eta$  the dynamic viscosity,  $Q$  the volumetric flow rate, and  $r$  the radius of the circular cross-section (Spurk 2008). Due to MEMS-processing, most of the microfluidic channels do not have a circular cross-section. Thus, the equation has to be adapted to rectangular cross-sections. In spite of the simple rectangular channel cross-section, no analytical solution is known to this flow problem. However, a Fourier sum can be found representing the solution (Bruus 2008). This is achieved by

$$Q = \frac{h^3 w}{12\eta} \frac{\Delta P}{L} \left[ 1 - \sum_{n=1,3,5,7,\dots}^{\infty} \frac{1}{n^5} \frac{192}{\pi^5} \frac{h}{w} \tanh\left(n\pi \frac{w}{2h}\right) \right], \quad (4.10)$$

where  $h$  is the height and  $w$  the width of the channel cross-section.

### **4.5.2 Integration of Channels into Polymer-Based Implants**

First micromachined silicon-based microchannels for neural engineering applications were already shown in 1997 when Chen et al. published channels integrated in silicon shaft electrodes. The channels were realized by ethylene-diamine pyrocatechol (EDP) etching of the silicon bulk and by covering the etched trench with thermal silicon oxide (Chen 1997). These devices were used to record a decreasing firing rate of single units during the application of kainic acid and  $\gamma$ -aminobutyric acid (GABA) in the superior and inferior colliculus of guinea pigs.

In recent years, a number of articles were published presenting polymer-based microchannels. Lee et al. used the polymer poly-benzocyclobutene (BCB) to fabricate a neural implant comprising a fluidic channel with a width of 40  $\mu\text{m}$  and a height of 10  $\mu\text{m}$  and three electrical recording sites (Lee 2004a). The channel was formed by a sacrificial layer of photoresist which was later dissolved after the BCB top layer was added. However, while the channel cover was made of BCB, this shaft electrode was completely stiff due to a 5-10  $\mu\text{m}$  thick silicon backbone which served as the bottom layer.



By also using a sacrificial layer of photoresist, Takeuchi et al. fabricated a parylene-based microdevice with tapered channel geometry comprising a cross-section at the channel outlet of 10  $\mu\text{m}$  height and 50  $\mu\text{m}$  width (Takeuchi 2005). The shaft is flexible and can be stiffened by filling the channel with polyethylene glycol (PEG). After inserting the stiff device into tissue, the PEG can be dissolved with water. The device was successfully inserted into rat cortex from which the dura mater was removed beforehand. Unit recording from the cortex was conducted by gold electrode sites located within the channel. The same method was used to generate multiple channels to be used as a peripheral nerve regeneration implant. Parallel parylene channels were fabricated and rolled up to build guidance structures for the regrowing nerve (Suzuki 2006).

As described in chapter 4.2.4, Metz et al. presented a device which was completely made up of PI (Fig. 4.20). The channels with a width of 50-200  $\mu\text{m}$  and a height of 5-20  $\mu\text{m}$  were realized by laminating the cover layer to a substrate layer with trenches structured with photodefinable PI (Metz 2004a).

Fiedler et al. presented channels integrated in a PDMS-based electrode which were structured by laser ablation. A PDMS layer containing dye which increased the light absorption of the silicone was spin coated onto a first PDMS layer without dye. With the laser, trenches were cut into the dyed silicone layer. By laminating a third silicone layer, channels were formed. Due to the laser ablation of PDMS, channels with a larger cross-section compared to devices structured by photolithography were fabricated with a width of 93  $\mu\text{m}$  and a height of 127  $\mu\text{m}$  (Fiedler 2008).

## 4.6 Optical Stimulation of Neural Tissue

In addition to the electrical and fluidic contact to the nervous tissue as mentioned in the preceding chapters, a third modality is of increasing interest for neuroscience. This is to establish an optical interface to the nervous tissue.

In recent years, a new form of neuronal stimulation has been developed in neuroscience. In 2005, the Deisseroth group was the first using light to stimulate neurons. Instead of using electrical voltage or current, the researchers succeeded in using light to directly stimulate neurons of the mouse CNS, by genetically modifying hippocampal neurons to express the light-sensitive algal protein channelrhodopsin 2 (ChR2) (Boyden 2005). These modified neurons became light-sensitive, in that they could be rapidly depolarized when exposed to blue light with a wavelength of about 470 nm. The halorhodopsin NpHR from the archaea strain *Natronomonas pharaonis* was found to be an antagonist to ChR2 as it induces a hyperpolarization of the neuron when activated by yellow light (593 nm). In 2007, NpHR and ChR2 were successfully co-expressed in cultured hippocampal neurons (Zhang 2007a). The expression of both proteins in the same neuron enables one to facilitate or inhibit the generation of action potentials by the cell by using either blue or yellow light, respectively. ChR2 exposed to blue light allows sodium ions to enter the cell and causing depolarization while the chloride pump NpHR when activated by yellow light leads to a hyperpolarization of the neuron (Zhang 2007a). Put simply, neuronal activity can be

switched on and off at the cellular level. With the methods of genetic manipulation, specific cell types can be modified and activated. This is in stark contrast to electrical stimulation, which typically activates many neurons in the vicinity of the electrode site. Moreover, optical stimulation has a high temporal precision and reverses rapidly (Zhang 2007b). Optical stimulation can be used not only in cell cultures but also in vivo, including freely moving rodents (Aravanis 2007; Gradinaru 2009). This new technology, termed *optogenetics* by Deisseroth in 2006 (Deisseroth 2006), has the potential to revolutionize the fields of neuroscience and neuroprosthetics (Gradinaru 2007). The demands it makes in terms of electrode design and production can be met with microsystems technology.

Grossmann et al. presented an in vitro approach by positioning an array of 64 by 64 high power micro-LEDs under a multielectrode array containing transfected neural cells. This network could be stimulated by the LED light (Grossman 2010). For in vivo use in cortical tissue, small waveguides for light transmission to the cells have to be combined with microelectrodes for the recording of electrical signals. A first approach was shown by Zhang et al. who integrated an optical fibre in an *Utah Array* (Zhang 2009a) and by Cho et al. who integrated a microstructured SU-8 waveguide on the shaft of a *Michigan Probe* (Cho 2010). By directly integrating optical modalities with MEMS-technology, microelectrodes can be manufactured that comprise defined and reproducible dimensions between electrode sites and optical stimulation sites.

### 4.6.1 Optical Waveguide Fundamentals

In order to transmit light from a light source to the target neurons within the brain tissue, optical waveguides are used. An optical waveguide is made of a dielectric material which is able to guide electromagnetic waves with wavelengths in the optical spectrum.

The most basic form of a waveguide is a slab waveguide which guides the light within a layer of dielectric material. The light is only confined in the direction of the normal vector of the layer. However, the most common optical waveguides used in technical applications are channel waveguides which confine the light in two directions. Thus this configuration resembles an optical wire with the light guided along the wire's lengths while confining it in height and width. Common types of waveguides are optical fibres and rectangular waveguides. Standard optical fibres used in telecommunication are made of glass and have a circular cross-section. Rectangular waveguides are fabricated with means of MEMS technology and are composed of different layers of thin-film deposited dielectrics. The MEMS-based deposition and structuring of the layers is the reason for the rectangular cross-section of the waveguides which are used in integrated optical circuits.

#### *refractive index*

Electromagnetic waves travel at different speed in different media. For light, vacuum is the reference medium. The refractive index of a material is a measure of how much the speed of light is reduced in that material compared to the light velocity in vacuum

$$n_{medium} = \frac{c}{v_{medium}} . \quad (4.11)$$

Where  $n_{medium}$  is the refractive index of a certain medium,  $c$  is the light velocity in vacuum and  $v_{medium}$  is the speed of light in the medium.

The refractive index depends mainly on the electric polarization of the medium (Askeland 2006) but can also be altered by a change in the packaging density of the material (Hougham 1996). In polymers, the refractive index can be fine-tuned through structure modification, physical aging, and guest doping. An example of guest doping is the incorporation of fluorine atoms into PIs which influence the refractive index in two different ways simultaneously. First, the refractive index is decreased by increasing the free volume which is caused by the greater steric volume of fluorine relative to hydrogen. Second, the polarizability is lowered as a result of the smaller electronic polarization of C-F bonds relative to C-H bonds (Hasegawa 2001). An increase in structural density can be induced e.g. by baking the material which leads to an increase in refractive index (Ma 2002). In waveguides made of silica, the difference in refractive index between the core and the cladding is typically less than 1 %.

### Optical Losses

Mostly, the total optical loss is the sum of losses from different sources. One phenomenon causing optical loss is *absorption*. If light is absorbed by the waveguide's material, the light is transformed into other energy forms such as heat and thus, the light wave loses energy. The absorption coefficient describes how much of the wave's energy is transferred to the material in which it is propagating. The two main sources for absorption of light in dielectric materials are *band edge absorption* and *free carrier absorption*. Band edge absorption occurs when a photon lifts an electron from the valence band to the conduction band. This can only happen if the absorbed photon has energy greater than the band gap. Thus, depending on the band edge, light with a smaller wavelength is absorbed by the medium while light with a larger wavelength can propagate. In contrast to band edge absorption, during free carrier absorption, light is absorbed by electrons which already are and stay in the conduction band after excitation (Reed 2004). These electrons are promoted to higher levels within the conductor band and fall back to lower energy states after some time. The absorption spectrum of this process is broad increasing monotonically with wavelength (Zappe 1995).

When a beam of light travels through a waveguide, it can be reflected by inclusions such as particles, bubbles, cracks, and voids. Also, a rough surface of the waveguide or stress-induced changes in the intrinsic structure of the waveguide's material can reflect the light. Due to the reflection at such material inhomogeneities, the light is reflected under different angles and thus does not longer contribute to the beam of light travelling along the waveguide. This process is called *scattering*.

In general, it is difficult to determine whether an energy loss is due to absorption of an optical material or scattering. One key value that differentiates absorption from scattering

is the inevitable generation of heat in the absorption process. This relationship can be used as basis for several measuring techniques to distinguish between these two forms of loss. Standard loss values for commercial glass optical fibres are below  $1 \text{ dB/km} = 10^{-5} \text{ dB/cm}$ . However, losses in semiconductor-based or MEMS-based optical waveguides are much larger. Here, standard values range from  $0.1 \text{ dB/cm}$  (Zappe 1995) to  $5 \text{ dB/cm}$  (Piruska 2006). Albeit these waveguides feature comparatively large loss values, they are still successfully implemented in integrated optics mostly comprising waveguide lengths  $<1 \text{ cm}$ . Thus, on chip-level, long-distance transmission plays a minor role.

### *The Cut-Back Technique*

A standard procedure to characterize the overall propagation loss of a channel waveguide is the cut-back technique. This destructive method measures the amount of light transmitted through sections of varying length for a constant input power. This is done by metering the output power of a single waveguide repeatedly as its end is gradually shortened, or, like the name suggests, cut back. With this technique, only a single loss value is obtained for the waveguide, irrespective of the loss mechanism.

The loss factor, or extinction coefficient,  $\alpha$  can be found by plotting the measured output power of the waveguide as a function of several different waveguide lengths. If the output power  $P_{out}$  is plotted in relation to the input power  $P_{in}$  as  $\ln(P_{out}/P_{in})$  over the waveguide lengths in cm, the resulting plot has a slope of  $-\alpha$  with the traditional unit  $\text{cm}^{-1}$  (Zappe 1995). Thus, the attenuation of the power at a certain distance  $z$  can be calculated with

$$P_{out}(z) = P_{in} e^{-\alpha z}. \quad (4.12)$$

Often, the output power is also specified in units of dB

$$dB = 10 \log \left( \frac{P_{out}}{P_{in}} \right). \quad (4.13)$$

Thus, the loss factor  $-\alpha_{dB}$ , or transmission loss, has units  $\text{dB/cm}$ , if the output power is plotted in dB as a function of the waveguide length in cm. The two expressions are connected by

$$\alpha_{dB} = \frac{10}{\ln(10)} \alpha. \quad (4.14)$$

Although the cut-back technique is a quick and simple way of measuring the propagation loss, the accuracy is limited by the reproducibility of input coupling and sensor alignment.

### *Coupling Loss*

A main issue concerning channel waveguides is the insertion of light into the waveguide. The simplest approach to contact two similar structures is the *butt coupling* technique which was also used in this work. The two waveguides are arranged with a minimal spacing in a way that their facets face each other. The coupling efficiency is high if the facets

are plain and are aligned parallel to each other with a minimal distance. The areas of the facets should overlap as precise as possible.

The *coupling loss*, or insertion loss, defines the grade of achieved coupling between the input fibre and the actual waveguide. It is defined as

$$cl = -10 \log_{10} \left( \frac{P_{out}}{P_{in}} \right) \quad (4.15)$$

with  $P_{in}$  as the input and  $P_{out}$  the output power. It can be reduced with index matching oil at the fibre-waveguide interface and by using a large core size for better mode matching (Ma 2002).

### The Ray Model

Instead of applying Maxwell's equations to describe the propagation of light waves, light can be modelled as a simple ray which is an idealized thin beam of light. The ray is perpendicular to the wavefront of the light. With some discrete rays describing the light field, the propagation of light through different media and optical components can be calculated. Thus, by describing a waveguide with the ray optic model, we ignore the wave nature of light. This is usually valid for waveguides with a comparatively large (i.e. larger than the light's wavelength) cross-section e.g. in the case of multimode waveguides used in this work (Snyder 1983).

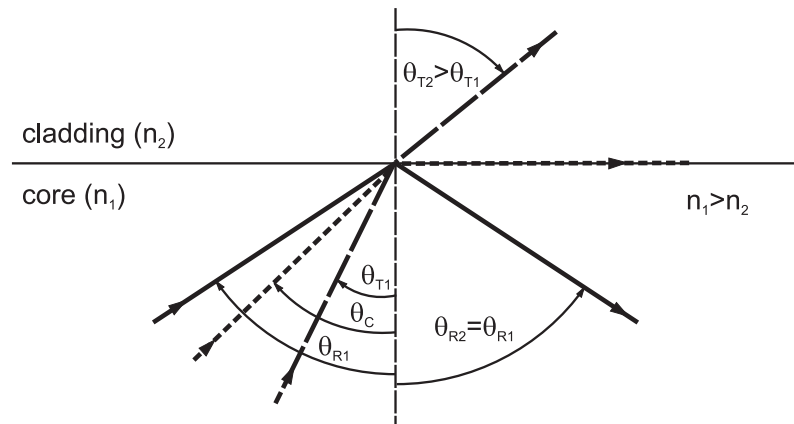


Fig. 4.22. Incidence of a ray of light on a core-to-cladding interface: light with an angle of incidence  $<\theta_C$  is transmitted while light with an angle  $>\theta_C$  is reflected at the interface.

The light is confined in the waveguide by total internal reflection. This is achieved if the waveguide material, the core, is surrounded by a second dielectric material, the cladding, with a lower refractive index than the core material. If the angle of incidence is larger than the critical angle, the light is reflected from the interface between core and cladding into the core material. Light with an angle of incidence smaller than the critical angle exits the core when it is refracted at the interface (Fig. 4.22). Applying Snell's law (Eq. 4.16), the critical angle  $\theta_C$  depends on the ratio of the refractive indices of the cladding ( $n_2$ ) and the core ( $n_1$ )

$$\theta_c = \arcsin\left(\frac{n_2}{n_1}\right). \quad (4.16)$$

Optical waveguides can be categorized in single-mode and multi-mode waveguides. In contrast to an electromagnetic wave propagating through free space, light travelling inside a waveguide meets certain restrictions due to the geometry and materials of the device. Light which is confined in a guide can be modelled as rays of light being reflected at the core-to-cladding interface and thus zigzagging from wall to wall while propagating along the waveguide's length. Rays with a phase shift of a multiple of  $2\pi$  interfere constructively which only happens for certain angles of incident at the core-to-cladding interface. Such rays correspond to waveguide modes if in addition to the adequate phase shift, the angle of incident is larger than the critical angle (Young 2000).

### 4.6.2 Polymer-Based Optical Waveguides

Today, optical fibres are substituting conventional electrical wires for high-speed data transfer. Although these fibres are a good solution for low-loss long distance transmission, they are insufficient for complex high-density circuitry. Glass fibres are difficult to fabricate, and are not compatible with planar PCB and MEMS processing techniques. Therefore new fabrication methods and materials for integrated optics are approached, such as silica on silicon, silicon oxynitride, lithium niobate, sol-gels and polymers (Eldada 2005). Due to the less expensive fibres, connectors and installation, polymer optical fibres are used in short distance applications such as high-speed home networks (Zubia 2001). The most frequently used material for polymer waveguides is Poly(methyl methacrylate) (PMMA) but a number of other polymers such as polycarbonate, polystyrene, benzocyclobutene, halogenated acrylate, and fluorinated PIs are also applied (Eldada 2002; Tanaka 1987; Ziemann 2008).

While glass fibres have a very low transmission loss in the range of 0.15 dB/km for a wavelength of 1.55  $\mu\text{m}$  (Gambling 2000), it is much higher in polymeric materials with about 0.2 dB/cm to 5 dB/cm (Kane 1995; Nordström 2007; Piruska 2006). The loss can be reduced to 0.01 dB/cm at 840 nm wavelength in halogenated polymers (Eldada 2000) in which hydrogen atoms are substituted by halogen atoms. The mass of halogen atoms is much larger than the mass of hydrogen atoms, thus, shifting the absorption band into the infra-red zone (Ziemann 2008).

In recent years, a number of MEMS devices with integrated polymer waveguides for in vitro biomedical applications were published. Such lab-on-a-chip configurations comprise microfluidic channels that guide biological samples and waveguides to read out optical signals from the samples like e.g. fluorescent markers (Leeds 2004). Shew et al. realized a Mach-Zehnder interferometer on a chip using two SU-8 resins with different refractive indices as core and cladding material for the waveguide. This device can be used in biochemical sensing and was able to detect different concentrations of saline solutions (Shew 2005). Apart from SU-8, PDMS is frequently used as a material for fluidic channel as well as waveguide fabrication. This is due to the easy processability of the material

which can be structured with a moulding process. The refractive index of PDMS can be adjusted by adding silicone oil to the PDMS precursor (Kee 2008). Kee et al. presented a PDMS waveguide with a cross-section of  $250\text{ }\mu\text{m}$  by  $250\text{ }\mu\text{m}$  and measured a transmission loss of  $0.25\text{ dB/cm}$  at a wavelength of  $491\text{ nm}$ . Lee et al. used polyurethane as core and PDMS as cladding material to realize waveguides with a large core cross-section of  $800\text{ }\mu\text{m}$  by  $1000\text{ }\mu\text{m}$  and a transmission loss of  $0.1\text{ dB/cm}$  at  $632\text{ nm}$  (Lee 2007).

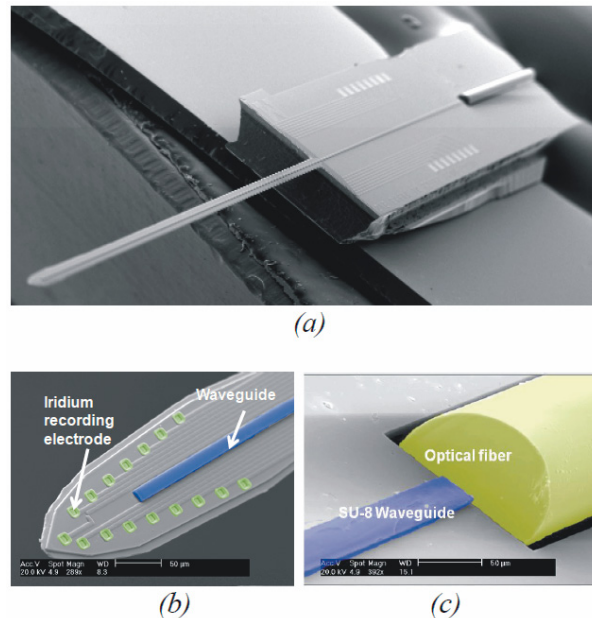


**Fig. 4.23. SU-8 waveguide integrated on a Michigan Probe** (a) Overview of the shaft and a part of the mounted optical fibre (b) Shaft tip with electrode sites and waveguide face (c) Butt coupling between waveguide and optical glass fibre (Cho 2010) ©2010 IEEE. Cho I-J, Baac H-W, and Yoon E. A 16-Site Neural Probe Integrated With a Waveguide for Optical Stimulation. *Proceedings of the 23rd IEEE International Conference on Micro Electro Mechanical Systems, Jan.24-28, Hong Kong. 2010. 995-998*

To this day, most in vivo applications are realized with standard glass fibres (Aravanis 2007; Zhang 2009a). In 2010, Cho et al. presented the first MEMS-based polymer waveguide which was integrated into a *Michigan Probe* (Cho 2010). They spin-coated SU-8 resin onto a silicon electrode shaft and structured it by photolithography. The waveguide had a length of  $5\text{ mm}$  and a cross-section of about  $5\text{ }\mu\text{m}$  by  $15\text{ }\mu\text{m}$  with a transmission loss of  $2.2\text{ dB/cm}$  at  $470\text{ nm}$ . While Cho et al. could show that light was conducted by the waveguide, it is still to prove whether the light's intensity is enough to stimulate genetically modified neurons in vivo.

## 5 Materials

In the area of neural implants for human applications, the number of used materials is limited. Materials have to be tested over years with respect to their suitability for an implantation in the human body over decades. Once a material is found to be adequate, changing or replacing would mean to start the demanding process of testing and regulatory approval again. A failure of the approval or of the material sometimes detected for the first time after years of use is a high financial risk for the company and in the latter a high risk for the patient. Therefore, implant manufacturers rely on well known standard materials like titanium, platinum, stainless steel (e.g. 316L), platinum-iridium alloys, and silicone (DiLorenzo 2008; Finn 2003). In contrast, in neuroscience and neural engineering research, scientists introduce new materials. In these fields implants are used in *in vitro* and animal testing that provide the opportunity to test new materials whose long-term behaviour is still unknown.

### 5.1 Polyimide

A prominent example of a material used in neuroprosthetic research but not in clinical practice is PI. As early as in 1982 PI was proposed as implant material for a cochlear prosthesis (Shamma-Donoghue 1982). Since then, research groups all over the world were working with PI publishing numerous scientific articles dealing with PI-based micro-machined neural implants (Boppart 1992; Rousche 2001; Shamma-Donoghue 1982; Stieglitz 2000) or the biocompatibility and stability of PI in a body environment (Haggerty 1989; Klinge 2001; Lago 2007b; Richardson Jr 1993; Sun 2008). The discussion whether PI is suitable for implantation still goes on and no final conclusion is drawn. While it is successfully used as substrate and insulation material in neural implants in research and even in clinical trials (Zrenner 2008) and is proposed to work in long-term applications, it still has no FDA approval. PI got a negative connotation with respect to implant application due to the strong degradation of Kapton (a trademark of DuPont, Wilmington, DE, USA, composed of PMDA-ODA type PI) in water (Bessonov 1987; Campbell 1988; Delasi 1971; Delasi 1972; Murray 2004). But PI is a group of materials containing polymers with diverse material properties. The new generation of PIs including the BPDA-PPD type show a much stronger resistance to water deterioration (Ghosh 1996) thus making them a promising material for neural implants. Contacting the complex and sensitive neural tissue requires small and flexible implants. Thus, it seems to be obvious that polymers are well suited as implant material. They act as a substrate to support the conductor paths and insulate them against the body liquid. PI is used due to its chemical and mechanical durability and the possibility to process it in a standard clean room facility whereby large numbers of electrodes and feature sizes in the micrometer range can be implemented.

Thus, there is the need to gain more information about the long-term behaviour of this material. Although the biocompatibility of PIs is studied and the material is often used in



animal experiments, the knowledge of its degradation behaviour in biological tissue remains poor. This lack of knowledge gave the motivation to conduct the study on PI long-term behaviour described in chapter 7. PI in general and the three PIs obtained from three different manufacturers used and tested in this work are presented in the following sub-chapters.

### 5.1.1 Polyimide Fundamentals

PI is often called a high performance plastic due to its outstanding thermal and chemical durability, and its good mechanical and electrical properties like a high Young's modulus, mechanical strength or high electrical resistance. However, the term *polyimide* does not only refer to one chemical structure but stands for a whole group of polymers.

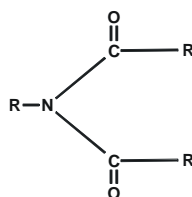


Fig. 5.1. Chemical structure of the imide group

The name *polyimide* derives from its characteristic imide group (Fig. 5.1) which all PI types contain. Beyond that, most PIs contain aromatic rings. In the 1950s, the company DuPont (DuPont, Wilmington, DE, USA) produced the first commercial PI film by processing an infusible and insoluble aromatic PI film via a fluid and soluble polymeric precursor. It was sold under the trade name Kapton H (Sroog 1996). Kapton is a poly(4,4'-oxydiphenylene-pyromellitimide), or PMDA-ODA, type PI. It is the best known type of PI and a lot of research was done on it (Delasi 1971; Delasi 1972; Delasi 1975; Murray 2004; Yang 1985; Yang 1986).

Tab. 5.1 Overview of the material properties of the three tested PIs

characteristic	unit	Pyralin PI2611	U-Varnish-S	Durimide 7510
manufacturer		HD-Microsystems	UBE Industries	Fujifilm
Type		BPDA-PPD	BPDA-PPD	not provided
tensile strength	MPa	350	392 (25µm thick film)	215
elongation	%	25	30	85
Young's modulus	GPa	8.5	8.83	2.5
breakdown voltage	kV/mm		150	
volume resistivity	Ω cm		$1.5 \cdot 10^{-16}$	
water absorption	%	1 (at 50% relative humidity, saturated)	1.4 (immersion in water at 23 °C for 24 h)	1.08 (at 50% relative humidity)
glass transition temperature	°C	360	>500	285

Common PIs like Kapton, PI2611 or U-Varnish-S are processed in a two-step method via a poly(amic acid) (Fig. 5.2). A diamine and a dianhydride are mixed with a dipolar solvent like N,N-dimethylacetamide or N-Methyl-2-pyrrolidone (NMP) and form a poly(amic acid).

In this state, the material can be purchased as PI precursor and can be formed by spin-coating or casting. While curing the material at temperatures between 350 °C and 450 °C, imidization takes place which is the closing of the imide rings.

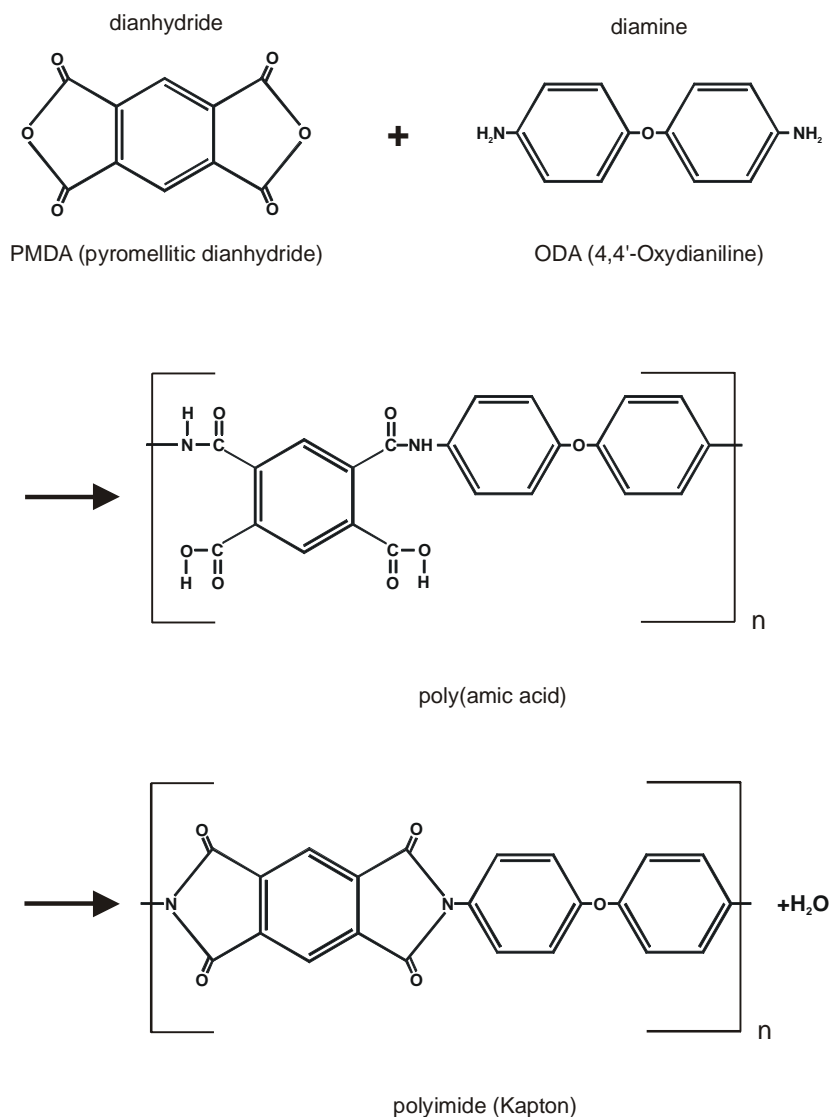


Fig. 5.2. The imidization process of a PMDA-ODA type PI (Kapton) (Takekoshi 1996)

### 5.1.2 PI2611

PI2611 (Fig. 5.3) is a trademark of HD Microsystems LLC (Parlin; NJ, USA) and was found to be a promising candidate for neural implants (Stieglitz 1998).

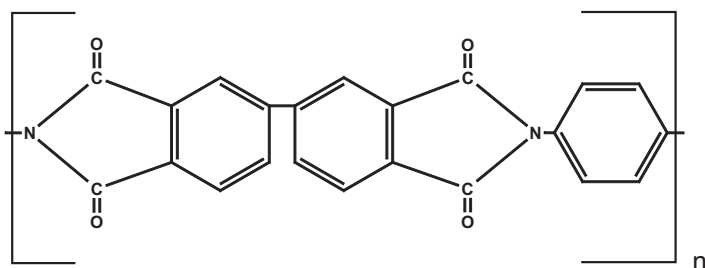


Fig. 5.3. Chemical structure of the BPDA-PPD type PI

It is well established in neural prostheses research (Kim 2009; Mercanzini 2008; Schuetler 2006; Stieglitz 2000) due to its low water uptake and its high durability. It is made of the dianhydride biphenyltetracarboxylic dianhydride (BPDA) and the diamine paraphenylenediamide (PPD).

### 5.1.3 U-Varnish-S

U-Varnish-S is a trademark of UBE Industries Ltd. (Tokyo, Japan) and is like PI2611 a BPDA-PPD type PI (Fig. 5.3).

### 5.1.4 Durimide 7510

Durimide 7510 is a trademark of FUJIFILM Electronic Materials Co., Ltd. (Tokyo, Japan). It contains a photo-initiator, acts like a negative type photosensitive polymer resin and contains an adhesion promoter. Its chemical structure is not provided by the manufacturer. Biocompatibility tests showed that Durimide was not toxic for cultured 3T3 fibroblast cells (Lee 2004b).

## 5.2 SU-8

SU-8 is an epoxy-based negative photoresist. I.e. if exposed to UV light (350-400 nm wavelength), its molecular chains cross-link and form a solid material. SU-8 can be processed with standard cleanroom equipment. Due to its high viscosity, layers with a thickness of about 120  $\mu\text{m}$  can be processed in a single spin coating step. If a filter is used to eliminate wavelength below 350 nm during exposure, vertical sidewalls are obtained and aspect ratios up to 190:1 can be achieved (Yang 2005). Features with a height of 2 mm can be structured. SU-8 comprises three main elements, the epoxy resin, the photoinitiator and the solvent. The basic component is the EPON resin (Shell Chemicals) including 4 Bisphenol A groups and 8 epoxy groups (Fig. 5.4). During polymerization, the epoxy groups highly cross-link and build the mechanical stable and chemically inert SU-8 polymer. The photosensitive component is triarylsulfonium hexafluoroantimonate salt which, upon UV irradiation, decomposes to form an acid which triggers the cross-linking of the epoxy groups and is accelerated by the temperature during the post exposure bake (del Campo 2007). The solvent used in the SU-8 2000 as well as in the SU-8 3000 series is cyclopentanone.

SU-8 was developed by IBM-Watson research centre and patented in 1989 (Hsu 2008). Since 1996 it is more and more used in MEMS applications. Today, it can be purchased from two companies: MicroChem Inc. (Newton, MA, USA) and Gersteltec SARL (Pully, Switzerland). SU-8 is chemically stable and has good mechanical and optical properties. Thus, it is used to form channels and valves in microfluidics as well as optical waveguides. Due to its biocompatibility (Grayson 2004; Kotzar 2002; Nam 2006; Voskerician 2003) it can be applied in bio-MEMS and was successfully used in neuroscience applications (Gawad 2009; Heuschkel 1998; Heuschkel 2002; Nam 2006).

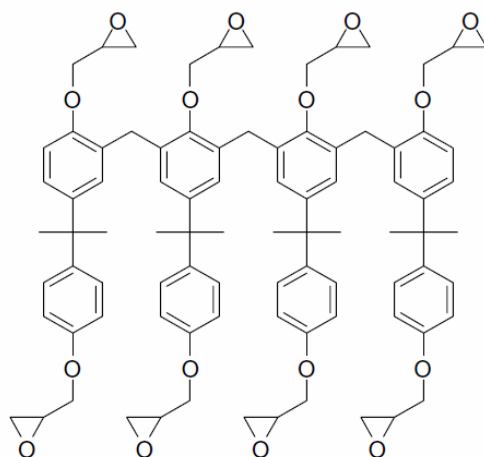


*Fig. 5.4. Chemical structure of the epoxy oligomer EPON contained in SU-8 formulation (del Campo 2007); Reprinted with permission: IOP Publishing Ltd.; del Campo A and Greiner C. SU-8: a Photoresist for High-Aspect-Ratio and 3D Submicron Lithography. Journal of Micromechanics and Microengineering. 2007; 17(6): R81*

The refractive index of SU-8 3000 ranges between 1.592 at 450 nm and 1.556 at 1200 nm. The transmission of light (at 500 nm wavelength) through a 50  $\mu\text{m}$  thick layer of cured SU-8 3000 is about 95 %. Regarding the wavelength of the light, transmission increases towards red light and decreases for light towards the ultraviolet range of the spectrum (SU-8 3000 2010). The optical properties depends on the processing parameters. Piruska et al. found the attenuation of waveguides made of SU-8 2000 in the range of 1-2 dB/cm, while waveguides with a longer soft bake and post exposure bake time had an attenuation of 3-5 dB/cm (Piruska 2006). The mechanical properties provided by the manufacturer are a Young's modulus of 2 GPa, a tensile strength of 73 MPa, and an elongation at break of 4.8 % (SU-8 3000 2010).

## 6 Aim and Own Approach

In the last three decades, the processing technology of PI-based flexible implants was developed and devices were tested with respect to their applicability as neural implants (Ceballos 2002; Lago 2007a; Stieglitz 2000). These studies mostly aimed at the application in clinical therapy and rehabilitation. While some scientists considered PI-based electrodes as promising candidates to be used in neuroprosthetics (Zrenner 2008) others disapproved PI as implant material (Loeb 1996). While the discussion on that topic goes on, PI was introduced into basic neuroscience (Molina-Luna 2007; Takahashi 2003).

### 6.1 Aim of this Thesis

This thesis aims to answer the following questions.

- Can flexible polymer-based microimplants significantly contribute to brain research in a way that goes beyond the results obtained with silicon-based MEMS implants which are currently commercially available from the two companies NeuroNexus and Blackrock Microsystems? Can such flexible microdevices fabricated with existing MEMS technology be applied in long-term recordings and supply neuroscientists with novel data?
- Is it possible to use MEMS-based electrode arrays to record neural data on the mesoscale? That is to provide an implant which records LFPs from significantly larger brain areas than reported for MEMS electrodes in literature.
- Is PI a suitable substrate material for the chronic implantation of flexible, MEMS-based implants?
- Can microimplants that comprise electrodes, a fluidic channel and an optical waveguide be efficiently used in optogenetic experiments in terms of an easy device handling, a simplified implantation, and a more convenient conduction of the experiment?

### 6.2 Own Approach

The questions raised in chapter 6.1 will be addressed separately and the engineering results will be evaluated in vivo in close collaboration with neuroscientific partners.

In this thesis, flexible, PI-based thin-film devices are proposed as efficient implants for neuroscientific research in terms of high channel data acquisition and chronic implantation. The large number of channels should be realized by MEMS processing to provide the scientists with a large amount of neural data. The thin and flexible devices are thought to better fit into brain matter without damaging the delicate tissue, providing a long-term stable contact to the tissue whose cellular structure is not significantly altered due to host

tissue responses which is important for neuroscientific experiments using chronically implanted devices.

For long-term applications a flexible, mechanically tough, chemically inert, and electrically insulating material has to be used as electrode substrate. PIs of the new generation were found to be promising candidates to fulfil all these demands. Such a PI is also used in this work to manufacture neural implants. Still, there is the need to collect more data and to further investigate the properties of this material with respect to its chronic use in a body environment. For this reason, the mechanical properties of three PIs from different manufacturers are tested during a long-term soaking test to obtain a basic knowledge concerning the stability of the material itself. To be able to investigate the PI behaviour systematically, this study is conducted as an *in vitro* experiment. By storing the polymer specimens in PBS, a large number of specimens can be tested. By the same token, specimens can be tested over a much longer time than usually reported and further stressed by storing them at body temperature as well as at elevated temperatures. A comparative study between the storage of PI in PBS and deionized water is conducted to evaluate the impact of salt ions on the long-term stability of the material.

To show the great potential of PI-based devices for neuroscience, a high-density epicortical electrode array with more than 100 channels was developed which can be chronically implanted. To achieve this, the implant as a whole assembly has to be small enough to fit on a macaque monkeys head using connectors that are standard in neuroscience. For this reason, the electrodes, cables and solder pads are integrated in one thin-film foil processed on wafer-level to achieve small feature sizes by applying MEMS technology. In the subsequent assembly, the connectors fitting into the neurophysiologic recording system are directly soldered into the foil. The form of the PI array is designed to fit onto the curved cortical surface without applying pressure to the cortex and to provide a good electrode-tissue contact. With the integrated flexible cables, the array can be implanted as a floating device to prevent the transmission of mechanical forces onto the cortex which would be generated by the relative movement between skull and brain, if a stiff electrode was attached to the skull. This array should bridge the gap between the large and bulky, low-channel PDMS-based electrode arrays used in clinical practice and the very small, silicon-based intracortical MEMS-implants which can only cover small parts of the cortex.

Another application of PI implants is the use of flexible floating shaft electrodes to intracortically record LFPs in a chronic implantation. Electrodes are designed to be usable in a minimally invasive implantation approach. An insertion tool has to be used to penetrate the meninges and to insert the shaft electrode into the brain matter via a small hole in the skull. After withdrawing of the insertion tool, only the flexible shaft remains in the cortex and is connected to the recording system via a flexible PI cable.

A third implementation of PI is its use as a shaft electrode substrate in which different recording and stimulation modalities can be integrated. These modalities are defined by the application of the devices in the field of optogenetics which is in the need of electrical, fluidic and optical contact to the nervous tissue. This shaft has to contact deeply lying

brain regions in the mouse. The starting point of the multimodal approach is the PI-based shaft electrode. An optical waveguide is integrated onto the PI substrate with a photolithography process on wafer-level. The channel is attached in a following hybrid assembly step. SU-8 is chosen as waveguide as well as channel material due to its good optical properties and processability with respect to high-aspect-ratio microstructures.

# 7 Polyimide Material Testing

As discussed in chapter 5.1, there is the need to evaluate whether PI is suited for the long-term use as an implant material. Albeit some studies present data dealing with the degradation of PI in a high temperature and/or humid environment (Bessonov 1987; Campbell 1988; Delasi 1971; Murray 2004), little is known about the long-term behaviour of PI stored in body tissue or at least saline solution. Nikles et al. reported on an increasing relative dielectric constant of 18 % measured in PI2611 after 400 days in phosphate buffered saline (PBS) at room temperature (Nikles 2003). In in vivo studies up to 12 months, no electrical failures could be observed (Ceballos 2002; Lago 2005). However, a decrease in tensile strength was reported on PI electrodes after 11 months in vivo (Schuettler 2003). In this work, PBS was used to obtain a solution in which the PI specimens could be stored at elevated temperatures to accelerate aging, which is a better model of body fluid than water and, as will be shown in this chapter, has an altogether different effect on the degradation behaviour of PI.

In this work<sup>1</sup>, the mechanical properties of PI foils were investigated to evaluate their applicability as a substrate material. After storing the material at 37 °C and at elevated temperatures (60 °C and 85 °C), the mechanical properties were examined with tensile tests, weighing tests and optical measurements in order to obtain information on the degradation behaviour. While the tensile testing showed changes in the mechanical properties like Young's modulus, stress and strain at break, or the fracture energy to determine the onset of mechanical material failures. The weighing test was used to gain information about mass loss, water uptake and the change of water uptake over time to detect the material degradation. Optical analysis methods like Fourier transform infrared spectroscopy (FTIR), X-Ray Diffractometry (XRD), and X-ray photoelectron spectroscopy (XPS) gave information about changes in the chemical structure, crystallinity, and chemical composition, respectively. In addition, it was evaluated whether a defect free foil could be obtained by the standard methods of processing thin-film PI foils used in neural engineering.

## 7.1 Test Paradigms and Methods

### 7.1.1 Tensile Tests

The tensile test with a uniaxial load is easy to conduct and provides a stress-strain curve as the standard parameter which is common and often used in engineering.

---

<sup>1</sup> Main parts of this chapter have been published as Rubehn B\* and Stieglitz T. In Vitro Evaluation of the Long-Term Stability of Polyimide as a Material for Neural Implants. *Biomaterials*. 2010; 31(13): 3449-3458

\* Test concept, specimen fabrication, literature and data analysis, writing of the paper, major parts of specimen testing



### *Specimen Layout*

The layout of the PI specimens met the requirements of ASTM D882-02 (ASTM 2002) but the dimensions were scaled down to make the specimens comparable to PI-based micro-implants. Rectangular specimens were made of MEMS-processed foils with a thickness of 6.4  $\mu\text{m}$  to 7.6  $\mu\text{m}$ , length 40 mm and width 1 mm.

### *MEMS-Processing*

Out of the large group of different PIs, three types (PI2611, U-Varnish-S, and Durimide 7510) were chosen. These three types which were introduced in chapter 5 were already used as implant material and/or showed a promising behaviour such as a low water uptake.

The PI precursors were spin coated on silicon wafers for 30 s at 2400 rpm (Durimide) and 2000 rpm, respectively (PI2611, U-Varnish-S). To enable detachment of the specimens from the wafer after processing, the wafers were cleaned in hydrofluoric acid for 15 s before spin coating (PI2611, U-Varnish-S). Since Durimide contains an adhesion promoter, the wafers had to be coated with a passivation layer of  $\text{C}_4\text{F}_8$  which inhibited the adhesion of the PI to the silicon. After spin coating, the wafers were put on a hotplate for 2 min at 120 °C (PI2611, U-Varnish-S) and at 100 °C (Durimide) respectively. Subsequently, Durimide was exposed to UV-light for 15 s at 9 mW/cm<sup>2</sup>. The PI layers were cured under nitrogen atmosphere (furnace: YES-459PB6-2PE-CP, Yield Engineering Systems Inc., San Jose, CA, USA). For Durimide and PI2611, the temperature was ramped up over 60 min and then hold for 60 min at 350 °C. For U-Varnish-S, the temperature was ramped up over 170 min and hold for 10 min at 450 °C. Two layers of the photoresist AZ9260 (MicroChemicals GmbH, Ulm, Germany) were spin coated at 1600 rpm for 30 s to form a layer of 28  $\mu\text{m}$ . A mask aligner (MA6, Süss MicroTec AG, Garching, Germany) was used to expose the photoresist through a chromium photomask; this defined the perimeters of the specimens. After developing (developer solution: AZ400K, MicroChemicals GmbH, Ulm, Germany), the structured photoresist protected the underlying PI in the following etching step. The PI was etched for 25 min in an  $\text{O}_2$ -plasma (200 W, 30 mTorr, 50 sccm  $\text{O}_2$ , RIE Multiplex, STS, Newport, UK). After stripping the photoresist in acetone, the specimens were pulled off the wafer by tweezers.

### *Specimen Storing*

After detaching from the wafer, the specimens were stored in phosphate buffered saline (PBS; 0.138 M NaCl, 0.0027 M KCl) with a pH-value of 7.4 (P3813, Sigma-Aldrich Chemie GmbH, Steinheim, Germany) at 37 °C, 60 °C and 85 °C, respectively. The temperature of 37 °C corresponds to the temperature of the human body, while 60 °C is said to be the upper limit for plastics in accelerated lifetime testing, under the assumption of ageing of the material due to Arrhenius behaviour (Hemmerich 1998; Scheirs 2000). The highest temperature of 85 °C was chosen because of its standard use in moisture testing of electronic devices. (For example, to investigate the influence of moisture in electronic packaging, specimens are stored at 85 °C and 85 % relative humidity for 168 h to 5000 h (Birolini

2007; Minges 1989)). Additionally, a group of specimens made of PI2611 was stored in deionized water at 85 °C. For each material, some specimens remained on the wafer and were stored as a reference at room temperature in an evacuated exsiccator to keep them dry.

### *Test Procedure*

The first measurement was conducted two weeks after immersing the specimens in solution and was then repeated every four weeks. During one measurement, 60 specimens were taken per material (15 per each temperature and 15 as reference, for PI2611 15 were additionally measured that were stored in deionized water to compare the influence of water and saline solution on the PI degradation). The specimens were taken out of the solution and allowed to dry on a sheet of paper for some minutes while cooling down to room temperature. Each specimen was clamped between the clamp jaws of a tensile tester (Z2.5 Zwicki-Line, Zwick/Roell, Ulm, Germany). The clamp jaws moved apart and when the initial load of 2 MPa was reached, the software started the measurement and the stress-strain curve was recorded until the specimen ruptured. The test velocity of the clamp jaws with respect to each other was 50 mm/min. The force acting on the specimen was measured with a 50 N load cell (KAP-TC, A.S.T. GmbH, Wolnzach, Germany). The stress-strain curve showed the stress (force per initial cross section) plotted over the strain (length difference between the initial length of the specimen and the elongated length, divided by the initial length). All statistic tests were conducted in GNU octave, version 3.0.1 (octave 2009).

### **7.1.2 Gravimetric Analysis**

A standard PI foil (210 mm by 300 mm by 25 µm, ca. 2.4 g, Upilex25S, UBE Europe) was purchased from the manufacturer. Upilex25S is the trade name of a foil made of the precursor resin U-Varnish-S. The foil was cleaned with acetone and isopropanol, cut into pieces of approximately 50 by 50 mm<sup>2</sup>, and stored in the same PBS solution as the tensile test specimens. Every 4 weeks the foil pieces were rinsed with deionized water and dried with a cloth. After allowing the pieces to dry at room temperature and pressure for 5 minutes, they were weighed on a standard laboratory weighing scale (TE64, Satorius, Göttingen, Germany). Subsequently, the foil was dried in a furnace at 85 °C for 24 h, weighed again to determine the dry mass without water, and put back into PBS at 85 °C.

### **7.1.3 Optical Analysis**

To evaluate whether the chemical or crystalline structure of the PI changed during the long-term test, the foils of the gravimetric analysis were tested with optical analysis methods.

#### *Fourier transform infrared spectroscopy (FTIR)*

An Upilex25S sample and a reference foil were measured with FTIR. The sample foil was stored in PBS at 85 °C for 17 months and the reference was obtained from the manufacturer and stored at normal ambient atmosphere. Both foils were dried for 24 h in an exsic-

cator and subsequently measured by FTIR (2000 FT-IR Scimitar Series, Varian, Orpington, Kent, UK) using an attenuated total reflectance (ATR) unit (MkII Golden Gate, Specac, Woodstock, GA, USA). On each specimen 10 measurements were conducted each at a different position on the foil.

#### *X-Ray Diffractometry (XRD)*

XRD can be used to detect whether the polymer is crystalline and whether the crystallinity changes during storing. Upilex25S foils were measured after 7 months (in PBS at 37 °C and 60 °C, in deionized water at 85 °C) and after 23 months (in PBS at 85 °C). The reference was a non-treated foil stored at normal ambient atmosphere. The specimens were taken out of solution, rinsed with deionized water, and dried for 24 h in an exsiccator at room temperature. Wide angle X-ray diffraction (WAXD) measurements were conducted with a Siemens D5000 (Siemens AG, Munich, Germany) in reflection mode.

#### *X-Ray Photoelectron Spectroscopy (XPS)*

To check whether ions of the PBS diffused into the polymer during storage, XPS measurements were conducted. Upilex25S foils were measured after 22 months (PBS at 85 °C) and 6 months (DI at 85 °C, PBS at 37 °C and PBS at 60 °C) of storing in solution. A non-treated foil stored at normal ambient conditions was used as a reference. After taking the foils out of solution, they were rinsed in deionized water for 3 min and dried for 24 h in a vacuum of  $2 \cdot 10^{-3}$  mbar. Measurements were performed with a Perkin Elmer PHI 5600 ESCA (Perkin Elmer, Waltham, MA, USA) using a magnesium X-ray source emitting photons with 1253.6 eV. The survey was measured with a step size of -0.8 eV and the detail with -0.025 eV.

#### **7.1.4 Measurement of Foil Defects**

As PI is used to insulate conductor paths from the surrounding body tissue, it is important to know whether the insulation layer is uniform and without defects. Does the way the chosen material is processed lead to a defect free PI film? An easy to execute method is to coat the precursor on an electrical conductive substrate and cover the cured layer with a fluid (Fig. 7.1). A voltage is applied between the substrate and the fluid. If there are holes in the PI layer electrolysis will start and gas bubbles will occur and centres of gas evolution are directly counted.

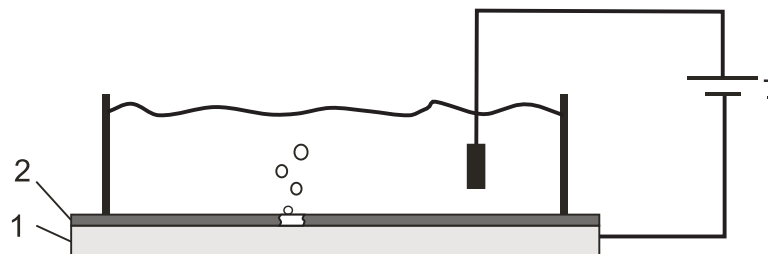


Fig. 7.1. Measurement set-up for defect detection, 1) conducting substrate, 2) PI layer (Rubehn 2007a)

### *Sample Preparation*

A metal layer of 10 nm chrome and 100 nm gold was vapour deposited on six 4" silicon wafers. The three PI precursors PI2611, U-Varnish-S, and Durimide 7510 were spin coated on the gold layer. After spin coating, the wafers were put on a hot plate for 2 min at 120 °C. Subsequently, PI2611 and U-Varnish-S were cured under nitrogen atmosphere for 60 min at 350 °C (PI2611) and for 10 min at 450 °C (U-Varnish-S), respectively. Durimide 7510 was exposed to ultraviolet light with 9 mW/cm<sup>2</sup> for 15 s before curing under nitrogen atmosphere at 350 °C. The coating process took place in a cleanroom to prevent particle inclusion in the PI layer (cleanroom class 4 (ISO 1999)). The PI layer thickness after curing was 6 µm. With a waterproof marker, a grid was drawn on the PI surface which separates the wafer in segments of 1 cm<sup>2</sup> to facilitate the counting of centres of gas evolution. For every material, the minimal observed area was 70 cm<sup>2</sup>. A plastic ring was glued to the wafer surface with silicone. On the outside of the ring a piece of PI was peeled off and the gold layer was contacted by soldering a copper wire to it.

### *Measurements*

The ring was filled with Ringer's solution. Subsequently, the wafer was placed in a vacuum chamber to release the gas bubbles located at the PI surface and in holes. We put a metal electrode in the solution which worked as the anode. The gold layer served as the cathode. A voltage of 2 V was applied while observing the PI surface through a microscope. The minimum voltage was 2 V because it was the lowest value at which gas bubbles appeared due to electrolysis. The emerged bubbles were counted and then wiped off. The counting was repeated to ensure that the bubbles were due to holes in the PI layer. Thereafter, we increased the voltage in steps of 5 V up to a total of 30 V. After every step the surface was observed in order to find new defects. The maximum voltage had to be higher than the maximum stimulation voltage of 12 V used to stimulate nerve fibres by implanted devices (Prutchi 2005).

## 7.2 Results

### *Tensile Tests*

A stress-strain curve was obtained from every tested specimen. A typical stress-strain curve with the specific values used to characterize the material behaviour is depicted in Fig. 7.2. The Young's modulus ( $E$  in GPa) is the gradient of the straight line representing the elastic behaviour of the material. The tensile strength ( $\sigma_{max}$  in MPa) coincided with the tensile stress at break. The strain maximum is the strain at break ( $\epsilon_{max}$  in % relating to the initial length). To characterize the plastic behaviour of the specimen at values far below strain at break, the stress at a strain value of 10 % was chosen ( $\sigma_{10}$  in MPa). As a measure of ductility, the fracture energy was calculated as the area under the stress-strain curve (Strobl 2007). Fig. 7.3 shows the development of the stress-strain curves for PI2611 over 17 months, stored in PBS at 85 °C. Each plot shows the curves of 15 specimens measured in one session. Curve (a) shows a dry reference stored at room temperature in

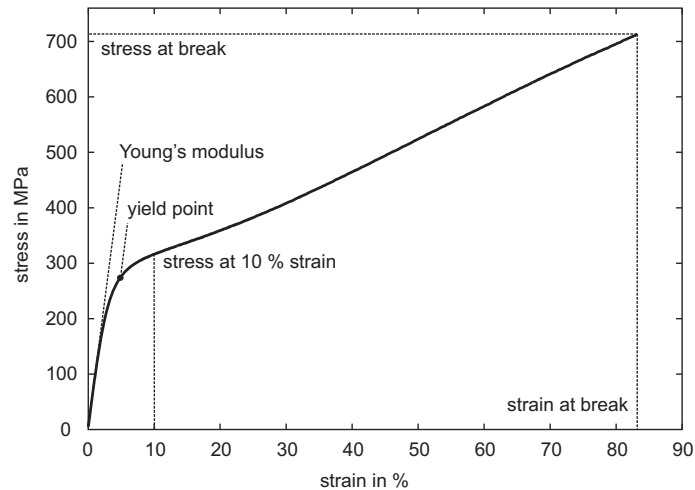


Fig. 7.2. Exemplary stress-strain curve; specific values used to characterize and compare the material properties of different samples are marked.

a dry atmosphere. Curves (b), (c) and (d) show the tensile behaviour of specimens stored in PBS after 8, 12, and 14 months respectively. The plot also contains a sample measured after 17 months in PBS with a maximum stress at break of 25 MPa and a maximum strain at break of 2 % and therefore is concealed by the other sample curves.

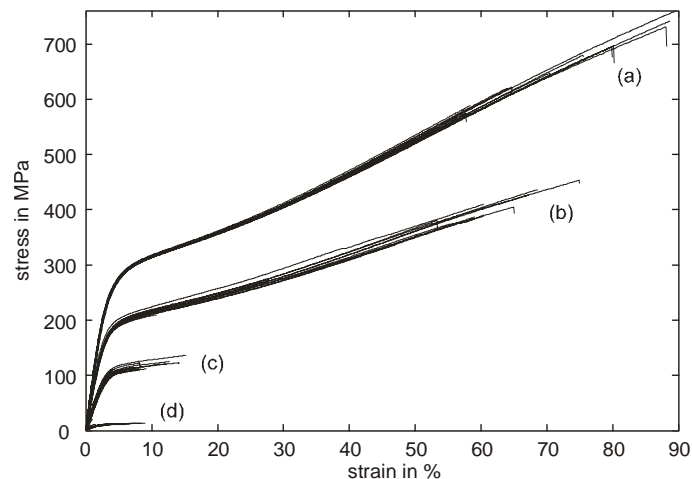
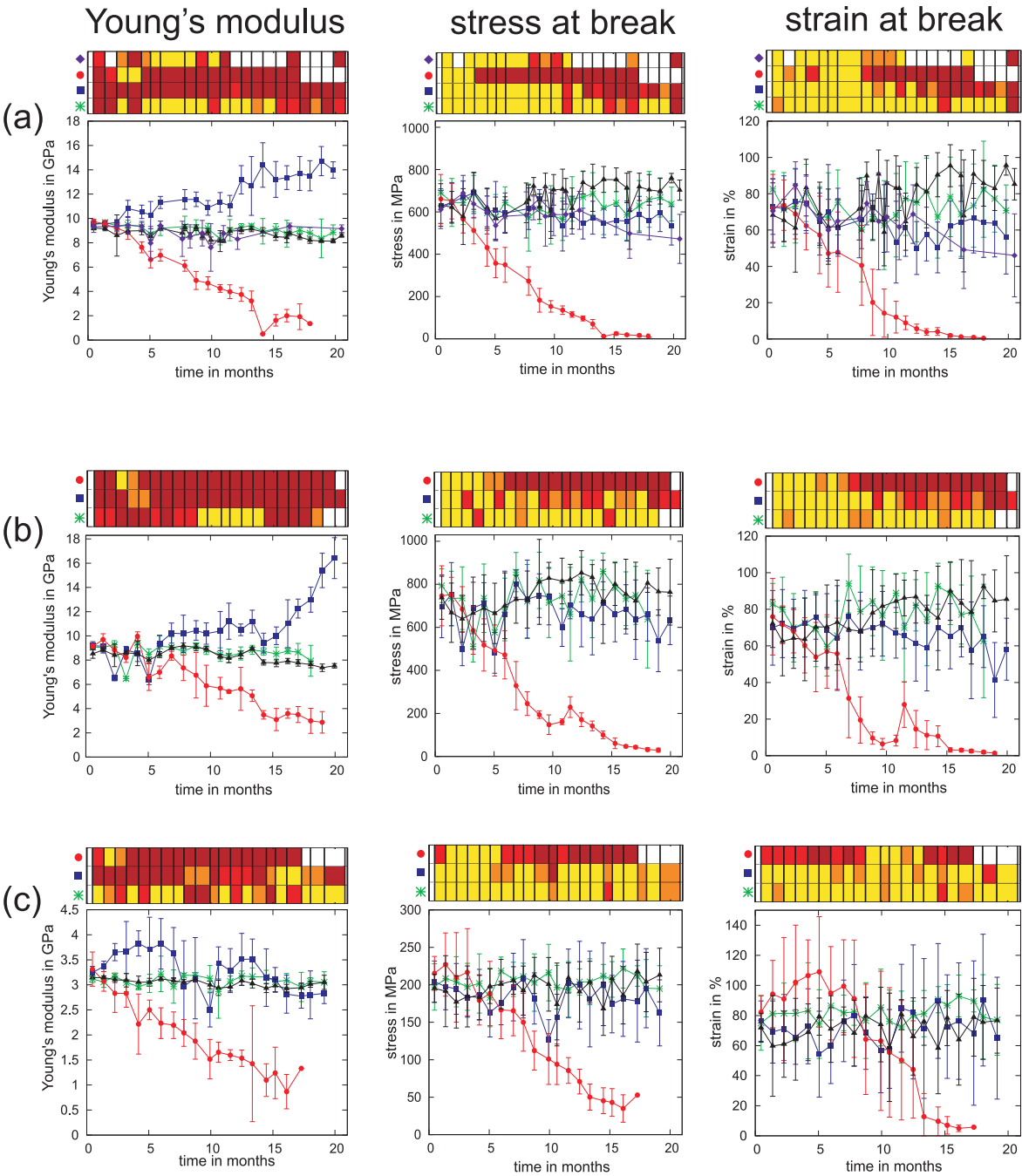


Fig. 7.3. Stress-strain curves of different samples of PI2611: (a) dry reference, (b-d) stored at 85 °C in PBS, (b) after 8 months, (c) after 12 months, (d) after 14 months

To give an overview over the long-term behaviour, the values of  $E$ ,  $\sigma_{max}$ ,  $\epsilon_{max}$ ,  $\sigma_{10}$  and fracture energy of every temperature and material are plotted over time of storage in PBS (Fig. 7.4). Each column depicts one specific value measured with each of the three PIs. Each row shows the different specific values of one PI: PI2611 (Fig. 7.4a), U-Varnish-S (Fig. 7.4b), and Durimide 7510 (Fig. 7.4c). Each point represents the mean of the values derived from one sample i.e. 10 to 15 tested specimens; error bars show  $\pm$  standard deviation. Each curve shows the development of one specific value derived from specimens stored at a certain temperature. Not all displayed values could be calculated from the data of 15 specimens due to measurement failures but represent at least 10 specimens. The stress-strain curve of every specimen was plotted and examined.



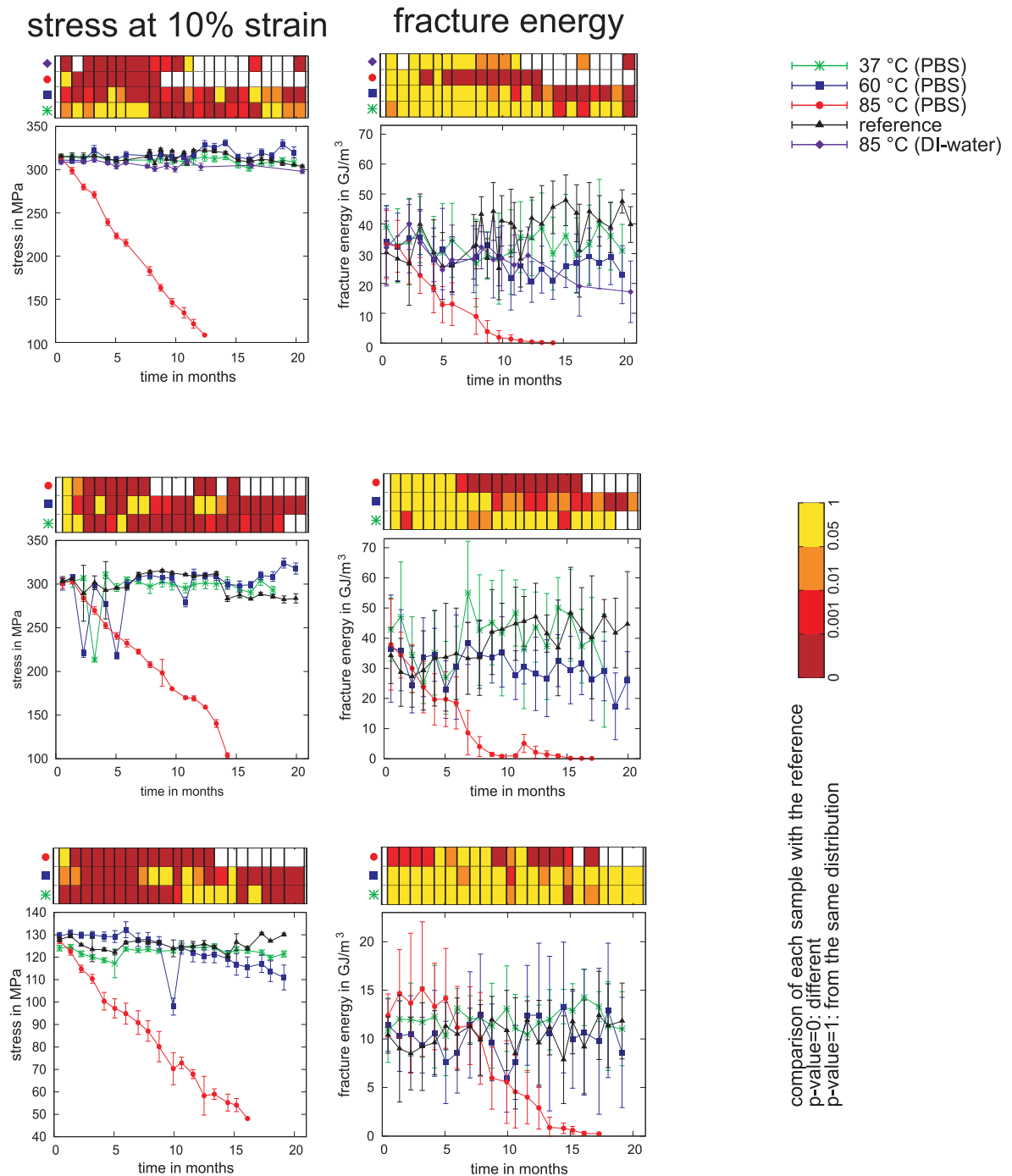


Fig. 7.4. Overview of the tensile test results: each column depicts one specific value measured with each of the three PIs. Each row shows the different specific values of one PI: (a) PI2611, (b) U-Varnish-S, and (c) Durimide 7510. The colour bar over each diagram represents the development of the  $p$ -value over time. Each field represents the  $p$ -value resulted from the Kolmogorov-Smirnov test. Values larger than 0.05 (yellow) show that there is no difference between sample and reference. Values less or equal 0.05 ( $0.05 \geq p\text{-value} > 0.01$  in orange;  $0.01 \geq p\text{-value} > 0.001$  in red,  $0.001 \geq p\text{-value}$  in dark red) stand for a significant difference between the sample and the reference sample.

Data that did not show a straight line directly at the beginning of the measurement were rejected, due to the fact that the data record of these specimens started before the stress reached the initial value of 2 MPa, resulting in erroneous specific values. This led to 531 samples out of a total of 3968 (13 %) being rejected, giving an average of 13 specimens per test sample. By comparing the data plots without the rejected data to those plots containing all data, no differences of the specific values and their development could be observed. However, the standard deviation was less when rejecting the erroneous data (Fig. 7.4).

The mechanical properties ( $E$ ,  $\sigma_{max}$ ,  $\epsilon_{max}$ ,  $\sigma_{10}$  and fracture energy) of each test sample were then tested for normality with the Anderson-Darling-Test. 66 % of the samples were normally distributed (95 % confidence interval); therefore the nonparametric two-sample Kolmogorov-Smirnov test was used to check whether the mechanical properties of the test samples differed significantly from those of the reference samples stored at room temperature and pressure. Probability ( $p$ ) values less than 0.05 led to the rejection the null hypothesis that the test sample and the reference sample derived from the same distribution.

Each comparison is depicted as a field in the colour bar above each plot. The horizontal bar shows the development of the  $p$ -value over time of the specimens stored at a certain temperature compared to the reference sample. Its colour indicates the size of the corresponding  $p$ -values: values larger than 0.05 are depicted in yellow, values less than or equal to 0.05 and larger than 0.01 are in orange, values less than or equal to 0.01 and larger than 0.001 are in red, and values less than or equal to 0.001 are in dark red. Each field of the colour bar corresponds to a point of the development curves in the plot below the colour bar.

The Young's Modulus shown in these plots was calculated by fitting a straight line to the measured values between 0.25 % and 0.5 % of strain. The standard values for calculating the Young's Modulus are between 0.05 % and 0.25 % of strain (Grellmann 2007). As mentioned above, due to the low value of 2 MPa as the starting point for the measurement, most of the measured stress-strain curves were inaccurate in this strain range. At larger strain values, the standard deviation of the Young's Modulus decreased, while the mean value and the development over time remained the same. The measured values of the reference samples correspond to values provided by the manufacturers (U-Varnish-S:  $E = 9.3$  GPa; PI2611:  $E = 8.45$  GPa; Durimide:  $E = 2.5$  GPa). The method for calculating the Young's Modulus used in this work is consistent with the standard method of drawing a tangent to the initial linear portion of the load-extension curve and calculating the gradient (ASTM 2002).

The  $\sigma_{10}$  values were only calculated for specimens that reached the 10 % strain value. Specimens that broke before this point had a stress of 0 MPa at 10 % strain and thus increased the standard deviation of the sample, thus the data of these specimens were not taken into account when calculating the mean and the standard deviation of the stress at



10 % strain (Fig. 7.4). For comparison we produced a similar plot including specimens that broke below 10 % the trend was identical, but with a higher standard deviation (data not shown).

Over the course of 20 months, the mechanical properties of all three PI types stored in PBS at 37 °C did not change with respect to the reference. This also applied to the specimens stored at 60 °C excluding the Young's modulus of PI2611 and U-Varnish-S. All data points showed a large standard deviation and a large day-to-day variation. Nevertheless, three significant changes could be observed. Specimens stored in PBS at 85 °C showed a decrease in all monitored specific values (Fig. 7.4, red dots). This was found for all three materials. The first samples that showed this trend and significantly differed from the reference samples were measured at the earliest in month number 2 ( $\sigma_{10}$  of PI2611) and at the latest in month number 14 ( $\epsilon_{max}$  of Durimide 7510), respectively. The second trend was only observed for the Young's modulus for specimens made of PI2611 and U-Varnish-S, namely: while the Young's modulus of specimens stored at 37 °C (Fig. 7.4, green crosses) remained constant at the reference level (Fig. 7.4, black triangles) and decreased at 85 °C, it increased at the storage temperature of 60 °C (Fig. 7.4, blue squares). In all other specific values, the 60 °C samples of all three PIs showed no significant trend over time. A third observation could be made by comparing the properties of PI2611 specimens stored at 85 °C in PBS and deionized water, respectively. All specific values decreased for materials stored in PBS whereas they remained similar to reference values for materials stored in deionized water (Fig. 7.4, violet diamonds).

### Gravimetric Analysis

By storing the PI foil Upilex25S in PBS at 85 °C, a decline in foil mass could be observed by measuring the foil directly after taking it out of solution (Fig. 7.5, squares) as well as after subsequent drying for 24 h at 85 °C in an oven (Fig. 7.5, dots). The values were normalized by the initial mass value of the foil at month 0. After immersing the foil for 32 months, it had lost approximately 8.2 % of its initial mass while the water absorption remained stable over time with a mean value of 1.46 %. The water absorption was calculated according to

$$A = \frac{m_{im} - m_{dry}}{m_{dry}} \cdot 100 \quad (7.1)$$

where  $A$  is the water absorption in %,  $m_{im}$  is the foil mass after immersion and  $m_{dry}$  the foil mass after drying for 24 h at 85 °C.

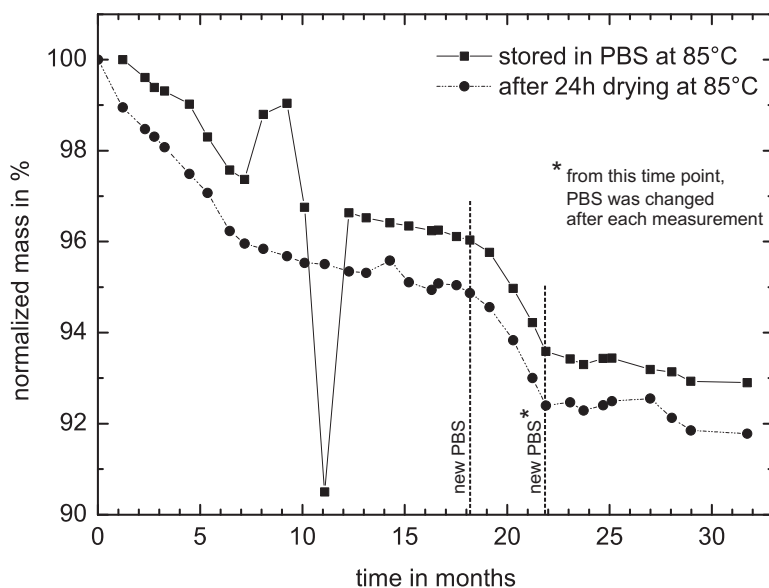


Fig. 7.5. The development of the mass of a PI film (Upilex25S, UBE) stored in PBS at 85 °C measured directly after taking the film out of solution (squares) and after subsequent drying for 24 h at 85 °C (dots). The values are normalized by the initial mass value of the foil at month 0.

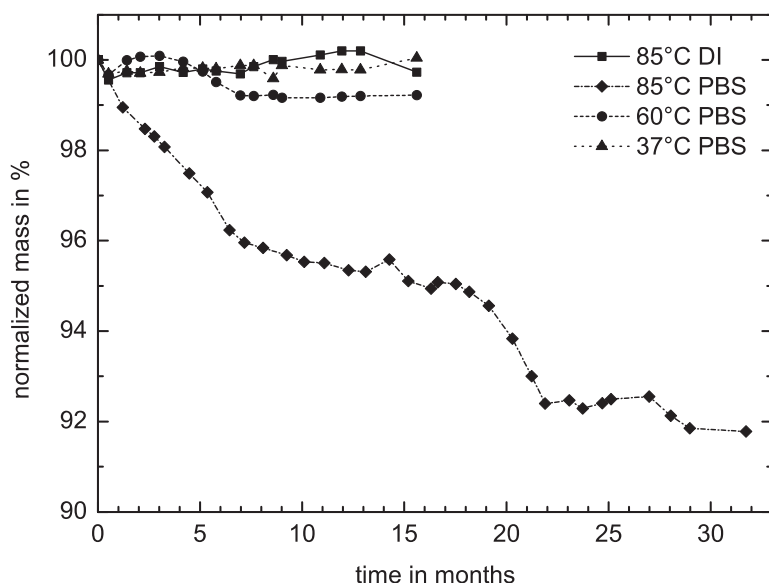


Fig. 7.6. The development of the mass of PI films (Upilex25S, UBE) after drying for 24 h at 85 °C. The foils were stored in PBS at 37 °C (triangles), 60 °C (dots), and 85 °C (diamonds) and in deionized water at 85 °C (squares). The values are normalized by the initial mass values of the foils at month 0.

In the first months the mass was significantly decreasing until reaching a limit at 95 % of the initial dry value. After replacing the PBS with new solution in month number 18, the mass loss continued. A second stop of the mass loss could be observed after month number 22 when  $m_{dry}$  reached 92.5 % of the initial value. Fig. 7.6 displays the mass of differently stored foils after drying. Compared to the foil stored in PBS at 85 °C (diamonds) that already lost mass after 2 months, the foils stored in PBS at 37 °C (triangles) and 60 °C (dots), and the sample stored in deionized water at 85 °C (squares) showed no

mass loss after 16 months. The water absorption of the unchanged samples was constant over time at 1.1 %. The water uptake of 1.46 % in samples stored in PBS at 85 °C corresponds with the information given by the manufacturer, which reports a water absorption of 1.4 % after immersing the sample in water at 23 °C for 24 h.

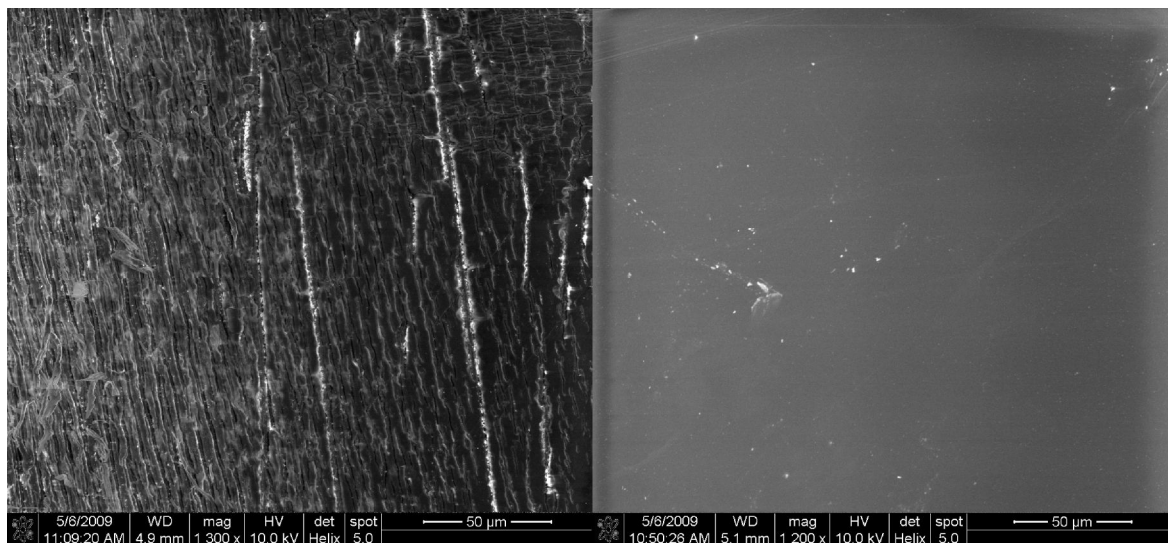


Fig. 7.7. Scanning electron microscope picture of a crease in an Upilex25S foil after 18 months of immersion in PBS at 85 °C (left), and of a reference foil as obtained from the manufacturer (right).

The foils stored in PBS at 85 °C also changed its macroscopic behaviour over time. Despite the fact that they were not subject to significant mechanical stress, these foils developed creases and started to split into pieces during rinsing with deionized water or while being handled during the monthly weighing process (Fig. 7.7, left).

### Optical Analysis

For FTIR spectroscopy, two foils were measured at 10 different positions each. The mean of the 10 measurements is shown in Fig. 7.8. No changes in light absorption could be observed.

The XRD measurement (Fig. 7.9) revealed a semi-crystalline structure of the polymer material. Two broad peaks could be observed at the angles of  $2\theta = 18^\circ$  and  $2\theta = 25.4^\circ$ , corresponding to a lattice spacing of the crystal regions of 4.7 Å and 3.4 Å respectively. The foils stored in PBS at 37 °C and 60 °C as well as in deionized water at 85 °C showed no change with respect to the reference, whereas the foil stored in PBS at 85 °C showed a decrease in crystallinity and a change in the crystal structure (the peak at  $18^\circ$  decreased and split up in two peaks at  $18^\circ$  and  $19^\circ$ ). A detailed measurement was conducted to determine whether the peak decreased or just changed to a higher one with less width and was concealed due to the measurement resolution. But even with a smaller angle step size, no peak was found (Fig. 7.9, detail).

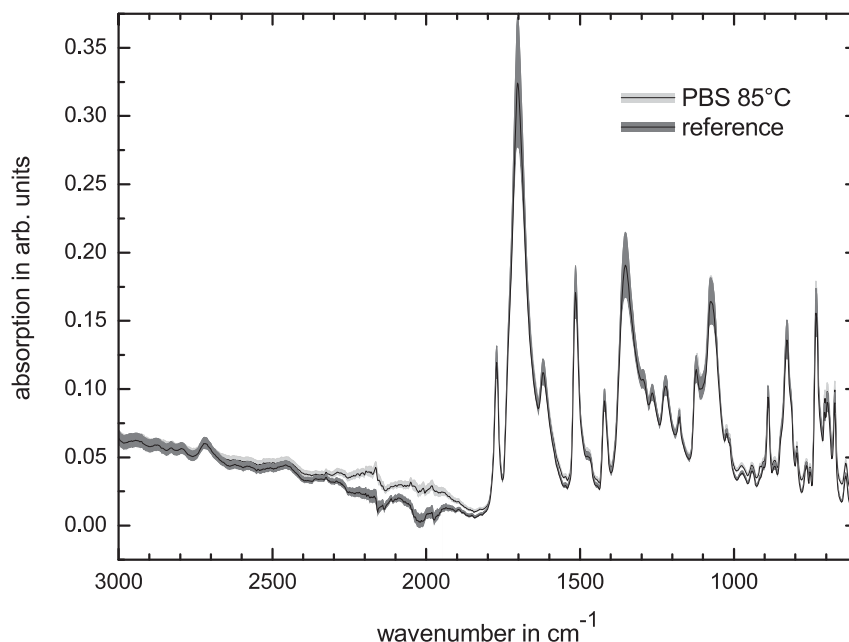


Fig. 7.8. Fourier transform infrared spectroscopy (FTIR) measurement of Upilex25S foils. The sample was stored for 17 months at 85 °C in PBS. The reference was stored at normal ambient conditions at room temperature. The black lines show the mean of 10 measurements conducted at different positions on the foils. The light grey (PBS, 85 °C) and the dark grey band (reference) depict the standard deviation calculated with the data of the 10 trials.

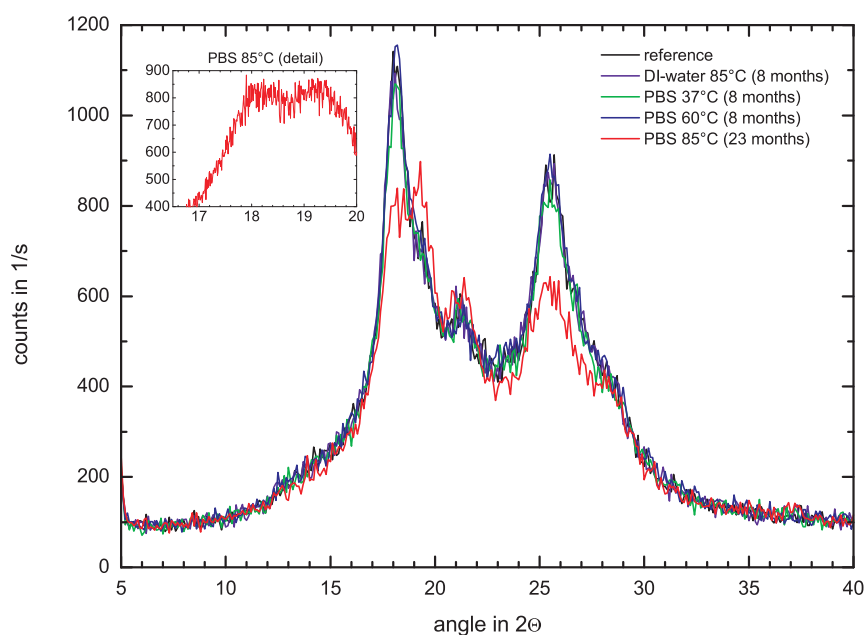


Fig. 7.9. X-Ray Diffractometry (XRD) of Upilex25S foils after 7 months in PBS (37 °C in green; 60 °C in blue), after 7 months in deionized water at 85 °C (pink), and after 23 months in PBS at 85 °C (red); The reference (black) represents a dry foil as received from the manufacturer.

XPS measurements (Fig. 7.10) gave no indication of contamination by sodium, potassium, chloride or phosphorous ions, for foils stored in deionized water, PBS, or for the reference. It is possible that the limited resolution of the survey spectrum would allow the significant

carbon peak to conceal a potassium peak in the K2p<sub>2/3</sub> region. Therefore we conducted a more detailed spectral measurement with a step size of -0.025 eV (Fig. 7.10b). Even at this higher resolution, no potassium could be observed. In contrast, a significant presence of calcium was observed in the test foils, as evidenced by a Ca2p peak at 350 eV in the survey spectrum, which was not observed in the references (Fig. 7.10a).

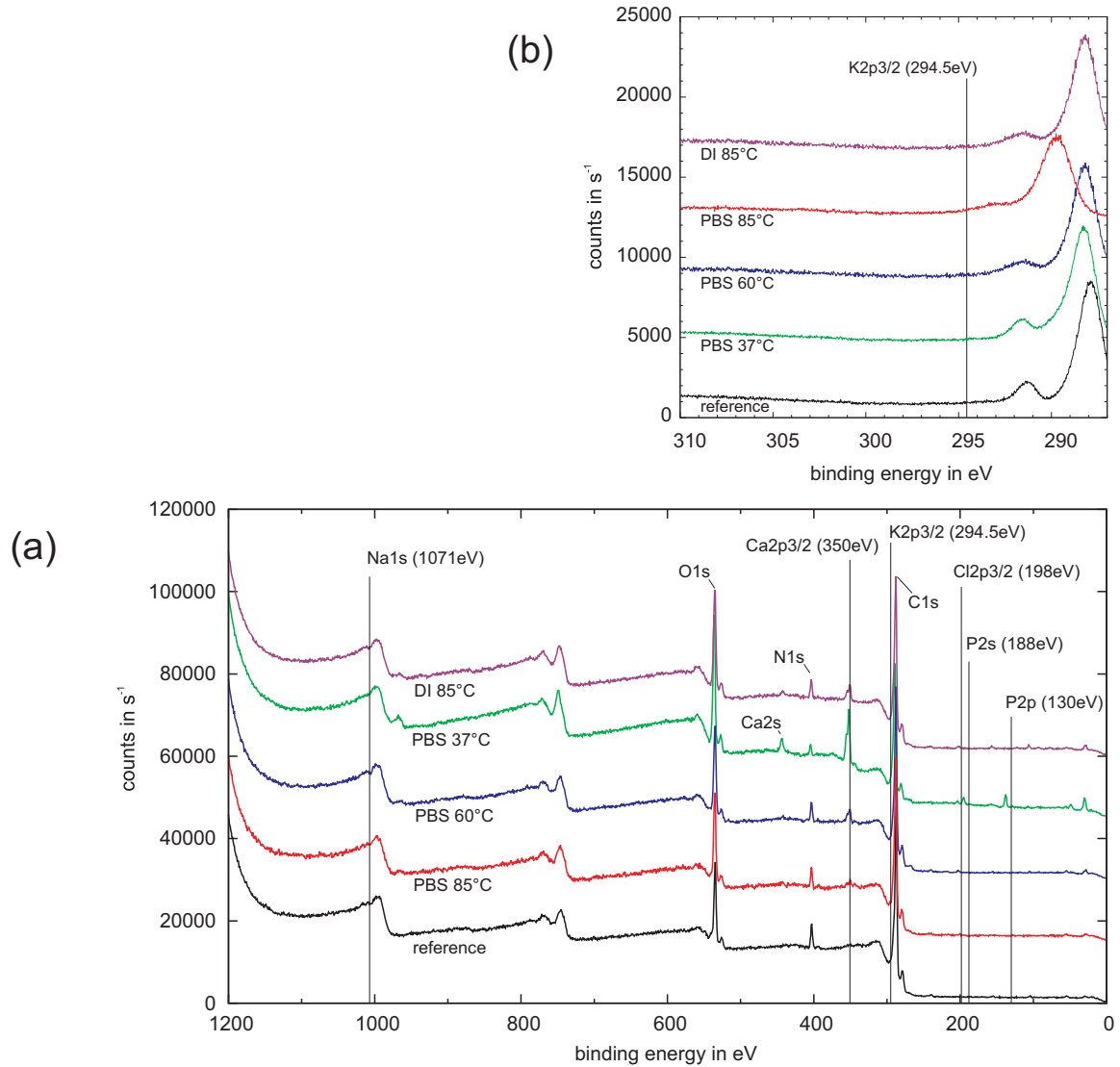


Fig. 7.10. XPS measurement of the Upilex25S foils after 6 months (in PBS at 37 °C and 60 °C respectively, in deionized water at 85 °C) and after 22 months in PBS at 85 °C. The reference represents a dry foil as received from the manufacturer. The survey spectrum was measured with a step size of -0.8 eV (a). (b) shows a close up of the K2p<sub>2/3</sub> peak region which is concealed in (a) by the C1s peak. This detailed spectrum was measured with a step size of -0.025 eV. The sample data are shifted in steps of 15000 counts per second (survey) and 4000 counts per second (detail) with respect to the reference to show the samples without overlapping each other.

### Measurement of Foil Defects

By applying a voltage, two responses could be observed: gas evolution (Fig. 7.11a) and delamination (Fig. 7.11c) of the PI from the underlying gold layer. The delaminated area became larger the longer a voltage was applied. Tab. 7.1 shows the number of spots

where gas evolution occurred at the respective voltage. The number of delamination areas is given in parentheses. For every material, the observed area was a minimum of 70 cm<sup>2</sup>. The size of the holes was between 100  $\mu\text{m}^2$  and 8500  $\mu\text{m}^2$  (Fig. 7.11d).

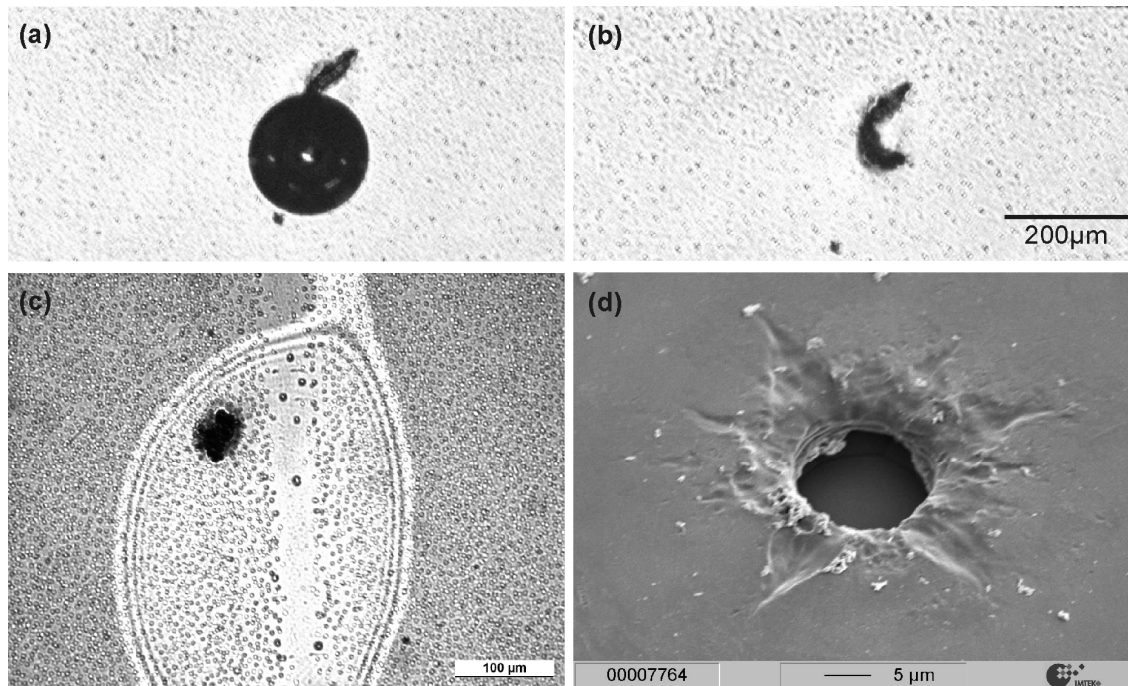


Fig. 7.11. (a) gas bubble caused by (b) a defect in the PI layer (Rubehn 2007a), (c) delaminated area (light area) caused by a defect (black spot) in the PI layer, (d) SEM micrograph of a hole in a PI layer (Rubehn 2007a)

Tab. 7.1 Number of measured defects

	PI2611		U-Varnish-S		Durimide 7510	
voltage in V	wafer 1	wafer 2	wafer 3	wafer 4	wafer 5	wafer 6
2	1	0	1	0	2	0
5	1	(1)	1	6	2	1 (1)
10	1	(1)	1	6 (1)	2 (2)	2 (1)
15	1	(1)	2	6 (1)	2 (3)	2 (1)
20	1	(1)	2	6 (1)	4 (3)	2 (1)
25	1	(1)	3	6 (1)	4 (3)	2 (1)
30	1	(1)	3	6 (1)		2 (1)
area in cm <sup>2</sup>	37	36	35	38	40	35

### 7.3 Discussion

The tensile test of the stored PI samples showed that both the large standard deviation and the day-to-day variation of the mechanical properties (Fig. 7.2) can be explained by the dimensions of the tensile test specimens. The ASTM 882-02 test specifications (ASTM 2002) describe the test procedure for foils using a minimum foil thickness of 625  $\mu\text{m}$  and a width of 5 mm. In contrast, we used specimens with a thickness of 7  $\mu\text{m}$  and a width of

1 mm. According to ASTM 882-02 this would be expected to enhance the effects of edge flaws. Notches at the edge have a higher influence on the measured properties of narrow and thin specimens than on ASTM-conforming specimens (ASTM 2002). Under a light microscope, the edges of the specimens were smooth, while scanning electron microscope images revealed a rough surface with ridges in the submicrometre range (Fig. 7.12) which could have contributed to the high standard deviation of values at break ( $\sigma_{max}$  and  $\epsilon_{max}$ ). This is consistent with a previous observation that the tensile strain at break shows high statistical scatter (Grellmann 2007).

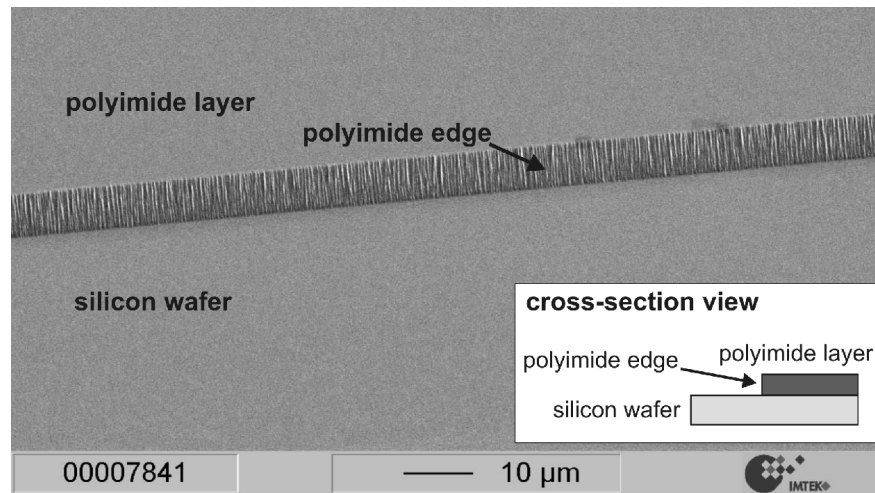


*Fig. 7.12. SEM photograph of the edge of a tensile test specimen structured with an oxygen plasma*

Nevertheless, the small dimensions of our test samples are in the range of those for micro-machined PI-based neural implants. Thus, this tensile test is more of a structural test than a purely materials-based analysis. Furthermore, a specimen made of a thin foil of spin-coated PI has different material properties from thicker, bulk material. Anisotropy can occur due to the forces that affect the precursor during spin coating, and due to the solvent loss and imidization of a thin film from a precursor solution which can in turn lead to a higher degree of molecular orientation of the preferential chain axis parallel to the foil surface (Coburn 1996; Ree 1992; Russell 1984; Seo 2001a). It was found that spin-coated PI material in the vicinity of the surface has a different morphology than in the bulk material, by nature of a higher degree of crystallinity (Factor 1991). Hence, the dimensions of the tensile test specimens we used and their manufacture are in close correspondence to the processing of PI for neural implants, and could provide useful insights into the behaviour of these materials during long-term implantation.

No difference in behaviour between the reference group and the group stored at 37 °C could be observed for any of the tested materials or monitored specific values. Additionally, no mass loss and no change in optically measured properties could be detected in Upilex25S at the same temperature. Based on these results, it can be concluded that the materials can be used at body temperature for a minimum time of 20 months. This is in agreement with the observation that PI sieve electrodes still function after 12 months im-

plantation in vivo (Ceballos 2002; Lago 2005). However, neither of these studies looked at possible changes in material properties of the implants. In contrast, Schuettler et al. reported on sieve electrodes made of PI2611 (Schuettler 2003). Examined after 11 months in vivo, these electrodes showed a decrease by 30 % of the initial stress at break as well as delamination of metal and PI. This could be due to a factor that was not included in our in vitro tests, namely the effect of enzymes on polymeric degradation, which has been described for other polymers like poly(ether urethanes) (Smith 1987). Thus, although PBS, by containing the same composition of ions and having the same pH value as body fluid, is a more accurate model of body fluid than water, it is not definite that the material shows equal behaviour in vivo and in PBS.

For specimens stored at 60 °C, the mechanical properties did not degrade over time. This demonstrates a high durability of all three types of PI in the presence of PBS. In addition, the measurements conducted with BPDA-PPD foils showed that over time, there was neither a decrease in mass nor a change in material properties measured optically. These results strengthen the hypothesis that the tested PIs are stable in vivo over a period of 20 months or more. The tests showed that the three PIs are superior to PMDA-ODA type PI which already degrades after 30 days in distilled water at room temperature (Delasi 1971).

An anomaly was found in the Young's modulus of BPDA-PPD type PIs at 60 °C. The Young's modulus increased constantly, starting at an initial value of 9 GPa and rising to 16 GPa after 20 months in solution. A possible explanation of this behaviour of the polymer could be that there was a redistribution of the constituent crystals due to the higher storage temperature. While the overall number of crystals did not vary (Fig. 7.9), the adhesion between neighbouring grains sliding over each other and the distribution of crystalline regions could have changed (Strobl 2007). This theory is supported by the observation that only the Young's modulus increased, while the properties at break remained constant (Fig. 7.4a,b), which would correspond to a change in the crystal arrangement. In the elastic section of the stress-strain-curve, the crystallinity and the arrangement of crystallites affect the Young's modulus. After reaching the yield point in the part of the plastic deformation (Fig. 7.2), crystallites slide upon each other and change their arrangements due to the increasing strain forgetting the initial crystallite arrangement in which they were positioned by the tempering at 60 °C. Hence, the Young's modulus increases while the properties at break remain at the same values as the reference. However, it remains unclear why the Young's modulus did not increase in deionized water at 85 °C. At this higher temperature, the crystallites should have even more energy to rearrange. Further studies will be needed in order to examine in more detail the changes in the underlying crystal structure of PI during long-term storage at different temperatures.

The increasing Young's modulus at 60 °C could be also explained with a theory described as antiplasticization (Wypych 2004). In general, plasticizers are known to cause an increase in elongation, decrease in tensile strength and Young's modulus. But a plasticizer in a polymer can sometimes increase the Young's modulus. Such a stiffening effect was



also found in PI immersed in water. Harper and Rao stored PI (PMDA-ODA) in distilled water at room temperature and at 90 °C, respectively, and found a significant increase in stiffness over time up to 270 days of immersion (Harper 1994). This effect was stronger for specimens stored at 90 °C than for those stored at room temperature. Our results at 60 °C are in good agreement with these findings. A water uptake of 1.1 % could act as a plasticizer (Cella 1996; Coburn 1996) and stiffen the material. Note that this model also fails to account for the constant values of specimens stored in PBS and deionized water at 37 °C and 85 °C respectively. However, these samples also have a water uptake of 1.1 % which would lead to a stiffening according to the antiplasticization theory.

Despite the fact that the Upilex25S foil showed a decreasing mass over time, no change in the light absorption of this foil could be observed with FTIR measurements (Fig. 7.8). This indicates that there were no breakages of chemical bonds in the material and that the changes in material properties were not due to changes in the chemical structure of the polymer. A first hypothesis explains the decline of the mechanical properties with the decrease of crystallinity (Fig. 7.9). A loss of crystal regions in the polymer can also be deduced from the stress-strain curves in Fig. 7.3. While the Young's modulus and therefore the stress at yield were decreasing over time, the strain at yield remained on a constant value of about 4 %. This is a specific behaviour of semi-crystalline polymers with a decrease in crystallinity (Strobl 2007). The decrease and the change of the crystalline structure can have a strong influence on the mechanical properties of the polymer and also on the diffusion rates of molecules like water and oxygen which contribute to the degradation of PIs (Cella 1996). The two broad peaks in the XRD spectrum show that the Upilex25S foil has crystal regions with a Bragg spacing of about 5 Å and 3.5 Å. This is consistent with results found in the literature giving peaks at  $2\theta = 18^\circ$ ,  $2\theta = 22^\circ$ , and  $2\theta = 25^\circ$  for a BPDA-PPD type PI which corresponds to Bragg spacings of 5 Å, 4 Å, and 3.5 Å, respectively (Coburn 1996; Seo 2001b). The change of crystallinity could be due to alkali metal ions having enough energy to penetrate into the crystal lattice. With 2.8 Å for potassium, 2 Å for sodium and 3.6 Å for chlorine, the ionic diameter of alkali metal ions are in the same order of magnitude as the lattice spacing of the PI. This hypothesis conflicts with the results found in the XPS measurement (Fig. 7.10) where no alkali salt ions could be detected in any of the foils.

An alternative hypothesis could explain the decrease of mechanical properties of specimens stored in PBS at 85 °C in terms of the leaching of low molecular weight components out of the foil. These components could either be additives added by the manufacturer to adjust the polymer properties, or unreacted molecules of the polyamic acid precursor not bound to the PI backbone. This could not only explain the decrease in mechanical properties but also the mass loss over time. Assuming that not all of the polyamic acid is converted to PI while curing, some percentage of the precursor molecule would therefore remain in the polymer. When exposed to PBS, amic acid molecules could be washed out, promoting the change in mechanical properties and mass (Delasi 1971). This change would not be observed in the IR spectrum due to a very strong imide peak at  $1720\text{ cm}^{-1}$ , which would conceal the weaker amide peak at  $1660\text{ cm}^{-1}$ . In contrast, the second amide

peak at  $1550\text{ cm}^{-1}$  only has a medium amplitude (Takekoshi 1996) and changes to it would be covered by other smaller peaks of the spectrum.

This second hypothesis is only valid if, after a certain time, a constant mass is reached which represents the actual PI backbone. During the weighing measurements lasting over 32 months, the mass loss nearly stopped after 22 months at a value of 92.5 % and reached 91.8 % after 32 months (Fig. 7.5). The constant value supports the second hypothesis but the measurement has to be continued to validate this value as the final mass. The first constant value of 95 % reached after 15 months can be explained with the saturation of the PBS in which the foil was stored. In month 18, the PBS was replaced with new solution and the mass loss continued. The constant value after 22 months was not due to PBS saturation because the PBS was replaced after each measurement. That some parts of the material are soluble to PBS at higher temperatures was found not only in the mass loss but also in the surface structure of the Upilex25S foil (Fig. 7.7). In some areas the material dissolved inhomogeneously, revealing a certain structure in the remaining polymer.

Reasons given for PI degradation in the literature usually include elevated temperature and/or humidity (Bessonov 1987; Campbell 1988; Delasi 1971; Murray 2004). Delasi found a decrease of stress and strain at break of about 35 % and 85 % respectively in Kapton foil after two weeks of immersion in distilled water at  $80\text{ }^{\circ}\text{C}$  (Delasi 1971). It was found that Kapton hydrolyzes when immersed in water (Campbell 1988; Delasi 1971). The results presented in this work do not show such behaviour for PI2611 and Upilex25S. PI2611 specimens stored in deionized water at elevated temperature of  $85\text{ }^{\circ}\text{C}$  did not show any decline in the tested mechanical properties. The Upilex25S foils did not show any decline in mass or change in optical properties. With a test period of 20 months for the tensile tests and 32 months for the gravimetric measurements, we examined BPDA-PPD type PIs considerably longer than was reported for Kapton foil in the literature (Bessonov 1987; Campbell 1988; Delasi 1971; Murray 2004). In contrast to specimens immersed in deionized water at  $85\text{ }^{\circ}\text{C}$ , specimens stored in PBS at  $85\text{ }^{\circ}\text{C}$  showed a rapid decrease in all quantities. Thus, it was not the combination of water and a temperature of  $85\text{ }^{\circ}\text{C}$  that led to a significant change in the mechanical properties, but rather the combination of a storage temperature of  $85\text{ }^{\circ}\text{C}$  with an immersion in PBS. This corresponds to the finding that PIs decompose in the presence of alkali metal salts at elevated temperatures (Cella 1996). Examples of these salts are potassium chloride and sodium chloride, both of which are found in significant concentrations in body fluids. With this work we could confirm that in comparison to Kapton, PIs based on the precursor molecules BPDA-PPD show a much higher stability with regard to water and temperature which corresponds to other studies (Moylan 1991; Seo 2001b; van Alsten 1994). These results imply that much research done on Kapton might not be representative of the whole group of PIs; by the same token, not all results found with PMDA-ODA type PI can be applied to BPDA-PPD PIs.

The sample stored at 85 °C in PBS had a constant water absorption over time of 1.46 %, whereas the samples showing no mass change seemed to swell less, with a constant water absorption of 1.1 %. In comparison, Kapton foils that show a stronger deterioration in water have a larger water uptake than the PIs tested in this work (Seo 2001b). The manufacturer specifies a water uptake of 2.8 % after an immersion of 24 h at 23 °C in water for Kapton HN and VN foils with a thickness of 25 µm.

As the XRD-measurement showed (Fig. 7.9), the crystalline structure of the PI in PBS at 85 °C changed. This implies that the temperature of 85 °C cannot be used to conduct accelerated aging tests. Due to the structural change, it is not possible to infer the long-term stability of the material at 37 °C from the results at 85 °C. Although the 85/85 test (1000 h at 85 °C and 85 % relative humidity) is used for testing polymer material (epoxy) in chip packaging (Minges 1989), temperatures above 60 °C are not recommended for accelerated shelf-life testing of polymers used in medical devices. Hemmerich stated that the life-time prediction methods based on the Arrhenius model become inaccurate at temperatures in excess of 60 °C, due to the large difference between the temperature during normal use and the elevated temperature while testing (Hemmerich 1998). This is consistent with the results presented in this work. While no changes in material behaviour could be observed at 37 °C and at 60 °C respectively, the deterioration of the material at 85 °C in PBS was drastic. But the behaviour at 85 °C does not necessarily give useful information about the long-term behaviour at 37 °C (Scheirs 2000), as demonstrated by the following example. The stress at 10 % strain of PI2611 is reduced by ¼ after 4.5 months in PBS at 85 °C. Applying the Hemmerich method (Hemmerich 1998), one can calculate the time duration needed to reach the same behaviour in specimens stored at 60 °C in PBS:

$$time_{el} = \frac{10 \cdot time_{at}}{Q_{10} \cdot (T_{el} - T_{at})}, \quad (7.2)$$

where  $time_{el}$  is the time duration of the test at the elevated temperature  $T_{el}$  and  $time_{at}$  is the time duration of the usage at the ambient temperature  $T_{at}$  (37 °C in the case of implanted materials). The reaction rate coefficient was found to be  $Q_{10}=2$  for medical polymers (Hemmerich 1998). That implies a doubling of the reaction rate for each 10 K. Based on the data of the specimens stored in PBS at 85 °C, the Hemmerich method predicts a decrease of ¼ of the initial stress value after a period of 22.5 months for specimens stored in PBS at 60 °C. As the results show (Fig. 7.4) the stress at 10 % strain at 60 °C did not decrease over 20 months but remained stable at the initial value. This indicates that at higher storage temperatures, degradation processes take place that do not develop at 37 °C or 60 °C. This becomes more clear when attempting to graph these values in an Arrhenius plot (Masterton 2008). The material stored at 37 °C, 60 °C, and at reference conditions, did not change over time, thus the reaction rate is zero for all three temperatures. The reaction rate of the material stored at 85 °C in PBS is 17 MPa/month (PI2611, stress at 10 % strain). Drawing an Arrhenius plot with these values does not result in a linear relationship of temperature and reaction rate. Hence, the values found at 85 °C are not linked to the values at 37 °C by the Arrhenius equation, which in turn indicates that

findings gathered from testing PIs at temperatures greater than 60 °C are not necessarily able to predict the long-term behaviour of these materials at 37 °C.

When testing the PI layers for defects, some holes first occurred at a higher voltage applied between the underlying gold layer and the Ringer's solution covering the PI. From the values given in Tab. 7.1, the defect densities at 2 V were 0.01 cm<sup>-2</sup> (Pyralin PI2611), 0.01 cm<sup>-2</sup> (U-Varnish-S) and 0.03 cm<sup>-2</sup> (Durimide 7510). At 30 V, the defect densities were 0.03 cm<sup>-2</sup>, 0.17 cm<sup>-2</sup>, and 0.13 cm<sup>-2</sup>, respectively. The delamination is also due to defects. Liquid enters through a defect and electrolysis starts at the gold surface. Instead of escaping through a pinhole the gas is caught under the PI layer and separates the two layers. Because of the small number of wafers, the defect densities resulting from the measurements give no usable value to compare the different materials. No statistics can be employed to find out whether the differences in defect density are due to material properties or to the cleanroom processing of the layers. Examining the holes under the microscope leads to the impression that they are due to particle inclusion and air bubbles which are embedded in the precursor while processing. This emphasizes the need for a particle free environment while processing. Compared to Pattee who did not produce the thin films under cleanroom conditions, the defect density of the thin films produced in this work could be minimized to less than 0.2 cm<sup>-2</sup> which is a factor of 4.5 times better (Pattee 1988).

## 8 ECoG-Electrode Array

As described in chapters 2.1 and 3.2, the brain is anatomically and functionally organized into separated regions. However, several studies support the notion that brain regions interact during information processing (Engel 2001; Mesulam 1998; Varela 2001). Thus, one of the major goals in neuroscience research is to determine the mechanisms that are responsible for neuronal interaction between several neuronal populations (Fries 2005). An interesting brain signal in the study of neuronal communication over large areas in the brain is the LFP (see chapter 4.1). Several studies showed that significant LFP modulations are related to sensory processing, motor planning, visuomotor interactions and higher cognitive functions such as attention, memory and decision making (Henrie 2005; Kreiman 2006; Liu 2006; Pesaran 2002; Pesaran 2008; Scherberger 2005; Womelsdorf 2006). Thus, using techniques that are able to record LFP signals from large parts of the brain might help to understand the underlying mechanisms that allow neuronal population interaction.

*Tab. 8.1. Dimensions and number of electrodes of different ECoG arrays used in research and clinical practice*

Manufacturer	Electrode Diameter in $\mu\text{m}$	Electrode Pitch (centre to centre) in $\mu\text{m}$	Conductor Path Pitch (centre to centre) in $\mu\text{m}$	Number of Electrodes	Area of the Array in $\text{mm}^2$
Ad-Tech	2300	5000	Wire diameter: 70 Insulation layer: 20	64	80 x 80
(Tsytarev 2006)	50	100	100	64	0.8 x 0.8
(Takahashi 2003)	80 x 80 (square)	225	50	69	2 x 2
(Molina-Luna 2007)	100	640/750	35	72	6.1 x 4.6
(Kitzmler 2006)	200 x 200 (square)	400	Bonding wires	16	1.4 x 1.4
This work	1000	2000/3000	30	252	35 x 60

For that purpose, a micromachined ECoG-electrode array which contains 252 electrode sites to cover large expanses of the cortex of a macaque's cortex was developed in this work<sup>2</sup>. Electrode arrays made for recording electrocorticograms are already widely used in research as well as in clinical therapy. Besides understanding fundamental brain functions, scientists are interested in how brain signals can be used in therapy to treat neurological disorders such as paralysis by using brain-machine interfaces (Hochberg 2006; Rickert 2005). In clinical practice, ECoG-electrode arrays are implanted onto the cortex to locate

<sup>2</sup> Main parts of this chapter have been published as Rubehn B\*, Bosman C, Oostenveld R, Fries P, and Stieglitz T. A MEMS-Based Flexible Multichannel ECoG-Electrode Array. *J Neural Eng.* 2009; 6(3): 036003

\* Processing, assembly, characterization, major parts of the design and writing

the seizure focus during the pre-surgical diagnosis of epilepsy (Nair 2008; Schramm 2008). While in clinical practice commercially available arrays (Ad-Tech Medical Instrument Corporation, Racine, WI, USA) with electrode diameters and electrode pitches in the millimetre scale are used, researchers in medicine and engineering try to scale down the dimensions to micrometre size. This in order to obtain a higher spatial resolution of brain signals from the cortex, which can be realized by using MEMS technology. In the last years, numerous groups presented precision engineered or MEMS-based electrode arrays (chapters 4.2.3 and 4.2.4). Most of these arrays have electrodes distributed over a small area with a small electrode pitch. Therewith, a high spatial resolution is obtained but the cortex region from which measurements can be taken is limited to the small array area (Kitzmilller 2006; Takahashi 2003; Tsytarev 2006). If recordings over larger areas of the brain are needed, most micromachined arrays fail because they only cover a small brain area. In small animals, a micromachined electrode array can cover a rat's motor cortex (Molina-Luna 2007) but cannot be used for larger cortex areas.

The array manufactured in this work has the electrodes equally distributed on a highly flexible substrate, which fits onto the cortex surface of a macaque's brain hemisphere. The electrode positioning is shown on a brain model made of MRI data (Fig. 8.1). Every dot represents a single electrode site. The main sulci are highlighted with lines.

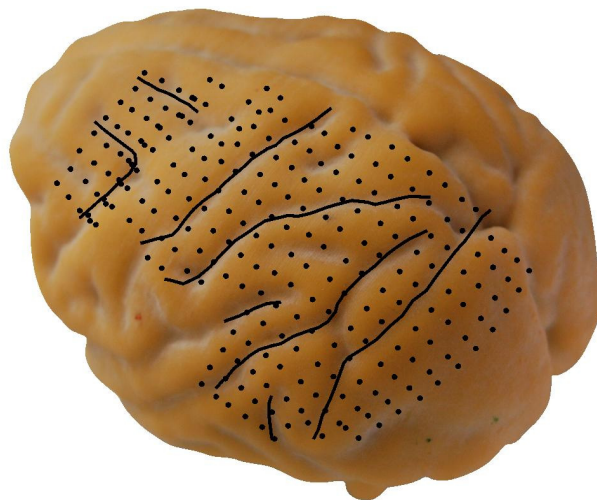


*Fig. 8.1. Three-dimensional plastic model of the macaque brain made by using MRI data (anterior left, posterior right). The main sulci are highlighted with lines. The dots represent the position of every single electrode site of the array.*

MEMS-technology was used not to produce very small electrodes sites with narrow electrode spacing but to arrange the large number of electrode sites, their cables and connectors on a flexible foil with reasonable dimensions to provide an electrode array which can be chronically implanted. While the electrode array covers an area of approximately 60 mm by 35 mm, the connector paths have to concentrate in a narrow ribbon cable which can be led through a small opening in the skull. Fig. 8.2 shows a schematic diagram of the position of the foil on the cortex and the connectors on the skull while the latter is opened during implantation.

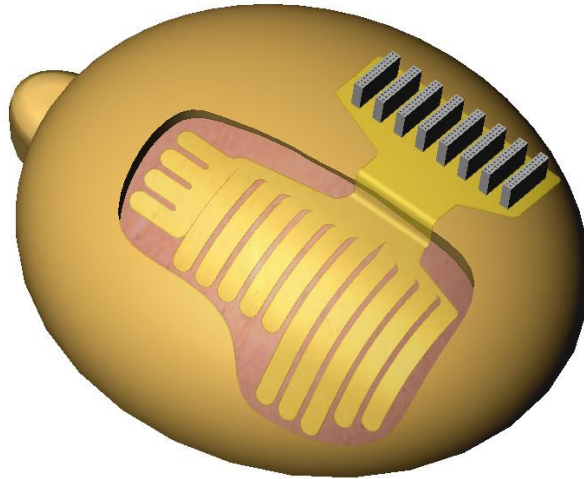


*Fig. 8.2. Schematic diagram of the flexible foil and its position. The head is facing to the left, the skull over the left hemisphere is opened and the PI foil is placed on the cortex while the connector part is fixed on the outside of the skull.*

To circumvent a rigid assembly as discussed in chapter 4.2.5, both the array and the cable are processed on wafer level as one device. Connectors are directly soldered to the thin cable after the lead-through to minimize space requirements of the assembly. With this setup only the flexible thin film array and cable are implanted whereas the larger connector part is fixed on the outside of the skull where it can be connected to a recording system. Even though the process of fabricating the PI foil is already presented elsewhere (Boppart 1992; Shamma-Donoghue 1982; Stieglitz 2000), this design and assembly introduces a new application for fundamental neuroscience and brain-computer interface related studies.

## 8.1 Material and Methods

### 8.1.1 Implant Layout

The physiological requirements led to a layout of the ECoG-electrode array where 252 electrodes were distributed over 14 fingers (Fig. 8.3, right). The fingers were designed to fit exactly the brain cortical surface of a macaque monkey. Their design allows the adaption of the array to the cortex's curvature and to facilitate the implantation procedure by placing every finger individually. The conductor paths merged in 11 ribbon cables, which were mechanically separated from each other to enhance flexibility (Fig. 8.3, middle). The electrodes have a diameter of 1 mm with electrode pitches of 2 mm, 2.5 mm, and 3 mm respectively. The connector paths have a width of 15  $\mu\text{m}$  and a pitch of 30  $\mu\text{m}$ , thus, MEMS-technology is necessary to process and to integrate the high number of connector paths into the electrode array foil.

The connector paths ended in solder pads to which 8 Omnetics connectors (NPD series, Omnetics Connector Corp., Minneapolis, MN, USA) can be soldered by through-hole-technology. To prevent the foil from tearing, the perimeters were designed to reduce mechanical stress at the notches (Fig. 8.3, a, b).

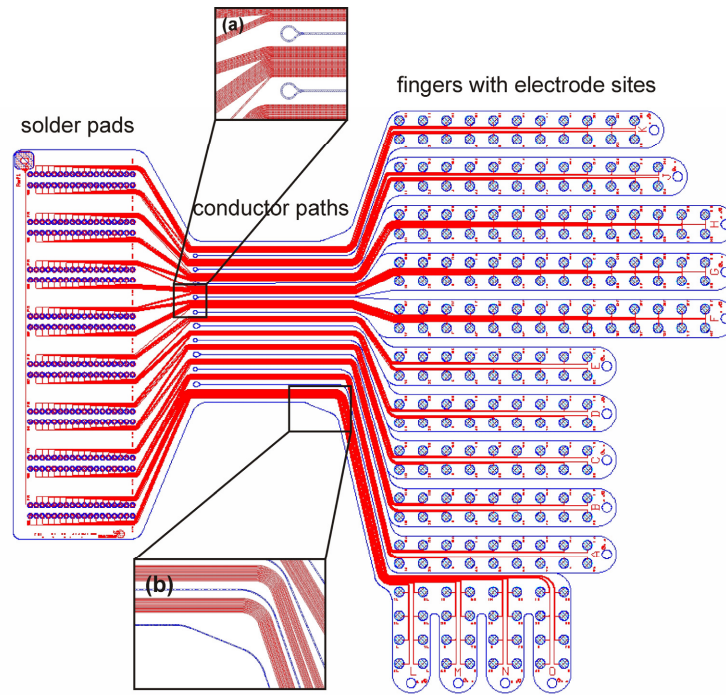


Fig. 8.3. Layout of the ECoG-array with 252 electrodes on 11 fingers (right), the ribbon cable (middle) and solder pads (left).

The substrate of the electrode array had to consist of a thin and flexible foil, which could adapt to the cortex's curvature. For this reason PI was chosen as the substrate material. It was processed as a 10  $\mu\text{m}$  thick foil on wafer level using standard micromachining tools and processes. Apart from being thin and flexible, PI is mechanically strong so that a 10  $\mu\text{m}$  thick foil can be handled and implanted without breaking.

### 8.1.2 MEMS Processing

The electrode array was made by cleanroom processing. After cleaning a 4" wafer with hydrofluoric acid for 15 s, the PI U-Varnish-S (UBE, Tokyo, Japan) was spin coated at 3000 rpm for 30 s. To evaporate the solvent, the wafer was put on a hotplate for 3 min at 120  $^{\circ}\text{C}$ . Subsequently, the PI was cured under nitrogen atmosphere at 450  $^{\circ}\text{C}$  for 10 min (furnace: YES-459PB6-2PE-CP, Yield Engineering Systems Inc., San Jose, CA, USA) resulting in a 5  $\mu\text{m}$  thick layer (Fig. 8.4a). Hexamethyldisiloxane (HMDS) was used as an adhesion promoter for the photoresist ma-N 1420 (Micro Resist Technology GmbH, Berlin, Germany) which was spin coated at 2700 rpm for 30 s. The 2.1  $\mu\text{m}$  thick layer of photoresist was structured by exposing it to UV light (mask aligner: MA6, Süss MicroTec AG, Garching, Germany) through a chromium mask. After the development (development solution: ma-D 533S, Micro Resist Technology GmbH, Berlin, Germany) the photoresist-free parts of the wafer defined the metal areas of the array. To improve the adhesion of the metal layer to the PI, the wafer was etched in an oxygen plasma (80 W, 30 mTorr; RIE Multiplex, STS, Newport, UK) for 30 s. Subsequently, a 300 nm layer of platinum was sputtered on the wafer (300 W, 7.5 min; Univex 500, Oerlikon Leybold Vacuum GmbH, Cologne, Germany). A lift-off step (immersion in acetone for 3 h including a 30 min ultrasonic treatment) removed the photoresist and the platinum on top of it.



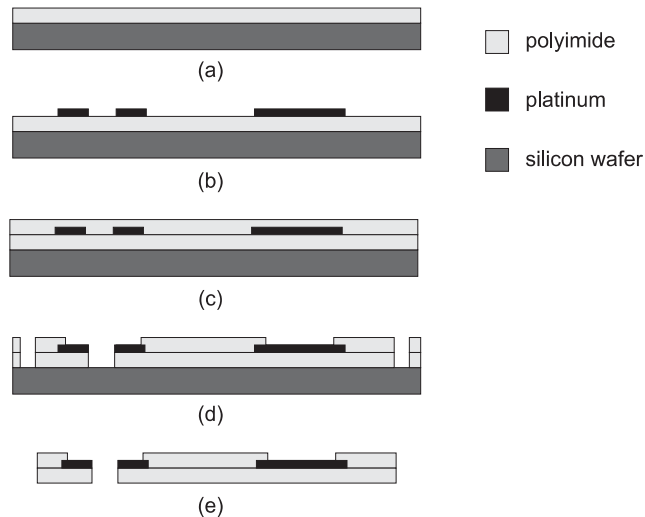


*Fig. 8.4. Process steps of the electrode array foil: (a) PI is spin coated on the wafer, (b) platinum is sputtered and structured, (c) second layer of PI, (d) dry etching of electrode openings, solder pads and perimeters, (e) detaching the foil from the wafer*

The platinum, which was directly sputtered onto the PI surface remained on the wafer and formed the electrodes sites and the conductor paths (Fig. 8.4b). After activating the PI surface in the oxygen plasma, a second layer of PI was spin coated and cured (Fig. 8.4c). Two layers of the photoresist AZ9260 (MicroChemicals GmbH, Ulm, Germany) were spin coated at 1600 rpm for 30 s to form a layer of 28  $\mu\text{m}$ . The photoresist was exposed and developed (AZ400K, MicroChemicals GmbH, Ulm, Germany). It protected the underlying PI in the following etching step from the oxygen plasma (200 W for 10 min and 100 W for 25 min, 30 mTorr; RIE Multiplex). This etching step opened the electrodes and solder pads, and it defined the array perimeter by etching both PI layers down to the silicon wafer (Fig. 8.4d). After stripping the photoresist with acetone, tweezers were used to pull the device off the wafer (Fig. 8.4e).

### 8.1.3 Assembly and Packaging

A custom-made soldering jig was developed to hold the PI foil and the connectors in place while soldering (Fig. 8.6). The base plate of the jig contained eight slots in which the connectors were inserted (Fig. 8.5b). A tapped through hole was located in the bottom of every slot, in which a bolt was placed. The foil was released from the wafer and put on the base plate. After aligning the foil to the underlying connectors, the latter were lifted by turning the bolts until the connector pins passed through the openings in the foil. A cover plate was mounted to the base plate to fixate the foil and shield it from solder and particles in the following soldering step. Soldering paste (SnBi, with 58 wt% Bi; LFM-65X A75C, Almit GmbH, Michelstadt, Germany) was dispensed with a dispenser (DX-200, OKI International GmbH, Hochheim, Germany) through a dispensing tip with an inner diameter of 250  $\mu\text{m}$  (blunt end stainless steel tips: I&J FISNAR, Fair Lawn, NJ, USA). The paste was soldered with a soldering iron at 250  $^{\circ}\text{C}$  (Fig. 8.5c). After removing the flux by rinsing the connector pins with acetone and isopropanol, epoxy (UHU plus endfest 300, UHU GmbH, Bühl, Germany) was applied on the pins, the solder, the PI foil and the connector bodies

to fixate the components mechanically. After curing of the epoxy at room temperature for 24 hours, the electrode array was released from the soldering jig.

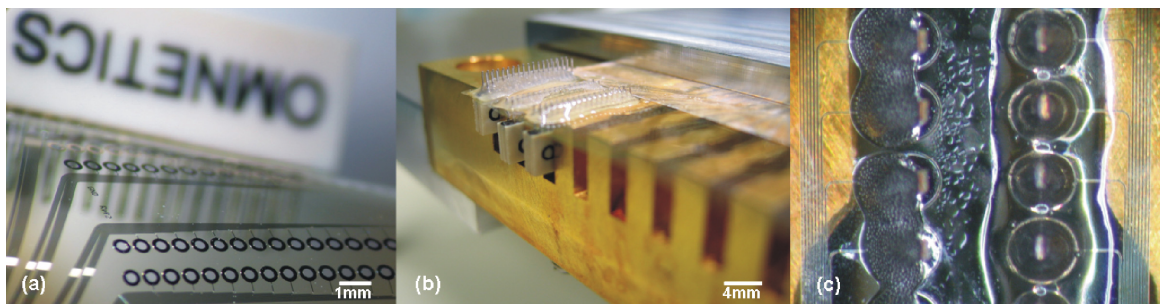


*Fig. 8.5. Soldering procedure of the omnetics connectors into the PI foil: (a) soldering pads, (b) base plate of the alignment tool, (c) connector pins with dispensed soldering paste (left) and after soldering (right)*

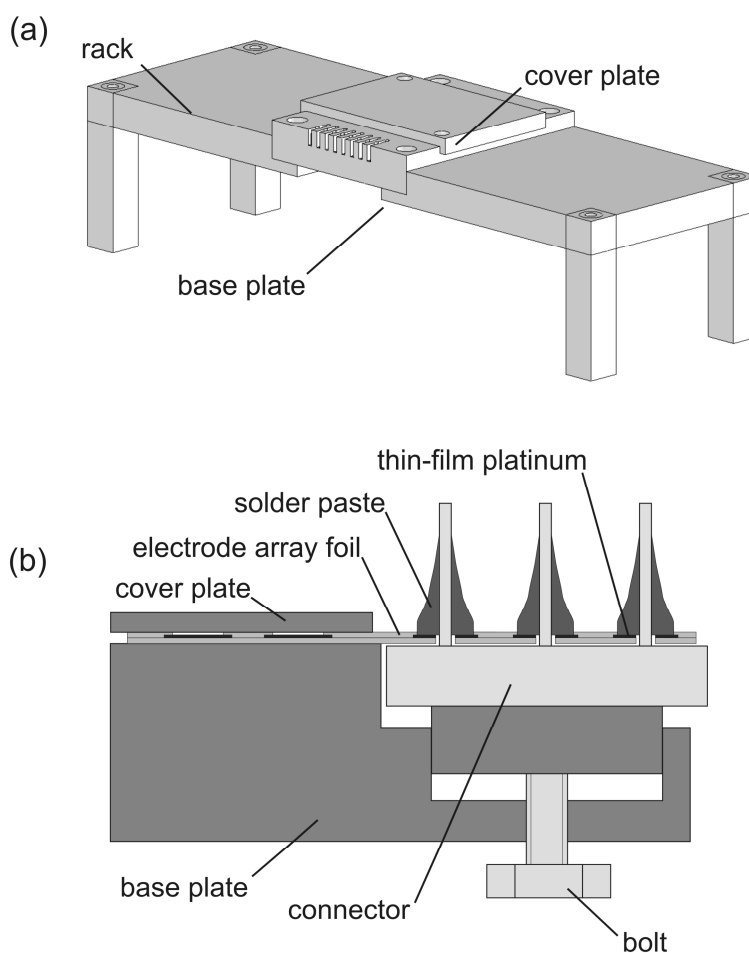


*Fig. 8.6. (a) the complete soldering jig, (b) a cross-sectional view of a slot with the foil and a connector in place while soldering*

### 8.1.4 Electrode Characterization

To verify the functionality of the ECoG-array, every electrode contact was characterized by electrochemical impedance spectroscopy with an impedance analyzer (Solartron 1260 and 1287, Solartron Analytical, Farnborough, UK). A three-electrode setup with a platinum

counter electrode and a silver/silver chloride reference electrode with 3M KCl bridging electrolyte was used in Ringer's solution at room temperature. With a measuring amplitude of 10 mV the impedance spectrum of the whole assembly was obtained between 1 Hz and 100 kHz, taking one measurement per decade. Impedance magnitude and phase were displayed in Bode plots.

The resistance of the conductor paths was extracted by contacting electrodes and solder pads with a needle prober, connected to a resistance meter (Multimeter 34401A, Agilent Technologies, Santa Clara, CA, USA).

The impedance between two neighbouring connector paths with a separation distance of 15  $\mu\text{m}$  over a length of 40 mm was measured. The connector paths were immersed in 0.9 % saline solution while the electrode sites were kept dry. The impedance spectrum was measured by electrical impedance spectroscopy with the impedance analyzer Solartron 1260 by applying a sine wave of 3 V amplitude, sweeping the frequencies from 1 Hz to 10 MHz. Additionally, the high-ohmic resistance between these two connector paths was measured with an electrometer (Keithley 6517A, Keithley Instruments Inc., Cleveland, OH, USA) by applying a DC voltage of -5 V to 15 V, measuring the current and calculating the resistance with a linear regression.

### 8.1.5 Implantation

The implantation and recording procedure was conducted at the Donders Institute for Brain, Cognition and Behaviour (Radboud University Nijmegen, Nijmegen, The Netherlands) by Pascal Fries and Conrado Bosman. All the surgical procedures reported here, were approved by the animal ethical committee of the Radboud University Nijmegen (Dier Experimenten Commissie van de Radboud Universiteit, Nijmegen, RU DEC 2004 151). Two adult male Rhesus monkeys (*Macaca Mulatta*) were trained to fix their eyes on a fixation point, located at the centre of a computer monitor at 49 cm distance from the head. After fixing the central point, visual stimuli appeared. Stimuli were 4° diameter sinusoidal gratings (0.4-0.8 cycles/degree) drifting unidirectionally within a circular aperture, located at approximately 4° eccentricity. One of the gratings was cued to be the target stimulus, and the monkeys' task was to detect a small change in the orientation of the target grating to obtain reward. After reliable performance of the task, the monkeys were subdurally implanted with the electrode array. Under general anaesthesia, a 6.5 cm by 4 cm craniotomy was performed using an Electric Pen Drive Neurospine 90.000K (Synthes-Stratec, Solothurn, Switzerland) to expose the complete left hemisphere. The autoclaved (15 min at 134 °C and 2 bar) electrode array was placed subdurally over the left hemisphere. The boneflap was placed back and attached to the rest of the skull with calcium phosphate bone substitute and covered with dental acrylic.

### 8.1.6 Recordings

Recordings were started 3 weeks after the surgery. The signals from the 252 electrodes were amplified with a gain of 20 by a headstage amplifier (Headstage 32V-G20, Plexon Inc., Dallas, TX, USA), low-pass filtered at 8 kHz and digitized at 32 kHz sampling fre-

quency (Digital Lynx, 256 channels, Neuralynx Tucson, AZ, USA). Using the Fieldtrip toolbox (<http://www.ru.nl/neuroimaging/fieldtrip/>) for Matlab (The MathWorks, Inc. Natick, MA, USA), the data was preprocessed and analyzed off line. LFP activity was obtained by low pass filtering at 200 Hz and downsampling to 1 kHz. To characterize the quality of the recorded signals, a time locked analysis and a power spectral analysis were performed. The time locked analysis was performed over data epochs containing 35 consecutive stimulus presentations. Epochs were subsequently averaged over time. Power spectral estimation was calculated for each channel over 20 successive epochs of 3 s length. Each epoch was tapered using discrete prolate spheroidal sequences (Slepian functions) (Jarvis 2001). Spectral power was then computed as an average across epochs and tapers. This multi taper method was used to optimize spectral concentration. In this analysis, tapering yielded a spectral concentration of  $\pm 1$  Hz. around each centre frequency.

## 8.2 Results

### 8.2.1 In Vitro

The electrode array was successfully processed and assembled (Fig. 8.7). The soldering of the Omnetics connectors to the PI foil led to a 99.5 % yield of properly connected, functional electrodes in three assembled devices. The fixation of the soldered connections by epoxy made the array a robust device that could be handled easily during characterization and surgery.

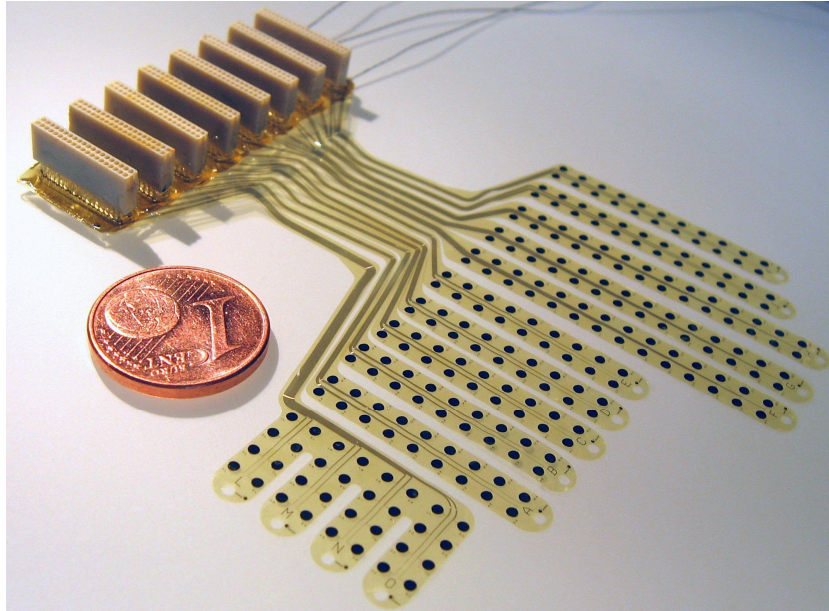


*Fig. 8.7. Fully assembled electrode array; the diameter of the coin is 16 mm.*

No damage of the array was observed during assembly, measurements or implantation. The connector part of the array attached on the outside of the skull fit into a volume of 42 mm by 20 mm by 10 mm. The electrochemical impedance spectrograms of all 252 electrodes located on one electrode array are shown in Fig. 8.8. Every grey curve represents the measurement data of one electrode site. The average value of all electrodes is

the black curve. The magnitude of the electrode impedances varied from 1.5 k $\Omega$  to 5 k $\Omega$  at 1 kHz. The resistances of the connector paths varied from 1 k $\Omega$  to 2 k $\Omega$  depending on the different connector paths' length. The cutoff frequency at which the impedance turned from a predominantly capacitive into a resistive behaviour was at 300 Hz. The impedance spectrogram of the electrode-electrolyte interface could be modelled with a basic electrical circuit model: an ohmic resistance parallel to a capacitor and both in series to a second ohmic resistance (Fig. 4.2). Fitting this model to the measured data of an exemplary electrode (software: Zview 2.8, Scribner Associates Inc., Southern Pines, NC, USA) resulted in  $R_F=143$  k $\Omega$ ,  $C_H=377$  nF and  $R_{ac}=1.7$  k $\Omega$ , where  $R_{ac}$  was the access resistance to the electrode surface. This access resistance consisted of the resistance of the electrolyte as well as the resistance of the array's conductor paths.  $R_F$  and  $C_H$  represented the metal-electrolyte interface.

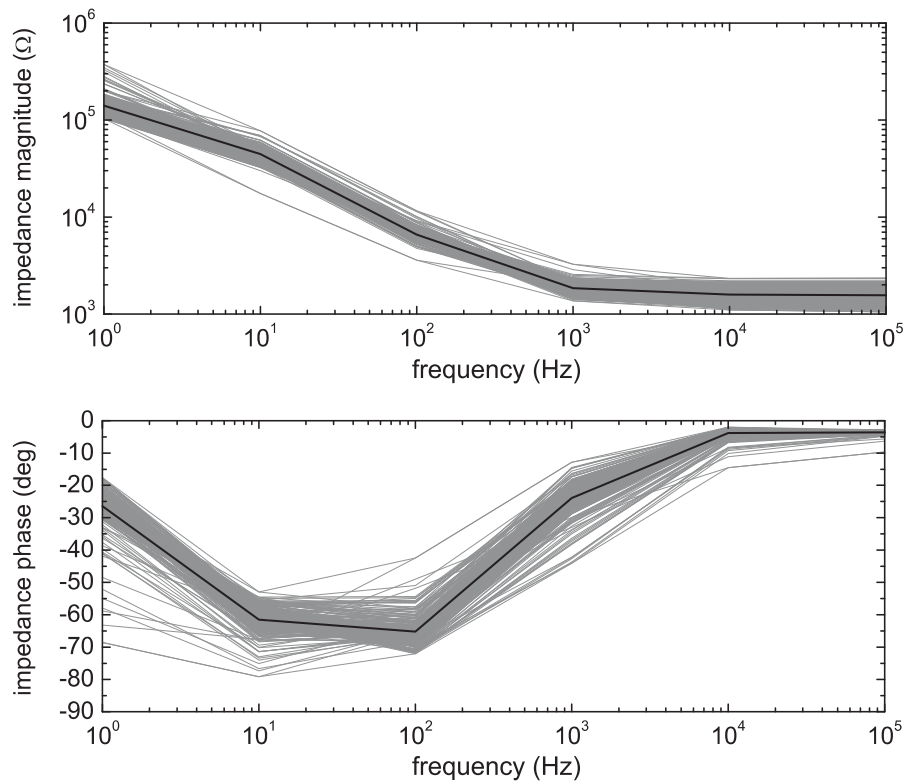


*Fig. 8.8. Impedance spectra of all 252 electrodes of the array; grey lines represent single electrodes, the black line is the average of all electrodes.*

The electrical impedance spectrum of the impedance between two neighbouring connector paths was measured and showed a purely capacitive behaviour (Fig. 8.9, dashed black line). The impedance was modelled as a capacitor in parallel to an ohmic resistance. With Zview 2.8, this model was fitted to the measured spectrum between 250 Hz and 1 MHz because the Solartron 1260 can only measure resistances up to 100 M $\Omega$ . This value was achieved at 250 Hz so that the resistance values at frequencies below 250 Hz were larger. This fitting resulted in a capacitance of 5.7 pF with the resistance of greater-than-or-equal 100 M $\Omega$ . The DC resistance between the two connector paths was determined with Keithley's electrometer and resulted in a resistance of 3.5 T $\Omega$  with the cable

immersed in saline solution. The simulation of the modelled impedance with 5.7 pF and 3.5 T $\Omega$  is shown in Fig. 8.9 (solid grey line).

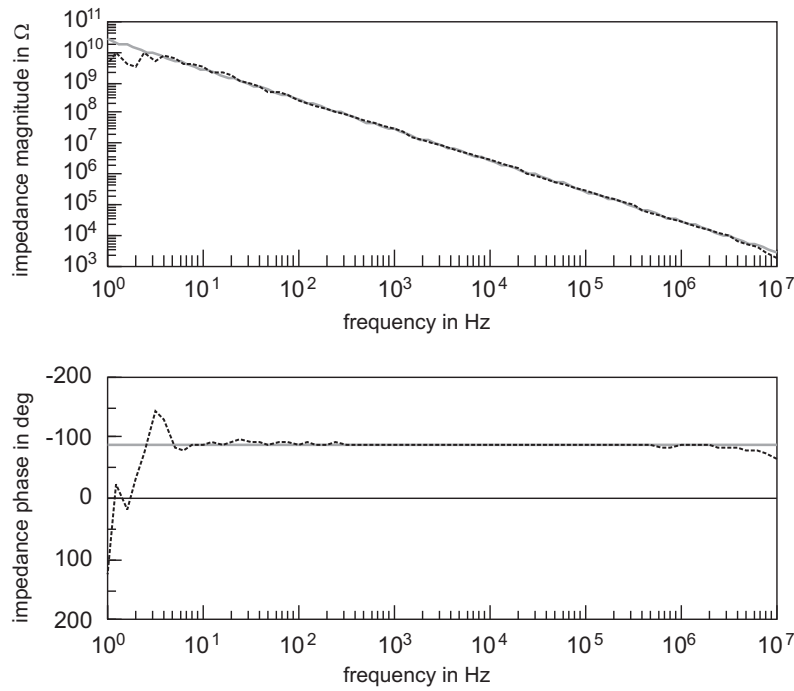


Fig. 8.9. The electrical impedance spectrum of two neighbouring connector paths (single measurement) with the cable immersed in saline solution while the electrodes were kept dry; the dashed line (black) shows the measurement and the solid line (grey) the simulation of a resistor (3.5 T $\Omega$ ) and a capacitance (5.7 pF) in parallel.

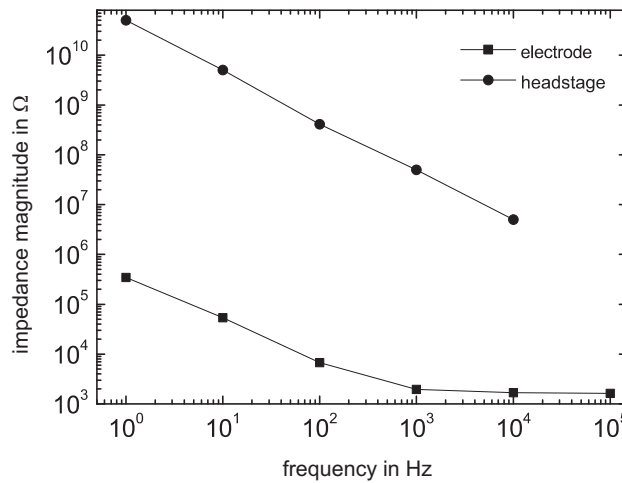


Fig. 8.10. The magnitude of impedance as function of frequency; the dots represent the input impedance of Plexon's headstage HST/32V-G20 (data provided by the manufacturer). The squares are the measured electrochemical impedance magnitude of the array's electrode with the highest impedance.

To obtain ECoG-signals with high amplitudes and low phase shifts during in vivo recordings, the input impedance of the headstage amplifier must be much higher than the electrode impedance.



Fig. 8.10 shows the impedance spectrum of Plexon's headstage HST/32V-G20 (circles) and of the electrode with the highest measured impedance of the array (squares). The smallest ratio is found at 10 kHz where the input impedance is 1000 times higher than the electrode impedance.

### 8.2.2 In Vivo

LFP signals were recorded from all electrodes while the monkey was awake and performing the visual task described in paragraph 8.1.5. Fig. 8.11a shows an example of 3 s of LFP activity observed from 12 out of the 252 channels distributed over the cortex. The exact position within the array is shown in the layout in Fig. 8.11b. Every dot stands for an electrode site. Bold dots in black represent the displayed electrodes in Fig. 8.11a. Channels number 1 to 12 are counted from anterior to posterior. Standard electrocorticographic signals were obtained from all electrodes. Fig. 8.11c shows the power spectrum of all 252 electrodes for a 3 s epoch. Grey lines represent single electrodes whereas the black line shows the average power spectrum of all electrodes. The figure shows the two expected physiological peaks of power at low frequencies. The first peak, centred at 3 Hz, corresponds to delta theta activity, the second one, centred at 18 Hz, represents the beta band. In Fig. 8.12 and Fig. 8.13, signals are plotted across the implantation time to evaluate the long-term performance of the electrodes.

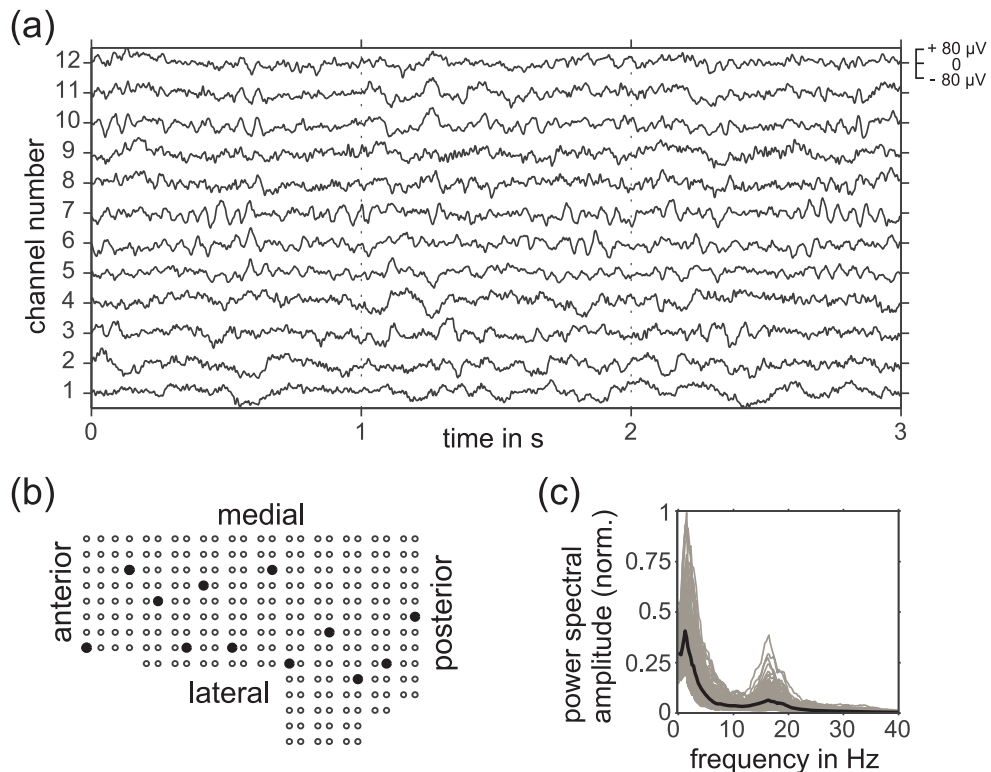
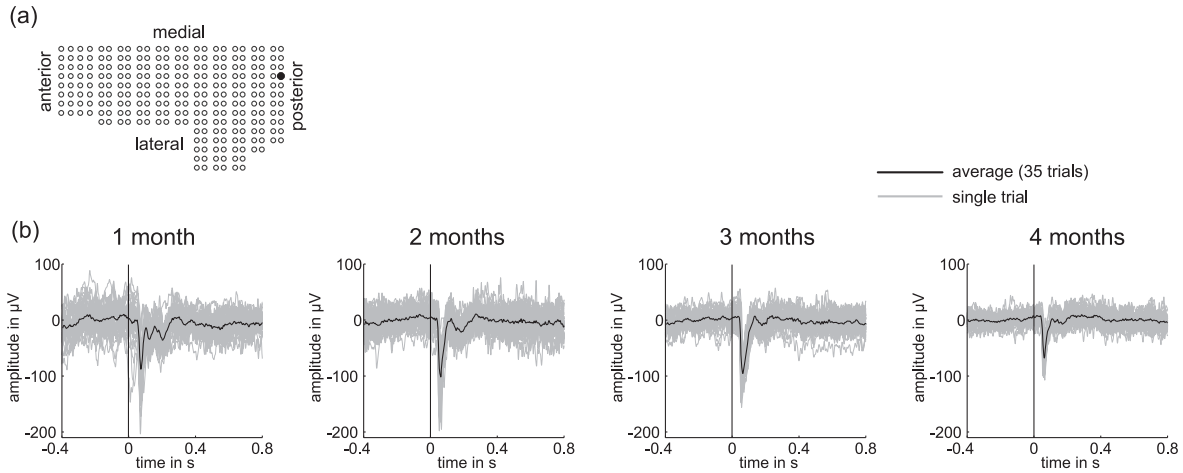


Fig. 8.11. (a) Example of 3 s of local field potential (LFP) activity observed in 12 of the 252 channels of the ECoG-electrode array. LFPs were recorded in an awake monkey during the performance of a visual task. (b) Layout of the ECoG-electrode array; bold black dots show the electrodes chosen for displaying in (a) (from anterior to posterior, channel number 1 to 12). (c) The power spectrum (fourier multitaper estimation, 3 s window length, 5 tapers) of 252 channels is plotted in grey, the average value in black.



**Fig. 8.12.** (a) The bold dot on the electrode array layout shows the selected channel. (b) Comparison between average and single trials of stimulus locked LFPs after implantation surgery. Time 0 s in each graph represents the onset of the stimulus ( $4^\circ$  sinusoidal grating). The grey lines represent 35 single trials. The black line shows the average over the 35 trials. The sessions were recorded after 1, 2, 3 and 4 months after implantation surgery.

In Fig. 8.12b, time 0 s in each graph is the onset of the visual stimulus. The response to a stimulus was measured with the same electrode (highlighted in Fig. 8.12a) 1, 2, 3 and 4 months after implantation. The black line shows the time-locked average over 35 trials from the same measurement session whereas the grey lines represent the 35 single trials. In the signals of all electrodes, two physiological relevant frequency bands could be found as peaks in the power spectrum (Fig. 8.11c). The power of the delta-theta (2 Hz-8 Hz), beta (15 Hz-25 Hz) and in addition alpha band (8 Hz-13 Hz) was calculated for a 3 s epoch in each measurement session and plotted over implantation time (Fig. 8.13a). Every grey line represents the power of one single electrode. The mean value of 252 electrodes with the standard deviation is depicted in black. The power of the three frequency bands remained stable over time. To evaluate the quality of visual evoked potentials over time, the maximum signal amplitude of an evoked potential (Fig. 8.13b, squares) and the noise (Fig. 8.13b, triangles) were calculated from the signals of 46 electrodes located on the visual cortex area V1 (Fig. 8.1, the first 4 columns of electrodes counted from posterior).

Due to the fact that not all cortex areas respond with an evoked potential to a visual stimulus, the noise of each electrode was calculated to obtain a measure of the performance of all electrodes. The dots (Fig. 8.13b) represent the mean of 252 electrodes with the standard deviation as error bars. The maximum signal amplitude was the maximum voltage in an interval of 50 ms to 100 ms after stimulus onset. As a measure of variance, the noise was defined as the standard deviation of the measured signal before stimulus onset. Both values were calculated from the data of a single trial. The mean of 35 trials obtained in one measurement session was calculated for each electrode. The values shown in Fig. 8.13b represent the mean and the standard deviation calculated from the values of 46 and 252 electrodes, respectively.



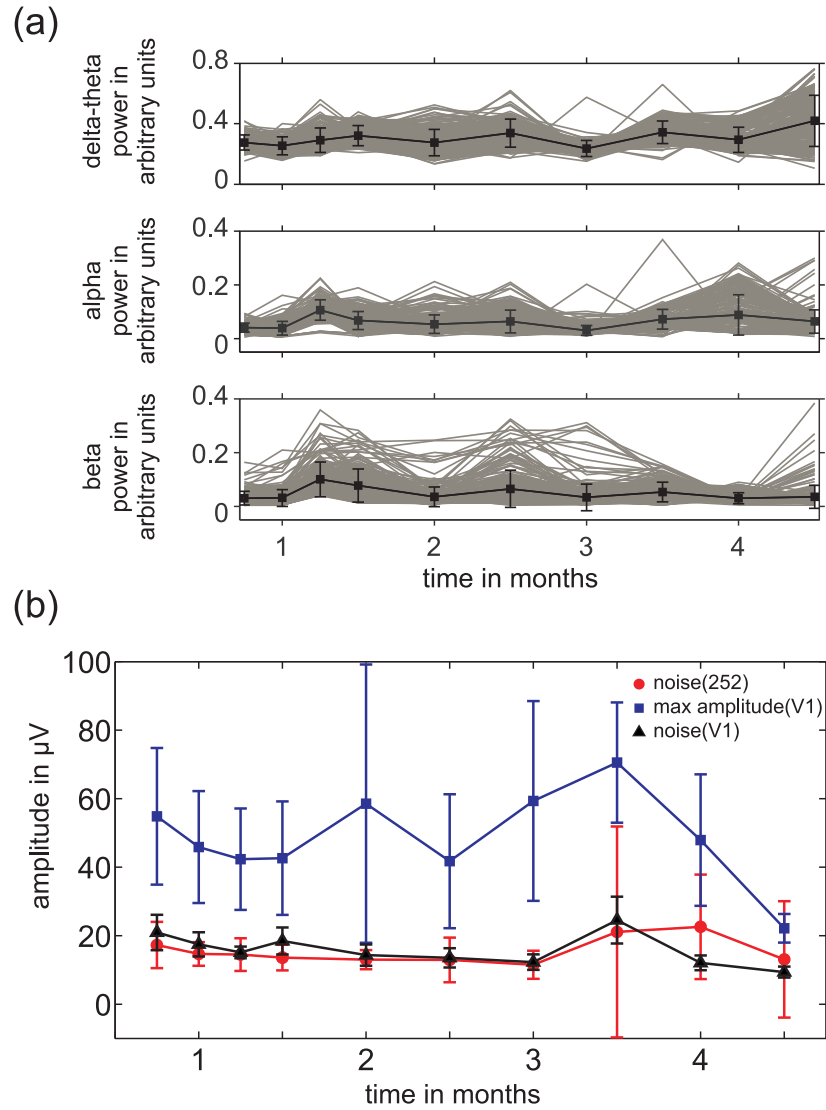


*Fig. 8.13. Signal stability over time: (a) The development of the beta (15 Hz-25 Hz), alpha (8 Hz-13 Hz), and delta-theta (2 Hz-8 Hz) band power over implantation time. Grey lines represent the 252 single electrode signals, the mean value of all electrodes with standard deviation is depicted in black. (b) Squares show the maximum signal amplitude of a visual evoked potential, the triangles show the noise before stimulus onset. Both graphs display the mean value and the standard deviation of 46 electrodes located on the visual cortex area V1. The dots represent the noise before stimulus onset of all electrodes. The mean value of 252 electrodes with standard deviation is depicted.*

The values were recorded in ten measurement sessions 0.75 months to 4.5 months after implantation surgery. While the maximum signal amplitude (solid) was changing due to varied stimulation parameters in different sessions (In the sessions at 2, 2.5, and 4.5 months, the stimulation parameters differed from the parameters in the other sessions.), the noise remained stable over time.

### 8.3 Discussion

The presented wafer-level manufactured ECoG-electrode array combines a large number of electrodes distributed over a relatively large area with integrated micromachined cables.

This reduced the assembly process to the soldering of the connectors to the array. In contrast to Huang et al. who connected a parylene-based micromachined ribbon cable to an Omnetics connector by gluing it with conductive epoxy (Huang 2008), the soldering process is more robust, easier to apply and thus more suited for a high-channel connection. Due to this single assembly step, the implanted part of the device remains thin and flexible and consists only of the micromachined foil made of the biocompatible materials PI and platinum (Klinge 2001; Lago 2007b; Richardson Jr 1993; Stensaas 1978) without any assembled adapter parts. The connector part of the array, containing the solder and the epoxy that were not tested for biocompatibility, was fixed on the outside of the skull. It was embedded in dental acrylic, thus, the solder and the epoxy were not in contact with the body. The connector part was made small enough to fit on a macaque monkey's head. By integrating the Omnetics connectors, the array can be directly connected to a neurophysiologic standard recording system (Headstage 32V-G20, Plexon Inc., Dallas, TX, USA).

The electrode diameter was chosen to minimize the impedance but still support the density of the electrode grid required to provide a high spatial resolution. In order to obtain a dense grid of electrodes over the cortex of a complete hemisphere, 2 mm as the minimum electrode pitch was chosen. This was limiting the electrode to 1 mm. In comparison to commercially available electrode arrays used in clinical diagnosis (e.g. Ad-Tech Medical Instrument Corporation, Racine, WI, USA) the impedance of our electrodes is higher. At 1 kHz we measured a minimum of 1.5 k $\Omega$  whereas the Ad-Tech grid electrodes had an impedance magnitude of about 400  $\Omega$  at 1 kHz (Henle 2008). However, the Ad-Tech grid had a larger electrode pitch (5 mm), an about 5 times larger electrode area (electrode diameter: 2.3 mm), a lower number of electrodes (64), and a thicker substrate material (2 mm). Therefore, it was not suitable for chronic high channel ECoG-measurements in animal neurophysiology. On the other hand, our electrode array combined a high number of electrodes with a thin foil substrate. Compared to other micromachined electrodes (5 k $\Omega$  to 10 k $\Omega$  (Molina-Luna 2007), 40 k $\Omega$  to 160 k $\Omega$  (Tsytsarev 2006) and 330 k $\Omega$  (Takahashi 2003), all at 1 kHz) our electrodes provided a lower impedance, which helped to measure high quality local field potential signals on the cortex (Fig. 8.12).

An impedance spectrum of two neighbouring connector paths was measured and fitted to a capacitance (5.7 pF) with a resistor (3.5 T $\Omega$ ) in parallel to it. These values show that the connector paths produce virtually no crosstalk when connected to biosignal amplifiers. These amplifiers have a maximum input impedance of some G $\Omega$  which is small compared to the impedance of the two neighbouring connector paths. This indicates that a neural signal measured on a neighbouring connector path is not originating from crosstalk inside the electrode array but from the conductivity of the biological tissue between the neighbouring electrode sites.

As discussed by Nelson (Nelson 2008), the ratio between the headstage's input impedance and the electrode impedance is crucial for an error-free recording of neural signals. The headstage impedance is at least three orders of magnitude higher than the electrode

impedance (Fig. 8.10). Thus, the ratio had no effect on the measured signal which was not attenuated or distorted in the range of interest.

Exemplary signals from 12 electrodes lying on different cortex areas showed normal ECoG characteristics (Fig. 8.11a). Furthermore, the power spectrum of each channel contained peaks at physiological frequency bands (theta band and beta band in Fig. 8.11c) whose power stayed stable over the implantation time (Fig. 8.13a). This indicated that all electrodes, while put on different cortex areas, had a good contact to the underlying tissue and thus were able to obtain neural signals during the course of 4.5 months.

So far, there was no decline in signal quality over time. Signals obtained from visual evoked potentials remained in the same order of magnitude and the noise did not change over months (Fig. 8.13b).

# 9 Transdural Shaft Electrodes

As shown in chapter 8, long-term stable LFP signals can be recorded by means of an epicortically implanted, micromachined thin-film electrode array. Signals from large parts of one cortical hemisphere could be obtained. After recording from the two-dimensional cortical surface, a next step in understanding the interaction between different brain regions during information processing would be to transfer the two-dimensional into a three-dimensional array and to record not only at the surface but within the brain tissue. An electrode shaft with a linear array of electrode sites can record at different depth when inserted into brain matter. If a number of such shaft electrodes is distributed over the cortex and inserted at the cortical areas of interest, a three-dimensional grid of electrode sites is obtained and LFPs can be recorded from different brain areas as well as different tissue depths. With the approach of inserting single shafts, the investigator is not dependent on a certain array layout to cover the areas of interest but can decide at short-term where to place the electrodes.

The single shaft electrodes that I will introduce in this chapter have a small, thin shank, enabling them to be inserted through very small holes (400  $\mu\text{m}$  in diameter) in the skull where the underlying dura mater is then penetrated. This approach is significantly less invasive than the surgery required for the implantation of the large epicortical ECoG-electrode array (chapter 8). It is anticipated that these small holes will close up more easily after surgery, minimising post-surgical complications. By using PI as the substrate material, shaft and cable are flexible and move with the brain matter, while the connector is attached to the surface of the skull. This should help to improve stability and quality of electrophysiological recordings.

However, as mentioned in chapters 4.2.2 and 4.2.4, shaft electrodes are supposed to have two contrary properties. First, they have to be stiff during insertion into brain tissue. Second, after insertion, they have to match the brain's modulus of elasticity in order not to damage the surrounding cortical tissue, while the implant's cable must not transfer force from the connector placed on the skull to the brain, which would cause relative motion between the device and the cortex. Thus the device has to be flexible so that the inserted part moves with the brain while the connector part is attached to the skull. This is especially challenging in the case of a flexible shaft electrode which has to penetrate not only cortical tissue but the tough dura mater. In this chapter an implant is presented which serves as a first step towards the three-dimensional electrode array setup described above, together with the development of a novel implantation technique.

## 9.1 Implant Design

### 9.1.1 Insertion Tool and Implantation Concept

To fulfil the contradicting requirements of stiffness during the insertion and flexibility during the course of a long-term implantation, a custom insertion tool was developed. While the

shaft itself is flexible, an insertion tool is used to penetrate the dura mater. The tool comprises a tungsten rod with a tapered tip and a diameter of 100  $\mu\text{m}$  and two tungsten rods with diameters of 50  $\mu\text{m}$  and blunt tips. The thicker rod is glued between the two thinner ones protruding beyond them as shown in Fig. 9.1. Tungsten was chosen as it is a standard electrode material in electrophysiology and tungsten rods are known to be stiff enough to penetrate the dura mater (Hubel 1957).

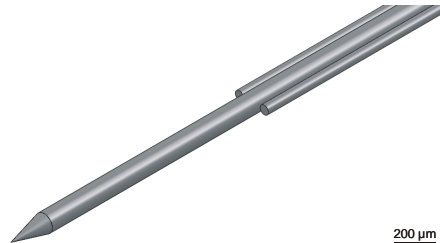


*Fig. 9.1. Schematic of the insertion tool comprising on tapered tungsten rod to penetrate the dura mater and cortical tissue and two blunt tungsten rods which are pushing the electrode into the tissue.*

For the implantation, the tapered rod slides into a U-shaped profile which is glued to the back of the shaft's tip (Fig. 9.2). The whole assembly is then inserted into the brain, with the tapered tip of the rod penetrating the dura mater while the two blunt rods bear against the back of the U-profile, pushing it through the hole in the dura mater and into the tissue. Since it is attached to the U-profile, the flexible shaft is inserted into the brain matter. After placing the shaft at the right position, the insertion tool is withdrawn leaving the PI shaft and the U-profile in the brain. The U-profile is made of SU-8 and has a relatively small cross-section of 270  $\mu\text{m}$  by 185  $\mu\text{m}$  and a length of 1 mm. With its cross-sectional dimensions, it is in the range of standard rod microelectrodes. With such electrodes, normal electrophysiology can be found even after many penetrations of the same cortical tissue.

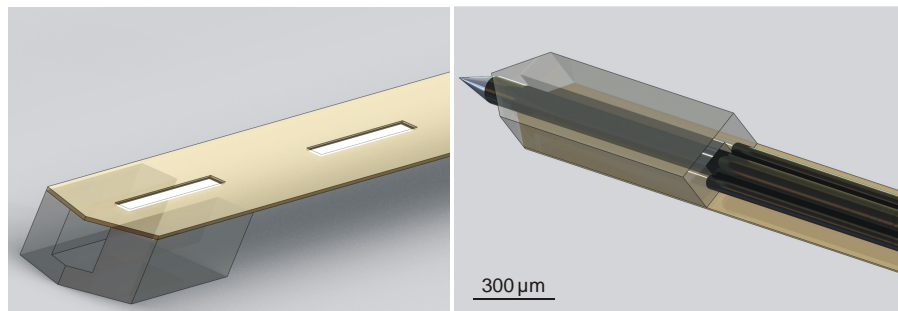


*Fig. 9.2. Schematic of the transdural shaft concept: an SU-8-based U-profile is glued to the backside of a PI-based shaft (left). An insertion tool comprising three tungsten rods is inserted to push the flexible electrode through the dura mater and the brain tissue (right).*

The here presented design has the advantage that only the U-profile has these dimensions and is stiff. The PI shaft directly behind the U-profile tip is very flexible and merges in a 75 mm long cable with a cross-section of 270  $\mu\text{m}$  by 10  $\mu\text{m}$  which mechanically decouples the shaft and the connector part helping the U-profile to float in the tissue. During insertion, the cortical tissue is pushed aside by the U profile passing and can then relax

due to the thin shaft following. Thus, it is anticipated that the implant will cause even less damage than standard rod microelectrodes.

### 9.1.2 Polyimide Shaft Electrode

The PI device consists of the implanted shaft as well as of an integrated cable and solder pads for the connector. The cable is about 75 mm long and has a cross-section of 270  $\mu\text{m}$  by 10  $\mu\text{m}$ . Thus, it mechanically decouples the shaft and the connector part. The cable is designed to be long enough to lead from the cortex through the drilled hole in the skull to contact a connector. For a chronic implantation, the connector can be stored in a recording chamber on the head between the recording sessions and can be taken out and connected to a recording system during recording. The connectors are soldered directly to the PI cable to provide a small and lightweight assembly.

The linear electrode array is placed on a shaft with a width of 370  $\mu\text{m}$  and consists of 8 rectangular electrode sites with an area of 100  $\mu\text{m}$  by 500  $\mu\text{m}$  and a pitch of 1 mm.

## 9.2 Manufacturing and Assembly

### 9.2.1 MEMS Processing of the Polyimide Shaft

The shaft was made of a 300 nm thick sputtered platinum layer, defining electrode sites, conductor paths and solder pads, sandwiched between two 5  $\mu\text{m}$  thick spin-coated PI foils (U-Varnish-S) as described in chapter 8.1.2.

### 9.2.2 MEMS Processing of the U-profile

The U-profiles were produced in a cleanroom with standard MEMS-technology equipment. A 100 nm thick  $\text{C}_4\text{F}_8$  passivation layer was deposited on a 4" polished silicon wafer using an ICP Multiplex (STS, Newport, UK). A first layer of SU 8 3025 (MicroChem Inc., Newton, MA, USA) was spin-coated at 4000 rpm for 30 s to obtain a 24  $\mu\text{m}$  thick layer. To evaporate the solvent, the wafer was heated on a hotplate at 65 °C for 3 min and at 95 °C for 6 min.

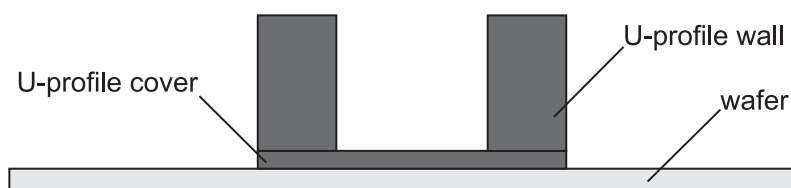


*Fig. 9.3. Schematic cross-section of the U-profile processing; the profile consists of two SU-8 layers forming the cover and the walls.*

To define the cover layer of the U-profile, the wafer was exposed to UV light with 160 mJ/cm<sup>2</sup> through a photolithography mask. After the post exposure bake (hotplate 65 °C for 3 min and 95 °C for 6 min), a second layer of SU-8 (SU-8 3050) was spin coated at 800 rpm obtaining a layer thickness of 160  $\mu\text{m}$ . Subsequently, the wafer was heated with a temperature profile ramping from room temperature to 65 °C with 2 K/min and holding at 65 °C for 15 min before ramping to 95 °C and holding it for 30 min. Both SU-8 layers

were exposed to UV light (270 mJ/cm<sup>2</sup>) in the mask aligner to define the U-profile walls. The following bake on the hotplate was conducted with the same profile which was used before exposure. The SU-8 structures were developed by immersing the wafer in mr-Dev 600 (micro resist technology GmbH, Berlin, Germany) for 15 min. To further cross-link the material, the wafer was baked at 200 °C for 5 min.

### 9.2.3 Assembly and Packaging

The U-profile was detached from the wafer by tweezers. With the tip of a needle, a small amount of epoxy glue (UHU endfest 300) was applied on the top side of the profile walls. The U-profile was attached to the rear side of the electrode shaft by tweezers. After aligning the SU-8 profile to the PI shaft, the device was put on a hotplate for 5 min at 70 °C. Due to the heat, the glue becomes less viscous and evenly fills the gap between the PI foil and the U-profile. In addition, the hotplate step increases the adhesion and accelerates the curing of the glue.

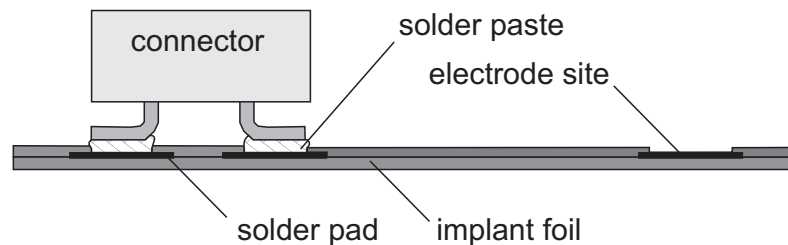


*Fig. 9.4. Direct connection of a PI shaft electrode and a SMD connector*

The electrical connection between the conductor paths on the shaft electrode and the neurophysiological recording system were made, as described in chapter 8.1.3, by directly soldering a connector to the solder pads on the PI foil (Fig. 9.4). While with the ECoG-electrode array, connector types for through-hole soldering was used, the transdural shaft was soldered to connectors of the SMD type. Solder paste (LFM-65X A75C) was dispensed on the solder pads and the connector pins were placed on the paste. Subsequently, the connector was soldered to the pads by heating the device to 250 °C on a hotplate for some seconds, contacting all pins simultaneously. After soldering, the devices were rinsed in acetone, isopropanol and DI-water to remove the flux residues. Subsequently, epoxy glue was applied between the connectors and the PI foil to mechanically secure the soldering sites.

### 9.2.4 Artificial Brain Model

To evaluate the insertion method, a brain phantom was made of an agar gel (1.8 wt% agar powder in water) simulating the cortical tissue, and was covered by a polyethylene (PE) foil which represented the meninges (standard household cling wrap with a thickness of 10-20 µm) (Haj Hosseini 2007).

### 9.2.5 Implantation and Recording

The implantation and recording procedure was carried out at the Ernst Strüngmann Institute in Cooperation with Max Planck Society (Frankfurt, Germany) by Pascal Fries and Chris Lewis. The experiment was conducted according to the guidelines of the Society for Neuroscience and the German law for the protection of animals, approved by the local government's ethical committee, and overseen by a veterinarian. In one cat, anaesthesia was induced with ketamine and maintained with a mixture of 70 % N<sub>2</sub>O, 30 % O<sub>2</sub> and halothane (0.4 %–0.6 %). The cat was paralyzed with pancuronium bromide applied intravenously (Pancuronium, Organon, 0.15 mg kg<sup>-1</sup> h<sup>-1</sup>). The right hemisphere was exposed by a trepanation over striate cortex (area 17). The insertion tool was mounted on a microdrive and the flexible shaft electrode was attached to it with sugar solution. The microdrive speed was manipulated by hand and the shaft was inserted perpendicular to the cortex to a depth of about 3 mm.

Signals were amplified by 10000 and band-pass filtered between 300 Hz and 3 kHz for MUA and between 1 Hz and 100 Hz for LFP. The signals were then sent to an analogue-to-digital converter and, after the detection of spikes, stored in computer memory.

## 9.3 Results

### 9.3.1 In Vitro

The shaft and U-profile were successfully assembled. The two parts could be accurately aligned and the glue could be applied without blocking the U-profile's channel. Fig. 9.5 shows the tip of an assembled shaft electrode. Although the hybrid assembly was chosen, it was easy to attach the U-profile to the shaft under a microscope by using tweezers.

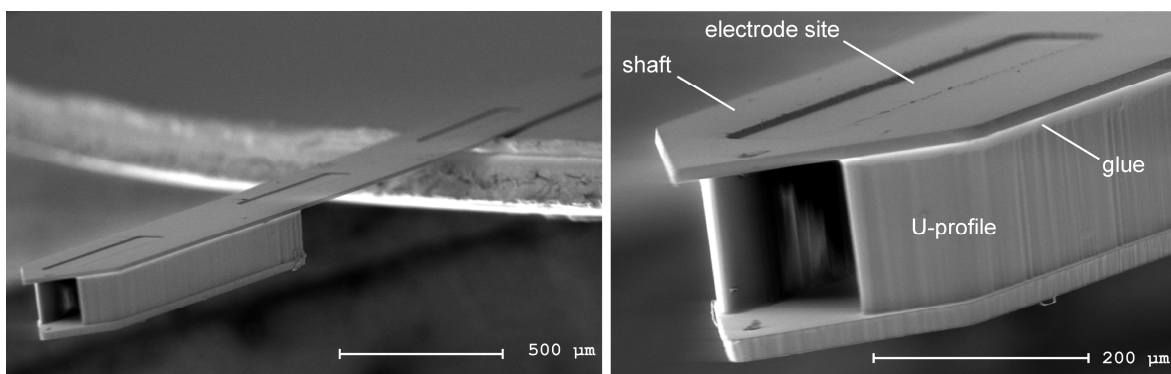


*Fig. 9.5. Scanning electron micrograph of an assembled shaft electrode (top); the close up of the tip shows the accurate alignment and epoxy application of the hybrid assembly (bottom).*

The impedance of the electrode sites were measured with electrical impedance spectroscopy as described in chapter 8.1.4. Fig. 9.6 depicts the impedance magnitude and phase over frequency for a device with 8 electrode sites with an area of 100 μm by 500 μm. The impedance at 1 kHz reaches from 70 kΩ to 115 kΩ and the cutoff frequency is about 3 kHz.



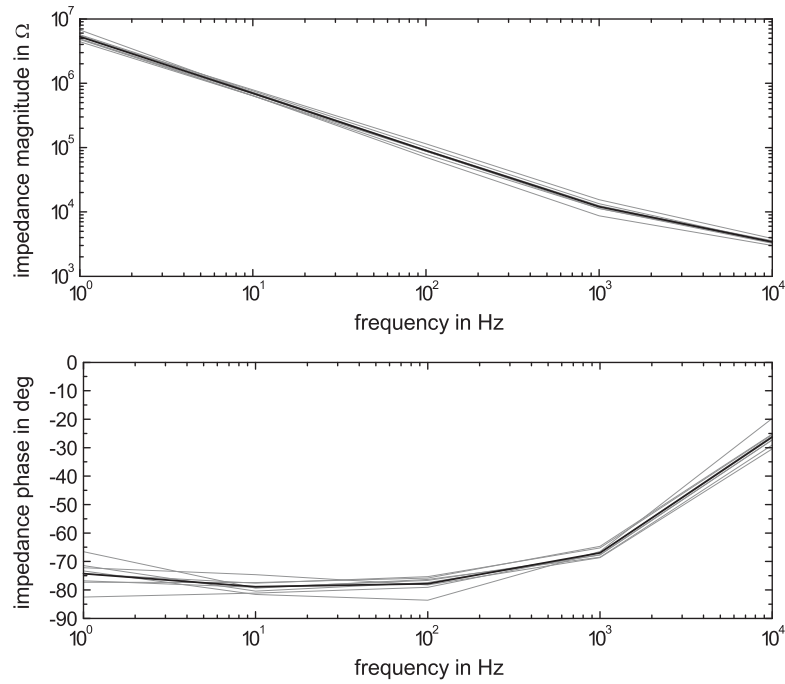


*Fig. 9.6. Electrical impedance spectroscopy of 8 electrode sites from one transdural shaft; the platinum sputtered electrode sites have an area of  $100\ \mu\text{m}$  by  $500\ \mu\text{m}$ . Single electrodes are in grey, the mean value of the 8 electrodes is depicted in black.*

#### *In Vitro Insertion Test*

The insertion tool was able to easily penetrate the PE foil of the artificial brain model and to insert the shaft at the desired depth of the gel (Fig. 9.7a). After carefully withdrawing the insertion tool, the shaft remained at its position in the gel (Fig. 9.7b). The procedure was successfully repeated 15 times to confirm the working principle.

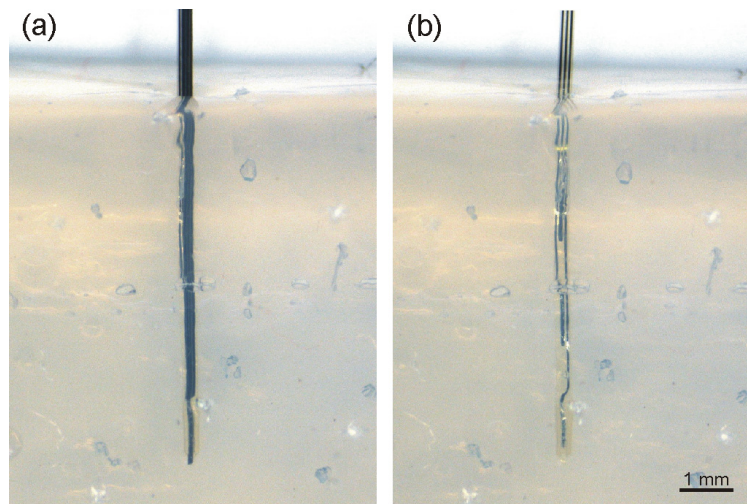


*Fig. 9.7. Insertion of a transdural shaft into the brain phantom: (a) Positioning of the shaft with help of the insertion tool, (b) shaft after withdrawing the insertion tool*

#### **9.3.2 In Vivo**

The in vivo experiment showed that the insertion tool combined with the flexible implant was easy to handle during implantation. However, while the shaft could be inserted into

the cortex, it was not possible to insert it through the closed dura or even pia mater. For this reason, the meninges were cut open prior to implantation. After insertion, LFPs as well as MUA could be recorded. Fig. 9.8 depicts event related potentials in the LFP signal to the given visual stimulus of a downward scrolling grating. 20 single trials are shown in grey and the average response in black with the onset of the visual stimulus at 1 s and the stimulus offset at 4 s. For the same stimulus parameters, Fig. 9.9 shows the MUA of one trial recorded by two electrodes (black and grey). Fig. 9.10 depicts 292545 superimposed spikes recorded during 240 trials thresholded and aligned in time.

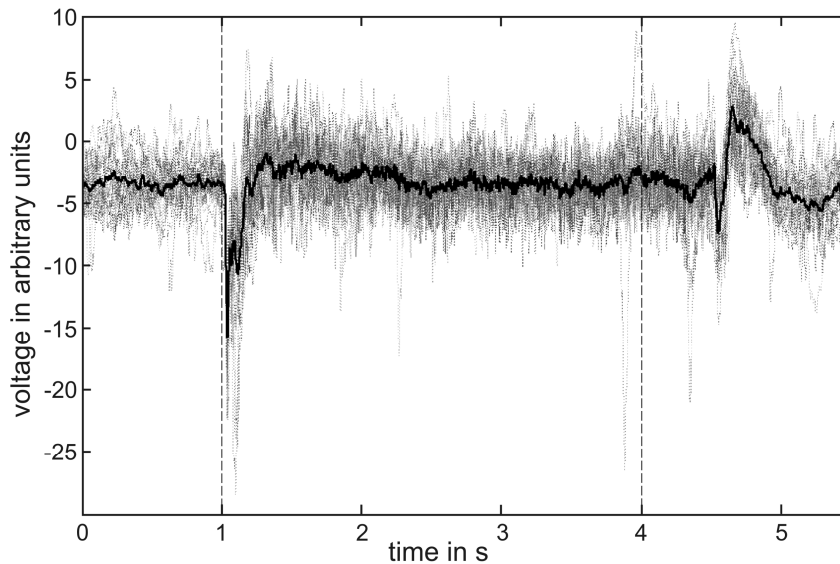


*Fig. 9.8. Event related potentials in the LFP signal: 20 single trials are depicted in grey and the average in black with the visual stimulus onset at 1 s and the offset at 4 s.*

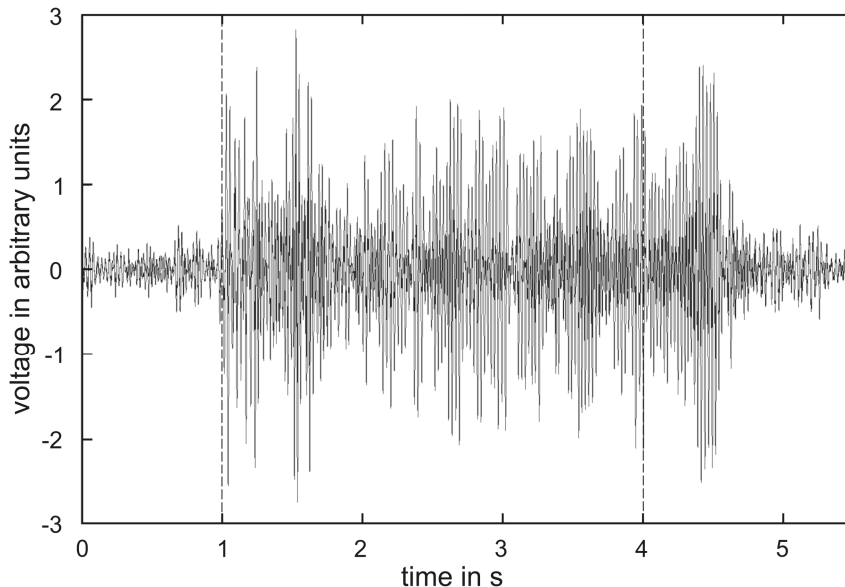


*Fig. 9.9. Event related gamma band filtered (25-90 Hz) LFP signals of one trial recorded with two electrode sites (grey and black)*

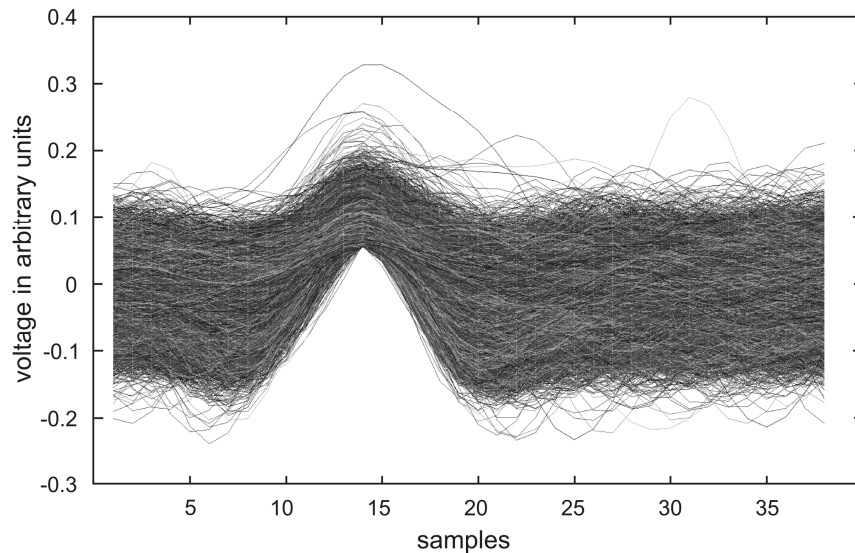


*Fig. 9.10. The thresholded waveforms of MUA signals recorded in 240 trials*

## 9.4 Discussion

Although the feature size of the U-profile was small, it could be easily attached to the shaft by using tweezers and a standard stereo microscope. While the insertion tests in the brain phantom were promising, the in vivo experiment revealed that the device was not able to penetrate the meninges. The U-profile's width was too large and could not be pushed through the hole which was pierced into the meninges by the insertion tool. Thus, further refinements of the design have to be done in order to penetrate the pia as well as the dura mater. The result of Olamat regarding the optimal shaft tip design can be used to develop devices which will be easier to insert (Olamat 2010). It was found that the PE foil did not resemble the meninges well enough to serve as a model. The real meninges are tougher and more elastic than the PE foil. The brain model has to be adapted to the findings of the in vivo experiment to obtain a more accurate prediction whether an electrode shaft is able to penetrate the meninges. This is, a material has to be found which resembles the toughness and elasticity in a more accurate way.

However, the shaft was successfully implanted into the cortex and visually evoked potentials could be recorded. The quality of the LFP and MUA signals (Fig. 9.8, Fig. 9.9 and Fig. 9.10) was excellent and showed the good applicability of the electrode's dimensions for intracortical recording.

With the insertion of the shaft through a small hole in the skull one would be able to distribute a large number of electrode sites over large areas of the cortex. Due to the minimally invasive surgery, the shafts do not have to be implanted in one long surgery but can be independently placed and adjusted in insertion depth in successive sessions. Thus, the amount of shaft that will be implanted is not dependent on the time frame of one surgery.

In contrast to the *Utah Array*, which comprises shafts with a length of about 2 mm and cannot be implanted in deeper lying cortex regions (Suner 2005), the long and flexible shaft presented in this work is not restricted to a certain implantation depth. While the im-

plantation tool has a certain size and will damage some neural tissue, it is withdrawn after implantation allowing the tissue to relax. With the help of the implantation tool, the long and flexible shaft can be implanted in deep cortical regions. To be able to insert a PI shaft into deep lying brain regions, Chen et al. added an extra metal layer to stiffen the PI shaft (Chen 2009) and thus, lost the main advantage of a flexible PI electrode shaft as the shaft will be stiff after the implantation and will cause tissue damage. In contrast, the shaft presented in this work will be flexible after the implantation and will float with the tissue.

## 10 Multimodal Electrodes

As already mentioned, there are different ways of interfacing the brain besides electrical recording and stimulation. In recent years, two modalities turned out to be particularly interesting: fluidic and optical contact to nervous tissue (chapters 4.5 and 4.6). In this chapter, I will describe a microimplant that combines these modalities with standard electrical recording. This implant was designed to facilitate optogenetic in vivo experiments. Combining these three modalities, optogenetic research can be conducted with one single electrode shaft which can be chronically implanted into freely moving mice. It comprises a microfluidic channel to apply a gene delivery vector to genetically modify neural cells in, an optical waveguide to transmit light into, and microelectrodes to record SUA from the brain region of interest.

### 10.1 Implant Concept

The basic component of the implant is a PI-based shaft including 9 platinum electrode sites with a diameter of 30  $\mu\text{m}$ . The thin-film layer composition is identical to the foil described in chapter 8.1 with a 300 nm thick platinum thin-film sandwiched between two 5  $\mu\text{m}$  thick PI layers. Within the PI foil, the electrode sites are connected via conductor paths on a flexible cable to solder pads designed to contact SMD omnetics connectors (Fig. 10.1). A SU-8 waveguide is placed on top of the PI shaft separated from the PI by a 200 nm thick tungsten-titanium layer. This metal cladding is needed to prevent the light from coupling into the PI substrate which has a higher refractive index than the SU-8. The waveguide ends in front of the electrode sites. Thus, neurons which are stimulated by the light exiting the waveguide will be closest to the electrode sites for recording. The channel is implemented by attaching a U-profile with an outer cross-section of 190  $\mu\text{m}$  by 65  $\mu\text{m}$ , an inner cross-section of 50  $\mu\text{m}$  by 45  $\mu\text{m}$  and a length of 7 mm to the rear side of the PI shaft. The U-profile was made of SU-8 and was processed on a separate wafer analogue to the U-profile described in chapter 9. The channel outlet at the tip of the shaft is a hole in the PI between two electrode sites. Thus, the fluid can be applied to the same tissue volume which is also electrically and optically contacted.

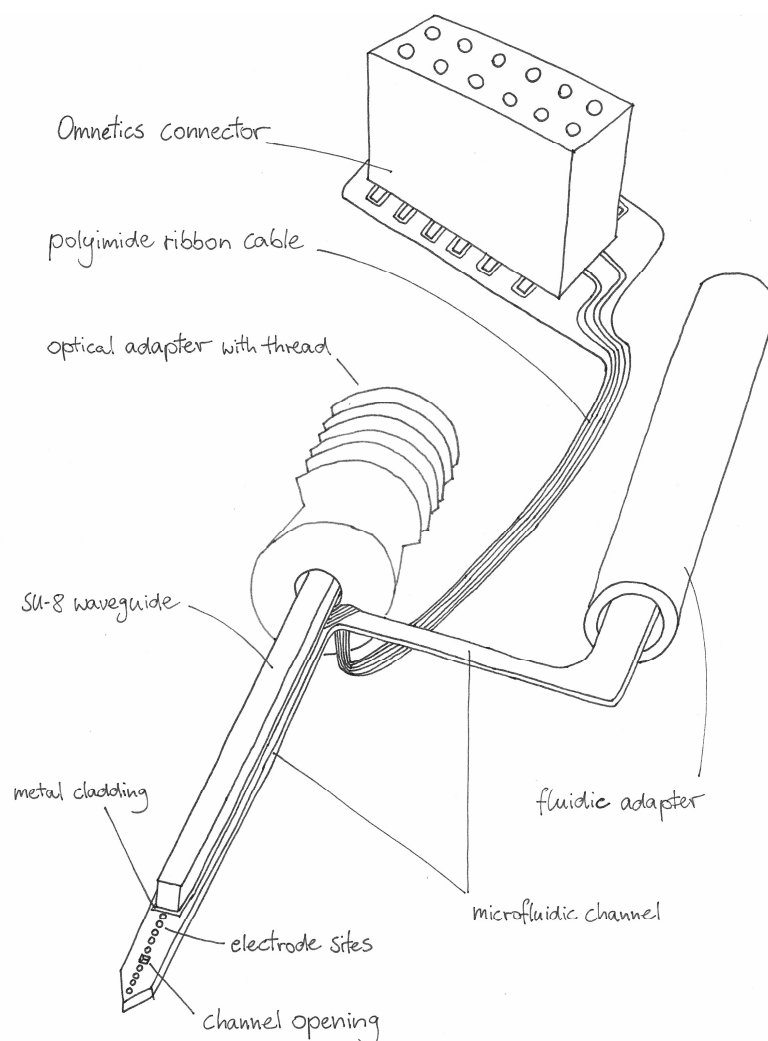


Fig. 10.1. Schematic diagram of the polymer-based shaft electrode assembly with 9 electrode sites, an integrated optical waveguide, and a hybrid assembled microchannel

## 10.2 MEMS Processing

### *Polyimide Shafts and Optical Waveguides*

Up to the curing of the second PI layer (Fig. 10.2a), the shafts were processed as described in chapter 8.1.2. After the curing, HMDS was applied on the PI layer and a 550 nm layer of LOR 3A resist (MicroChem, Newton, MA, USA) was spin coated at 1000 rpm and baked on a hotplate for 60 s at 150 °C. Subsequently, a layer of photosensitive resist (AZ1518, Clariant, Wiesbaden, Germany) was applied on top of the LOR resist by spin-coating a 2 µm thick layer at 4000 rpm and baked for 50 s at 100 °C on a hotplate. The photoresist was exposed to UV light through a chromium mask to define the areas of the metal cladding (90 mJ/cm<sup>2</sup>, proximity exposure type with an exposure gap of 100 µm) (Fig. 10.2b). Due to the very large exposure dose and the proximity contact, the exposed areas are larger than defined on the mask. This is necessary as the same mask is used later to define the SU-8 waveguide structures which have to fit onto the area of the metal cladding. The AZ1518 was developed in AZ 762 MIF (MicroChemicals GmbH, Ulm, Germany) for 100 s, After a hotplate bake for 50 s at 115 °C, the LOR was developed in

AZ 400 K (MicroChemicals) for 55 s. A 200 nm thick layer of tungsten-titanium alloy (10 % titanium) was sputter deposited at 300 W for 9 min. The resist and the not required metal parts were rinsed in a lift-off step using Nano PG Remover (MicroChem) at 50 °C for 5 h.

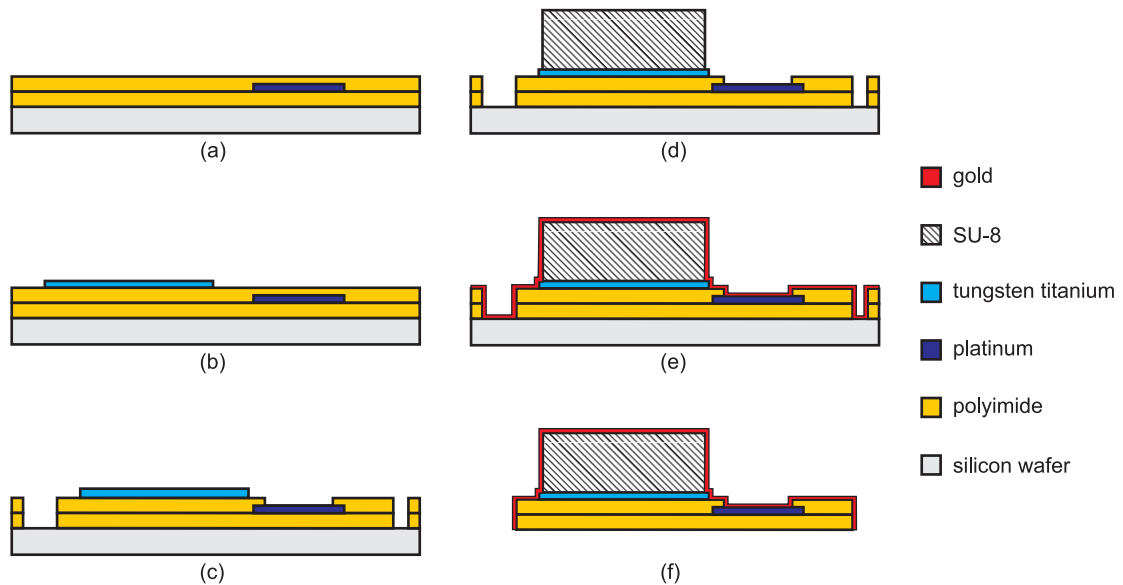


Fig. 10.2. MEMS process steps of a PI shaft electrode with integrated SU-8 waveguide

The PI electrode and solder pad openings as well as the perimeters of the shaft were defined by photolithography (photoresist: AZ9260) and  $O_2$ -plasma etching as described in chapter 8.1.2 (Fig. 10.2c). The waveguides (Fig. 10.2d) were formed by spin-coating two layers of SU-8 3050 at 2000 rpm with an intermediate hotplate bake at 65 °C for 5 min and at 95 °C for 20 min. After a second hotplate step with the same parameters, the SU-8 layer with a thickness of about 160  $\mu\text{m}$  was exposed to UV light through the same chromium mask used for the metal cladding with 500  $\text{mJ}/\text{cm}^2$ . An I-line filter was used to eliminate radiation below 350 nm from the mercury vapor lamp spectrum to obtain vertical side walls (avoiding T-Topping). To polymerize the material, a post exposure bake was conducted on a hotplate at 65 °C for 5 h. The SU-8 structures were developed with mr-Dev 600 (micro resist technology GmbH, Berlin, Germany) for 15 min while applying ultrasound. As a last processing step, the complete wafer was covered with a 200 nm thick sputtered gold layer to complete the metal cladding of the waveguides (Fig. 10.2e). The devices were released from the wafer by pulling them off with tweezers (Fig. 10.2f).

### SU-8 U-Profiles

The channel profiles were processed as described in chapter 9.2.2. SU-8 3025 was spin coated at 4500 rpm to form a 20  $\mu\text{m}$  thick channel cover, while the walls with a height of 45  $\mu\text{m}$  were made of SU-8 3050 spin coated at 4000 rpm.

## 10.3 Hybrid Assembly

The PI shafts as well as the SU-8 channels were pulled off the wafers by tweezers. Epoxy (UHU endfest 300) was applied to the channel walls using a tapered tungsten wire. After

attaching and aligning the channel to the rear side of the shaft, the epoxy was cured at 70 °C on a hotplate for 15 minutes.

The channel inlet was glued to a metal tube with an inner diameter of 410  $\mu\text{m}$  (blunt end stainless steel tips: I&J FISNAR, Fair Lawn, NJ, USA) which can be connected to the tubing of the pump during the experiment.

The waveguide is glued into a custom made optical connector (Steffen Wolff, Friedrich Miescher Institute, Basel, Switzerland). This connector is designed to be attached to the skull and can be connected to a standard optical silica fibre (diameter 200  $\mu\text{m}$ ) during recording sessions.

The tip of the shafts with the electrode sites and the waveguide front end as well as the solder pads for the omnetics connectors were opened by dipping these parts into potassium iodide/iodine solution for 2.5 min. Subsequently, a silver wire used as ground electrode and the omnetics connector were soldered to the platinum solder pads. For the omnetics connector SMD soldering was used as described in chapter 9.2.3.

### 10.4 In Vitro Results

The 150  $\mu\text{m}$  thick SU-8 waveguide and the 200 nm tungsten titanium cladding compensate their intrinsic stress in a way that the device when released from the wafer results in a straight shaft. Devices without the waveguide bent into the wafer plane, while devices without cladding layer bent out of the wafer plane.

The multimodal shaft electrode could be assembled as described in chapter 10.3. Fig. 10.3 shows an assembled device with an adapter for each modality connected to the MEMS-processed PI shaft. Fig. 10.4 depicts a close-up of the shaft's tip with the channel, channel opening, waveguide and electrode sites.

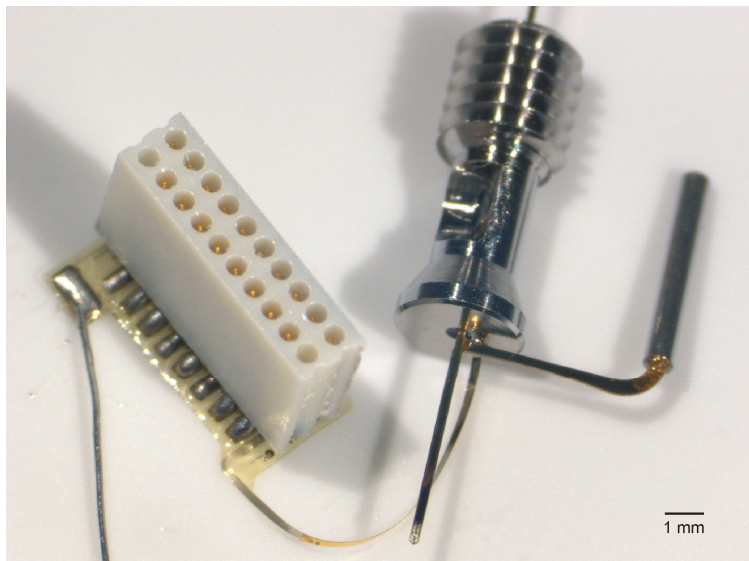


*Fig. 10.3. Fully assembled multimodal shaft electrode with electrical connector, optical adapter and fluidic adapter (from left to right)*



Although the application of the epoxy glue to the channel walls and the attachment to the electrode shaft requires very steady hands, the yield of functional channels was about 100 %. In Fig. 10.5, the impedance magnitude and phase of 9 electrode sites of one shaft are shown as a function of frequency. The impedance magnitude at 1 kHz is about 50 k $\Omega$  to 90 k $\Omega$  with an access resistance of about 15 k $\Omega$  and a cutoff frequency of about 4000 Hz.

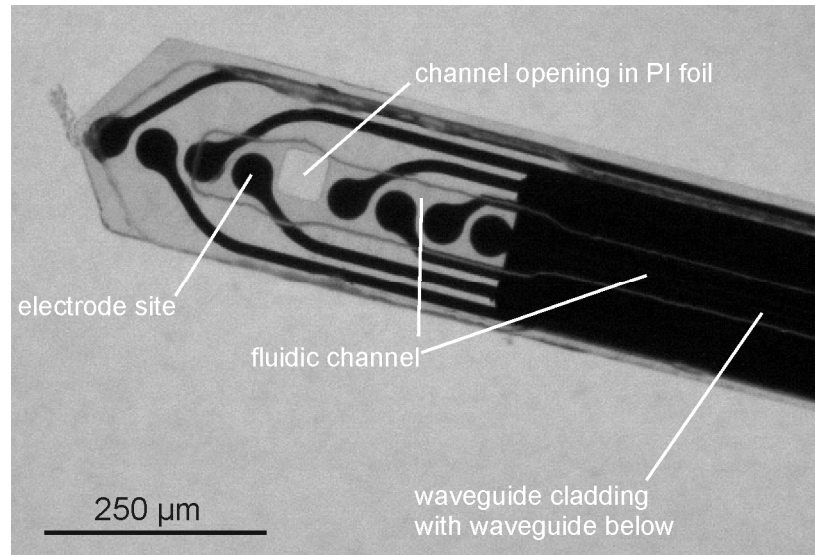


Fig. 10.4. Photograph of the tip of the multimodal shaft electrode from below.

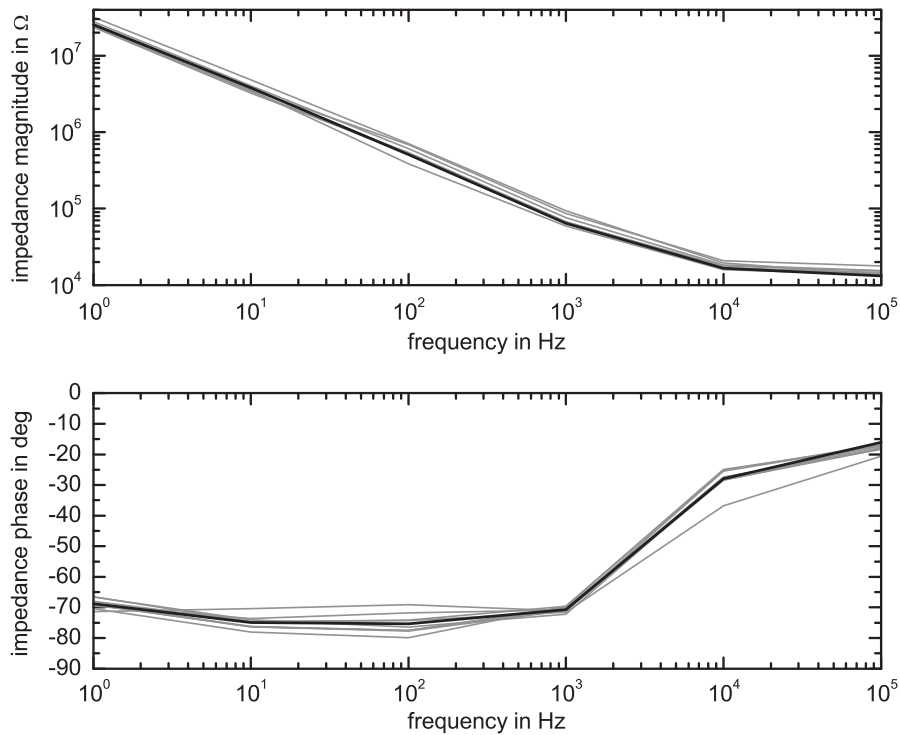


Fig. 10.5. Electrical impedance spectroscopy of 9 electrode sites from one multimodal shaft; the platinum sputtered electrode sites have a diameter of 30  $\mu\text{m}$ . Single electrodes are in grey, the mean value of the 9 electrodes is depicted in black.

### 10.4.1 Characterization of the Fluidic Channel

The microchannel was attached to a pressure sensor (RBIP015DB, Sensortech GmbH, Puchheim, Germany) which was connected to a flow rate sensor (ASL 1430, Sensirion, Staefa, Switzerland). Water was supplied by connecting the flow rate sensor to a water reservoir. The fluid pressure was controlled by connecting the reservoir to an adjustable air pressure supply. Fig. 10.6 depicts the flow rate as a function of the pressure drop over the length of the microchannel. The measured values are shown as squares while the theoretically calculated values are represented as straight line. The values were calculated with the Hagen-Poiseuille equation for rectangular channel cross-sections (Eq.4.10) applying the dynamic viscosity of water at 25 °C:  $\eta = 8.904 \cdot 10^{-4}$  Pa·s.

For the application of the gene delivery vector in mice, a pressure of 1.38 bar is used which corresponds to a flow rate of about 240  $\mu\text{L}/\text{min}$  (Fig. 10.6). Thus, the required amount of fluid of 500 nL (Wolff 2010) can be delivered to the target tissue in 125 ms.

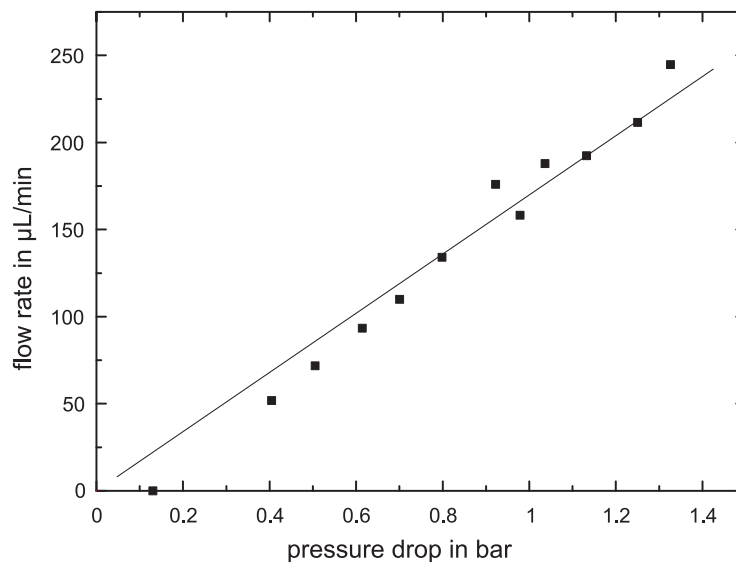


Fig. 10.6. The flow rate as a function of fluid pressure; the squares show the measured values, the straight line represents the theoretical values calculated with the Hagen-Poiseuille equation for rectangular cross-sections with a width of 50  $\mu\text{m}$ , a height of 45  $\mu\text{m}$  and a length of 7 mm.

### 10.4.2 Characterization of the Optical Waveguide

With the same process as described in chapter 10.2, test waveguides were fabricated on a PI substrate with a cross-section of 150  $\mu\text{m}$  by 150  $\mu\text{m}$  and a length of 6.5 cm. Both ends of the waveguide were opened by etching the gold cladding with a drop of potassium iodide/iodine solution.

A waveguide was fixed on a three-axis micropositioner. The cleaved side of an optical fibre (one cleaved end and one end with FC connector, 62.5  $\mu\text{m}$  core diameter, graded index, multimode patch cable, Thorlabs, Newton, NJ, USA) was fixed on a second micropositioner. The waveguide and the optical fibre were aligned in a way that the front ends face each other. To enhance the light coupling from the fibre into the waveguide, UV light curing optical glue (Norland Optical Adhesive 81, Norland Products Inc., Cranbury, NJ,

USA) was applied at the interface. With the optical glue applied, the waveguide and the fibre could still be positioned to each other. Laser light was coupled into the optical fibre via the FC connector to find the optimal alignment. When maximum light power was measured at the waveguide output, the alignment position was fixed by curing the glue with UV light.

Waveguides were characterized using the cutback method. Laser light with a wavelength of 473 nm and 593 nm respectively was coupled into the waveguide by connecting the optical fibre glued to it to the respective laser light source. Light leaving the waveguide was measured while the waveguide was cut by 2.5 mm at a time to obtain the waveguide's attenuation. Light power was measured with an optical multimeter.

Fig. 10.7 depicts the transmitted light power as a function of the waveguide length. The measurement for both wavelengths was conducted with the same waveguide with a cross-section of 150  $\mu\text{m}$  by 150  $\mu\text{m}$ . The input power i.e. the output power of the optical fibre was 21 mW (473 nm) and 14 mW (593 nm). The background power of the room's illumination was measured during every measurement step and was found to be about 45  $\mu\text{W}$  at 593 nm and 98  $\mu\text{W}$  at 473 nm wavelengths. The values in Fig. 10.7 were adjusted by subtracting the respective background power from the measured values.

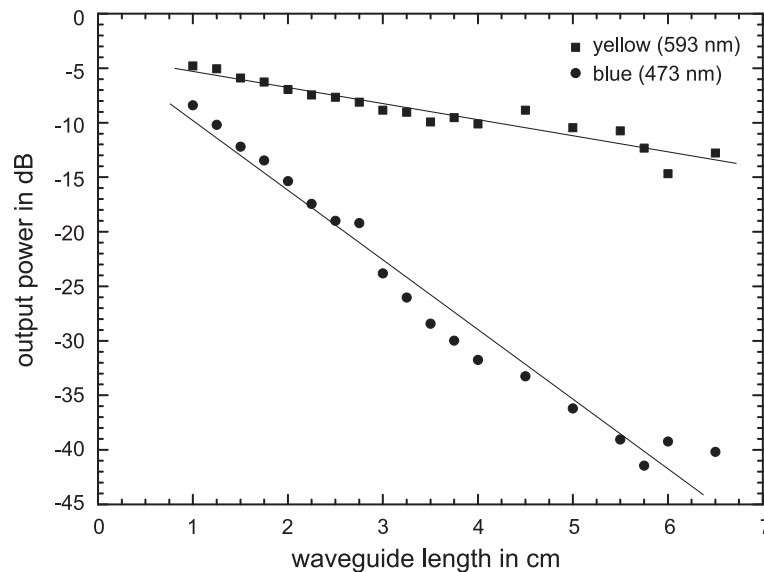


*Fig. 10.7. The waveguide's output power as a function of waveguide length measured with yellow and blue light*

By using a linear fit (Fig. 10.7, straight lines), the transmission loss could be obtained as the slope of the linear fit with -6.4 dB/cm (473 nm) and -1.5 dB/cm (593 nm). The coupling loss between the optical fibre and the waveguide was estimated by the ordinate intercept of the linear fit which was -3.4 dB (473 nm) and -3.8 dB (593 nm). From this data, the output power of a 15 mm long waveguide is 1.35 mW (-12 dB) at 473 nm and 3.6 mW (-6 dB) at 593 nm.

The 15 mm long waveguides of fully assembled multimodal shafts were connected to an optical fibre via the optical adapter. For less coupling losses, the waveguide face at the

optic adapter was polished (Aluminum Oxide Lapping Sheets, Thorlabs, Newton, NJ, USA) and oil was applied between the faces of the two light guiding structures. At the wavelength of 473 nm, the output power of the waveguides was 1 to 2 mW while the output power of the optical fibre was 35 mW. Thus, the loss of light power due to the coupling loss between optical fibre and waveguide and the attenuation within the waveguide accounts for -15.4 to -12.4 dB.

## 10.5 In Vivo Results

### 10.5.1 Experimental Procedure

A first chronic implantation of the multimodal shaft was conducted by Steffen Wolff and Philip Tovote at the Friedrich Miescher Institute (Basel, Switzerland). Two mice (C57/B16J wild-type) were anaesthetized with Isofluran and chronically implanted with fully functional multimodal shaft electrodes. With a velocity of 10  $\mu\text{m/s}$ , the shafts were slowly inserted into the basal amygdala with the help of a hydraulic pump. The device was fixated on the skull with two screws, Cyanoacrylate and dental cement.

### 10.5.2 First Results

The shaft was easy to implant. The implanted device could be connected to the recording and stimulation setup via the electrical connector, the optical and the fluidic adapter. Light and fluid could be applied to the brain tissue. In this experiment, no further validation of the working principle of the implant could be accomplished as it was not possible to record electrical activity of the brain tissue, neither during implantation nor after 7 and 10 days after the implantation surgery.

## 10.6 Discussion

### 10.6.1 In Vitro

The optical adapter and the electrical connector had to be located on separate parts of the PI foil to be able to contact them to the optical fibre of the laser system via an optic connector and to the headstage of the neurophysiological recording system, respectively. Thus, in the presented design these two parts were connected by a flexible PI ribbon cable which gave the opportunity to place the parts at different locations on the mouse's head.

After the concept of attaching a 1 mm long U-profile to the rear side of a PI shaft was introduced in chapter 9.2.3, the same assembling technique could also be successfully used to attach U-profiles with a length of about 20 mm to a shaft. Although the manual attachment of the channel to the PI shaft was possible and resulted in a high yield of functional devices, this process is very time-consuming compared to a batch process on wafer level. Nonetheless, the obtained devices were functional and the fabrication was reproducible. This channel concept is independent of the materials and the microfabrication

process of the shaft electrodes and the U-profile and thus, gives the opportunity to fabricate the U-profile from an e.g. biodegradable material.

The manual assembly was identified as a general problem of multimodal electrodes. Each modality had to be separately connected to the macroscopic world of recording systems, light sources and fluid pumps. Each new modality adds a further manual assembly step after the batch processing.

The SU-8 channels were found to be relatively brittle and tend to break when handled during the connection to the tube of the pump system. Thus, in a next approach, it would be favourable to also use PI as the channel material which has a larger tensile strength and elongation at break than SU-8. SU-8 was chosen for its easy processability of thick layers and high aspect ratios. A highly viscous, photodefinable PI could be a good candidate for a new channel approach.

While the fabrication of PDMS-based channels is a standard procedure (Melin 2007; Unger 2000), the implementation of microchannels into PI on wafer-level is challenging. Metz et al. published a fabrication method of integrated channels by laminating two separately processed PI foils onto each other (Metz 2004a). While the group described the channels in different publications (Metz 2001b; Metz 2001a; Metz 2004b), no parameters for a reliable process could be found in this work by following the processing instructions given by the published articles. As a look into the literature revealed, most of the presented polymer-based channel concepts were published once without further development or use in neuroscientific applications (Pellinen 2005; Takeuchi 2005) which is an indicator for either a lack of interest in the neuroscience community to use microchannels or unreliable processes which could not be adapted to the need of neuroscientific research. Today, the only commercially available microelectrode containing a microchannel can be purchased from NeuroNexus. This device is a silicon shaft with a hybrid assembled fused silica catheter which is glue below the silicon shaft (Harris 2010; NeuroNexus 2008; Rohatgi 2009)

In the optical waveguides, the attenuation of blue light (-6.4 dB/cm) was higher than of yellow light (-1.5 dB/cm). This corresponds to the literature showing that the attenuation increases with decreasing wavelength of the light (Piruska 2006). The measured attenuation of the presented waveguides was in the range of values which could be found in the literature which was -1 dB to -5 dB for cross-sections of about 50  $\mu\text{m}$  by 50  $\mu\text{m}$  and wavelengths above 600 nm (Piruska 2006).

With a cross-sectional area of 150  $\mu\text{m}$  by 150  $\mu\text{m}$ , the presented waveguides are large compared to the waveguide presented by Cho et al. (Cho 2010) who fabricated SU-8 waveguides with a cross-section of 5  $\mu\text{m}$  by 15  $\mu\text{m}$  and reported a transmission loss of -2.2 dB/cm at 470 nm. As the fabrication method and the waveguide materials is equivalent, it is remarkable that Cho et al. found less attenuation in a waveguide comprising a cross-sectional area which was about 300 times smaller than the waveguides presented in this thesis. Cho et al. were the first to fabricate a device with an on wafer-level

integrated waveguide. All other publications described the hybrid integration of a standard optical fibre (Gradinaru 2007; Zhang 2009b; Zhang 2009a). The hybrid integration of an optical fibre into the electrode shaft has the advantage of an implanted light guide with very low attenuation. The drawback of the hybrid assembly is the poor reproducibility of the hand-made approach. The MEMS-integrated polymer waveguide has a higher light attenuation but comprises very defined and reproducible dimensions e.g. the distance between the waveguide end face and the first electrodes site. With MEMS-integration the size of the shaft can be reduced.

While waveguides can also be integrated on silicon shafts, polyimide has the advantage not to exhibit the photoelectric effect. As many research groups work with visual evoked potentials or laser light stimulation of neurons, materials that convert the light energy into electrical energy can produce artefacts in the recorded signals (Sirota 2010). Artefacts due to the photoelectric effect were even reported for tungsten electrodes illuminated by blue laser light at a wavelength of 473 nm (Han 2009). This is remarkable as the photoelectric work function of tungsten is 4.32 eV (Lide 1997) which corresponds to a wavelength of less or equal 287 nm. Thus, photons of the used blue laser light should not have enough energy to remove electrons from the metal surface. However, this phenomenon can be explained with the Becquerel effect which is a voltage generated between two electrodes immersed in a fluid when one of the electrodes is illuminated (Korlyakov 1969; Zorzos 2009).

### 10.6.2 In Vivo

Today, the only commercially available microelectrode with an integrated light guiding structure is a *Michigan Probe* with a hybrid assembled standard optical fibre glued to the silicon shaft (NeuroNexus 2010). While the shaft electrode itself is small the assembled device comprising a PCB with the electrical and optical connectors is relatively large to be used in a chronic implantation in freely moving mice. The device developed in this thesis has an integrated optical waveguide which is directly assembled to an optical adapter. This adapter was developed by the neuroscientific partners to be chronically implantable. Thus, the complete device fit on the mouse's head and was lightweight enough to be chronically implanted.

With the first chronically implanted devices, no electric activity of the neurons could be recorded. During this experiment it was not possible to identify the problem. One possible reason could be that cells are accumulated at the blunt tip of the waveguide during insertion. These damaged cells would be located directly on the electrode array and thus, inhibit a good electrical contact between active neurons and the electrode sites. It has to be checked in further experiments whether it is due to this particular shaft design that no neural activity could be recorded.

# 11 Discussion

In this thesis, electrodes were developed for two of the most exciting fields of contemporary neuroscience. In cognitive neuroscience, high-channel recording of extended cortical areas help to investigate coherence of oscillating neural signals (Fries 2001b). In the new and promising field of optogenetics, the implementation of fluidic and optic structures into microimplants allows to apply gene delivery vectors (Boyden 2005) and light to a certain brain area while recording from it electrically. With the implants manufactured in this work, novel data sets could be recorded which could not have been provided by conventional electrodes and which are of high interest for the neuroscientific community.

The presented electrodes were developed in close cooperation with neuroscientific partners to obtain a good applicability and a design that follows the requirements specified by the neuroscientific experiment. Only if engineers and neuroscientists work closely together, the combination of a technology such as microsystems engineering with neuroscience can be used in a sensible manner to develop better devices and procedures (Loeb 1992). That is, engineers, as well as neuroscientists, need some basic knowledge and understanding of the respective other field.

Some of the engineering concepts presented in this work were already shown elsewhere (Boppart 1992; Shamma-Donoghue 1982; Stieglitz 2000) but had a strong impact on neuroscientific research after the adaptation to neuroscientific applications in the CNS. One part of this work was to implement technical concepts on the basis of neuroscientific and physiological requirements in terms of material selection, design and assembly. Due to the variable design, electrodes based on PI foil substrates can be applied in a variety of setups to record from cortical structures. Large-area, epicortically implanted devices can be realized as well as thread-like shaft electrodes which can be used to record from within the cortex. Both setups benefit from the thin and flexible PI foils which can prevent significant damage to the nervous tissue. PI-based implants can be used as thin foils because the material is very tough and easy to handle compared to a silicone device with the same foil thickness. The PI protects the thin-film metal layer and prevents it from cracking when handled roughly during surgery. As the material has these advantageous mechanical properties, it was tested for its long-term stability.

## *Long-Term Testing of Polyimides*

The long-term material study carried out in this work can be of considerable interest to scientists working in the fields of neuroprosthetics, neuroscience and implantable polymers. The long-term behaviour of PIs of the new generation which were stored in PBS over the course of 20 months was described. This time period is beyond what was found in literature both dealing with biomedical and other applications of this material (Ceballos 2002; Delasi 1971; Lago 2005; Murray 2004; Nikles 2003; Schuettler 2003). While many researchers are using PI as a promising implant material, little is known about its long-term stability in a body-like environment. By immersing the material in PBS and simulta-

neously stressing it at elevated temperatures, a broad overview of the aging behaviour was given. The findings were confirmed by a large set of experimental data (in the tensile tests 258 samples were tested with a sample size of  $n \geq 10$ ). Therefore, these results contribute to the fundamental knowledge about BPDA-PPD type PI as a biomaterial.

Over the course of 20 months the three tested PIs were stable in PBS at body temperature and even at 60 °C. No decrease in the measured properties with respect to the reference could be found which showed the long-term stability of the tested materials. In contrast to PMDA-ODA type PIs (e.g. Kapton) which deteriorates in a humid and/or warm environment (Bessonov 1987; Campbell 1988; Delasi 1971; Murray 2004), the PIs tested in this work showed no decline in mechanical properties and did not dissolve when stored in a warm, salt ion containing aqueous solution. This indicates that these PIs are superior to PMDA-ODA type PI which already degrades after 30 days in distilled water at room temperature (Delasi 1971). In contrast, for Upilex25S, no decline in mass was found after 32 months in PBS at 37 °C and 60 °C or even in deionized water at 85 °C. Water cannot be used as a medium for biomedical testing as a significant difference in behaviour of BPDA-PPD type PI stored in PBS compared to specimens stored in deionized water could be observed. While this PI type was even stable in water at 85 °C it was sensitive to salt ions of the PBS solution at 85 °C. All tested PIs showed a decrease in the measured mechanical properties when stored in PBS at 85 °C.

The presented results showed that the values found with PBS at 85 °C could not be used to predict the long-term behaviour of the material at body temperature using the Arrhenius equation. This suggests that at higher storage temperatures, degradation processes take place that do not develop at 37 °C or 60 °C. This notion was also supported by Hemmerich and Murray (Hemmerich 1998; Murray 2004).

While PI was dismissed as an implant material by Loeb et al. who tested PI-2550 (HD Microsystems LLC, Parlin; NJ, USA) and found changes in mechanical properties (Loeb 1996), this was not found to be a problem with the PIs studied in this work. As PI is the name for a group of materials, each PI type has to be tested separately in order to evaluate its applicability as an implant material.

Further in vivo tests have to reveal whether PI is also stable in a body environment comprising not only saline solution but enzymes and defence cells of the body's immune system.

### *The 252-channel ECoG-Electrode Array*

It could be shown that PI-based electrode arrays can be employed in long-term recording of LFP signals at the cortical surface. At the time of writing, the ECoG-electrode array was implanted for 10 months and recordings were constantly conducted during this period. No decline in signal quality or electrode loss could be observed.

The presented multielectrode array bridges the gap between microelectrodes implemented on silicon shafts and the large epicortical PDMS arrays used in clinical practice. With its relatively large electrode diameters of 1 mm and an electrode distribution over an



area of 3.5 cm by 6 cm, this implant provides the possibility to record high quality LFP signals over large areas.

Electrode arrays based on PI foils with a thickness of 10  $\mu\text{m}$  are thin and flexible enough to adapt to the cortex without applying a significant force to the cortical surface. In contrast, standard PDMS-based electrode grids, used for subdural recording in pre-surgical epilepsy diagnosis, have a foil thickness of about 2 mm rendering the device relatively stiff and bulky. Large-area PDMS electrode grids are associated with higher complication rates such as interference in haemal circulation which could be due to the pressure applied by the rigid PDMS foil (Wong 2009) which can also lead to a depression of the underlying cortical matter (Bullara 1979). This appears to be one reason why they can only be applied over the course of some weeks.

This problem was not observed with the subdurally implanted ECoG-electrode array manufactured in this work. While the presented PI foil was covered large parts of one hemisphere of a macaque monkey, no decline in neural signal or in cognitive function of the animal was observed over the course of 10 months post-implantation. Due to the thin foil, the mass and the intrinsic mechanical stress of the implant are very low and do not compress the underlying cortical tissue. By the same token, the flexible foil is attached to the cortical surface by capillary forces and thus, forms a good contact to the tissue while following the curvature of the cortex.

While a lot of new and interesting MEMS implants have been developed and published in the engineering science community, most of the designs did not make the transition into a tool actually used in neuroscience research (apart from the silicon-based electrodes distributed by NeuroNexus and Blackrock Microsystems). Although in vivo studies demonstrating functionality are included, engineering publications often remain a proof of principle. In contrast, the presented ECoG-array was manufactured by microstructuring PI foils, a process presented almost 30 years ago (Shamma-Donoghue 1982) and refined in the last 10 years (Stieglitz 2000). However, by combining a high-channel array at the mesoscale with microcables, a small connector assembly and a design that is adapted to the cortical topography, an implant concept was established that has provided the neuroscience community with a yield of in vivo neural data which, to this extent, was never recorded before. With this data set, a new step forward could be done towards the understanding of the mechanisms through which brain regions are able to interact with each other in order to process information and produce behaviourally relevant responses (Fries 2005). The large number of electrodes combined with the flexibility of a thin-film array allows simultaneous recording over several brain areas. This electrode array is able to record neuronal activity from early visual areas (e.g. V1) to prefrontal regions, such as the frontal eye fields. Extensive sampling over large brain areas can help to reveal the mechanisms of interaction between neuronal populations during the development of a cognitive task. In comparison, other microelectrode arrays presented in the literature comprise only a small number of channels and have, due to cables and PCBs, a relatively large overall assembly which is not suited to upscale the design to a number of channels

>100 (Hollenberg 2006; Kitzmiller 2006; Molina-Luna 2007; Myllymaa 2009; Takahashi 2003). The presented design was taken a step further by Kim et al. in terms of an even more compatible implant which was able to follow the cortical surface into the sulci. They developed an epicortical array made of an extremely thin PI mesh (2.5  $\mu\text{m}$ ) which could not be handled during surgery. For this reason, they attached the mesh to a silk substrate which dissolved after implantation (Kim 2010).

For the ECoG-electrode array presented in this work, the long-term stability in vivo could be proven for a period of up to 10 months. If this time span can be further extended, this array could be a promising candidate for the use as a BCI electrode array competing versus laser-cut microstructures made of an about 100  $\mu\text{m}$  to 500  $\mu\text{m}$  thick PDMS foil with an incorporated 12.5  $\mu\text{m}$  thick platinum foil (Henle 2010; Schuettler 2005). While these materials are standard biocompatible implant materials the approach has the problem of cracking metal leads due to the very stretchable PDMS which cannot protect the platinum foil. While this is not a problem in the presented ECoG-electrode array, PI-based microimplants comprise only a few hundred nanometre thick platinum layer which can be electrochemically destroyed. Even if the implant is only used for recording, the input bias current of a permanent connected amplifier could lead to electrode dissolution.

While the application of microelectrode arrays based on flexible PI substrates in human neuroprosthetics is still being discussed, it could be shown that these implants are a powerful tool for neuroscientific research. Although the hardware of the electrode arrays is still under development, there is an ongoing discussion whether epicortical signals can be used for BCIs. In recent years, some publications suggested that epicortically recorded cortex signals could be sufficient for BCI applications (Chao 2010; Mehring 2003; Pesaran 2002). Slutzky et al. proposed an optimal electrode spacing of about 2 mm for epicortical recording in humans and Leuthardt et al. found that an 16-channel epicortical electrode array with an electrode spacing of 1 mm was sufficient to separate different aspects of hand movement in humans (Leuthardt 2009; Slutzky 2010). The dimensions of the presented array dimensions correspond well to the suggested parameters. This, together with the signal fidelity recorded over time, provide an indication that neuroprosthetic devices could be developed using an ECoG-electrode array as the neural interface which is similar to the device developed in this work.

### *The Transdural Approach*

The flexible transdural shaft electrode was developed to be inserted in a minimally invasive surgery through a small drilled hole in the skull and to penetrate the meninges and the cortex with the help of an insertion tool which could be withdrawn after insertion. With stiff tungsten rods as an insertion tool and a stereotaxic positioning setup, the flexible shaft can be precisely implanted in cortical and subcortical target regions. While the first in vitro insertion studies were promising, the setup could not penetrate the pia mater in an in vivo experiment. The tapered tip of the insertion tool could easily penetrate the pia, but the U-profile which was attached to the shaft tip and accommodated the insertion tool was too

bulky to follow the tip through the hole in the elastic meninges. Using a U-profile with a sharper tip and a smaller cross-section could help to circumvent that problem.

However, after incising the pia, the shaft could be inserted into the cortical tissue and LFPs as well as MUA were recorded. The excellent quality of the signals supported the idea to use the shaft electrodes to establish a three-dimensional electrode array by distributing a number of shafts across the cortex. By extending the two-dimensional epicortical array into a three-dimensional array, it would be possible to chronically record neural signals from the whole cortical volume. As the *Michigan Probe* or the *NeuroProbes* concept, each shaft comprises a linear electrode array and thus, can record from different cortical depths at one cortical location.

While the hybrid assembly is a serial, time-consuming fabrication step, it provides the possibility to manufacture the U-profile independently from the PI process. This could simplify the use of a biodegradable material which dissolves after implantation so that only the completely flexible shaft would remain in the tissue.

For long-term recording, it is crucial to have a floating implantation setup to prevent tissue damage which is caused by the movement of the brain relative to the skull. A stiff electrode attached to the skull would transfer force onto the tissue, intensify tissue response and thus, result in the decline of the recorded signals (Biran 2007; Kim 2004). With its flexible shaft and cable, the presented device can be used in a floating setup.

### *Multimodal Electrodes for Optogenetics*

A microelectrode with the ability to transfer fluids, light and electrical signals in a chronic implantation would be a major step towards the application of optogenetics in freely moving rodents. In this work, a microimplant was manufactured which could connect the target brain tissue via these three modalities. While the implementation of either fluidic channels (Lee 2004a; Metz 2004a; Takeuchi 2005) or optical waveguides (Cho 2010; Mankodiya 2009; Zhang 2009a) into neural implants was already described by other groups, the here presented implant was, to my knowledge, the first to combine all three modalities in a single device.

Due to the use of PI as a substrate material, the device comprised an integrated flexible cable which gave the possibility to place the electrical connector independently from the electrode shaft and optical adapter on the skull of the mouse. This is important for the convenient connection of the optical fibres and electrical connectors of the external stimulation and recording setup. A second advantage of polyimide as the substrate materials is that it does not exhibit photoelectric effects like silicon and thus, does not cause artefacts in optical stimulation of neural tissue.

The presented shaft electrode is relatively stiff due to the microfluidic channel with a height of 60  $\mu\text{m}$  and the optical waveguide with a height of 150  $\mu\text{m}$  and thus, can penetrate the cortical tissue without an insertion tool. However, as the implant is completely polymer-based, a reduction of the shaft height could result in a thin and flexible device.

A disadvantage of SU-8 is its increasing absorption of light at lower wavelengths. While the presented waveguides had an attenuation of -1.5 dB/cm at 593 nm, it increased to -6.4 dB/cm at 473 nm. It remains to be evaluated whether the SU-8 waveguide integrated on a shaft electrode can transmit enough light to stimulate not only single neurons in the vicinity of the waveguide's tip, but a larger volume such as the amygdala of mice which is needed to conduct experiments described in chapter 2.2.2.

One option to circumvent the light attenuation would be to search for a polymer material with a lower absorption in the required wavelengths or to integrate light sources directly onto the shaft. In addition to the attenuation problem, the assembly of the microdevice is challenging and time consuming due to the different modalities. If LEDs were integrated directly onto the shaft, the assembly and connection of the optical adaptor would not be needed and would be replaced by a simple electric connection to access the LEDs. A first concept of a microimplant comprising LEDs was proposed by Bernstein (Bernstein 2008).

While the SU-8 channel structures were easy to process, the material was found to be difficult to handle in the *in vivo* experiment due to its brittleness and the low tensile strength and elongation at break values. Thus, it would be favourable to fabricate PI-based channels as PI has comparably much better mechanical properties. Moreover, the integration of PI channels into the fabrication process (Metz 2004a) at the wafer-level would decrease the hybrid assembly time significantly.

The *in vivo* experiment showed that the multimodal shaft electrode can be easily implanted and that fluids as well as light can be delivered to the brain tissue. However, no further evaluation of the implant could be done as it was not possible to record electrical activity from the neural tissue in the pilot experiments. It has to be investigated in further tests whether this was due to a design error, a problem with fabrication or implantation, or a recording failure.

## 12 Summary

In this chapter the results of the thesis are summarized by answering the questions posed in chapter 6.1.

- Can flexible polymer-based microimplants significantly contribute to brain research in a way that goes beyond the results obtained with silicon-based MEMS implants which are currently commercially available from the two companies NeuroNexus and Blackrock Microsystems? Can such flexible microdevices fabricated with existing MEMS technology be applied in long-term recordings and supply neuroscientists with novel data?
- Is it possible to use MEMS-based electrode arrays to record neural data on the mesoscale? That is to provide an implant which records LFPs from significantly larger brain areas than reported for MEMS electrodes in literature.

Based on MEMS-processing techniques of PI-based microelectrodes found in the literature, similar fabrication technology was established at the IMTEK cleanroom facility. This standard process was used to manufacture a 252-channel ECoG-electrode array designed to epicortically record LFPs from large parts of the macaque monkey's cortex (Rubehn 2009b). Two animals were successfully implanted with the arrays by the project partners and high-quality data was recorded over a period of up to 10 months at the time of writing (Rubehn 2009a). No loss of channels was observed. This long-term recording of large regions of a brain hemisphere with a large number of channels provided neuroscientists with a unique and novel dataset which can be used to further investigate complex brain functions (Bosman 2010a; Bosman 2010b; Micheli 2010).

With an array size of about 35 by 60 mm<sup>2</sup> and an electrode diameter of 1 mm, the dimensions of the MEMS-based ECoG-electrode array are clearly in the mesoscale range. MEMS fabrication technology was used to accommodate the large number of channels in the limited space of the device and to obtain a very thin and flexible implant.

With the same process, flexible shaft electrodes were manufactured and hybrid assembled with a small channel-like structure attached to the tip of the shaft. This structure was then used to guide a custom made insertion tool which was able to penetrate the cortical matter and position the flexible shaft in the brain. With electrode sites with an area of 100 µm by 500 µm, high-quality LFPs as well as MUA were recorded by the project partners (Rubehn 2010c).

- Is PI a suitable substrate material for the chronic implantation of flexible, MEMS-based implants?

The mechanical properties of three PIs (PI2611, U-Varnish-S, Durimide 7510) were studied in a long-term soaking test. While about 4000 microprocessed specimens were tested over the course of 20 months, a decrease in the values of the monitored properties was not observed, neither for those specimens stored in PBS (at 37 °C or 60 °C), nor for those

kept in deionized water at 85 °C. The same behaviour was found in a gravimetric analysis of Upilex25S foils. No changes in mass or water uptake were found. Only the foils immersed in PBS at 85 °C showed a mass loss of 8.2 % after 32 months as well as all three PIs showed a significant decrease in the measured mechanical properties over time. These are promising results for the application of the tested PIs in a bodily environment given that the materials were stable over time in the model environment at 37 °C and even 60 °C (Rubehn 2007a; Rubehn 2007b; Rubehn 2010a).

- Can microimplants that comprise electrodes, a fluidic channel and an optical waveguide be efficiently used in optogenetic experiments in terms of an easy device handling, a simplified implantation, and a more convenient conduction of the experiment?

A SU-8 waveguide structure was integrated on wafer level into the standard PI process (Rubehn 2010d). By attaching a U-shaped profile to the rear side of the shaft in hybrid assembly step, a first prototype for a microelectrode was manufactured which can be used in in vivo optogenetic experiments. This single shaft electrode was made for simultaneous fluid delivery, optical stimulation and electrical recording in neural tissue. A first implantation into mice showed promising results with respect to the implantation procedure and the feasibility of connecting the implanted device to the recording and optical stimulation setup.

## 13 Outlook

This thesis shows that polymer-based microimplants can be used to obtain novel neural data. However, it represents just the starting point for a whole range of possible applications. There are numerous neuroscientific questions which could be answered with data provided by specifically designed MEMS-based implants. The following paragraphs give some ideas of how the work of this thesis could be continued to further harness the potential that exists at the interface between MEMS technology and neuroscience.

Flexible shaft electrodes (chapter 9) can be used to build a three-dimensional intracortical electrode array by distributing a number of shafts over large parts of the cortex. Each shaft is supposed to be inserted separately in a minimally invasive surgery. To achieve this, the presented design has to be optimized so that it becomes possible to insert the flexible shaft through the dura mater. A first step is to minimize the dimensions of the U-profile and the insertion tool. This in turn generates the problem that a tungsten rod thinner than 100  $\mu\text{m}$  is not able to penetrate the dura mater without buckling. Thus, a material has to be found which is stiff enough and can be machined in the micrometre range to form the required shape which fits into the U-profile. Possible candidates are ceramics or metals coated with diamond-like carbon.

Besides solving the insertion problem, the processing of the PI foils has to be extended to obtain devices with two layers of metallization to increase the number of electrode sites per shaft without increasing the shaft width.

To lessen the impact of the shaft on the neural tissue, a biodegradable material could be used to fabricate the U-profiles. After insertion, the U-profile would be dissolved with only the flexible and thin PI shaft remaining in the tissue.

In the current design, the electrode sites are located at the front while the U-profile is attached to the rear side of the shaft. It remains to be investigated whether signals with the same quality can be recorded if the U-profile is attached to the front side of the shaft occupying the first millimetre at the tip of the shaft with the electrode sites placed behind it. If this configuration turns out to record neural signals of sufficient quality, the whole device could be manufactured on one wafer by processing the U-profile on top of the PI foil using a sacrificial layer to form the inner channel of the U-profile. This would circumvent the manual assembly step which was used in this thesis.

The long-term stability of intracortical recording with these shaft electrodes has to be evaluated in a chronic implantation. The data should be directly compared to the long-term data obtained from the epicortical electrode array (chapter 8) to evaluate both approaches. A next step would be to combine both electrode types to be able to record epicortically and intracortically simultaneously.

A major development in the manufacturing of shaft electrodes for optogenetic measurements would be to directly integrate LEDs onto the PI foil. This would circumvent the as-

sembly of the optical adapter and can result in a LED-waveguide-interface with less attenuation of light power. It has to be evaluated whether other polymers could be used as waveguide materials that do not attenuate blue light as much as SU-8 does. To circumvent the time-consuming hybrid assembly step of the SU-8 channel, the channel has to be integrated in the production process on wafer level. It would be an advantage to fabricate the channel entirely with PI as it is less brittle and has a larger tensile strength than SU-8 and thus, such a channel would be easier to handle during assembly and surgery.

If this method proves reasonable, the integrated waveguide could be used for other light transmitting applications such as direct optical stimulation at a wavelength of about 1.85  $\mu\text{m}$  (Izzo 2007) and 2.12  $\mu\text{m}$  (Wells 2007) or for tissue imaging in the vicinity of an electrode interface such as optical coherence tomography (Mehta 2004).

Regarding the encouraging data and the positive feedback from the neuroscience partners on the flexible implants described in this thesis, it could be worthwhile to establish a standard for flexible electrode arrays which could be analogue to the commercialized silicon-based microimplants, the *Utah Array* and the *Michigan Probe*.



## Literature

- Aarts AAA, Neves HP, Puers RP, and Van Hoof C. An Interconnect for Out-Of-Plane Assembled Biomedical Probe Arrays. *Journal of Micromechanics and Microengineering*. 2008; 18(6): 1-7
- Adrian ED. Afferent Discharges to the Cerebral Cortex from Peripheral Sense Organs. *The Journal of Physiology*. 1941; 100: 159-191
- Adrian ED and Zotterman Y. The Impulses Produced by Sensory Nerve-Endings. *The Journal of Physiology*. 1926; 61(2): 151-171
- Andersson H, van der Wijngaart W, Enoksson P, and Stemme G. Micromachined Flow-Through Filter-Chamber for Chemical Reactions on Beads. *Sensors and Actuators B: Chemical*. 2000; 67(1-2): 203-208
- Andrushko VA and Verano JW. Prehistoric Trepanation in the Cuzco Region of Peru: A View into an Ancient Andean Practice. *American Journal of Physical Anthropology*. 2008; 137(1): 4-13
- Aravanis AM, Wang L-P, Zhang F, Meltzer LA, Morgi MZ, Schneider MB, and Deisseroth K. An Optical Neural Interface: In Vivo Control of Rodent Motor Cortex with Integrated Fiberoptic and Optogenetic Technology. *Journal of Neural Engineering*. 2007; 4(3): 143-156
- Asano E, Juhász C, Shah A, Muzik O, Chugani DC, Shah J, Sood S, and Chugani HT. Origin and Propagation of Epileptic Spasms Delineated on Electrocorticography. *Epilepsia*. 2005; 46(7): 1086-1097
- Askeland DR and Phulé PP. *The Science and Engineering of Materials*. 5 ed. Toronto: Nelson Education. 2006
- ASTM. 882-02 Standard Test Method for Tensile Properties of Thin Plastic Sheeting. ASTM International. 2002
- Badi AN, Kertesz TR, Gurgel RK, Shelton C, and Normann RA. Development of a Novel Eighth-Nerve Intraneural Auditory Neuroprosthesis. *The Laryngoscope*. 2003; 113(5): 833-842
- Bai Q, Wise KD, and Anderson DJ. A High-Yield Microassembly Structure for Three-Dimensional Microelectrode Arrays. *IEEE Transactions on Biomedical Engineering*. 2000; 47(3): 281-289
- Bak MJ, Girvin JP, Hambrecht FT, Kufta CV, Loeb GE, and Schmidt EM. Visual Sensations Produced by Intracortical Microstimulation of the Human Occipital Cortex. *Medical and Biological Engineering and Computing*. 1990; 28(3): 257-259
- Banerjee A, Meredith RM, Rodriguez-Moreno A, Mierau SB, Auberson YP, and Paulsen O. Double Dissociation of Spike Timing-Dependent Potentiation and Depression by Subunit-Prefering NMDA Receptor Antagonists in Mouse Barrel Cortex. *Cerebral Cortex*. 2009; 19(12): 2959-2969

- Bard P. Studies on the Cortical Representation of Somatic Sensibility: Harvey Lecture, February 17, 1938. *Bulletin of the New York Academy of Medicine*. 1938; 14(10): 585-607
- Barna JS, Arezzo JC, and Vaughan J. A New Multielectrode Array for the Simultaneous Recording of Field Potentials and Unit Activity. *Electroencephalography and Clinical Neurophysiology*. 1981; 52(5): 494-496
- Beebe X and Rose TL. Charge Injection Limits of Activated Iridium Oxide Electrodes with 0.2 ms Pulses in Bicarbonate Buffered Saline. *IEEE Transactions on Biomedical Engineering*. 1988; 35(6): 494-495
- Berger H. Über das Elektrenkephalogramm des Menschen. *Archiv für Psychiatrie und Nervenkrankheiten*. 1929; (87): 527-570
- Bernstein JG, Han X, Henninger MA, Ko EY, Qian X, Franzesi GT, McConnell JP, Stern P, Desimone R, and Boyden ES. Prosthetic Systems for Therapeutic Optical Activation and Silencing of Genetically-Targeted Neurons. *Proceedings of the Society of Photo-Optical Instrumentation Engineers*. 2008; 6854
- Bessonov MI, Koton MM, Kudryavtsev VV, and Laius LA. *Polyimides. Thermally Stable Polymers*. 1 ed. New York: Consultants Bureau, New York. 1987. 1-318
- Biran R, Martin DC, and Tresco PA. The Brain Tissue Response to Implanted Silicon Microelectrode Arrays is Increased when the Device is Tethered to the Skull. *Journal of Biomedical Material Research Part A*. 2007; 82A(1): 169-178
- Birolini A. *Reliability Engineering*. Berlin Heidelberg: Springer Verlag. 2007. 98
- Bliss TVP and Collingridge GL. A Synaptic Model of Memory: Long-Term Potentiation in the Hippocampus. *Nature*. 1993; 361(6407): 31-39
- Bliss TVP and Lømo T. Long-Lasting Potentiation of Synaptic Transmission in the Dentate Area of the Anaesthetized Rabbit Following Stimulation of the Perforant Path. *Journal of Physiology*. 1973; 232(2): 331-356
- Boppart SA, Wheeler BC, and Wallace CS. A Flexible Perforated Microelectrode Array for Extended Neural Recordings. *IEEE Transactions on Biomedical Engineering*. 1992; 39(1): 37-43
- Boretius T, Badia J, Pascual-Font A, Andreu D, Azevedo-Coste Ch, Divoux J-L, Stieglitz T, Navarro X, and Yoshida K. Transverse Intrafascicular Multichannel Electrode (TIME) an Interface to Peripheral Nerves: Preliminary In-Vivo Results in Rats. *14th Annual Conference of the IFESS, Sept. 14-17, Seoul, Korea*. 2009
- Bosman CA, Womelsdorf T, Oostenveld R, Rubehn B, de Weerd P, Stieglitz T, and Fries P. 252-Site Subdural LFP Recordings in Monkey Reveal Large-Scale Effects of Selection Attention. *COSYNE 2010 - 7th Computational and Systems Neuroscience Meeting, Feb.25-28, Salt Lake City, UT, USA*. 2010a. 194
- Bosman C, Schoffelen J.M., Bastos A, Oostenveld R, Womelsdorf T, Rubehn B, de Weerd P., Stieglitz T, and Fries P. Inter-Areal Gamma- and Beta-Band Synchronization Networks and their Modulation by Attention. *in preparation*. 2010b;

- Boyden ES, Zhang F, Bamberg E, Nagel G, and Deisseroth K. Millisecond-Timescale, Genetically Targeted Optical Control of Neural Activity. *Nature Neuroscience*. 2005; 8(9): 1263-1268
- Bradley DC, Troyk PR, Berg JA, Bak M, Cogan S, Erickson R, Kufta C, Mascaro M, McCreery D, Schmidt EM, Towle VL, and Xu H. Visuotopic Mapping Through a Multichannel Stimulating Implant in Primate V1. *Journal of Neurophysiology*. 2005; 93(3): 1659-1670
- Braitenberg V and Schüz A. *Cortex: Statistics and Geometry of Neuronal Connectivity*. Berlin Heidelberg: Springer-Verlag. 1998
- Bressler SL, Coppola R, and Nakamura R. Episodic Multiregional Cortical Coherence at Multiple Frequencies During Visual Task Performance. *Nature*. 1993; 366(6451): 153-156
- Brindley GS. Electrode-Arrays for Making Long-Lasting Electrical Connexion to Spinal Roots. *The Journal of Physiology*. 1972; 222(2): 135-136
- Brindley GS, Polkey CE, and Rushton DN. Sacral Anterior Root Stimulators for Bladder Control in Paraplegia. *Paraplegia*. 1982; 20: 365-381
- Broca P. On the Site of the Faculty of Articulated Speech (English Translation). *Archives of Neurology*. 1865; 43: 1065-7210
- Brodmann K. *Vergleichende Lokalisationslehre der Grosshirnrinde in ihren Prinzipien dargestellt auf Grund des Zellenbaues*. Leipzig: Barth. 1909
- Brummer SB and Turner MJ. Electrochemical Considerations for Safe Electrical Stimulation of the Nervous System with Platinum Electrodes. *IEEE Transactions on Bio-medical Engineering*. 1977; 24(1): 59-63
- Bruus H. *Theoretical Microfluidics*. Oxford: Oxford University Press. 2008. 51
- Bullara LA, Agnew WF, Yuen TG, Jacques S, and Pudenz RH. Evaluation of Electrode Array Material for Neural Prostheses. *Neurosurgery*. 1979; 5(6): 681-686
- Burns BD and Robson JG. "Weightless" Micro-Electrodes for Recording Extracellular Unit Action Potentials from the Central Nervous System. *Nature*. 1960; 186(4720): 246-247
- Burrige J, Haugland M, Larsen B, Pickering RM, Svaneborg N, Iversen HK, Brogger Christensen P, Haase J, Brennum J, and Sinkjaer T. Phase II Trial to Evaluate the ActiGait Implanted Drop-Foot Stimulator in Established Hemiplegia. *Journal of Rehabilitation Medicine*. 2007; 39(3): 212-218
- Buzsáki G. The Gamma Buzz: Gluing by Oscillations in the Waking Brain. *Rhythms of the Brain*. New York: Oxford University Press. 2006. pp. 231-261
- Campbell FJ, Brewer AK, Orr RJ, Janicke TA, and Bruning AM. Hydrolytic Deterioration of Polyimide Insulation on Naval Aircraft Wiring. *Annual Report: Conference on Electrical Insulation and Dielectric Phenomena, Oct. 16-20, Ottawa, Ont., Canada*. 1988. 180-188
- Campbell PK, Jones KE, Huber RJ, Horch KW, and Normann RA. A Silicon-Based, Three-Dimensional Neural Interface: Manufacturing Processes for an Intracortical

- Electrode Array. *IEEE Transactions on Biomedical Engineering*. 1991; 38(8): 758-768
- Cantrell DR, Inayat S, Taflove A, Ruoff RS, and Troy JB. Incorporation of Electrode-Electrolyte Interface into Finite-Element Models of Metal Microelectrodes. *Journal of Neural Engineering*. 2008; 5: 54-67
- Carod-Artal FJ and Vázquez-Cabrera CB. Neurological Paleopathology in the Pre-Columbine Cultures of the Coast and the Andean Plateau (II). The History of Cranial Trepanations. *Revista de Neurologia*. 2004; 38(9): 886-894
- Caton R. The Electric Currents of the Brain. *British Medical Journal*. 1875; 2(765): 278
- CE Mark for Cyberonic's Vagus Nerve Stimulator. <http://www.cyberonics.com/en/press-room/>. 2004; last access 16 September 2010
- CE Mark for Neurodan's Drop Foot Stimulator. 2006; last access 16 September 2010
- CE Mark for St. Jude's Deep Brain Stimulator treating Parkinson's Disease. <http://www.sjm.com/corporate/media-room/media-kits/patient-conditions-and-therapies/deep-brain-stimulation-for-parkinsons-disease.aspx>. 2009; last access 16 September 2010
- Ceballos D, Valero-Cabre A, Valderrama E, Schuettler M, Stieglitz T, and Navarro X. Morphologic and Functional Evaluation of Peripheral Nerve Fibres Regenerated Through Polyimide Sieve Electrodes over Long-Term Implantation. *Journal of Biomedical Materials Research*. 2002; 60: 517-528
- Celio MR, Spreafico R, De Biasi S, and Vitellaro-Zuccarello L. Perineuronal Nets: Past and Present. *Trends in Neurosciences*. 1998; 21(12): 510-515
- Cella JA. Degradation and Stability of Polyimides. in Ghosh MK and Mittal KL, Eds. *Polyimides: Fundamentals and Applications*. New York: Marcel Dekker. 1996. pp. 343-365
- Chao ZC, Nagasaka Y, and Fujii N. Long-term Asynchronous Decoding of Arm Motion Using Electrographic Signals in Monkey. *Frontiers in Neuroprosthetics*. 2010; 3(3): 1-10
- Chen J, Wise KD, Hetke JF, and Bledsoe Jr SC. A Multichannel Neural Probe for Selective Chemical Delivery at the Cellular Level. *IEEE Transactions on Biomedical Engineering*. 1997; 44(8): 760-769
- Chen Y-Y, Lai H-Y, Lin S-H, Cho C-W, Chao W-H, Liao C-H, Tsang S, Chen Y-F, and Lin S-Y. Design and Fabrication of a Polyimide-Based Microelectrode Array: Application in Neural Recording and Repeatable Electrolytic Lesion in Rat Brain. *Journal of Neuroscience Methods*. 2009; 182(1): 6-16
- Cheng K, Waggoner RA, and Tanaka K. Human Ocular Dominance Columns as Revealed by High-Field Functional Magnetic Resonance Imaging. *Neuron*. 2001; 32(2): 359-374
- Cheung KC. Implantable Microscale Neural Interfaces. *Biomedical Microdevices*. 2007; 9(6): 923-938

- Cho I-J, Baak H-W, and Yoon E. A 16-Site Neural Probe Integrated with a Waveguide for Optical Stimulation. *Proceedings of the 23rd IEEE International Conference on Micro Electro Mechanical Systems, Jan.24-28, Hong-Kong*. 2010. 995-998
- Coburn JC and Pottiger MT. Thermal Curing in Polyimide Films and Coatings. in Ghosh MK and Mittal KL, Eds. *Polyimides: Fundamentals and Applications*. New York: Marcel Dekker. 1996. pp. 207-247
- Cogan SF. Neural Stimulation and Recording Electrodes. *Annual Review of Biomedical Engineering*. 2008; 10: 275-309
- Cohen MX, Axmacher N, Lenartz D, Elger CE, Sturm V, and Schlaepfer TE. Nuclei Accumbens Phase Synchrony Predicts Decision-Making Reversals Following Negative Feedback. *Journal of Neuroscience*. 2009; 29(23): 7591-7598
- Cooper R. Electrodes. *American Journal of EEG Technology*. 1963; 3(4): 91-101
- Cooper R, Winter AL, Crow HJ, and Walter WG. Comparison of Subcortical, Cortical and Scalp Activity Using Chronically Indwelling Electrodes in Man. *Electroencephalography and Clinical Neurophysiology*. 1965; 18(3): 217-228
- Cubelli R and Montagna CG. A Reappraisal of the Controversy of Dax and Broca. *Journal of the History of the Neurosciences*. 1994; 3(4): 215-226
- Delasi R. Effect of Water on the Properties of a Glass-Polyimide Laminate. *Journal of Material Science*. 1975; 10(11): 1951-1958
- Delasi R. Thermal Regeneration of the Tensile Properties of Hydrolytically Degraded Polyimide Film. *Journal of Applied Polymer Science*. 1972; 16(11): 2909-2919
- Delasi R and Russell J. Aqueous Degradation of Polyimides. *Journal of Applied Polymer Science*. 1971; 15: 2965-2974
- Deisseroth K, Feng G, Majewska AK, Miesenbock G, Ting A, and Schnitzer MJ. Next-Generation Optical Technologies for Illuminating Genetically Targeted Brain Circuits. *Journal of Neuroscience*. 2006; 26(41): 10380-10386
- del Campo A and Greiner C. SU-8: a Photoresist for High-Aspect-Ratio and 3D Submicron Lithography. *Journal of Micromechanics and Microengineering*. 2007; 17(6): R81
- DeRobertis EDP and Bennett HS. Submicroscopic Vesicular Component in the Synapse. *Federation Proceedings American Physiological Society*. 1954; 13: 35
- DeRobertis EDP and Vaz Ferreira A. Submicroscopic Changes of the Nerve Endings in the Adrenal Medulla after Stimulation of the Splanchnic Nerve. *Journal of Biophysical and Biochemical Cytology*. 1957; 3(4): 611
- DiLorenzo DJ and Bronzino JD. *Neuroengineering*. Boca Raton: CRC Press. 2008
- DiSalle F, Scarabino T, Esposito F, Aragri A, Santopaolo O, Elefante A, Cirillo M, Cirillo S, and Elefante R. High-Field Strength Functional MRI. in U Salvolini and T Scarabino, Eds. *High Field Brain MRI: Use in Clinical Practice*. Berlin Heidelberg: Springer-Verlag. 2006. pp. 107-132

- Djourno A and Eyries C. Auditory Prosthesis by Means of a Distant Electrical Stimulation of the Sensory Nerve with the Use of an Indwelt Coiling. *La Presse Médicale*. 1957; 65: 1417
- Du Bois-Reymond E. *Untersuchungen über thierische Elektrizität*. Berlin: Georg Reimer. 1848
- Eckhorn R, Bauer R, Jordan W, Brosch M., Kruse W, Munk M, and Reitboeck HJ. Coherent Oscillations: A Mechanism of Feature Linking in the Visual Cortex? *Biological Cybernetics*. 1988; 60(2): 121-130
- Edell DJ, Toi VV, McNeil VM, and Clark LD. Factors Influencing the Biocompatibility of Insertable Silicon Microshafts in Cerebral Cortex. *IEEE Transactions on Biomedical Engineering*. 1992; 39(6): 635-643
- Ehrlich I, Humeau Y, Grenier F, Cioocchi S, Herry C, and Lüthi A. Amygdala Inhibitory Circuits and the Control of Fear Memory. *Neuron*. 2009; 62(6): 757-771
- Eldada L. Polymer Integrated Optics: Promise vs. Practically. DuPont Photonics Technologies (Photonics West). 2002
- Eldada L, Fujita J, Radojevic A, Gerhardt R, and Izubara T. Hybrid Organic-Inorganic Optoelectronic Subsystems on a Chip. DuPont Photonics Technologies (Photonics West). 2005
- Eldada L and Shacklette LW. Advances in Polymer Integrated Optics. *IEEE Journal of Selected Topics in Quantum Electronics*. 2000; 6(1): 54-68
- Engel AK, Fries P, and Singer W. Dynamic Predictions: Oscillations and Synchrony in Top-Down Processing. *Nature Reviews Neuroscience*. 2001; 2(10): 704-716
- Engel AK, Roelfsema PR, Fries P, Brecht M, and Singer W. Role of the Temporal Domain for Response Selection and Perceptual Binding. *Cerebral Cortex*. 1997; 7(6): 571-582
- EU. European Commission Project: TIME (Transverse, Intrafascicular Multichannel Electrode system for induction of sensation and treatment of phantom limb pain in amputees). *in the 7th Framework Program*. 2009; <http://www.project-time.eu/> last access 21.09.2010
- Factor BJ, Russell TP, and Toney MF. Surface-Induced Ordering of an Aromatic Polyimide. *Physical Review Letters*. 1991; 66(9): 1181-1184
- FDA. Approval of Medtronic Activa® Dystonia Therapy. <http://www.fda.gov/MedicalDevices/ProductsandMedicalProcedures/DeviceApprovalsandClearances/Recently-ApprovedDevices/ucm082535.htm>. 2003; last access 30 May 2010
- FDA. Approval of Cyberonics VNS Therapy System. <http://www.fda.gov/MedicalDevices/ProductsandMedicalProcedures/DeviceApprovalsandClearances/Recently-ApprovedDevices/ucm078532.htm>. 2005; last access 30 May 2010
- Ferree TC, Clay MT, and Tucker DM. The spatial resolution of scalp EEG. *Neurocomputing*. 2001; 38-40: 1209-1216

- Ferster D. Is Neural Noise Just a Nuisance? *Science*. 1996; 273(5283): 1812-0
- Fiedler E, Schuettler M, Henle C, Zengerle R, and Stieglitz T. Integration of Microfluidic Channels Into Laser-Fabricated Neural Electrode Arrays. In: J.van der Sloten, P.Verdonck, M.Nyssen, J.Haueisen (Eds.): *ECIFMBE (European Conference of the International Federation for Medical and Biological Engineering), IFMBE Proceedings 22*. 2008. 2431-2434
- Finger S. *Origins of Neuroscience: A History of Explorations into Brain Function*. New York: Oxford University Press. 1994
- Finn WE and LoPresti PG. *Handbook of Neuroprosthetic Methods*. Boca Raton: CRC Press. 2003
- Flourens JP. Experimental Researches on the Properties and Functions of the Nervous System in the Vertebrate Animal. in Dennis W., Ed. *Readings in the History of Psychology*. Great Yarmouth: C & J Read. 2007. pp. 129-139
- Franks W, Schenker I, Schmutz P, and Hierlemann A. Impedance Characterization and Modelling of Electrodes for Biomedical Applications. *IEEE Transactions on Bio-medical Engineering*. 2005; 52(7): 1295-1302
- Fries P. A Mechanism for Cognitive Dynamics: Neuronal Communication Through Neuronal Coherence. *Trends in Cognitive Sciences*. 2005; 9(10): 474-480
- Fries P. Neuronal Gamma-Band Synchronization as a Fundamental Process in Cortical Computation. *Annual Review of Neuroscience*. 2009; 32(1): 209-224
- Fries P, Reynolds JH, Rorie AE, and Desimone R. Modulation of Oscillatory Neuronal Synchronization by Selective Visual Attention. *Science*. 2001a; 291: 1560-1563
- Fries P, Neuenschwander S, Engel AK, Goebel R, and Singer W. Rapid Feature Selective Neuronal Synchronization Through Correlated Latency Shifting. *Nature Neuroscience*. 2001b; 4(2): 194-200
- Fritsch G and Hitzig E. *Ueber die elektrische Erregbarkeit des Grosshirns*. Berlin: G. Eichler. 1870
- Gallese V, Fadiga L, Fogassi L, and Rizzolatti G. Action Recognition in the Premotor Cortex. *Brain*. 1996; 119(2): 593-609
- Galtrey CM and Fawcett JW. The role of chondroitin sulfate proteoglycans in regeneration and plasticity in the central nervous system. *Brain Research Reviews*. 2007; 54(1): 1-18
- Gambling WA. The Rise and Rise of Optical Fibers. *IEEE Journal of Selected Topics in Quantum Electronics*. 2000; 6(6): 1084-1093
- Gawad S, Giugliano M, Wessling B, Markram H, Schnakenberg U, Renaud P, and Morgan H. Substrate Arrays of Iridium Oxide Microelectrodes for In Vitro Neuronal Interfacing. *Frontiers in Neuroengineering*. 2009; 2(1): 1.1-1.7
- Geddes LA. Historical Evolution of Circuit Models for the Electrode-Electrolyte Interface. *Annals of Biomedical Engineering*. 1997; 25: 1-14

- Geddes LA and Baker LE. Electrodes. *Principles of Applied Biomedical Instrumentation*. 3 ed. New York, Chichester, Brisbane, Toronto, Singapore: John Wiley & Sons. 1989. pp. 315-452
- George MS, Sackheim HA, Rush AJ, Marangell LB, Nahas Z, Husain MM, Lisanby S, Burt T, Goldman J, and Ballenger JC. Vagus Nerve Stimulation: A New Tool for Brain Research and Therapy. *Biological Psychiatry*. 2000; 47: 287-295
- Ghosh MK and Mittal KL. *Polyimides: Fundamentals and Applications*. New York: Marcel Dekker Inc. 1996. 1-912
- Ghovanloo M and Najafi K. A Wireless Implantable Multichannel Microstimulating System-on-a-Chip With Modular Architecture. *IEEE Trans Neural Syst Rehabil Eng*. 2007; 15(3): 449-457
- Gielen S, Krupa M, and Zeitler M. Gamma Oscillations as a Mechanism for Selective Information Transmission. *Biological Cybernetics*. 2010; 103(2): 151-165
- Gogolla N, Caroni P, Luthi A, and Herry C. Perineuronal Nets Protect Fear Memories from Erasure. *Science*. 2009; 325(5945): 1258-1261
- Gradinaru V, Mogri M, Thompson KR, Henderson JM, and Deisseroth K. Optical Deconstruction of Parkinsonian Neural Circuitry. *Science*. 2009; 324(5925): 354-359
- Gradinaru V, Thompson KR, Zhang F, Mogri M, Kay K, Schneider MB, and Deisseroth K. Targeting and Readout Strategies for Fast Optical Neural Control In Vitro and In Vivo. *Journal of Neuroscience*. 2007; 27(52): 14231-14238
- Gray CM, Maldonado PF, Wilson M, and McNaughton BL. Tetrodes Markedly Improve the Reliability and Yield of Multiple Single-Unit Isolation from Multi-Unit Recordings in Cat Striate Cortex. *Journal of Neuroscience Methods*. 1995; 63: 43-54
- Gray CM and Singer W. Stimulus-Specific Neuronal Oscillation in the Cat Visual Cortex: A Cortical Functional Unit. *Society for Neuroscience*. 1987; Abstr. 13, 404.3
- Gray CM. The Temporal Correlation Hypothesis of Visual Feature Integration: Still Alive and Well. *Neuron*. 1999; 24(1): 31-47
- Gray CM, Engel AK, König P, and Singer W. Synchronization of Oscillatory Neuronal Responses in Cat Striate Cortex: Temporal Properties. *Visual Neuroscience*. 1992; 8(04): 337-347
- Gray CM, König P, Engel AK, and Singer W. Oscillatory responses in cat visual cortex exhibit inter-columnar synchronization which reflects global stimulus properties. *Nature*. 1989; 338(6213): 334-337
- Gray JAB and Svaetichin G. Electrical Properties of Platinum Tipped Micro-Electrodes in Ringer's Solution. *Acta Physiologica Scandinavica*. 1951; 24(2-3): 278-284
- Grayson ACR, Shawgo RS, Johnson AM, Flynn NT, Li Y, Cima MJ, and Langer R. A BioMEMS Review: MEMS Technology for Physiologically Integrated Devices. *Proceedings of the IEEE*. 2004; 92(1): 6-21
- Green JD. A Simple Microelectrode for Recording from the Central Nervous System. *Nature*. 1958; 182(4640): 962



- Grellmann W and Seidler S. *Polymer Testing*. München: Carl Hanser Verlag. 2007
- Grossman N, Poher V, Grubb MS, Kennedy GT, Nikolic K, McGovern B, Berlinguer Palmini R, Gong Z, Drakakis EM, Neil MA, Dawson MD, Burrone J, and Degenaar P. Multi-Site Optical Excitation Using ChR2 and Micro-LED Array. *J Neural Eng*. 2010; 7(1)
- Grundfest H. Stainless Steel Micro-Needle Electrodes Made by Electrolytic Pointing. *Rev Sci Instrum*. 1950; 21(4): 360-361
- Grundfest H and Campbell B. Origin, Conduction and Termination of Impulses in the Dorsal Spino-Cerebellar Tract of Cats. *Journal of Neurophysiology*. 1942; 5(4): 275-294
- Gualtierotti T and Bailey P. A neutral buoyancy micro-electrode for prolonged recording from single nerve units. *Electroencephalography and Clinical Neurophysiology*. 1968; 25(1): 77-81
- Haggerty HS and Lusted HS. Histological Reaction to Polyimide Films in the Cochlea. *Acta Otolaryngol*. 1989; 107(1-2): 13-22
- Haj Hosseini N, Hoffmann R, Kisban S, Stieglitz T, Paul O, and Ruther P. Comparative Study on the Insertion Behavior of Cerebral Microprobes. *Proceedings of the 29th Annual International Conference of the IEEE EMBS, Aug.23-26, Lyon, France*. 2007. 4711-4714
- Han X, Qian X, Bernstein JG, Zhou Hh, Franzesi GT, Stern P, Bronson RT, Graybiel AM, Desimone R, and Boyden ES. Millisecond-Timescale Optical Control of Neural Dynamics in the Nonhuman Primate Brain. *Neuron*. 2009; 62(2): 191-198
- Hanna GR and Johnson RN. A Rapid and Simple Method for the Fabrication of Arrays of Recording Electrodes. *Electroencephalography and Clinical Neurophysiology*. 1968; 25(3): 284-286
- Harper BD and Rao JM. Some Effects of Water Immersion on the Mechanical Behavior of a Polyimide Film. *Journal of Electronic Packaging*. 1994; 116(4): 317-319
- Harris S, Myles J, Zheng Y, and Berwick J. Does Neural Input or Processing Play a Greater Role in the Magnitude of Neuroimaging Signals? *Frontiers in Neuroengineering*. 2010; 2(15)
- Harrison RR, Watkins PT, Kier RJ, Lovejoy RO, Black DJ, Greger B, and Solzbacher F. A Low-Power Integrated Circuit for a Wireless 100-Electrode Neural Recording System. *IEEE Journal of Solid-State Circuits*. 2007; 42(1): 123-133
- Hasegawa M and Horie K. Photophysics, Photochemistry, and optical Properties of Polyimides. *Prog Polym Sci*. 2001; 26: 259-335
- Hebb DO. *The organization of behavior*. New York: Wiley. 1949
- Helmholtz Hv. Ueber einige Gesetze der Vertheilung elektrischer Ströme in körperlichen Leitern, mit Anwendung auf die thierisch-elektrischen Versuche (Schluss.). *Annalen der Physik und Chemie*. 1853; 165(7): 353-377

- Helmholtz Hv. Messungen über den zeitlichen Verlauf der Zuckung animalischer Muskeln und die Fortpflanzungsgeschwindigkeit der Reizung in den Nerven. *Archiv für Anatomie, Physiologie und wissenschaftliche Medizin*. 1850a; 276-364
- Helmholtz Hv. Versuche über die Fortpflanzungsgeschwindigkeit der Reizung in den sensiblen Nerven des Menschen. Mittheilung für die physikalische Gesellschaft in Berlin. 1850b
- Hemmerich KJ. General Aging Theory and Simplified Protocol for Accelerated Aging of Medical Devices. *Medical Plastics and Biomaterials Magazine*. 1998; 4: 16-24
- Henle C. personal communication. *Laboratory for Biomedical Microtechnology, University of Freiburg, Germany*. 2008;
- Henle C. personal communication. *Laboratory for Biomedical Microtechnology, University of Freiburg - IMTEK, Germany*. 2010;
- Henrie JA and Shapley R. LFP Power Spectra in V1 Cortex: The Graded Effect of Stimulus Contrast. *Journal of Neurophysiology*. 2005; 94(1): 479-490
- Herry C, Ciocchi S, Senn V, Demmou L, Müller C, and Lüthi A. Switching on and off Fear by Distinct Neuronal Circuits. *Nature*. 2008; 454(7204): 600-606
- Heuschkel MO, Fejtl M, Raggenbass M, and Renaud P. A Three-Dimensional Multi-Electrode Array for Multi-Site Stimulation and Recording in Acute Brain Slices. *Journal of Neuroscience Methods*. 2002; 114: 135-148
- Heuschkel MO, Guérin L, Buisson B, Bertrand D, and Renaud P. Buried Microchannels in Photopolymer for Delivering of Solutions to Neurons in a Network. *Sensors and Actuators B: Chemical*. 1998; 48(1-3): 356-361
- Hochberg LR, Serruya MD, Friehs GM, Mukand JA, Saleh M, Caplan AH, Branner A, Chen D, Penn RD, and Donoghue JP. Neuronal Ensemble Control of Prosthetic Devices by a Human with Tetraplegia. *Nature*. 2006; 442(7099): 164-171
- Hodgkin AL and Huxley AF. Action Potentials Recorded from Inside a Nerve Fibre. *Nature*. 1939; 144: 710-711
- Hollenberg BA, Richards CD, Richards R, Bahr DF, and Rector DM. A MEMS Fabricated Flexible Electrode Array for Recording Surface Field Potentials. *Journal of Neuroscience Methods*. 2006; 153: 147-153
- Hougham G, Tesoro G, and Viehbeck A. Influence of Free Volume Change on the Relative Permittivity and Refractive Index in Fluoropolyimides. *Macromolecules*. 1996; 29(10): 3453-3456
- Hsu T-R. *MEMS and Microsystems: Design, Manufacture, and Nanoscale Engineering*. Hoboken: John Wiley and Sons. 2008
- Huang R, Pang C, Tai Y-C, Emken J, Ustun C, Andersen RA, and Burdick JW. Integrated Parylene-Cabled Silicon Probes for Neural Prosthetics. *Proceedings of the 21th IEEE Annual Conference on MEMS; Jan 13-17, Tucson, AZ, USA*. 2008. 240-243
- Hubel DH. Tungsten Microelectrode for Recording from Single Units. *Science*. 1957; 125(3247): 549-550

- Humphrey DR and Schmidt EM. Extracellular Single-Unit Recording Methods. in AA Boulton, GB Baker, and CH Vanderwolf, Eds. *Neuromethods, Vol. 15. Neurophysiological techniques. Applications to neural systems*. 1 ed. Clifton, N.J.: The Humana Press Inc. 1990. pp. 1-64
- Isaacs RE, Weber DJ, and Schwartz AB. Work Toward real-Time Control of a Cortical Neural Prothesis. *IEEE Transactions on Rehabilitation Engineering*. 2000; 8(2): 196-198
- ISO. ISO 14644-1: Cleanrooms and Associated Controlled Environments - Part 1: Classification of Air Cleanliness (ISO 14644-1 : 1999). 1999
- Izzo AD, Walsh JT, Jansen ED, Bendett M, Webb J, Ralph H, and Richter CP. Optical Parameter Variability in Laser Nerve Stimulation: A Study of Pulse Duration, Repetition Rate, and Wavelength. *IEEE Transactions on Biomedical Engineering*. 2007; 54(6): 1108-1114
- Janssen P, Srivastava S, Ombelet S, and Orban GA. Coding of Shape and Position in Macaque Lateral Intraparietal Area. *Journal of Neuroscience*. 2008; 28(26): 6679-6690
- Jarvis MR and Mitra PP. Sampling Properties of the Spectrum and Coherency of Sequences of Action Potentials. *Neural Computation*. 2001; 13: 717-749
- Jellema T and Weijnen JAWM. A Slim Needle-Shaped Multiwire Microelectrode for Intracerebral Recording. *Journal of Neuroscience Methods*. 1991; 40(2-3): 203-209
- Jensen RJ and Rizzo JFI. Activation of Ganglion Cells in Wild-Type and rd1 Mouse Retinas with Monophasic and Biphasic Current Pulses. *Journal of Neural Engineering*. 2009; 6(3): 035004
- Johnson MD, Kao OE, and Kipke DR. Spatiotemporal pH Dynamics Following Insertion of Neural Microelectrode Arrays. *Journal of Neuroscience Methods*. 2007; 160: 276-287
- Johnson MD, Otto KJ, and Kipke DR. Repeated Voltage Biasing Improves Unit Recordings by Reducing Resective Tissue Impedances. *IEEE Transactions on Neural Systems and Rehabilitation Engineering*. 2005; 13(2): 160-165
- Kandel ER, Schwartz JH, and Jessell TM. *Principles of Neural Science*. 4 ed McGraw-Hill. 2000
- Kane CF and Krchnavek RR. Benzocyclobutene Optical Waveguides. *IEEE Photonics Technology Letters*. 1995; 7(5): 535-537
- Kaneko H, Suzuki S, Okada J, and Akamatsu M. Classifying Neuronal Spikes from Multi-unit Recording by Using a Multisite Electrode. *Proceedings of the 18th Annual International Conference of the IEEE Engineering in Medicine and Biology Society, Oct 13-Nov 3, Amsterdam, The Netherlands*. 1996. paper 928
- Katzner S, Nauhaus I, Benucci A, Bonin V, Ringach D, and Carandini M. Local Origin of Field Potentials in Visual Cortex. *Neuron*. 2009; 61(1): 35-41
- Kee JS, Poenar DP, Neuzil P, and Yobas L. Monolithic Integration of Poly(dimethylsiloxane) Waveguides and Microfluidics for On-Chip Absorbance Measurements. *Sensors and Actuators B: Chemical*. 2008; 134(2): 532-538

- Kennedy RT, Thompson JE, and Vickroy TW. In Vivo Monitoring of Amino Acids by Direct Sampling of Brain Extracellular Fluid at Ultralow Flow Rates and Capillary Electrophoresis. *Journal of Neuroscience Methods*. 2002; 114(1): 39-49
- Kenney L, Bultstra G, Buschman R, Taylor P, Mann G, Holsheimer J, Nene A, Tenniglo M, van der Aa H, and Hobby J. An Implantable Two Channel Drop Foot Stimulator: Initial Clinical Results. *Artificial Organs*. 2002; 26(3): 267-270
- Kerrigan JF, Litt B, Fisher RS, Cranstoun S, French JA, Blum DE, Dichter M, Shetter A, Baltuch G, Jaggi J, Krone S, Brodie M, Rise M, and Graves N. Electrical Stimulation of the Anterior Nucleus of the Thalamus for the Treatment of Intractable Epilepsy. *Epilepsia*. 2004; 45(4): 346-354
- Kim D-H, Viventi J, Amsden JJ, Xiao J, Vigeland L, Kim Y-S, Blanco JA, Panilaitis B, Frechette ES, Contreras D, Kaplan DL, Omenetto FG, Huang Y, Hwang K-C, Zakin MR, Litt B, and Rogers JA. Dissolvable Films of Silk Fibroin for Ultrathin Conformal Bio-Integrated Electronics. *Nature Materials*. 2010; 9(6): 511-517
- Kim JH and Richardson R. A Developmental Dissociation of Context and GABA Effects on Extinguished Fear in Rats. *Behavioral Neuroscience*. 2007b; 121(1): 131-139
- Kim JH and Richardson R. A Developmental Dissociation in Reinstatement of an Extinguished Fear Response in Rats. *Neurobiology of Learning and Memory*. 2007a; 88(1): 48-57
- Kim Y-T, Hitchcock RW, Bridge MJ, and Tresco PA. Chronic Response of Adult Rat Brain Tissue to Implants Anchored to the Skull. *Biomaterials*. 2004; 25(12): 2229-2237
- Kim YH, Lee C, Ahn KM, Lee M, and Kim YJ. Robust and Real-Time Monitoring of Nerve Regeneration Using Implantable Flexible Microelectrode Array. *Biosensors and Bioelectronics*. 2009; 24(7): 1883-1887
- Kipke DR, Pellinen DS, and Vetter RJ. Advanced Neural Implants Using Thin-Film Polymers. *Circuits and Systems, 2002.ISCAS 2002.IEEE International Symposium on*. 2002. IV-173
- Kisban S, Janssen P, Herwik S, Stieglitz T, Paul O, and Ruther P. Hybrid Microprobes for Chronic Implantation in the Cerebral Cortex. *30th Annual International IEEE EMBS Conference, August 20-24, Vancouver, British Columbia, Canada*. 2008. 2016-2019
- Kitzmiller J, Beversdorf D, and Hansford D. Fabrication and Testing of Microelectrodes for Small-Field Cortical Surface Recordings. *Biomedical Microdevices*. 2006; 8: 81-85
- Klinge PM, Vafa MA, Brinker T, Brandis T, Walter GF, Stieglitz T, Samii M, and Wewetzer K. Immunohistochemical Characterization of Axonal Sprouting and Reactive Tissue Changes After Long-Term Implantation of a Polyimide Sieve Electrode to the Transected Adult Rat Sciatic Nerve. *Biomaterials*. 2001; 22(17): 2333-2343
- Koch KP, Schuettler M, and Stieglitz T. Considerations on Noise of Electrodes in Combination with Amplifiers for Bioelectrical Signal Recording. *Biomedizinische Technik*. 2002; 47(Suppl 1 Pt 2:514-6): 514-516
- Korlyakov ED. The Becquerel Effect. *Russian Physics Journal*. 1969; 12(8): 1054-1056

- Kotzar G, Freas M, Abel P, Fleischman AJ, Roy S, Zorman C, Moran AM, and Melzak J. Evaluation of MEMS Materials of Construction for Implantable Medical Devices. *Biomaterials*. 2002; 23(13): 2737-2750
- Kovacs GTA. Introduction to the Theory, Design, and Modeling of Thin-Film Microelectrodes for Neural Interfaces. in DA Stenger and TM McKenna, Eds. *Enabling Technologies for Cultured Neural Networks*. San Diego, California: Academic Press, Inc. 1994. pp. 121-165
- Kralik JD, Dimitrov DF, Krupa DJ, Katz DB, Cohen D, and Nicolelis MAL. Techniques for Long-Term Multisite Neuronal Ensemble Recordings in Behaving Animals. *Methods*. 2001; 25: 121-150
- Kreiman G, Hung CP, Kraskov A, Quiroga RQ, Poggio T, and DiCarlo JJ. Object Selectivity of Local Field Potentials and Spikes in the Macaque Inferior Temporal Cortex. *Neuron*. 2006; 49(3): 433-445
- Kreiter AK and Singer W. Oscillatory Neuronal Response in the Visual Cortex of the Awake Macaque Monkey. *European Journal of Neuroscience*. 1992; 4: 369-375
- Kringelbach ML, Jenkinson N, Green AL, Owen SLF, Hansen PC, Cornelissen PL, Holliday IE, Stein J, and Aziz TZ. Deep brain stimulation for chronic pain investigated with magnetoencephalography. *NeuroReport*. 2007; 18(3)
- Krüger J and Bach M. Simultaneous Recording with 30 Microelectrodes in Monkey Visual Cortex. *Exp Brain Res*. 1981; 41(2): 191-194
- Krüger J, Caruana F, Dalla Volta R, and Rizzolatti G. Seven Years of Recording from Monkey Cortex with a Chronically Implanted Multiple Microelectrode. *Frontiers in Neuroengineering*. 2010; 3: 6
- Lacour SP, Atta R, FitzGerald JJ, Blamire M, Tarte E, and Fawcett JW. Polyimide Micro-Channel Arrays for Peripheral Nerve Regenerative Implants. *Sensors and Actuators A: Physical*. 2008; 147(2): 456-463
- Lago N, Ceballos D, Rodriguez FJ, Stieglitz T, and Navarro X. Long Term Assessment of Axonal Regeneration Through Polyimide Regenerative Electrodes to Interface the Peripheral Nerve. *Biomaterials*. 2005; 26: 2021-2031
- Lago N, Udina E, Ramachandran A, and Navarro X. Neurobiological Assessment of Regenerative Electrodes for Bidirectional Interfacing Injured Peripheral Nerves. *IEEE Transactions on Biomedical Engineering*. 2007a; 54(6): 1129-1137
- Lago N, Yoshida K, Koch KP, and Navarro X. Assessment of Biocompatibility of Chronically Implanted Polyimide and Platinum Intrafascicular Electrodes. *IEEE Transactions on Biomedical Engineering*. 2007b; 54(2): 281-290
- Laming PR and Syková E. *Glial Cells: their Role in Behaviour*. Cambridge: Cambridge University Press. 1998
- Lashley KS. Mass Action in Cerebral Function. *Science*. 1931; 73(1888): 245-254
- Leach J, Achyuta AKH, and Murthy SK. Bridging the Divide Between Neuroprosthetic Design, Tissue Engineering and Neurobiology. *Frontiers in Neuroengineering*. 2010; 2(18): 1-19

- LeDoux JE. Emotion Circuits in the Brain. *Annual Review of Neuroscience*. 2000; 23(1): 155-184
- Lee KK, He J, Clement RS, Massia SP, and Kim B. Biocompatible Benzocyclobutene (BCB)-Based Neural Implants with Micro-Fluidic Channel. *Biosensors and Bioelectronics*. 2004a; 20: 404-407
- Lee KK, He J, Singh A, Massia SP, Ehteshami G, Kim B, and Raupp GB. Polyimide-Based Intracortical Neural Implant with Improved Structural Stiffness. *Journal of Micromechanics and Microengineering*. 2004b; 14: 32-37
- Lee KS, Lee HLT, and Ram RJ. Polymer Waveguide Backplanes for Optical Sensor Interfaces in Microfluidics. *Lab on a Chip*. 2007; 7: 1539-1545
- Leeds AR, Van Keuren ER, Durst ME, Schneider TW, Currie JF, and Paranjape M. Integration of Microfluidic and Microoptical Elements Using a Single-Mask Photolithographic Step. *Sensors and Actuators A: Physical*. 2004; 115(2-3): 571-580
- Leuthardt EC, Freudenberg Z, Bundy D, and Roland J. Microscale Recording from Human Motor Cortex: Implications for Minimally Invasive Electrocorticographic Brain-Computer Interfaces. *Neurosurgical FOCUS*. 2009; 27(1): E10
- Lewis CM, Baldassarre A, Committeri G, Romani GL, and Corbetta M. Learning Sculpts the Spontaneous Activity of the Resting Human Brain. *Proceedings of the National Academy of Sciences*. 2009; 106(41): 17558-17563
- Lide DR. *CRC Handbook of Chemistry and Physics*. 78 ed. Boca Raton, New York: CRC Press. 1997. 12-124
- Liu J and Newsome WT. Local Field Potential in Cortical Area MT: Stimulus Tuning and Behavioral Correlations. *Journal of Neuroscience*. 2006; 26(30): 7779-7790
- Liu X, Demosthenous A, and Donaldson N. Platinum Electrode Noise in the ENG Spectrum. *Medical and Biological Engineering and Computing*. 2008; 46(10): 997-1003
- Loeb GE, Bak MJ, and Duysens J. Long-Term Unit Recording from Somatosensory Neurons in the Spinal Ganglia of the Freely Walking Cat. *Science*. 1977; 197: 1192-1194
- Loeb GE and Peck RA. Cuff Electrodes for Chronic Stimulation and Recording of Peripheral Nerve Activity. *Journal of Neuroscience Methods*. 1996; 64: 95-103
- Loeb GE and Schulman JH. The Transfer of Technology from the Laboratory to the Real World. in RB Stein, PH Peckham, and DB Popovic, Eds. *Neural Prostheses. Replacing Motor Function after Disease or Disability*. New York: Oxford University Press. 1992. pp. 329-341
- Logothetis NK, Pauls J, Augath M, Trinath T, and Oeltermann A. Neurophysiological Investigation of the Basis of the fMRI Signal. *Nature*. 2001; 412(6843): 150-157
- Logothetis NK. The Underpinnings of the BOLD Functional Magnetic Resonance Imaging Signal. *Journal of Neuroscience*. 2003; 23(10): 3963-3971
- Lopes da Silva F. Neural Mechanisms Underlying Brain Waves: from Neural Membranes to Networks. *Electroencephalography and Clinical Neurophysiology*. 1991; 79(2): 81-93

- Ma H, Jen AKY, and Dalton LR. Polymer-Based Optical Waveguides: Materials, Processing, and Devices. *Advanced Materials*. 2002; 14(19): 1339-1365
- Maffei L and Rizzolatti G. Unit responses of the lateral geniculate body to light flashes during wakefulness and synchronized sleep. *Cellular and Molecular Life Sciences*. 1965; 21(10): 599-600
- Malsburg Cvd. The What and Why of Binding: The Modeler's Perspective. *Neuron*. 1999; 24(1): 95-104
- Malsburg Cvd. The Correlation Theory of Brain Function. MPI Biophysical Chemistry, Internal Report 81-2. reprinted in. in Domany E., van Hemmen J.L., and Schulten K., Eds. *Models of Neural Networks II*. Berlin: Springer. 1981.
- Malsburg Cvd and Schneider W. A Neural Cocktail-Party Processor. *Biological Cybernetics*. 1986; 54: 29-40
- Mankodiya K, Krapohl D, Hammad S, Xie Y, Klinger M, and Hofmann UG. A Simplified Production Method for Multimode Multisite Neuroprobes. *Proc 4th International IEEE/EMBS Conference on Neural Engineering, Apr 29 - May 2, Antalya, Turkey*. 2009. 211-214
- Marin C and Fernández E. Biocompatibility of Intracortical Microelectrodes: Current Status and Future Prospects. *Frontiers in Neuroengineering*. 2010; 3: 8
- Marshall WH. Cortical Representation of Tactile Sensibility as Indicated by Cortical Potentials. *Science*. 1937; 85(2207): 388-390
- Martin JH. *Neuroanatomy: Text and Atlas* McGraw-Hill Professional. 2003
- Masterton WL and Hurley CN. *Chemistry: Principles and Reactions*. Belmont: Brooks/Cole Cengage Learning. 2008
- McCreery DB, Agnew WF, Yuen TGH, and Bullara LA. Charge Density and Charge Per Phase as Cofactors in Neural Injury Induced by Electrical Stimulation. *IEEE T Bio-Med Eng*. 1990; 37(10): 996-1001
- McNaughton BL, O'Keefe J, and Barnes CA. The Stereotrode: A New Technique for Simultaneous Isolation of Several Single Units in the Central Nervous System from Multiple Unit Records. *Journal of Neuroscience Methods*. 1983; 8: 391-397
- Mehring C, Nawrot M, de Olivera SC, Vaadia E, Schulze-Bonhage A, Aertsen A, and Ball T. Comparing Information about Arm Movement Direction in Single Channels of Local and Epicortical Field Potentials from Monkey and Human Motor Cortex. *Journal of Physiology and Pharmacology*. 2004; 98(4-6): 498-506
- Mehring C, Rickert J, Vaadia E, de Oliveira SC, Aertsen A, and Rotter S. Inference of Hand Movements from Local Field Potentials in Monkey Motor Cortex. *Nature Neuroscience*. 2003; 6(12): 1253-1254
- Mehta AmD, Jung JC, Flusberg BA, and Schnitzer MJ. Fiber Optic In Vivo Imaging in the Mammalian Nervous System. *Current Opinion in Neurobiology*. 2004; 14: 1-12
- Melin J and Quake SR. Microfluidic Large-Scale Integration: The Evolution of Design Rules for Biological Automation. *Annual Review of Biophysics and Biomolecular Structure*. 2007; 36: 213-231

- Mercanzini A, Cheung K, Buhl DL, Boers M, Maillard A, Colin P, Bensadoun JC, Bertsch A, and Renaud P. Demonstration of Cortical Recording Using Novel Flexible Polymer Neural Probes. *Sensors and Actuators A: Physical*. 2008; 143(1): 90-96
- Merrill DR, Bikson M, and Jefferys JGR. Electrical Stimulation of Excitable Tissue: Design of Efficacious and Safe Protocols. *Journal of Neuroscience Methods*. 2005; 141: 171-198
- Mesulam M-M. From Sensation to Cognition. *Brain*. 1998; 121(6): 1013-1052
- Metz S, Bertsch A, and Renaud P. Flexible Polyimide Probes with Microelectrodes and Embedded Microfluidic Channels for Simultaneous Drug Delivery and Multi-Channel Monitoring of Bioelectric Activity. *Biosensors and Bioelectronics*. 2004a; 19(10): 1309-1318
- Metz S, Holzer R, and Renaud P. Fabrication of Flexible, Implantable Microelectrodes with Embedded Fluidic Microchannels. *Proceedings of the Transducers '01/ Eurosensors XV. The 11th International Conference on Solid-State Sensors and Actuators, Jun 10-14, Munich, Germany*. 2001b
- Metz S, Holzer R, and Renaud P. Polyimide-Based Microfluidic Devices. *Lab Chip*. 2001a; 1: 29-34
- Metz S, Trautmann C, Bertsch A, and Renaud P. Polyimide Microfluidic Devices with Integrated Nanoporous Filtration Areas Manufactured by Micromachining and Ion Track Technology. *Journal of Micromechanics and Microengineering*. 2004b; 14: 324-331
- Micheli C, Bosman C, Womelsdorf T, Oostenveld R, Rubehn B, De Weerd P, Stieglitz T, and Fries P. Combining High-Density Electrocorticography (ECoG) in Macaque Monkey with Source Reconstruction. *7th Forum of European Neuroscience - FENS, Jul.3-7, Amsterdam, The Netherlands*. 2010. 139.13
- Milner PM. A Model for Visual Shape Recognition. *Psychological Review*. 1974; 81(6): 521-535
- Minges ML. *Electronic Materials Handbook: Packaging* ASTM International. 1989. 962
- Missios S. Hippocrates, Galen, and the Uses of Trepanation in the Ancient Classical World. *Neurosurgical FOCUS*. 2007; 23(1): 1-9
- Mitzdorf U. Current Source-Density Method and Application in Cat Cerebral Cortex: Investigation of Evoked Potentials and EEG Phenomena. *Physiological Reviews*. 1985; 65(1): 37-100
- Molina-Luna K, Buitrago MM, Hertler B, Schubring M, Haiss F, Nisch W, Schulz JB, and Luft AR. Cortical Stimulation Mapping Using Epidurally Implanted Thin-Film Micro-electrode Arrays. *Journal of Neuroscience Methods*. 2007; 161: 118-125
- Moylan CR, Best ME, and Ree M. Solubility of Water in Polyimides: Quartz Crystal Microbalance Measurements. *Journal of Polymer Science Part B: Polymer Physics*. 1991; 29(1): 87-92
- Müller J. *Handbuch der Physiologie des Menschen für Vorlesungen*. Coblenz: Verlag J. Hölscher. 1834



- Murray S, Hillman C, and Pecht M. Environmental Aging and Deadhesion of Polyimide Dielectric Films. *Journal of Electronic Packaging*. 2004; 126(3): 390-397
- Musallam S, Bak MJ, Troyk PR, and Andersen RA. A Floating Metal Microelectrode Array for Chronic Implantation. *Journal of Neuroscience Methods*. 2007; 160: 122-127
- Musallam S, Conrneil BD, Greger B, Scherberger H, and Andersen RA. Cognitive Control Signals For Neural Prosthetics. *Science*. 2004; 305(July): 258-262
- Myers KM and Davis M. Mechanisms of Fear Extinction. *Molecular Psychiatry*. 2006; 12(2): 120-150
- Myllymaa S, Myllymaa K, Korhonen H, Töyräs J, Jääskeläinen JE, Djupsund K, Tanila H, and Lappalainen R. Fabrication and Testing of Polyimide-Based Microelectrode Arrays for Cortical Mapping of Evoked Potentials. *Biosensors and Bioelectronics*. 2009; 24(10): 3067-3072
- Nair DR, Burgess R, McIntyre CC, and Lüders H. Chronic Subdural Electrodes in the Management of Epilepsy. *Clinical Neurophysiology*. 2008; 119(1): 11-28
- Nam Y, Wheeler BC, and Heuschkel MO. Neural Recording and Stimulation of Dissociated Hippocampal Cultures Using Microfabricated Three-Dimensional Tip Electrode Array. *Journal of Neuroscience Methods*. 2006; 155(2): 296-299
- Navarro X, Calvet S, Rodriguez FJ, Stieglitz T, Blau C, Buti M, Valderrama E, and Meyer J-U. Stimulation and Recording from Regenerated Peripheral Nerves Through Polyimide Sieve Electrodes. *Journal of the Peripheral Nervous System*. 1998; 3(2): 91-101
- Naylor DE, Liu H, and Wasterlain CG. Trafficking of GABA<sub>A</sub> Receptors, Loss of Inhibition, and a Mechanism for Pharmacoresistance in Status Epilepticus. *Journal of Neuroscience*. 2005; 25(34): 7724-7733
- Nelson MJ, Pouget P, Nilsen EA, Patten CD, and Schall JD. Review of Signal Distortion Through Metal Microelectrode Recording Circuits and Filters. *Journal of Neuroscience Methods*. 2008; 169(1): 141-157
- NeuroNexus. Hybrid Fluidic Probes. *Catalog, NeuroNexus Technologies*. 2008; [http://www.neuronexustech.com/Portals/0/Catalog%20&%20Manual/catalog\\_mar08.pdf](http://www.neuronexustech.com/Portals/0/Catalog%20&%20Manual/catalog_mar08.pdf), last access 21.09.2010
- NeuroNexus. Optoelectrode Arrays, O-Series. *Datasheet, NeuroNexus Technologies*. 2010; <http://www.neuronexustech.com/LinkClick.aspx?fileticket=05CpCpgm7-U%3d&tabid=114>, last access 21.09.2010
- Neves HP and Ruther P. The NeuroProbes Project. *Proceedings of the 29th Annual International Conference of the IEEE/EMBS, Aug.22-26, Lyon, France*. 2007. 6442-6444
- Niebur E, Koch C, and Rosin C. An Oscillation-Based Model for the Neuronal Basis of Attention. *Vision Research*. 1993; 33(18): 2789-2802
- Niedermeyer E and Lopes da Silva FH. *Electroencephalography: Basic Principles, Clinical Applications, and Related Fields*. Philadelphia: Lippincott Williams & Wilkins. 2005

- Nikles SA, Pellinen DS, Kitagawa J, Bradley RM, Kipke DR, and Najafi K. Long Term In Vitro Monitoring of Polyimide Microprobe Electrical Properties. *Proceedings of the 25th Annual International Conference of the IEEE EMBS, Sept. 17-21, Cancun, Mexico*. 2003. 3340-3343
- Nordström M, Zauner DA, Boisen A, and Hübner J. Single-Mode Waveguides With SU-8 Polymer Core and Cladding for MOEMS Applications. *Journal of Lightwave Technology*. 2007; 25(5): 1284-1289
- Nunez PL and Srinivasan R. *Electric Fields of the Brain: the Neurophysics of EEG*. 2 ed. New York: Oxford University Press. 2006
- O'Keefe J and Bouma H. Complex Sensory Properties of Certain Amygdala Units in the Freely Moving Cat. *Experimental Neurology*. 1969; 23(3): 384-398
- O'Keefe J and Recce ML. Phase Relationship Between Hippocampal Place Units and the EEG Theta Rhythm. *Hippocampus*. 1993; 3(3): 317-330
- octave. GNU octave, version 3.0.1; <http://www.octave.org>. 2009.
- Ogawa S, Lee TM, Kay AR, and Tank TW. Brain Magnetic Resonance Imaging with Contrast Dependent on Blood Oxygenation. *Proceedings of the National Academy of Sciences*. 1990; 87(24): 9868-9872
- Olamat AE, *Physical and FEM Simulation of Microprobe Insertion into a Model of Brain Tissue*. Master's Thesis, Institute of Signal Processing, Universität zu Lübeck, Germany. 2010.
- Otto KJ, Johnson MD, and Kipke DR. Voltage Pulses Change Neural Interface Properties and Improve Unit Recordings with Chronically Implanted Microelectrodes. *IEEE Transactions on Biomedical Engineering*. 2006; 53(2): 333-340
- Palay SL and Palade GE. The Fine Structure of Neurons. *J Biophysic and Biochem Cytol*. 1955; 1(1): 69
- Pattee RW, McConica CM, and Baughman K. Polyimide Film Properties and Selective LPCVD of Tungsten on Polyimide. *Journal of The Electrochemical Society: Solid-State Science and Technology*. 1988; 135(6): 1477-1483
- Pellinen DS, Moon T, Vetter RJ, Miriani R, and Kipke DR. Multifunctional Flexible Polyimide-Based Intracortical Microelectrodes. *Proceedings of the IEEE Engineering in Medicine and Biology 27th Annual Conference, Shanghai, China, Sept 1-4*. 2005. 5272-5275
- Penfield W and Boldrey E. Somatic Motor and Sensory Representation in the Cerebral Cortex of Man as Studied by Electrical Stimulation. *Brain*. 1937; 60(4): 389-443
- Pereira EAC, Green AL, Nandi D, and Aziz TZ. Deep Brain Stimulation: Indications and Evidence. *Expert Review of Medical Devices*. 2007; 4(5): 591-603
- Pesaran B. Uncovering the Mysterious Origins of Local Field Potentials. *Neuron*. 2009; 61(1): 1-2
- Pesaran B, Nelson MJ, and Andersen RA. Free Choice Activates a Decision Circuit Between Frontal and Parietal Cortex. *Nature*. 2008; 453: 406-409

- Pesaran B, Pezaris JS, Sahani M, Mitra PP, and Andersen RA. Temporal Structure in Neuronal Activity During Working Memory in Macaque Parietal Cortex. *Nature Neuroscience*. 2002; 5(8): 805-811
- Petersen SE, Fox PT, Posner MI, Mintun M, and Raichle ME. Positron Emission Tomographic Studies of the Cortical Anatomy of Single-Word Processing. *Nature*. 1988; 331(6157): 585-589
- Pfeuffer J, van de Moortele P-F, Yacoub E, Shmuel A, Adriany G, Andersen P, Merkle H, Garwood M, Ugurbil K, and Hu X. Zoomed Functional Imaging in the Human Brain at 7 Tesla with Simultaneous High Spatial and High Temporal Resolution. *NeuroImage*. 2002; 17(1): 272-286
- Phelps ME, Hoffman EJ, Mullani MA, and Ter-Pogossian MM. Application of Annihilation Coincidence Detection to Transaxial Reconstruction Tomography. *Journal of Nuclear Medicine*. 1975; 16(3): 210
- Piruska A, Bhagat AAS, Zhou K, Peterson ETK, Papautsky I, and Seliskar CJ. Characterization of SU-8 Optical Multimode Waveguides for Integrated Optics and Sensing on Microchip Devices. *P SPIE*. 2006; 6112: 611207-1-611207-8
- Pistohl T, Ball T, Schulze-Bonhage A, Aertsen A, and Mehring C. Prediction of Arm Movement Trajectories from ECoG-Recordings in Humans. *Journal of Neuroscience Methods*. 2007; 167(1): 105-114
- Polikov VS, Tresco PA, and Reichert WM. Response of Brain Tissue to Chronically Implanted Neural Electrodes. *Journal of Neuroscience Methods*. 2005; 148(1): 1-18
- Posner MI, Petersen SE, Fox PT, and Raichle ME. Localization of Cognitive Operations in the Human Brain. *Science*. 1988; 240(4859): 1627-1631
- Prutchi D, Norris M, and . *Design and Development of Medical Electronic Instrumentation - A Practical Perspective of the Design, Construction, and Test of Medical Devices*. Hoboken, New Jersey: John Wiley & Sons. 2005
- Purves D and Williams SM. *Neuroscience*. Sunderland, MA: Sinauer Associates. 2001
- Ramón y Cajal S. *Recuerdos de mi vida*. 3 ed. Madrid: Imprenta de Juan Pueyo. 1923
- Ratner BD and Bryant SJ. Biomaterials: Where We Have Been Going and Where We Are Going. *Annual Review of Biomedical Engineering*. 2004; 6: 41-75
- Ree M, Chen K-J, Kirby DP, Katzenellenbogen N, and Grischkowsky D. Anisotropic Properties of High-Temperature Polyimide Thin Films: Dielectric and Thermal-Expansion Behaviors. *Journal of Applied Physics*. 1992; 72(5): 2014-2021
- Reed GT and Knights AP. *Silicon Photonics: an Introduction*. Chichester: John Wiley & Sons. 2004
- Reitböck HJ and Werner G. Multi-Electrode Recording System for the Study of Spatio-Temporal Activity Patterns of Neurons in the Central Nervous System. *Cellular and Molecular Life Sciences*. 1983; 39(3): 339-341
- Richardson Jr RR, Miller JA, and Reichert WM. Polyimides as Biomaterials: Preliminary Biocompatibility Testing. *Biomaterials*. 1993; 14(8): 627-635

- Rickert J, Cardoso de Oliveira S, Vaadia E, Aertsen A, Rotter S, and Mehring C. Encoding of Movement Direction in Different Frequency Ranges of Motor Cortical Local Field Potentials. *Journal of Neuroscience*. 2005; 25(39): 8815-8824
- Rijkhoff NJM. Neuroprostheses to Treat Neurogenic Bladder Dysfunction: Current Status and Future Perspectives. *Child's Nervous System*. 2004; 20: 75-86
- Robblee LS and Rose TL. Electrochemical guidelines for selection of protocols and electrode materials for neural stimulation. in WF Agnew and DB McCreery, Eds. *Neural Prostheses - Fundamental Studies*. 1 ed. Englewood Cliffs, New Jersey: Prentice Hall. 1990. pp. 25-66
- Rodger DC, Fong AJ, Li W, Ameri H, Ahuja AK, Gutierrez C, Lavrov I, Zhong H, Menon PR, Meng E, Burdick JW, Roy RR, Edgerton VR, Weiland JD, Humayun MS, and Tai Y-C. Flexible Parylene-Based Multielectrode Array Technology for High-Density Neural Stimulation and Recording. *Sensors and Actuators B: Chemical*. 2008; 132: 449-460
- Rodriguez FJ, Ceballos D, Schuettler M, Valero-Cabre A, Valderrama E, Stieglitz T, and Navarro X. Polyimide Cuff Electrodes for Peripheral Nerve Stimulation. *Journal of Neuroscience Methods*. 2000; 98(2): 105-118
- Roelfsema PR, Engel AK, Konig P, and Singer W. Visuomotor Integration is Associated with Zero Time-Lag Synchronization Among Cortical Areas. *Nature*. 1997; 385(6612): 157-161
- Rohatgi P, Langhals NB, Kipke DR, and Patil PG. In Vivo Performance of a Microelectrode Neural Probe with Integrated Drug Delivery. *Neurosurg Focus*. 2009; 27(1): 1-11
- Roopun AK, LeBeau FEN, Ramell J, Cunningham MO, Traub RD, and Whittington MA. Cholinergic Neuromodulation Controls Directed Temporal Communication in Neocortex in Vitro. *Frontiers in Neural Circuits*. 2010; 4(8)
- Roskies AL. The Binding Problem. *Neuron*. 1999; 24(1): 7-9
- Rousche PJ and Kipke DR. Future FES Systems - Next Generation of Cortical Devices. in KW Horch and GS Dhillon, Eds. *Neuroprosthetics - Theory and Practice*. Singapore: World Scientific Publishing Co. Pte. Ltd. 2004. pp. 1197-1216
- Rousche PJ, Pellinen DS, Pivin Jr DP, Williams JC, Vetter RJ, and Kipke DR. Flexible Polyimide-Based Intracortical Electrode Arrays with Bioactive Capability. *IEEE Transactions on Biomedical Engineering*. 2001; 48(3): 361-371
- Rubehn B, Bosman C, Oostenveld R, Fries P, and Stieglitz T. A MEMS-Based Flexible Multichannel ECoG-Electrode Array. *Journal of Neural Engineering*. 2009a; 6(3): 036003
- Rubehn B, Fries P, and Stieglitz T. MEMS-Technology for Large-Scale, Multichannel ECoG-Electrode Array Manufacturing. *4th European Conference of the International Federation for Medical and Biological Engineering*. 2009b. 2413-2416
- Rubehn B and Stieglitz T. Measurement of Defects in Spin Coated Polyimide Films. *Proc of the 29th Ann Internat Conf of the IEEE EMBS*. 2007a. 183-185

- Rubehn B and Stieglitz T. In Vitro Evaluation of the Long-Term Stability of Polyimide as a Material for Neural Implants. *Biomaterials*. 2010a; 31(13): 3449-3458
- Rubehn B and Stieglitz T. Mechanische Langzeitstabilität von Polyimid als Substratmaterial für Mikrotechnisch Gefertigte Implantate. *Biomed Tech*. 2007b. 2 pages
- Rubehn B. non-published measurements. *Laboratory for Biomedical Microtechnology, University of Freiburg - IMTEK, Germany*. 2010b;
- Rubehn B, Lewis C, Fries P, and Stieglitz T. Flexible Shaft Electrodes for Transdural Implantation and Chronic Recording. *Proceedings of the 15th Annual Conference of the IFESS, Sept.8-12, Vienna, Austria*. 2010c
- Rubehn B and Stieglitz T. A Flexible Neural Shaft Electrode with Integrated Optical Waveguide. *44.Jahrestagung der Deutschen Gesellschaft für Biomedizinische Technik, Oct.5-8, Rostock-Warnemünde, Germany*. 2010d
- Russell TP. A Small-Angle X-Ray Scattering Study of an Aromatic Polyimide. *Journal of Polymer Science: Polymer Physics*. 1984; 22(6): 1105-1117
- Ruther P, Frey O, Herwik S, Kisban S, Seidl K, Spieth S, Schumacher A, Koudelka-Hep M, Paul O, Stieglitz T, and Zengerle R. The NeuroProbes Project-Multifunctional Probe Arrays for Neural Recording and Stimulation. *Proceedings of the 13th Annual Conference of the IFESS, Sept. 21-25, Freiburg, Germany*. 2008; Biomed. Tech., Vol. 53 (2008) Suppl. 1: 238-240
- Sah P, Westbrook RF, and Lüthi A. Fear Conditioning and Long-term Potentiation in the Amygdala. *Annals of the New York Academy of Sciences*. 2008; 1129: 88-95
- Salcman M and Bak MJ. Design, Fabrication, and in Vivo Behavior of Chronic Recording Intracortical Microelectrodes. *IEEE Transactions on Biomedical Engineering*. 1973; 20(4): 253-260
- Salcman M and Bak MJ. A New Chronic Recording Intracortical Microelectrode. *Medical and Biological Engineering and Computing*. 1976; 14: 42-50
- Salinas E and Sejnowski TJ. Impact of Correlated Synaptic Input on Output Firing Rate and Variability in Simple Neuronal Models. *Journal of Neuroscience*. 2000; 20(16): 6193-6209
- Scheirs J. *Compositional and Failure Analysis of Polymers: a Practical Approach* John Wiley and Sons. 2000. 410
- Scherberger H, Fineman I, Musallam S, Dubowitz DJ, Bernheim KA, Pesaran B, Corneil BD, Gilliken B, and Andersen RA. Magnetic Resonance Image-Guided Implantation of Chronic Recording Electrodes in the Macaque Intraparietal Sulcus. *Journal of Neuroscience Methods*. 2003; 130(1): 1-8
- Scherberger H, Jarvis MR, and Andersen RA. Cortical Local Field Potential Encodes Movement Intentions in the Posterior Parietal Cortex. *Neuron*. 2005; 46(2): 347-354
- Schmidt EM, Bak MJ, and McIntosh JS. Long-Term Chronic Recording from Cortical Neurons. *Experimental Neurology*. 1976; 52(3): 496-506

- Schramm J and Clusmann H. The Surgery of Epilepsy. *Neurosurgery*. 2008; 62(2): 463-481
- Schuettler M, Koch KP, and Stieglitz T. Investigations on Explanted Micromachined Nerve Electrodes. *Proceedings of the 8th Annual International Conference of the IFESS, Jul 1-5, Maroochydore, Australia*. 2003. 306-310
- Schuettler M, Seetohul V, Taylor J, and Donaldson NdN. Velocity-Selective Recording from Frog Nerve Using a Multi-Contact Cuff Electrode. *Proceedings of the 28th Annual International Conference of the IEEE EMBS, Aug 31 - Sep 3, New York, USA*. 2006. 2962-2965
- Schuettler M and Stieglitz T. 18polar Hybrid Cuff Electrodes for Stimulation of Peripheral Nerves. *Proceedings of the 5th Annual Conference of the IFESS, Jun 18-20, Aalborg, Denmark*. 2000. 265-268
- Schuettler M, Stiess S, King BV, and Suaning GJ. Fabrication of Implantable Microelectrode Arrays by Laser Cutting of Silicone Rubber and Platinum Foil. *Journal of Neural Engineering*. 2005; 2(1): S121-S128
- Schulze-Bonhage A. Deep brain stimulation: a new approach to the treatment of epilepsy. *Deutsches Ärzteblatt International*. 2009; 106(24): 407-412
- Schwann T. *Mikroskopische Untersuchungen über die Uebereinstimmung in der Struktur und dem Wachstum der Thiere und Pflanzen*. Berlin: Verlag der Sander'schen Buchhandlung, G.E. Reimer. 1839
- Schwartz AB. Cortical Neural Prosthetics. *Annual Review of Neuroscience*. 2004; 27: 487-507
- Schwartz AB, Cui XT, Weber DJ, and Moran DW. Brain-Controlled Interfaces: Movement Restoration with Neural Prosthetics. *Neuron*. 2006; 52(1): 205-220
- Seitz PR. French Origins of the Cochlear Implant. *Cochlear Implants International*. 2002; 3(2): 77-86
- Seo J, Han C-S, and Han H. Water-Sorption Behaviors of Poly (3,4'-Oxydiphenylene Pyromellitimide) Films Depending on the Thickness Variation. *Journal of Polymer Science Part B: Polymer Physics*. 2001a; 39(6): 669-676
- Seo J and Han H. Water Diffusion Studies in Polyimide Thin Films. *Journal of Applied Polymer Science*. 2001b; 82(3): 731-737
- Seymour JP and Kipke DR. Neural Probe Design for Reduced Tissue Encapsulation in CNS. *Biomaterials*. 2007; 28(25): 3594-3607
- SfN. About the Society for Neuroscience. *Homepage of the Society for Neuroscience*. 2010; [http://www.sfn.org/index.aspx?pagename=about\\_SfN](http://www.sfn.org/index.aspx?pagename=about_SfN), last access: 21.09.2010
- Shamma-Donoghue SA, May GA, Cotter NE, White RL, and Simmons FB. Thin-Film Multielectrode Arrays for a Cochlear Prosthesis. *IEEE Transactions on Electron Devices*. 1982; ED-29(1): 136-144

- Shew BY, Kuo CH, Huang YC, and Tsai YH. UV-LIGA Interferometer Biosensor Based on the SU-8 Optical Waveguide. *Sensors and Actuators A: Physical*. 2005; 120(2): 383-389
- Siegel M and Donner TH. Linking Band-Limited Cortical Activity to fMRI and Behavior. in M Ullsperger and S Debener, Eds. *Simultaneous EEG and fMRI: Recording, Analysis, and Application*. New York: Oxford University Press. 2010.
- Silver IA and Erecinska M. Extracellular Glucose Concentration in Mammalian Brain: Continuous Monitoring of Changes During Increased Neuronal Activity and Upon Limitation in Oxygen Supply in Normo-, Hypo-, and Hyperglycemic Animals. *Journal of Neuroscience*. 1994; 14(8): 5068-5076
- Singer W. Synchronization of Cortical Activity and its Putative Role in Information Processing and Learning. *Annual Review of Physiology*. 1993; 55(1): 349-374
- Singer W and Gray CM. Visual Feature Integration and the Temporal Correlation Hypothesis. *Annual Review of Neuroscience*. 1995; 18(1): 555-586
- Singer W. Neuronal Synchrony: A Versatile Code for the Definition of Relations? *Neuron*. 1999; 24(1): 49-65
- Singh A, Zhu H, and He J. Improving Mechanical Stiffness of Coated Benzocyclobutene (BCB) Based Neural Implant. *Proceedings of the 26th Annual International Conference of the IEEE EMBS, Sep 1-5, San Francisco, USA*. 2004. 4298-4301
- Sirota A. personal communication. *Center for Integrative Neuroscience, University of Tuebingen*. 2010;
- Slutzky MW, Jordan LR, Krieg T, Chen M, Mogul DJ, and Miller LE. Optimal Spacing of Surface Electrode Arrays for Brain-Machine Interface Applications. *Journal of Neural Engineering*. 2010; 7(2): 1-9
- Smith R, Williams DF, and Oliver C. The Biodegradation of Poly(Ether Urethanes). *Journal of Biomedical Materials Research*. 1987; 21: 1149-1166
- Snyder AW and Love JD. *Optical Waveguide Theory*. Dordrecht: Kluwer Academic Publishers. 1983
- Sonn M and Feist WM. A Prototype Flexible Microelectrode Array for Implant-Prosthesis Applications. *Medical and Biological Engineering and Computing*. 1974; 12(6): 778-791
- Sotelo C. Viewing the Brain Through the Master Hand of Ramon y Cajal. *Nature Reviews Neuroscience*. 2003; 4(1): 71-77
- Spurk JH and Aksel N. *Fluid Mechanics*. 2 ed. Berlin Heidelberg: Springer-Verlag. 2008
- Squire LR, Bloom FE, Spitzer NC, du Lac S, Ghosh A, and Berg D. *Fundamental Neuroscience*. 3 ed. Burlington, San Diego, London: Academic Press. 2008
- Srinivasan R, Russell DP, Edelman GM, and Tononi G. Increased Synchronization of Neuromagnetic Responses during Conscious Perception. *Journal of Neuroscience*. 1999; 19(13): 5435-5448

- Sroog CE. History of the Invention and Development of the Polyimides. in Ghosh MK and Mittal KL, Eds. *Polyimides: Fundamentals and Applications*. New York: Marcel Dekker. 1996. pp. 1-6
- Staba RJ, Wilson CL, Bragin A, Fried I, and Engel J, Jr. Quantitative Analysis of High-Frequency Oscillations (80-500 Hz) Recorded in Human Epileptic Hippocampus and Entorhinal Cortex. *Journal of Neurophysiology*. 2002; 88(4): 1743-1752
- Starr PA, Rau GM, Davis V, Marks WJ, Jr., Ostrem JL, Simmons D, Lindsey N, and Turner RS. Spontaneous Pallidal Neuronal Activity in Human Dystonia: Comparison With Parkinson's Disease and Normal Macaque. *Journal of Neurophysiology*. 2005; 93(6): 3165-3176
- Stensaas SS and Stensaas LJ. Histopathological evaluation of materials implanted in the cerebral cortex. *Acta Neuropathologica*. 1978; 41(2): 145-155
- Stieglitz T. Materials for Stimulation and Recording - Electrode Materials for Recording and Stimulation. in KW Horch and GS Dhillon, Eds. *Neuroprosthetics - Theory and Practice*. Singapore: World Scientific Publishing Co. Pte. Ltd. 2004. pp. 475-516
- Stieglitz T, *Konzept und Entwicklung einer Flexiblen Elektrode zur Multi-Interfaszikulären Ableitung von Elektroneurogrammen und zur Stimulation am Peripheren Nerven*. Dissertation an der Technische Fakultät der Universität des Saarlandes, 1998.
- Stieglitz T. Flexible Biomedical Microdevices with Double-Sided Electrode Arrangements for Neural Applications. *Sensors and Actuators A: Physical*. 2001; A 90: 203-211
- Stieglitz T, Beutel H, Keller R, Blau C, and Meyer J-U. Development of Flexible Stimulation Devices for a Retina Implant System. *Proceedings of the 19th Annual International Conference of the IEEE EMBS, Oct 30 - Nov 2, Chicago (USA)*. 1997a. 2307-2310
- Stieglitz T, Beutel H, and Meyer J-U. A Flexible, Light-Weighted Multichannel Sieve Electrode with Integrated Cables for Interfacing Regenerating Peripheral Nerves. *Sensors and Actuators A: Physical*. 1997b; 60(1-3): 240-243
- Stieglitz T, Beutel H, Schuettler M, and Meyer J-U. Micromachined, Polyimide-Based Devices for Flexible Neural Interfaces. *Biomedical Microdevices*. 2000; 2(4): 283-294
- Stieglitz T, Rubehn B, Henle C, Kisban S, Herwik S, Ruther P, and Schuettler M. Brain-Computer Interfaces: An Overview of the Hardware to Record Neural Signals from the Cortex. *Progress in Brain Research*. 2009; 175: 297-315
- Stieglitz T, Ruf HH, Gross M, Schuettler M, and Meyer J-U. A Biohybrid System to Interface Peripheral Nerves after Traumatic Lesions: Design of a High Channel Sieve Electrode. *Biosensors and Bioelectronics*. 2002; 17(8): 685-696
- Stieglitz T. Integration of Microfluidic Capabilities into Micromachined Neural Implants. *International Journal of Micro-Nano Scale Transport*. 2010; 1(2): 139-158
- Stone JL and Miles ML. Skull Trepanation among the Early Indians of Canada and the United States. *Neurosurgery*. 1990; 26(6): 1015-1020
- Strobl G. *The Physics of Polymers: Concepts for Understanding their Structures and Behavior*. 3 ed. Berlin Heidelberg: Springer Verlag. 2007. 417-424



- Strumwasser F. Long-Term Recording from Single Neurons in Brain of Unrestrained Mammals. *Science*. 1958; 127(3296): 469-470
- SU-8 3000. Datasheet. *Microchem Corp.*, Newton, MA, USA. 2010;
- Sun Y, Lacour SP, Brooks RA, Rushton N, Fawcett JW, and Cameron RE. Assessment of the Biocompatibility of Photosensitive Polyimide for Implantable Medical Device Use. *Journal of Biomedical Materials Research Part A*. 2008; 90(3): 648-655
- Suner S, Fellows MR, Vargas-Irwin C, Nakata GK, and Donoghue JP. Reliability of Signals from a Chronically Implanted, Silicon-Based Electrode Array in Non-Human Primate Primary Motor Cortex. *IEEE Transactions on Neural Systems and Rehabilitation Engineering*. 2005; 13(4): 524-541
- Suzuki T, Kotake N, Mabuchi K, and Takeuchi S. Flexible Regeneration-Typ Nerve Electrode with Integrated Microfluidic Channels. *Proceedings of the International Conference on Microtechnology in Medicine and Biology, May 9-12, Okhawa, Japan*. 2006. 303-305
- Suzuki T, Mabuchi K, and Takeuchi S. A 3D Flexible Parylene Probe Array for Multichannel Neural Recording. *Proceedings of the 1st International IEEE EMBS Conference on Neural Engineering, Mar 20-22, Capri Island, Italy*. 2003. 154-156
- Swartz BE and Goldensohn ES. Timeline of the History of EEG and Associated Fields. *Electroencephalography and Clinical Neurophysiology*. 1998; 106(2): 173-176
- Takahashi H, Ejiri T, Nakao M, Nakamura N, Kaga K, and Herve T. Microelectrode Array on Folding Polyimide Ribbon for Epidural Mapping of Functional Evoked Potentials. *IEEE Transactions on Biomedical Engineering*. 2003; 50(4): 510-516
- Takekoshi T. Synthesis of Polyimides. in Ghosh MK and Mittal KL, Eds. *Polyimides: Fundamentals and Applications*. New York: Marcel Dekker. 1996. pp. 7-48
- Takeuchi S, Ziegler D, Yoshida Y, Mabuchi K, and Suzuki T. Parylene Flexible Neural Probes Integrated with Microfluidic Channels. *Lab on a Chip*. 2005; 5(5): 519-523
- Tanaka A, Sawada H, and Wakatsuki N. New Plastic Optical Fiber Using Polycarbonate Core. *Fujitsu Scientific and Technical Journal*. 1987; 23(3): 166-176
- Thomas. Datasheet: 4 Core Multielectrode. *Thomas Recording GmbH*. 2010; [www.ThomasRecording.com](http://www.ThomasRecording.com), last access 15.09.2010
- Thornell G. Lilliputian Reflections. *Proceedings of the Micro Structure Workshop (MSW'98), Mar 24-25, Uppsala, Sweden*. 1998. 24.1-24.6
- Tsytsarev V, Taketani M, Schottler F, Tanaka S, and Hara M. A New Planar Multielectrode Array: Recording from a Rat Auditory Cortex. *Journal of Neural Engineering*. 2006; 3(4): 293-298
- Unger MA, Chou H-P, Thorsen T, Scherer A, and Quake SR. Monolithic Microfabricated Valves and Pumps by Multilayer Soft Lithography. *Science*. 2000; 288(5463): 113-116
- Ungerstedt U. Microdialysis - Principles and Applications for Studies in Animals and Man. *Journal of Internal Medicine*. 2009; 230(4): 365-373

- Urban GA. Micro- and Nanobiosensors - State of the Art and Trends. *Measurement Science and Technology*. 2009; 20(1): 012001
- van Alsten JG and Coburn JC. Structural Effects on the Transport of Water in Polyimides. *Macromolecules*. 1994; 27(14): 3746-3752
- van der Wijngaart W, *Designing Microfluidic Control Components*. Dissertation, Microsystem Technology - Department of Signals, Sensors and Systems. Royal Institute of Technology, Stockholm. 2002.
- van Rotterdam A. Biophysical Aspects of EEG and MEG Generation. in E Niedermeyer and F Lopes da Silva, Eds. *Electroencephalography: Basic Principles, Clinical Applications and Related Fields*. 1 ed. Baltimore, Munich: Urban & Schwarzenberg. 1982. pp. 15-26
- Varela F, Lachaux J-P, Rodriguez E, and Martinerie J. The Brainweb: Phase Synchronization and Large-Scale Integration. *Nat Rev Neurosci*. 2001; 2(4): 229-239
- Verzeano M. Activity of Cerebral Neurons in the Transition from Wakefulness to Sleep. *Science*. 1956; 124(3217): 366-367
- Voskerician G, Shive MS, Shawgo RS, Recum Hv, Anderson JM, Cima MJ, and Langer R. Biocompatibility and Biofouling of MEMS Drug Delivery Devices. *Biomaterials*. 2003; 24(11): 1959-1967
- Waldert S, Pistohl T, Braun C, Ball T, Aertsen A, and Mehring C. A Review on Directional Information in Neural Signals for Brain-Machine Interfaces. *Journal of Physiology - Paris*. 2009; 103(3-5): 244-254
- Ward MP, Rajdev P, Ellison C, and Irazoqui PP. Toward a Comparison of Microelectrodes for Acute and Chronic Recordings. *Brain Research*. 2009; 1282: 183-200
- Weber J and Czarnetzki A. Trepanationen im frühen Mittelalter im Südwesten von Deutschland - Indikationen, Komplikationen und Outcome. *Zentralblatt für Neurochirurgie*. 2001; 62: 10-14
- Weiland JD and Anderson DJ. Chronic Neural Stimulation with Thin-Film, Iridium Oxide Electrodes. *IEEE Transactions on Biomedical Engineering*. 2000; 47(7): 911-918
- Weiland JD, Humayun MS, Liu W, and Greenberg RJ. Stimulating Neural Activity. in WE Finn and PG LoPresti, Eds. *Handbook of Neuroprosthetic Methods*. Boca Raton, Florida: CRC Press. 2003.
- Wells J, Konrad P, Kao C, Jansen ED, and Mahadevan-Jansen A. Pulsed Laser Versus Electrical Energy for Peripheral Nerve Stimulation. *Journal of Neuroscience Methods*. 2007; 163: 326-337
- Wernicke C. *Der aphasische Symptomencomplex: eine psychologische Studie auf anatomischer Basis*. Breslau: Cohn & Weigert. 1874
- Wheeler RA, Roitman MF, Grigson PS, and Carelli RM. Single Neurons in the Nucleus Accumbens Track Relative Reward. *International Journal of Comparative Psychology*. 2005; 18(4): 320-332
- Wichmann T and DeLong MR. Deep Brain Stimulation for Neurologic and Neuropsychiatric Disorders. *Neuron*. 2006; 52(1): 197-204

- Wilke M, Logothetis NK, and Leopold DA. Local Field Potential Reflects Perceptual Suppression in Monkey Visual Cortex. *Proceedings of the National Academy of Sciences*. 2006; 103(46): 17507-17512
- Williams JC, Hippensteel JA, Dilgen J, Shain WG, and Kipke DR. Complex Impedance Spectroscopy for Monitoring Tissue Responses to Inserted Neural Implants. *Journal of Neural Engineering*. 2007; 4(4): 410-423
- Wilson GS and Gifford R. Biosensors for Real-Time in Vivo Measurements. *Biosensors and Bioelectronics*. 2005; 20(12): 2388-2403
- Wilson MA and McNaughton BL. Dynamics of the hippocampal ensemble code for space. *Science*. 1993; 261(5124): 1055-1058
- Wise KD. Silicon Microsystems for Neuroscience and Neural Prostheses. *IEEE Engineering in Medicine and Biology Magazine*. 2005; 24(5): 22-29
- Wise KD, Anderson DJ, Hetke JF, Kipke DR, and Najafi K. Wireless Implantable Microsystems: High-Density Electronic Interfaces to the Nervous System. *Proceedings of the IEEE*. 2004; 92(1): 76-96
- Wise KD, Angell JB, and Starr A. An Integrated Circuit Approach to Extracellular Microelectrodes. *Digest of the 8th ICMBE*. 1969. 14
- Wise KD, Angell JB, and Starr A. An Integrated-Circuit Approach to Extracellular Microelectrodes. *IEEE Transactions on Biomedical Engineering*. 1970; BME-17(3): 238-247
- Wolbarsht ML, MacNichol EF, and Wagner HG. Glass Insulated Platinum Microelectrode. *Science*. 1960; 132(3436): 1309-1310
- Wolff S. personal communication. *Friedrich Miescher Institute, Basel, Switzerland*. 2010;
- Womelsdorf T, Fries P, Mitra PP, and Desimone R. Gamma-Band Synchronization in Visual Cortex Predicts Speed of Change Detection. *Nature*. 2006; 439: 733-736
- Womelsdorf T, Johnston K, Vinck M, and Everling S. Theta-Activity in Anterior Cingulate Cortex Predicts Task Rules and their Adjustments Following Errors. *Proceedings of the National Academy of Sciences*. 2010; 107(11): 5248-5253
- Womelsdorf T, Schoffelen J-M, Oostenveld R, Singer W, Desimone R, Engel AK, and Fries P. Modulation of Neuronal Interactions Through Neuronal Synchronization. *Science*. 2007a; 316: 1609-1612
- Womelsdorf T and Fries P. The Role of Neuronal Synchronization in Selective Attention. *Current Opinion in Neurobiology*. 2007b; 17(2): 154-160
- Wong CH, Birkett J, Byth K, Dexter M, Somerville E, Gill D, Chaseling R, Fearnside M, and Bleasel A. Risk Factors for Complications During Intracranial Electrode Recording in Presurgical Evaluation of Drug Resistant Partial Epilepsy. *Acta Neurochirurgica*. 2009; 151(1): 37-50
- Wypych G. Plasticizer Motion and Diffusion. in Wypych G, Ed. *Handbook of Plasticizers*. Toronto: ChemTec Publishing. 2004. pp. 151-170

- Yang DK, Koros WJ, Hopfenberg HB, and Stannett VT. Sorption and Transport Studies of Water in Kapton Polyimide.I. *Journal of Applied Polymer Science*. 1985; 30(3): 1035-1047
- Yang DK, Koros WJ, Hopfenberg HB, and Stannett VT. The Effects of Morphology and Hygrothermal Aging on Water Sorption and Transport in Kapton® Polyimide. *Journal of Applied Polymer Science*. 1986; 31(6): 1619-1629
- Yang R and Wang W. A Numerical and Experimental Study on Gap Compensation and Wavelength Selection in UV-Lithography of Ultra-High Aspect Ratio SU-8 Microstructures. *Sensors and Actuators B: Chemical*. 2005; 110(2): 279-288
- Yeager JD, Phillips DJ, Rector DM, and Bahr DF. Characterization of Flexible ECoG Electrode Arrays for Chronic Recording in Awake Rats. *Journal of Neuroscience Methods*. 2008; 173(2): 279-285
- Yoshida K, Pellinen D, Pivin D, Rousche P, and Kipke DR. Development of the Thin-Film Longitudinal Intrafascicular Electrode. *Proceedings of the 5th Annual Conference of the IFESS, Jun 18-21, Aalborg, Denmark*. 2000. 279-284
- Young M. *Optics and Lasers: Including Fibers and Optical Waveguides*. 5 ed. Berlin Heidelberg: Springer-Verlag. 2000
- Zappe HP. *Introduction to Semiconductor Integrated Optics*. 1 ed. Norwood, MA: Artech House, Inc. 1995. i-xx; 1-371
- Zhang F, Wang L-P, Brauner M, Liewald JF, Kay K, Watzke N, Wood PG, Bamberg E, Nagel G, Gottschalk A, and Deisseroth K. Multimodal Fast Optical Interrogation of Neural Circuitry. *Nature*. 2007a; 446(5): 633-641
- Zhang F, Aravanis AM, Adamantidis A, de Lecea L, and Deisseroth K. Circuit-Breakers: Optical Technologies for Probing Neural Signals and Systems. *Nature Reviews Neuroscience*. 2007b; 8(8): 577-581
- Zhang J, Laiwalla F, Kim JA, Urabe H, Van Wagenen R, Song Y-K, Connors BW, and Nurmikko AV. A Microelectrode Array Incorporating an Optical Waveguide Device for Stimulation and Spatiotemporal Electrical Recording of Neural Activity. *31st Annual International Conference of the IEEE EMBS, Sept.2-6, Minneapolis, MN, USA*. 2009a. 2046-2049
- Zhang J, Laiwalla F, Kim JA, Urabe H, Wagenen RV, Song Y-K, Connors BW, Zhang F, Deisseroth K, and Nurmikko AV. Integrated Device for Optical Stimulation and Spatiotemporal Electrical Recording of Neural Activity in Light-Sensitized Brain Tissue. *Journal of Neural Engineering*. 2009b; 6(5): 1-13
- Zhong Y and Bellamkonda RV. Biomaterials for the Central Nervous System. *Journal of The Royal Society Interface*. 2008; 5(26): 957-975
- Ziemann O, Krauser J, Zamzow PE, and Daum D. *POF Handbook - Optical Short Range Transmission Systems*. 2 ed. Berlin Heidelberg: Springer-Verlag. 2008
- Zorzos A, Fonstad Jr. CG, and Boyden E. Light-proof Electrodes for In-situ Monitoring of Neural Function. *Microsystems Technology Laboratories (MIT) Annual Research Report*. 2009; <http://www-mtl.mit.edu/research/ar.html>, last access 22.09.2010

- Zrenner E, Wilke R, Sachs H, Bartz-Schmidt K, Gekeler F, Besch D, Greppmaier U, Harscher A, Peters T, Wrobel G, Wilhelm B, Bruckmann A, and Stett A. Visual Sensations Mediated by Subretinal Microelectrode Arrays Implanted into Blind Retinitis Pigmentosa Patients. *Proceedings of the 13th Annual Conference of the IFESS, Sept.21-25, Freiburg, Germany.* 2008
- Zubia J and Arrue J. Plastic Optical Fibers: An Introduction to Their Technological Processes and Applications. *Optical Fiber Technology.* 2001; 7(2): 101-140

## Own Publications

### Peer Reviewed Journal Articles

Rubehn B, Bosman C, Oostenveld R, Fries P, and Stieglitz T. A MEMS-Based Flexible Multichannel ECoG-Electrode Array. *Journal of Neural Engineering*. 2009; 6(3): 036003

Rubehn B and Stieglitz T. In Vitro Evaluation of the Long-Term Stability of Polyimide as a Material for Neural Implants. *Biomaterials*. 2010; 31(13): 3449-3458

Stieglitz T, Rubehn B, Henle C, Kisban S, Herwik S, Ruther P, and Schuettler M. Brain-Computer Interfaces: An Overview of the Hardware to Record Neural Signals from the Cortex. *Progress in Brain Research*. 2009; 175: 297-315

Bosman CA, Schoffelen J-M, Oostenveld R, Womelsdorf T, Brunet N, Rubehn B, Stieglitz T, de Weerd P, and Fries P. Stimulus Selection through Selective Synchronization between Monkey Visual Areas. *in preparation*

Esmailbeigi H, Rubehn B, Stieglitz T, and Rousche PJ. Micro-Fabrication of 3-Dimensional Neurotrophic Flexible Polyimide-Based Electrodes. *in preparation*

### Peer Reviewed Conference Contributions

Kisban S, Rubehn B, and Stieglitz T. Investigations on the Mechanical Strength of Flexible Microimplants. *Proceedings der gemeinsamen Jahrestagung der Deutschen, Österreichischen und Schweizerischen Gesellschaft für Biomedizintechnik, Zürich, Sep.6-9. 2006*

Rubehn B, Kisban S, and Stieglitz T. Mechanical Characterization of Flexible Substrates for Neural Microimplants. *Proceedings of the 11th Annual Conference of the IFESS, Sep.12-15, Miyagi-Zao, Japan. 2006; 106-108*

Rubehn B and Stieglitz T. Measurement of Defects in Spin Coated Polyimide Films. *Proceedings of the 29th Annual International Conference of the IEEE EMBS, Aug.23-26, Lyon, France. 2007; 183-185*

Kisban S, Herwik S, Seidl K, Rubehn B, Jezzini A, Umilta MA, Fogassi L, Stieglitz T, Paul O, and Ruther P. Microprobe Array with Low Impedance Electrodes and Highly Flexible Polyimide Cables for Acute Neural Recording. *Proceedings of the 29th Annual International Conference of the IEEE EMBS, Aug.23-26, Lyon, France. 2007; 175-178*

Rubehn B and Stieglitz T. Mechanische Langzeitstabilität von Polyimid als Substratmaterial für Mikrotechnisch Gefertigte Implantate. *41. Jahrestagung der Deutschen Gesellschaft für Biomedizinische Technik, Sep.26-29, Aachen, Germany. 2007, in Biomedizinische Technik 52, Suppl., Proc. BMT 2007, ISSN 09394990*

- Ruther P, Herwik S, Kisban S, Seidl K, Spieth S, Rubehn B, Haj Hosseini N, Steigert J, Daub M, Paul O, Stieglitz T, Zengerle R, and Neves HP. NeuroProbes - Development of Modular Multifunctional Probe Arrays for Neuroscience. *Proceedings of the Mikrosystemtechnik Kongress, Oct.15-17. 2007*; 739-742
- Schuettler M, Triantis IF, Rubehn B, and Stieglitz T. Matrix Cuff Electrodes for Fibre and Fascicle Selective Peripheral Nerve Recording and Stimulation. *Proceedings of the 12th Annual Conference of the IFESS, Philadelphia, PA, USA. 2007*; 4th Paper of Session 9
- Stieglitz T, Rubehn B, Henle C, and Schuettler M. Comparison of Two Different Approaches to Manufacture Electrode Arrays for Epicortical Brain-Machine-Interfaces. *Materials Research Society (MRS) Spring Meeting, Symposium M: Materials and Technology for Flexible, Conformable, and Stretchable Sensors and Transistors, Mar.24-28, San Francisco, USA. 2008*; M12.4
- Kisban S, Moser D, Rubehn B, Stieglitz T, Paul O, and Ruther P. Fatigue Testing of Polyimide-Based Micro Implants. In: J. van der Sloten, P. Verdonck, M. Nyssen, & L. Haueisen (Eds.), *4th European Conference of the International Federation for Medical and Biological Engineering (ECIFMBE 2008, IFMBE Proceedings 22)*, Nov.23–27, Antwerp, Belgium, 2008; 1594-1597
- Rubehn B, Fries P, and Stieglitz T. MEMS-Technology for Large-Scale, Multichannel ECoG-Electrode Array Manufacturing. In: J. van der Sloten, P. Verdonck, M. Nyssen, and L. Haueisen (Eds.), *4th European Conference of the International Federation for Medical and Biological Engineering (ECIFMBE 2008, IFMBE Proceedings 22)*, Nov.23–27, Antwerp, Belgium, 2008; 2413–2416
- Esmailbeigi H, Rubehn B, Stieglitz T, and Rousche PJ. Development of a Novel 3-Dimensional Neurotrophic Neural Interface for an Auditory Cortical Prosthesis. *BMES Annual Meeting, Oct.7-10, Pittsburgh, PA, USA. 2009*
- Bosman C, Womelsdorf T, Oostenveld R, Rubehn B, De Weerd P, Stieglitz T, and Fries P. 252-Site Subdural LFP Recordings in Monkey Reveal Large-Scale Effects of Selection Attention. *7th Computational and Systems Neuroscience Meeting COSYNE, Feb.25-28, Salt Lake City, USA. 2010*; III-8
- Rubehn B, Lewis C, Fries P, and Stieglitz T. Flexible Shaft Electrodes for Transdural Implantation and Chronic Recording. *Proceedings of the 15th Annual Conference of the IFESS, Sep.8-12, Vienna, Austria, 2010*; *Artificial Organs. 34*(8): abstr.no.60
- Townsend B, Stitt I, Engler G, Engel AK, Rubehn B, and Stieglitz T. Development of a Thin-Film Array for Cortical Stimulation. *Proceedings of the 15th Annual Conference of the IFESS, Sep.8-12, Vienna, Austria, 2010*; *Artificial Organs. 34*(8): abstr.no.79

Rubehn B and Stieglitz T. A Flexible Neural Shaft Electrode with Integrated Optical Waveguide. *44. Jahrestagung der Deutschen Gesellschaft für Biomedizinische Technik, Oct.5-8, Rostock-Warnemünde, Germany.* 2010

Rubehn B and Stieglitz T. Mechanical Long-term Stability of Polyimide as a Material for Neural Implants. *Materials Research Society (MRS) Fall Meeting, Symposium OO: Multiscale Mechanics of Hierarchical Biological, Bioinspired, and Biomedical Materials, Nov.28-Dec.3, Boston, USA.* 2010; OO5.3

## Other Publications

Stieglitz T, Rubehn B, Henle C, and Schuettler M. Brain Computer Interfaces for Recording and Stimulation. *Weltkongress für Orthopädie und Rehatechnik, May 21-24, Leipzig, Germany.* 2008

Rubehn B, Fries P, and Stieglitz T. MEMS-Basierte Flexible Elektrodenarrays für (Epi-) Kortikale Sonden in den Neurowissenschaften. *2. Dresdner Medizintechnik Symposium, Dec.1-3. Dresden, Germany.* 2008

Stieglitz T, Rubehn B, Henle C, Meier W, and Schuettler M. Gehirn-ComputerSchnittstellen zur Ableitung und Stimulation. *Orthopädie-Technik.* 2009; 376-382

Bosman CA, Womelsdorf T, Oostenveld R, Rubehn B, De Weerd P, Stieglitz T, and Fries P. 252-Site Subdural LFP Recordings in Monkey Reveal Large-Scale Effects of Selective Attention. *7th Forum of European Neuroscience - FENS, Jul.3-7, Amsterdam, The Netherlands.* 2010; Abstr. vol 5, 139.1

Micheli C, Bosman CA, Womelsdorf T, Oostenveld R, Rubehn B, De Weerd P, Stieglitz T, and Fries P. Combining High-Density Electrocorticography (ECoG) in Macaque Monkey with Source Reconstruction. *7th Forum of European Neuroscience - FENS, Jul.3-7, Amsterdam, The Netherlands.* 2010; Abstr. vol 5, 139.13

Bosman CA, Womelsdorf T, Oostenveld R, Rubehn B, De Weerd P, Stieglitz T, and Fries P. 252-site subdural LFP recordings in monkeys unveil dynamical interareal communication modulated by selective attention. *40th annual meeting of the Society of Neuroscience, Nov.13-17, San Diego, CA, USA.* 2010; 413.5/OOO47



## Awards

Rubehn B, Bosman C, Oostenveld R, Fries P, and Stieglitz T. A MEMS-Based Flexible Multichannel ECoG-Electrode Array. *Journal of Neural Engineering*. 2009; 6(3): 036003

This journal publication was one out of eleven article selected as the *Highlights 2009* by the Journal of Neural Engineering:

“A selection of papers that highlight the very best research published in Journal of Neural Engineering during 2009. A special collection of papers that represent the breadth and excellence of the work published in the journal last year. The articles were selected for their presentation of outstanding new research, receipt of the highest praise from our international referees and the highest number of downloads last year.”

(<http://iopscience.iop.org/1741-2552/page/Highlights%202009>)

Page 174 contains personal information (CV) and is therefore not included in the online publication.

## Acknowledgements

I am very thankful for the excellent time I had at IMTEK and in Freiburg while working on my thesis. This was due to a lot of people.

First of all, I want to thank my supervisor Prof. Dr. Thomas Stieglitz who gave me the opportunity to work in his laboratory and who introduced me to the fascinating world of neuroprosthetics. I am very grateful for his everlasting support, the freedom to conduct my own research ideas, the kind working atmosphere and the immediate response whenever things had to happen fast.

I also want to express my gratitude to Prof. Dr. Ulrich Hofmann (Institute for Signal Processing, University of Lübeck) for his instant and cheerful acceptance to co-referee my thesis.

Many thanks to my neuroscientific partners Prof. Dr. Pascal Fries, Dr. Conrado Bosman, Dr. Robert Oostenveld, and Chris Lewis at the Donders Institute for Brain, Cognition and Behaviour (Radboud University, Nijmegen, The Netherlands) and the Ernst Strüngmann Institute (Frankfurt am Main) who always supplied me with information, neural data, and good ideas and who managed to never break my MEMS-based implants. They all made our cooperation easy, productive and great fun. Special thanks go to Pascal who spent a lot of his precious time to acquaint me with state-of-the-art neuroscience. Working with such a dedicated scientist was a constant source of motivation for me.

Furthermore, I would like to thank Steffen Wolff and Dr. Philip Tovote of Andreas Lüthi's group at the Friedrich Miescher Institute (Basel, Switzerland) for the fruitful collaboration during the development of the multimodal shaft electrodes. They implanted these electrodes into mice and helped me to characterize the light transmission of the optical waveguides in their lab.

Special thanks go to the IMTEK-RSC cleanroom staff. Without them keeping the cleanroom up and running and their all-embracing process knowledge, this work would not have been possible. Their instant help and infinite patience listening to everything that could possibly go wrong lit up even my darkest hours of cleanroom processing.

You are the heart of IMTEK - keep up the good work!

Large parts of this thesis were conducted within the project "The Hybrid Brain" of the Bernstein Focus Neurotechnology Freiburg/Tübingen. I gratefully acknowledge the financial support of the German Federal Ministry of Education and Research (BMBF grant 01GQ0830) which made the work within this project possible.

A big thank you goes to all my colleagues of the Laboratory for Biomedical Microtechnology who are responsible for the great atmosphere in our group and without whom this work would not have been possible. Special thanks go to Dr. Martin Schüttler who was never at a loss for a good tip and Dr. Benjamin Townsend who read large parts of this

## Acknowledgements

---

thesis and tutored me in English and neuroscience. Thanks to my room mates Christina Haßler and René von Metzen for their pleasant company throughout the years.

I want to thank my diploma students Sebastian Kisban, Stefan Reimers and Tim Boretius who explained the fields of material testing, fluidics and optics to me and my student assistants Tobi Holzhammer, Nils Lass and Nora Haas who were a great help in the clean-room and during the long-term material testing.

Many thanks to the staff of the Laboratory for Micro-optics (IMTEK) who let me work in their lab and always had a helping hand. I would especially like to thank Bernd Aatz who searched the labs for all the devices I needed and explained them to me and Dr. Andreas Seifert who helped me to understand the properties of my waveguides.

A warm thank you belongs to all my other IMTEK colleagues who were always willing to help and to share their knowledge and expertise with me.

I want to conclude this thesis by thanking my family and friends who all were responsible for the right environment which made me able to write this thesis. I particularly want to thank

my parents for their support especially throughout my diploma studies and for raising me the way they did – I could not think of better parents,

my sister Heike for her skillful help which kept me from losing my countenance while working with You-Know-Which software,

the AHS Triathlon (Universität Freiburg) and the Tri Team Freiburg for keeping me sane and healthy and for all the fun I had,

the Black Forest for being always there for me and for all the countless hours I was allowed to spend beneath its trees and on its meadows alone or with good friends,

my boyfriend Jan for his all-embracing support and for bringing exact the right amounts of calm and excitement into my life.

Vielen Dank euch allen!

Freiburg im Oktober 2010